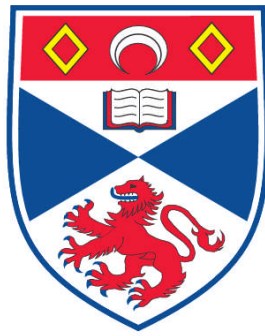


**THE PROPAGATION AND DAMPING OF SLOW
MAGNETOACOUSTIC WAVES IN THE SOLAR ATMOSPHERE**

Nicholas Robert Owen

**A Thesis Submitted for the Degree of PhD
at the
University of St. Andrews**



2012

**Full metadata for this item is available in
Research@StAndrews:FullText
at:**

<http://research-repository.st-andrews.ac.uk/>

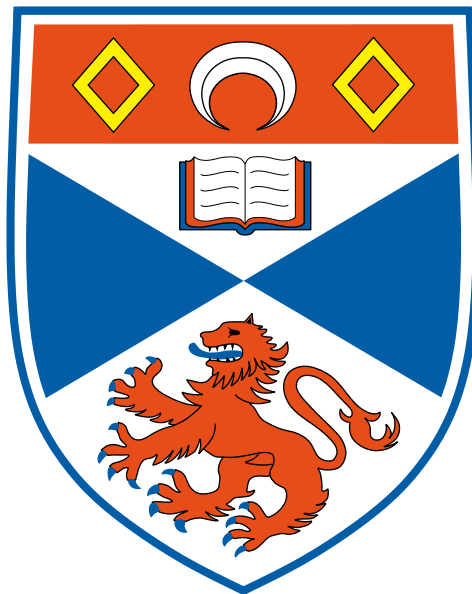
Please use this identifier to cite or link to this item:

<http://hdl.handle.net/10023/3215>

This item is protected by original copyright

The Propagation and Damping of Slow Magnetoacoustic Waves in the Solar Atmosphere

Nicholas Robert Owen



Thesis submitted for the degree of Doctor of Philosophy
of the University of St Andrews

30 November 2011

Abstract

The propagation and damping of slow magnetoacoustic waves in the solar atmosphere is investigated, with particular emphasis placed on waves with periodicities of five minutes. The basic model of a uniform temperature loop is extended by the addition of an equilibrium temperature gradient allowing study of wave propagation from the transition region to the corona. The inclusion of thermal conduction produces a phase shift between the perturbations in velocity, density and temperature, which for a non-uniform equilibrium temperature varies along the loop and may be observable as a phase shift between intensity and Doppler shift observations. Forward modelling of the simulation results, for both constant and non-constant equilibrium temperature profiles, is undertaken in order to establish the observational consequences for TRACE, SoHO/CDS and Hinode/EIS. Slow waves propagating in a non-uniform equilibrium temperature loop are seen to damp rapidly in the corona, however, as a result of the ionisation balance, the inclusion of damping can actually increase the amplitude of some parts of the oscillation.

The ability of several data analysis techniques to identify oscillation signatures are examined. In particular, empirical mode decomposition was found to be a very useful technique for extracting oscillations from a wide range of data sets and is capable of intrinsically determining background trends. Co-spatial and co-temporal TRACE 171 Å, CDS and EIS data are analysed for evidence of propagating slow waves. Slow waves with periods of 210 s to 370 s are found with amplitudes of 1.2% to 3.4% in the corona and 2.3% to 6.0% in the transition region.

Declaration

1. Candidates declarations:

I, Nicholas Robert Owen, hereby certify that this thesis, which is approximately 50,000 words in length, has been written by me, that it is the record of work carried out by me and that it has not been submitted in any previous application for a higher degree.

I was admitted as a research student in October 2006 and as a candidate for the degree of Doctor of Philosophy in October 2007; the higher study for which this is a record was carried out in the University of St Andrews between 2006 and 2011.

Signature:..... **Date:**

2. Supervisors declaration:

I hereby certify that the candidate has fulfilled the conditions of the Resolution and Regulations appropriate for the degree of Doctor of Philosophy in the University of St Andrews and that the candidate is qualified to submit this thesis in application for that degree.

Signature:..... **Date:**

3. Permission for electronic publication:

In submitting this thesis to the University of St Andrews I understand that I am giving permission for it to be made available for use in accordance with the regulations of the University Library for the time being in force, subject to any copyright vested in the work not being affected thereby. I also understand that the title and the abstract will be published, and that a copy of the work may be made and supplied to any bona fide library or research worker, that my thesis will be electronically accessible for personal or research use unless exempt by award of an embargo as requested below, and that the library has the right to migrate my thesis into new electronic forms as required to ensure continued access to the thesis. I have obtained any

third-party copyright permissions that may be required in order to allow such access and migration, or have requested the appropriate embargo below.

The following is an agreed request by candidate and supervisor regarding the electronic publication of this thesis:

- (i) Access to printed copy and electronic publication of thesis through the University of St Andrews.

Signature of Candidate:.....

Signature of Supervisor:.....

Date:

Acknowledgements

I would like to acknowledge CASE funding from PPARC/STFC and from RAL. Big thanks to Richard, Danielle and everybody at RAL, especially the football team, for making it such a fun place to be. I am grateful to Alan for suggesting the topic for my last chapter and to Clare for being supportive and understanding with my corrections. I am also grateful to Chris Brady for all the early coding work he put in. Thanks to all my friends, Lisa, Joe, Pete, Owain, Annie, Moony, Emily and Helen for being so great and for always being there for me. Sorry I have been so quiet over the last few years. Lisa, Joe, Pete, Owain, Moony and Helen, I really appreciate that you all came up to visit, it was always fun, particularly as, without fail, Pete always brought gorgeous sunshine. Special thanks to Moony, you are the only one who truly knows what its like. Believe it or not but life was actually pretty good fun when you were around, I will always miss midnight corridor Frisbee. Although you and your "pet" moving in to Scooniehill Road was without doubt the worst day of my life! Biggest thanks of all my friends goes to Owain for always reminding me you are there and for being completely amazing as well as very patient and understanding. Lawrence, I am really proud of you, especially for being brave enough to change and move on when you saw something better. I have always looked up to you, more then I am sure you realise, and its you above everything else that always makes me try my best. Wherever you are I will always be there for you. Louise its true, I really cannot believe that someone so unforgettable thinks that I am unforgettable too. You have made, and will always make, my life so much better than I ever imagined. Despite everything, one look from you and I smile. We really are perfect together. Its time to get the man you fell in love with back. The biggest thanks of all have to go to Mum and Dad, you have always been there for me and for Louise and I know you always will be. I know Lawrence and I have not made life very easy for you lately, but you still never fail to support us. I physically could not have done these last two months without you, let alone the rest before that. There are no better parents in the world, not even close. Do not worry, I am still glad of my choice, whats five years in a lifetime of being happy, bubbly and smiley.

Contents

Declaration	2
Contents	i
1 Introduction	1
1.1 The Sun	1
1.1.1 The Transition Region and the Solar Corona	2
1.2 Magnetohydrodynamics	3
1.2.1 MHD Waves	5
1.3 Coronal Seismology	6
1.3.1 Propagating Slow Magnetoacoustic Waves	7
1.4 Instruments	9
1.5 Outline of Thesis	10
2 Slow Wave Simulations	11
2.1 Introduction	11
2.2 Wave Theory	12
2.3 Lare1d Code and Model	13
2.3.1 Gravitational Stratification	14
2.3.2 Model Conditions	16
2.3.3 Boundary Conditions	16
2.4 Code Testing At Uniform Temperature Equilibrium	18
2.4.1 Ideal Medium	18
2.4.2 Gravitationally Stratified Medium	20
2.4.3 Optically Thin Radiation	22
2.4.4 Compressive Viscosity	24
2.4.5 Optically Thin Radiation, Compressive Viscosity and Gravitational Stratification	26
2.4.6 Thermal Conduction	27
2.4.7 All Damping Mechanisms	36
2.4.8 All Damping Mechanisms and Gravitational Stratification	37

2.5	Non-Uniform Temperature Equilibrium	37
2.5.1	Without Gravitational Stratification Or Damping	39
2.5.2	Gravitationally Stratified Medium	41
2.5.3	Compressive Viscosity	42
2.5.4	Thermal Conduction	43
2.5.5	Compressive Viscosity and Thermal Conduction	46
2.5.6	Compressive Viscosity, Thermal Conduction and Gravitational Stratification	48
2.6	Simulation Conclusions	48
3	Forward Modelling	50
3.1	Introduction	50
3.1.1	Forward Modelling Code	51
3.2	Intensity along the Loop	53
3.2.1	Uniform Temperature Equilibrium	53
3.2.2	Non-Uniform Equilibrium Temperature	65
3.3	Intensity as a Function of Time	69
3.4	Forward Modelling Conclusions	74
4	Data Analysis Techniques	77
4.1	Introduction	77
4.2	Techniques and Data Analysis	79
4.2.1	Single Oscillation	80
4.2.2	Multiple Oscillations	91
4.2.3	Beat Wave	97
4.2.4	EMD Boundary Conditions	99
4.2.5	Time Dependent Oscillation	101
4.2.6	Reduced Cadence	106
4.3	Data Analysis Conclusions	109
5	Slow Wave Observations	112
5.1	Introduction	112
5.2	TRACE and CDS Observations	114
5.2.1	30th April 2003	114
5.2.2	29th April 2003	124
5.3	TRACE, CDS and EIS Observations	130
5.4	Observations Conclusions	134
6	Conclusions	136
	Appendix A: Thomas Algorithm in Lare1d	141

Appendix B: TRACE and CDS Observations

143

Bibliography

149

Chapter 1

Introduction

1.1 The Sun

The Sun is a fairly typical star which is roughly half way through its 9.6 billion year life time. It has a mass of 1.99×10^{30} kg and a radius of 6.96×10^5 km (696 Mm or $1 R_{\odot}$), making it around 330,000 times the mass and a hundred times the radius of the Earth. What makes the Sun unique amongst the myriad of stars in the universe is its proximity to us. The distance from the Sun to the Earth is 1.5×10^8 km or 1 AU, whereas the distance to our next nearest star, Proxima Centauri, is around 267,000 AU. This vast difference makes the Sun very special as we feel its effects every day and are able to study it in far greater detail than any other star.

The Sun consists of two main parts, the interior and the atmosphere. Starting from the centre and moving outwards, the solar interior consists of the core (0 to $0.25 R_{\odot}$), the radiative zone ($0.25 R_{\odot}$ to $0.71 R_{\odot}$) and the convection zone ($0.71 R_{\odot}$ to $1 R_{\odot}$) and is linked to the solar atmosphere by the photosphere (depth of 550 km), which is the visible surface of the Sun that we see. The solar atmosphere contains the chromosphere (width of around 2000 km), the transition region (width of around 100 km - 200 km) and the corona. By mass, the Sun consists of 74% Hydrogen, 24% Helium and 1% other elements which is in the form of an ionised gas called a plasma. In the Sun's core the Hydrogen is converted to Helium by nuclear fusion, producing solar neutrinos, and consequently heats the core to temperatures of around 15 MK.

Globally the Sun is in hydrostatic equilibrium, where the inward pressure from gravitational collapse is balanced by outward radiation pressure. The 15 MK temperature and the 1.6×10^5 kg m⁻³ density decrease radially from the Sun's core. By $0.25 R_{\odot}$ the temperature has fallen to around 7 MK and the density to 1.3×10^4 kg m⁻³, which are too low for nuclear fusion to occur. This is the start of the radiative zone, so named because the energy flowing through it is mainly transported by radiative diffusion. At $0.71 R_{\odot}$ the temperature drops below 2 MK, with a density of 100 kg m⁻³, and Hydrogen atoms form. These atoms are very efficient at absorbing photons, which limits the energy flow by radiation, and so here, at the start of the convection zone, energy is mainly transported by convection. Above the convection zone is a

thin layer called the photosphere, where the temperature is between 6600 K and 4400 K and the density $3 \times 10^{-4} \text{ kg m}^{-3}$.

Due to the high density below the photosphere the mean free path, that is the distance that emitted photons can travel before being absorbed, is short (compared to the radius of the Sun). Consequently, photons travel only a short distance before being absorbed and cannot travel directly to us, hence the interior of the Sun is opaque and cannot be directly observed. Energy gradually flows from the core, but photons that reach the surface have been absorbed and emitted many times. This process takes the photons around 170,000 years to travel from the core to the photosphere. The lower density of the photosphere allows photons emitted in this region to escape without being reabsorbed, hence the photosphere is visible to us but the interior below is not. We can see around 400 km into the photosphere before it becomes opaque, which is a very short distance compared to the solar radius (696,000 km), giving the Sun the appearance of a very defined surface. As the Sun is opaque below the photosphere it emits radiation almost as an ideal blackbody with the photospheric temperature of 5973 K. Blackbody radiation emitted at this temperature has a wavelength in the visible spectrum, hence the photosphere is visible to us. The outer atmosphere also emits visible light, but the density of this region is far lower than the photosphere, hence the light is masked by the far brighter photospheric emission. This light can be seen during a solar eclipse when the moon blocks the light from the photosphere.

By the top of the photosphere the temperature and density have decreased to 4400 K and $8 \times 10^{-5} \text{ kg m}^{-3}$, respectively. Above this, the density continues to fall, with a density of $10^{-8} \text{ kg m}^{-3}$ in the chromosphere and $10^{-12} \text{ kg m}^{-3}$ at the base of the corona. In contrast, the temperature stops decreasing and starts increasing from 4400 K at the top of the photosphere to 25,000 K in the chromosphere and then rises rapidly to 1 MK at the base of the corona. The region of this rapid rise in temperature is called the transition region and is around 100 km to 200 km thick.

1.1.1 The Transition Region and the Solar Corona

The solar atmosphere and particularly the transition region is of particular interest due to the increase in temperature above the photosphere. The nuclear fusion in the core is the energy source for the entire Sun, with this heat flowing out from the core. However, with this energy source alone it is not possible for the solar atmosphere to be hotter than the photosphere as temperature should decrease with distance from a heat source. The solar atmosphere must therefore contain another heat source or sources that produce heat directly in the atmosphere. This heating mechanism must account for the relatively small increase in the temperature of the chromosphere (4400 K to 25,000 K), the rapid increase in temperature in the transition region (around 1 MK) and the extremely high temperatures of some parts of the corona (above 5 MK). The solar wind also requires energy. The higher density of the chromosphere compared to the corona means that the energy required to heat the chromosphere by 20,000 K (10^3 W m^{-3}) is greater than that required to heat the corona by 1 MK ($8 \times 10^2 \text{ W m}^{-3}$ in quiescent regions). The exact heating mechanism is not entirely clear, although the energy is thought to be provided by either (or both) the release of stored magnetic energy through magnetic reconnection or by the damping of waves, most likely Alfvén waves.

The solar corona is a very dynamic region of the Sun which, due to the low density and the highly ionised

nature of the plasma, is dominated by the Sun's ever changing magnetic field. In the corona the magnetic pressure dominates the plasma pressure and therefore the plasma is guided along magnetic field lines. Additionally, thermal conduction is very low across magnetic field lines compared to along field lines. These two effects result in long and relatively thin loops of plasma called coronal loops. The regions of the corona where the magnetic field is open are called corona holes and here the plasma can flow out of the corona and contribute to the solar wind. The corona consists of regions of quiet Sun and active regions, both of which are dynamic. Many different phenomena are observed in the quiet Sun, including x-ray bright points and prominences or filaments. X-ray bright points are transient features which emit very localised radiation at x-ray wavelengths. Prominences or filaments are coronal regions with much higher density than the surrounding plasma. Active regions contain many coronal loops following closed magnetic field lines where the magnetic field is concentrated and therefore particularly intense. Additionally, active regions contain many dynamical processes such as solar flares where large amounts of stored magnetic energy are released (10^{25} J) and coronal mass ejections where vast amounts of plasma are ejected into space (10^{12} kg). However, some solar flares and coronal mass ejections do not originate in active regions, but in quiescent filaments.

1.2 Magnetohydrodynamics

Due to the high temperatures, the gas that comprises the Sun is ionised and is termed a plasma. In addition, the Sun contains a very strong and dynamic magnetic field which attracts and repels the ions and the electrons of the plasma. This action moves the plasma which alters the electric field and in turn affects the magnetic field. This process results in very complex behaviour which requires the properties of each particle to be calculated in order to fully describe the plasma. The plasma can also be described by kinetic theory, where distribution functions are found for each particle species (i.e. protons or electrons) by averaging over many particles of each species. Despite simplifying the treatment from every particle to the distribution functions of each individual species, the plasma description is still very complex and numerically intensive. This limits the scale and range of plasma processes that can be studied. By simplifying the mathematical treatment further, whilst still maintaining the essential physics, a wider range of phenomenon and processes can be studied.

Magnetohydrodynamics (or simply MHD) is a single fluid description of a conducting fluid, derived by integrating moments of the distribution functions of each species over velocity space. The MHD equations are a combination of Maxwell's equations of electromagnetism and the Navier-Stokes fluid equations, where Ohm's law is used to couple these two sets of equations. The MHD equations consist of Ampere's law and the equations of mass continuity, motion and energy together with a gas law (Priest 1982). Under the MHD approximation, Ampere's law is given by,

$$\mathbf{j} = \frac{\nabla \times \mathbf{B}}{\mu_0}, \quad (1.1)$$

where \mathbf{j} is the current density, \mathbf{B} the magnetic field and μ_0 the magnetic permeability of free space. The displacement current has been neglected from Eq. (1.1) as the plasma velocity is assumed to be non-relativistic,

i.e. $v \ll c$, where c is the speed of light. The magnetic field is subject to the solenoid condition,

$$\nabla \cdot \mathbf{B} = 0. \quad (1.2)$$

The induction equation is derived from the MHD equations using Ampere's law (Eq. (1.1)), Ohm's law,

$$\mathbf{j} = \sigma(\mathbf{E} + \mathbf{v} \times \mathbf{B}), \quad (1.3)$$

and Faraday's law,

$$\nabla \times \mathbf{E} = -\frac{\partial \mathbf{B}}{\partial t}, \quad (1.4)$$

to give,

$$\frac{\partial \mathbf{B}}{\partial t} = \nabla \times (\mathbf{v} \times \mathbf{B}) - \nabla \times (\eta \nabla \times \mathbf{B}), \quad (1.5)$$

where \mathbf{E} is the electric field, σ is the electrical conductivity, \mathbf{v} the velocity, t is time and η is the magnetic diffusivity, which is assumed to remain constant. The equation of mass continuity is given by,

$$\frac{\partial \rho}{\partial t} + \nabla \cdot (\rho \mathbf{v}) = 0, \quad (1.6)$$

where ρ is the plasma density. The equation of motion, which includes the Lorentz force in addition to forces due to gravity and viscosity is defined as,

$$\frac{\partial \mathbf{v}}{\partial t} = -(\mathbf{v} \cdot \nabla) \mathbf{v} - \frac{1}{\rho} \nabla p + \frac{1}{\rho} (\mathbf{j} \times \mathbf{B}) - \mathbf{g} + \nu \nabla^2 \mathbf{v}, \quad (1.7)$$

where p is the plasma pressure, \mathbf{g} the gravitational acceleration and the approximation of compressive viscosity is used with the coefficient of kinematic shear viscosity ν , which is assumed constant (Priest 1982). Note that the viscosity term has been simplified by assuming an incompressible flow and thereby neglecting the bulk viscosity term. The energy equation, which includes thermal conduction, optically thin radiation, background coronal heating, ohmic heating and viscous heating, is given by,

$$\begin{aligned} \frac{\partial \epsilon}{\partial t} = & -\mathbf{v} \cdot \nabla \epsilon - \frac{p}{\rho} \nabla \cdot \mathbf{v} + \frac{1}{\rho} \nabla \cdot (\kappa_{\parallel} \cdot \nabla_{\parallel} T) - \rho \tilde{\chi} T^{\alpha} + \frac{H_0}{\rho} \\ & + \frac{j^2}{\sigma \rho} + \nu \left(\frac{1}{2} \left(\frac{\partial v_i}{\partial x_j} + \frac{\partial v_j}{\partial x_i} \right)^2 - \frac{2}{3} (\nabla \cdot \mathbf{v})^2 \right), \end{aligned} \quad (1.8)$$

where ϵ is the specific internal energy, κ_{\parallel} the coefficient of thermal conduction along magnetic field lines, T the plasma temperature and H_0 is the unknown coronal heating term. The optically thin radiation term is approximated by a piecewise continuous function where the heating coefficients $\tilde{\chi}$ and α are temperature dependant, as given by Priest (1982). It has been assumed that $\kappa_{\perp} \ll \kappa_{\parallel}$, where κ_{\perp} is the coefficient of thermal conduction perpendicular to the magnetic field lines. The assumption of optically thin radiation is valid in the Sun for temperatures greater than $10^{4.3}$ K (Priest 1982). The specific internal energy and the

perfect gas law are given by,

$$\epsilon = \frac{p}{(\gamma - 1)\rho}, \quad (1.9)$$

and

$$p = \frac{\bar{R}\rho T}{\bar{\mu}}, \quad (1.10)$$

respectively, where γ is the ratio of specific heat capacities of the plasma, \bar{R} the molecular gas constant and $\bar{\mu}$ is the mean atomic weight.

A single fluid model can be used when collisionality is sufficiently high to keep the plasma velocity distribution close to a Maxwell-Boltzmann distribution. The spatial and temporal scales over which these collisions occur are characterised by the mean free path, λ_m , and the collision time, τ_c , respectively, in addition to the Debye length, λ_D , which is the distance outside of which the action of a single ion can be neglected due to shielding from many ions. The assumption of a single fluid is valid if the collision time is shorter than typical timescales, τ , and the mean free path and the Debye length are much less than the typical length scales, L , of the plasma. Therefore, the MHD approximation is valid if $\tau_c \ll \tau$, $\lambda_m \ll L$ and $\lambda_D \ll L$. The collision time in the corona is of order 10^{-2} s, which is much shorter than the typical period of coronal oscillations, which range from seconds to tens of minutes. The mean free path and the Debye length in the corona are around 6×10^4 m and 0.01 m, respectively, which are both far smaller than the typical length (10^7 m to 10^8 m) of an active region loop (Priest 1982). They are also far smaller than the wavelength, λ , of a sound wave with five minute periodicity travelling along such a loop at 1 MK ($\lambda = 4.5 \times 10^7$ m).

1.2.1 MHD Waves

The Sun is a compressible plasma that can support magnetoacoustic and Alfvén waves, which have been observed throughout both the solar interior and the solar atmosphere. The behaviour of waves in the Sun can be very complicated due to plasma structuring by strong magnetic fields, density stratification and non-uniform temperatures. Using MHD, the behaviour and nature of waves in the Sun can be studied and understood. There are three distinct types of MHD waves with different properties, namely, Alfvén, fast magnetoacoustic and slow magnetoacoustic.

In an ideal gas a sound wave causes compressions and rarefactions that propagate isotropically at the sound speed, c_s , given by,

$$c_s = \sqrt{\frac{\gamma p}{\rho}} = \sqrt{\frac{\gamma \bar{R} T}{\bar{\mu}}}. \quad (1.11)$$

A sound wave is a velocity, density and pressure perturbation. However, oscillations in a conducting plasma such as the corona also cause an associated magnetic perturbation, hence they are no longer sound waves, but magnetic disturbances. The magnetic field causes anisotropic wave propagation with different propa-

gation speeds. The propagation speed of a magnetic disturbance is given by either the Alfvén speed, v_A , or by a combination of the sound and Alfvén speeds. The Alfvén speed is given by,

$$v_A = \frac{B}{\sqrt{\mu_0 \rho}}. \quad (1.12)$$

The importance of the magnetic field in a region can be quantified by the plasma beta, β , which is the ratio of the plasma and magnetic pressures, defined as,

$$\beta = \frac{2\mu_0 p}{B^2}. \quad (1.13)$$

In the corona, typical values of the temperature ($T = 10^6$ K), the density ($\rho = 10^{-12}$ kg m⁻³) and the magnetic field strength ($B = 10^{-3}$ T) give $\beta \sim 10^{-2}$. Therefore, in the corona the magnetic pressure is greater than the plasma pressure, hence the properties of waves within this region are strongly affected by the magnetic field. The plasma beta can be related to the ratio of the square of the sound and Alfvén speeds,

$$\beta = \frac{2}{\gamma} \frac{c_s^2}{v_A^2}, \quad (1.14)$$

which, in the corona, gives a sound speed that is much slower than the Alfvén speed. Of the three wave types only the Alfvén wave is incompressible and does not cause compressions and rarefactions of the plasma. It is a transverse oscillation which propagates at the Alfvén speed in the direction of the magnetic field. Both the fast and slow magnetoacoustic waves are compressible, thereby affecting the plasma pressure as they propagate. These two waves travel at speeds which are a combination of the sound and Alfvén speeds. The fast wave propagates almost isotropically with a maximum speed, c_f , perpendicular to the magnetic field,

$$c_f^2 = c_s^2 + v_A^2, \quad (1.15)$$

whereas the slow wave propagates anisotropically guided along magnetic field lines at a speed, c_T ,

$$c_T^2 = \frac{c_s^2 v_A^2}{c_s^2 + v_A^2}. \quad (1.16)$$

If $\beta \ll 1$ and hence $c_s^2 \ll v_A^2$ then Eq. (1.16) becomes $c_T^2 \approx c_s^2$ and slow waves propagate at approximately the sound speed. In the absence of a magnetic field only the fast magnetoacoustic wave exists, which travels isotropically at the sound speed. The exact nature and properties of these waves depends on the geometry and the properties of the medium through which they propagate and can be very complex. An overview of MHD wave theory in the solar atmosphere is given by Roberts (2004).

1.3 Coronal Seismology

The area of helioseismology probes the inside of the Sun by analysing solar vibrations. This is analogous to how vibrations from earthquakes are used to determine the structure of the Earth's interior. Similarly in coronal seismology, coronal waves and oscillations are studied to determine properties of the corona.

Global coronal seismology was originally proposed by Uchida (1970) and Roberts et al. (1984) suggested the use of local coronal seismology combining MHD wave theory and observations in order to determine properties of the solar corona. Wave parameters such as periods, amplitudes and propagation speeds are measured and compared to theoretical models to give estimates of, for example, the coronal magnetic field strength. Determining the magnetic field strength of the corona is particularly important as the effects of the magnetic field dominate the coronal plasma. A large number of MHD waves have been observed in the solar atmosphere including both fast and slow mode oscillations. Overviews of the waves observed are extensive and can be found in, for example, Erdélyi et al. (2003); Aschwanden (2004); Wang (2004); Nakariakov and Verwichte (2005); De Moortel (2005, 2006) and more recently in Banerjee et al. (2007) and De Moortel (2009).

1.3.1 Propagating Slow Magnetoacoustic Waves

Sound waves of varying frequencies (p-modes) are excited by turbulent convection and propagate through the interior of the Sun. Interference between these waves produces a global oscillation with a period of around five minutes which causes the solar surface to vibrate with this same period. These p-modes are generally treated as purely acoustic waves due to the high plasma beta ($\beta \sim 10^2$), although within sunspots $\beta \sim 1$. As these waves propagate through the atmosphere the magnetic field becomes increasingly dominant, hence, these sound waves are guided by magnetic field lines and termed slow magnetoacoustic waves. Wave propagation in a gravitationally stratified medium is governed by the Klein-Gordon equation (Eq. (11) of Roberts 2004), which contains an acoustic cut off frequency, Ω_c , which, for an isothermal atmosphere, is given by,

$$\Omega_c = \frac{\gamma g}{2c_s}. \quad (1.17)$$

Using Eq. (1.11), the acoustic cut off period, P_c , can be written as,

$$P_c = \frac{4\pi}{g} \sqrt{\frac{\bar{R}T}{\gamma\bar{\mu}}}. \quad (1.18)$$

This acoustic cut off period is lowest at the top of the photosphere where the solar temperature minimum is located. Waves with periods above this should not propagate into the solar atmosphere and are termed evanescent. Using $g = 274 \text{ m s}^{-1}$, $\bar{R} = 8.3 \times 10^3 \text{ m}^2 \text{ s}^{-2} \text{ K}^{-1}$, $\gamma = 5/3$, $\bar{\mu} = 0.6$ and $T = 4400 \text{ K}$ gives an acoustic cut off period of $P_c \approx 280 \text{ s}$, hence sound waves with oscillation periods of five minutes are in theory evanescent. However, slow magnetoacoustic waves in the solar corona with periods of around five minutes have been observed. Waves propagating along inclined field lines experience a reduced gravitational attraction compared to waves propagating radially outwards and hence, have a lower cut off frequency which allows wave leakage into the solar atmosphere (De Pontieu et al. 2005; McIntosh and Jefferies 2006).

Propagating intensity perturbations have been detected in the corona, firstly in polar plumes by Ofman et al. (1997) using SoHO/UVCS and by DeForest and Gurman (1998) with SoHO/EIT. These intensity oscillations have been interpreted as propagating slow waves (Ofman et al. 1999, 2000b). Such oscillations have

also been observed along coronal loops with SoHO/EIT (Berghmans and Clette 1999) and with TRACE (Nightingale et al. 1999; Schrijver et al. 1999; De Moortel et al. 2000). Oscillations with a periodicity of five minutes have been observed simultaneously with SoHO/EIT and TRACE 171 Å (Robbrecht et al. 2001) as well as with TRACE 171 Å and TRACE 195 Å (King et al. 2003). Marsh et al. (2003, 2004) and Marsh and Walsh (2006) detected oscillations with periodicity of five minutes using co-temporal and co-spatial observations from TRACE 171 Å and SoHO/CDS. Oscillations were detected over a temperature range of 35,000 K to 1 MK, covering the chromosphere, the transition region and the corona. Two statistical studies with many detections of propagating slow waves are given in De Moortel et al. (2002a,b) and McEwan and De Moortel (2006), where the oscillations were observed to damp rapidly and were only detected in the corona for 8.9 ± 4.4 Mm.

The observations of propagating intensity oscillations have prompted many theoretical studies in order to interpret the phenomenon. Nakariakov et al. (2000) presented a 1D theoretical model interpreting propagating intensity oscillations as slow magnetoacoustic waves. The model included viscosity, thermal conduction, gravity and non-linear effects and was further developed by Tsiklauri and Nakariakov (2001). De Moortel and Hood (2003, 2004); De Moortel et al. (2004a) performed numerical simulations of the damping of slow waves for the solar corona with an atmosphere of uniform equilibrium temperature. This work compared theoretically predicted damping rates with those observed by TRACE and examined the effects of damping due to compressive viscosity, thermal conduction, optically thin radiation and mode coupling. They also included gravitational stratification and field line divergence and found that a combination of thermal conduction, gravitational stratification and field line divergence was capable of explaining the rapid damping observed. Propagating acoustic waves are discussed by Klimchuk et al. (2004) in the context of coronal seismology. By using a combination of analytical theory, numerical modelling and data analysis they found that the main effects on intensity perturbations are due to pressure and temperature stratification and dissipation due to thermal conduction.

By studying these damping mechanisms and wave propagation throughout the solar atmosphere the importance and effects of each mechanism can be seen. Knowledge of wave propagation and damping is also of general interest to increase the use and accuracy of work in the field of coronal seismology. In particular, it may be possible to investigate the structuring of coronal loops below the spatial resolution of observations using propagating slow waves (King et al. 2003; Nakariakov and Verwichte 2005). If a loop consisted of multiple strands (which were not resolved) at different temperatures, slow waves would propagate along each strand at a different speed. Consequently, observations of the same loop from emission lines sensitive to different temperatures would give different propagation speeds. However, note that the interpretation of the observations of propagating disturbances discussed above as slow magnetoacoustic waves has been questioned recently (Wang (2011) and references therein). It is argued that these intensity variations are due to periodic plasma flows rather than waves (De Pontieu and McIntosh 2010), where for flows both energy and matter propagate, rather than just energy as for waves.

1.4 Instruments

Observations are essential in order to improve our understanding of the Sun both by directly observing processes and by constraining and guiding theoretical models. As mentioned previously, the transition region and the corona mainly emit radiation at EUV wavelengths. The Earth's atmosphere absorbs most of this radiation and therefore space based instruments are required. The Transition Region and Coronal Explorer (TRACE, Handy et al. 1999) and the Solar and Heliospheric Observatory (SoHO, Domingo et al. 1995) are two spaced based instruments launched in the 1990's which vastly improved the available observational data for the Sun and its atmosphere. In particular, high cadence and spatial resolution allowed many coronal oscillations to be observed. The lack of oscillation detections with Yohkoh is most likely due to a low filling factor, that is, only a fraction of an observed region emits radiation at a particular wavelength.

TRACE is an imaging telescope which has a field of view of typically $512''$ by $512''$ and can therefore observe many different solar features. TRACE observes in eight different passbands over a wavelength range of 171 \AA to 5000 \AA . These passbands are sensitive to radiation within a particular wavelength range, for example the 171 \AA passband detects radiation from 160 \AA to 189 \AA . This filtering of wavelength allows radiation emitted from specific ions which exist at specific temperatures to be observed. These ions and temperatures are found using atomic modelling such as CHIANTI (Dere et al. 1997). However, these observations can still contain contributions from many different emission lines and can therefore be difficult to interpret. For example, the 171 \AA passband contains contributions from 34 emission lines from O II to O VII and Fe VI to Fe XXVI, corresponding to a temperature range of 0.16 MK to 2 MK.

SoHO contains 12 different instruments to study various regions of, and processes in, the Sun. For example, GOLF (Gabriel et al. 1995) and VIRGO (Fröhlich et al. 1995) study helioseismology, MDI (Scherrer et al. 1995) measures the photospheric magnetic field and the solar atmosphere is observed by an imager EIT (Delaboudinière et al. 1995) and three spectrometers (SUMER (Wilhelm et al. 1995), UVCS (Kohl et al. 1995) and CDS (Harrison et al. 1995)). Spectrometers such as the Coronal Diagnostic Spectrometer (CDS) observe radiation in even narrower passbands than those of TRACE. For example the CDS Mg x 624 \AA line observes radiation for a 5 \AA range from 622 \AA to 627 \AA . This results in emission from a few or perhaps even a single ion, giving observations of the Sun which are easier to interpret than wider passbands. CDS detects radiation over a wavelength range of 150 \AA to 800 \AA which is sensitive to temperatures from 10^4 K to several 10^6 K , allowing the Sun to be studied in detail for a range of temperatures. Additionally, spectroscopic observations allow the line of sight velocity to be determined. However, the wavelength resolution reduces the two spatial dimensions to one spatial dimension. Therefore, CDS produces one dimensional images with a thin rectangular slit compared to two dimensional images from TRACE.

Hinode (Kosugi et al. 2007) was launched in 2006 and contains three instruments to study the Sun in optical, EUV and x-ray wavelengths. Of particular interest for observing coronal oscillations is the Extreme Ultraviolet Imaging Spectrometer (EIS, Culhane et al. 2007) which observes two wavelength ranges from 170 \AA to 210 \AA and 250 \AA to 290 \AA , corresponding to temperatures between 0.04 MK and 20 MK. By using a wide slot rather than a narrow slit, EIS is able to make spectroscopic observations over a larger field of view.

An important method to aid understanding of the physical processes occurring in the Sun is forward mod-

elling. Using the density and temperature profiles from theoretical models, instrument response functions and data from chemical models, forward modelling recreates the observations of a particular instrument. By comparing forward modelling results with actual observations, theoretical models can be constrained and made more realistic, allowing the dominant physical processes to be identified and understood.

1.5 Outline of Thesis

The propagation and damping of slow magnetoacoustic waves from the transition region to the corona is studied theoretically using numerical modelling and the observational properties of these waves are examined using forward modelling. In addition to this, the analysis techniques used to detect such oscillations are investigated and observational data from the transition region and the corona is analysed for evidence of propagating slow waves.

Numerical simulations of propagating slow waves, with periods of five minutes, are undertaken in Chapter 2. This modelling is initially performed for loops with uniform equilibrium temperature before this basic model is extended by the addition of an equilibrium temperature gradient. The model covers a temperature range of 0.33 MK to 1.25 MK which allows the study of wave propagation from the transition region to the corona. As slow waves are observed to decay rapidly, the effects of damping due to thermal conduction, compressive viscosity and optically thin radiation are included in the model, in addition to gravitational stratification. Using this model, the plasma properties of the loop, i.e. energy/temperature, density and velocity, are examined.

In Chapter 3 the plasma properties determined in Chapter 2 are forward modelled for three different instruments. This modelling allows a better understanding of the observational consequences and the signatures of slow waves and also allows a more direct comparison between the numerical results and observational data. Forward modelling is performed for TRACE, SoHO/CDS and Hinode/EIS with both the uniform and non-uniform models of Chapter 2. The observational consequences of damping due to thermal conduction and compressive viscosity are examined.

Some of the techniques used to analyse observational data, and identify oscillations, are investigated. Chapter 4 examines the ability of each technique to identify both single and multiple oscillations with constant and non-constant background trends. The effects of damping, wave beating (interference between similar oscillation frequencies) and reduced cadence are also included. Chapter 5, observational data is analysed for evidence of propagating slow waves and the properties of those waves are determined. Co-spatial and co-temporal TRACE, CDS and EIS data are analysed using a range of emission lines from a transition region temperature of 50,000 K to a coronal value of 7.5 MK.

Finally, in Chapter 6 conclusions are drawn and possible areas for extension and future work are discussed.

Chapter 2

Slow Wave Simulations

2.1 Introduction

Propagating intensity oscillations have been observed along coronal loops since 1999 (Berghmans and Clette 1999; Nightingale et al. 1999; Schrijver et al. 1999) and have been interpreted as propagating slow waves (e.g. Nakariakov et al. 2000). In addition, De Pontieu et al. (2005) found that slow waves could propagate into the solar atmosphere along inclined magnetic field lines and many more observations of coronal intensity oscillations have now been made using TRACE, SoHO and Hinode (see Chapter 5). This has prompted further theoretical work in order to understand the nature and properties of propagating slow waves. However, the interpretation of these observations as propagating slow waves has recently been questioned (e.g. De Pontieu and McIntosh 2010).

Simulations of the damping of slow waves have been undertaken in the solar corona which has been modelled as a region of uniform equilibrium temperature (e.g. De Moortel and Hood 2003, 2004; De Moortel et al. 2004a). This work compared theory with observational data of predicted damping rates from TRACE. The uniform temperature equilibrium of one million Kelvin used in De Moortel and Hood (2003, 2004); De Moortel et al. (2004a) represents the solar corona, however, in order to study the propagation of these waves from the photosphere through the chromosphere and transition region and into the corona, a non uniform equilibrium temperature profile representing these regions of the solar atmosphere is required. This extension of the basic model allows the propagation and damping of slow waves to be examined throughout the solar atmosphere rather than just in the corona. Klimchuk et al. (2004) modelled propagating slow waves along coronal loops with an equilibrium temperature profile using analytical theory, numerical simulations and data analysis, whilst Fedun et al. (2009) used 3D numerical simulation to examine the leakage of slow waves propagating from the photosphere into the solar atmosphere.

The simulations in this chapter will study waves with periodicity of a few minutes, representing p-mode propagation from the solar surface. Acoustic waves propagating downwards in the sub-photosphere are

The work in this chapter is based on Owen et al. (2009)

studied by Shelyag et al. (2009) in a gravitationally stratified plasma. The effects of gravitational stratification are included in our model, in addition to three damping mechanisms, namely, compressive viscosity, optically thin radiation and thermal conduction as in De Moortel and Hood (2003, 2004).

The model assumes a purely vertical magnetic field, hence, as slow waves are guided by magnetic field lines their propagation is modelled in only one dimension. A 1D model was used by Ofman and Wang (2002) to show that thermal conduction causes rapid damping of standing slow waves in coronal loops, but this work did not study propagating disturbances. Ofman et al. (2000a) also use a 1D model to study propagating slow waves, in polar plumes, and include the effects of gravitational stratification and compressive viscosity, but not thermal conduction. Observations of propagating coronal oscillations have shown that perturbations in density are usually less than 10% of the background magnitude (De Moortel et al. 2002b). This process can, therefore, be considered linear, hence, we are only concerned with the linear solution to the MHD equations.

The equations, which are solved numerically, are described in Section 2.2, with the model and numerical code used described in Section 2.3. The code was initially tested for uniform temperature equilibria, the results of which are discussed in Section 2.4 with Section 2.5 discussing the results with a non-uniform temperature equilibrium.

2.2 Wave Theory

To simulate the propagation of slow waves in the solar atmosphere the MHD equations of mass continuity, motion, energy and induction with an equation of state are solved. To investigate the effects of damping, the ideal MHD equations must include terms for the damping mechanisms required. As mentioned earlier these are compressive viscosity, optically thin radiation and thermal conduction. Gravitational stratification is also included in the equations. The MHD equations (Priest 1982) to be solved, including the extra terms are:

Equation of Mass Continuity:

$$\frac{\partial \rho}{\partial t} + \nabla \cdot (\rho \mathbf{v}) = 0, \quad (2.1)$$

Equation of Motion:

$$\frac{\partial \mathbf{v}}{\partial t} = -(\mathbf{v} \cdot \nabla) \mathbf{v} - \frac{1}{\rho} \nabla p + \frac{1}{\rho} (\mathbf{j} \times \mathbf{B}) - \mathbf{g} + \nu \nabla^2 \mathbf{v}, \quad (2.2)$$

Energy Equation:

$$\frac{\partial \epsilon}{\partial t} = -\mathbf{v} \cdot \nabla \epsilon - \frac{p}{\rho} \nabla \cdot \mathbf{v} + \frac{1}{\rho} \nabla \cdot (\kappa_{\parallel} \cdot \nabla_{\parallel} T) - \rho \tilde{\chi} T^{\alpha} + \frac{H_0}{\rho} + \nu \left(\frac{1}{2} \left(\frac{\partial v_i}{\partial x_j} + \frac{\partial v_j}{\partial x_i} \right)^2 - \frac{2}{3} (\nabla \cdot \mathbf{v})^2 \right), \quad (2.3)$$

Induction Equation:

$$\frac{\partial \mathbf{B}}{\partial t} = \nabla \times (\mathbf{v} \times \mathbf{B}), \quad (2.4)$$

Equation of State:

$$\epsilon = \frac{p}{(\gamma - 1)\rho}. \quad (2.5)$$

2.3 Lare1d Code and Model

The Lare1d code as described by Arber et al. (2001) was used. It is a finite volume, shock capturing code that solves the non-linear MHD equations. As Lare1d is a non-linear code, linear effects will be modelled using small wave amplitudes, the effects of the non-linear terms are then assumed to be negligible.

The wave is driven at the lower boundary of the model to represent p-mode propagation from the solar surface.

Eqs. (2.1 to 2.4) are non-dimensionalised using,

$$\begin{aligned} \rho &= \rho_{00}\bar{\rho}, & p &= p_{00}\bar{p}, & \mathbf{v} &= v_{A0}\bar{\mathbf{v}}, & \mathbf{B} &= B_{00}\bar{\mathbf{B}}, & \epsilon &= \epsilon_{00}\bar{\epsilon}, & t &= \tau\bar{t}, & T &= T_{00}\bar{T}, & x &= \bar{x}L, \\ g &= g_{00}\bar{\mathbf{g}}, & \nu &= \nu_{00}\bar{\nu}, & \eta &= \eta_{00}\bar{\eta}, & \tilde{\chi} &= \tilde{\chi}_{00}\bar{\tilde{\chi}}, & \nabla &= \bar{\nabla}/L & L &= v_{A0}\tau, & \kappa_{\parallel} &= \kappa_{\parallel 00}\bar{T}^{\frac{5}{2}}, \end{aligned}$$

with

$$\epsilon_{00} = \frac{p_{00}}{\rho_{00}},$$

and

$$v_{A0}^2 = \frac{B_{00}^2}{\mu_0 \rho_{00}}.$$

This gives,

$$\frac{\partial \bar{\rho}}{\partial \bar{t}} = -\bar{\rho}(\bar{\nabla} \cdot \bar{\mathbf{v}}) - \bar{\mathbf{v}}(\bar{\nabla} \cdot \bar{\rho}), \quad (2.6)$$

$$\frac{\partial \bar{\mathbf{v}}}{\partial \bar{t}} = -(\bar{\mathbf{v}} \cdot \bar{\nabla})\bar{\mathbf{v}} - \frac{1}{\bar{\rho}}\bar{\nabla}\bar{p} + \frac{1}{\bar{\rho}}(\bar{\nabla} \times \bar{\mathbf{B}}) \times \bar{\mathbf{B}} - G\bar{\mathbf{g}} + \frac{e}{\bar{\rho}}\bar{\nabla}^2\bar{\mathbf{v}}, \quad (2.7)$$

$$\begin{aligned} \frac{\partial \bar{\epsilon}}{\partial \bar{t}} &= -\bar{\mathbf{v}} \cdot \bar{\nabla}\bar{\epsilon} - (\gamma - 1)\bar{\epsilon}\bar{\nabla} \cdot \bar{\mathbf{v}} + \frac{d}{\bar{\rho}}\bar{\nabla}(\bar{\epsilon}^{5/2}\bar{\nabla}_{\parallel}\bar{\epsilon})\bar{\epsilon}^{\alpha} \\ &\quad - r\bar{\rho} + \frac{H_*}{\bar{\rho}} + \frac{e}{\bar{\rho}}(\bar{\nabla}\bar{\mathbf{v}} \cdot \bar{\nabla}\bar{\mathbf{v}}), \end{aligned} \quad (2.8)$$

$$\frac{\partial \bar{\mathbf{B}}}{\partial \bar{t}} = -(\bar{\mathbf{v}} \cdot \bar{\nabla})\bar{\mathbf{B}} + (\bar{\mathbf{B}} \cdot \bar{\nabla})\bar{\mathbf{v}} - \bar{\mathbf{B}}(\bar{\nabla} \cdot \bar{\mathbf{v}}), \quad (2.9)$$

where

$$e = \frac{4}{3} \frac{\nu_{00}}{v_{A0}^2 \tau \rho_{00}}, \quad (2.10)$$

$$d = \left(\frac{(\gamma - 1) \tilde{\mu}}{R} \right)^{7/2} \frac{\epsilon_{00}^{3/2} \kappa_{\parallel 00}}{\tau \rho_{00}}, \quad (2.11)$$

$$r = \left(\frac{(\gamma - 1) \tilde{\mu}}{R} \right)^\alpha \tilde{\chi} \tau \rho_{00} \epsilon_{00}^{(\alpha-1)}, \quad (2.12)$$

$$G = \frac{g_{00} \tau}{v_{A0}}, \quad (2.13)$$

$$H_* = \frac{H_0 \tau}{p_{00}}, \quad (2.14)$$

and \bar{v} , $\bar{\eta}$ and $\bar{\chi}$ are equal to unity as these quantities are considered constant.

A constant magnetic field along the x-axis is included which guides the waves, allowing a one-dimensional model. Hence, dropping bars from dimensionless quantities for clarity, Eqs. (2.6 to 2.9) become,

$$\frac{\partial \rho}{\partial t} = -\rho \frac{\partial v}{\partial x} - v \frac{\partial \rho}{\partial x}, \quad (2.15)$$

$$\frac{\partial v}{\partial t} = -v \frac{\partial v}{\partial x} - \frac{1}{\rho} \frac{\partial p}{\partial x} - G g + \frac{e}{\rho} \frac{\partial^2 v}{\partial x^2}, \quad (2.16)$$

$$\frac{\partial \epsilon}{\partial t} = -v \frac{\partial \epsilon}{\partial x} - (\gamma - 1) \epsilon \frac{\partial v}{\partial x} + \frac{d}{\rho} \frac{\partial}{\partial x} \left(\epsilon^{5/2} \frac{\partial \epsilon}{\partial x} \right) - r \rho \epsilon^\alpha + \frac{H_*}{\rho} + \frac{e}{\rho} \left(\frac{\partial v}{\partial x} \right)^2, \quad (2.17)$$

$$\frac{\partial B}{\partial t} = 0, \quad (2.18)$$

where, to model a closed coronal loop, gravity is given by $g = \cos\left(\frac{\pi x}{L}\right)$.

2.3.1 Gravitational Stratification

The inclusion of gravity produces non-uniform equilibrium pressure and density, which are found from the equilibrium equation of motion, by linearising Eq. (2.16) when viscosity is neglected, i.e. $e = 0$,

$$\frac{\partial p}{\partial x} = -\rho_0 G g. \quad (2.19)$$

Linearising Eq. (2.5) with $\epsilon = \epsilon_{00}(\epsilon_0 + \epsilon_1)$, $p = p_{00}(p_0 + p_1)$ and $\rho = \rho_{00}(\rho_0 + \rho_1)$, where subscript 0 and subscript 1 terms are equilibrium and perturbed quantities respectively, gives,

$$\epsilon_0 = \frac{p_0}{(\gamma - 1)\rho_0}, \quad (2.20)$$

$$\epsilon_1 = \frac{p_1}{(\gamma - 1)\rho_0} - \frac{p_0 \rho_1}{(\gamma - 1)\rho_0^2}. \quad (2.21)$$

Substituting Eq. (2.20) into Eq. (2.19), gives,

$$\frac{\partial p}{\partial x} = -\frac{G g p_0}{(\gamma - 1)\epsilon_0},$$

$$\begin{aligned}
\int_{\widehat{p}_0}^{p_0} \frac{dp}{p_0} &= -\frac{G}{(\gamma-1)\epsilon_0} \int_0^x g \, dx, \\
\ln \frac{p_0}{\widehat{p}_0} &= -\frac{G}{(\gamma-1)\epsilon_0} \int_0^x \cos\left(\frac{\pi x}{L}\right) dx, \\
&= -\frac{LG}{(\gamma-1)\pi\epsilon_0} \sin\left(\frac{\pi x}{L}\right), \\
p_0 &= \widehat{p}_0 \exp\left(-\left[\frac{LG}{(\gamma-1)\pi\epsilon_0} \sin\left(\frac{\pi x}{L}\right)\right]\right), \tag{2.22}
\end{aligned}$$

where $p_0 = \widehat{p}_0 e^{ikx}$. Assuming a uniform equilibrium energy, i.e. $\epsilon_0 = \text{const}$, then from Eq. (2.20) the equilibrium density is,

$$\rho_0 = \widehat{\rho}_0 \exp\left(-\left[\frac{LG}{(\gamma-1)\pi\epsilon_0} \sin\left(\frac{\pi x}{L}\right)\right]\right), \tag{2.23}$$

where $\rho_0 = \widehat{\rho}_0 e^{ikx}$ and $\widehat{p}_0/\widehat{\rho}_0 = \text{const}$.

The pressure scale height, Λ , is defined as,

$$\Lambda = \frac{p_0}{\rho_0 G g}, \tag{2.24}$$

and the integrated pressure scale height, H , as,

$$\frac{1}{H} = \int_0^x \frac{dx}{\Lambda}. \tag{2.25}$$

Substituting ρ_0 and p_0 from Eq. (2.20) and g into Eq. (2.24) gives,

$$\Lambda = \frac{(\gamma-1)\epsilon_0}{G \cos\left(\frac{\pi x}{L}\right)}, \tag{2.26}$$

which, using Eq. (2.25), becomes,

$$\frac{1}{H} = \frac{G}{(\gamma-1)\epsilon_0} \int_0^x \cos\left(\frac{\pi x}{L}\right) dx, \tag{2.27}$$

giving,

$$\frac{1}{H} = \frac{LG}{(\gamma-1)\pi\epsilon_0} \sin\left(\frac{\pi x}{L}\right), \tag{2.28}$$

hence, Eq. (2.23) is expressed as,

$$\rho_0 = \widehat{\rho}_0 e^{-\frac{1}{H}}. \tag{2.29}$$

2.3.2 Model Conditions

The model has the following conditions,

$$\begin{aligned}
 \gamma &= 5/3, \\
 T_{00} &= 10^6 \text{ K}, \\
 \rho_{00} &= 1.67 \times 10^{-12} \text{ kg m}^{-3}, \\
 \tau &= 300 \text{ s}, \\
 B &= 10.2 \text{ G}, \\
 c_s &= 152 \text{ km s}^{-1}, \\
 v_A &= 705 \text{ km s}^{-1}, \\
 \beta &= 0.056,
 \end{aligned}$$

where γ , T_{00} , ρ_{00} and τ are chosen to be consistent with De Moortel and Hood (2003). In Lare1d, this gives a magnetic field, B , of 1.7 G, which is multiplied by 6 to give a typical coronal value of 10.2 G (Miralles 2011). These values are then used to calculate the values of the sound speed, c_s , Alfvén speed, v_A and the plasma beta, β , which are also typical of the solar corona (Miralles 2011).

2.3.3 Boundary Conditions

The wave is driven at the lower boundary as $\sin(2\pi t)$, where $\omega = 2\pi$, with the upper boundary line-tied to the equilibrium values, as shown in Table 2.1, where A is the velocity amplitude and is chosen to be 0.001.

Boundary		Conditions		
		Velocity (v)	Density (ρ)	Energy (ϵ)
$x = 0$	(lower)	$A \sin(2\pi t)$	$\rho_0 + \hat{\rho}_1 A \sin(2\pi t)$	$\epsilon_0 + \hat{\epsilon}_1 A \sin(2\pi t)$
$x = x_{max}$	(upper)	0	ρ_0	ϵ_0

Table 2.1: Boundary conditions for Lare1d.

The relative amplitudes of the driven density and energy are given by $\hat{\rho}_1$ and $\hat{\epsilon}_1$ respectively, and are found from the D'Alembert solution for a rightwards propagating wave in an ideal medium. The wave equation in an ideal medium, with velocity c , is given by,

$$\frac{\partial^2 v}{\partial t^2} = c^2 \frac{\partial^2 v}{\partial x^2}, \tag{2.30}$$

where the D'Alembert solution for a rightwards propagating wave is given by,

$$v = F(x - ct). \tag{2.31}$$

Linearising Eq. (2.15) with no gravitational stratification, i.e $\rho_0 = \text{const}$, gives,

$$\begin{aligned}\frac{\partial \rho_1}{\partial t} &= -\rho_0 \frac{\partial v}{\partial x}, \\ &= -\rho_0 F'(x - ct), \\ \rho_1 &= -\rho_0 \int F'(x - ct) dt.\end{aligned}\tag{2.32}$$

From Eq. (2.31) and Table 2.1,

$$\begin{aligned}F(x - ct) &= A \sin(x - ct), \\ F'(x - ct) &= A \cos(x - ct), \\ \int F'(x - ct) dt &= \frac{A}{-c} \sin(x - ct), \\ &= \frac{v}{-c},\end{aligned}$$

which, substituting into Eq. (2.32) gives,

$$\rho_1 = \frac{\rho_0}{c} v.\tag{2.33}$$

The same treatment of Eq. (2.17) without thermal conduction or optically thin radiation gives,

$$\epsilon_1 = \frac{(\gamma - 1)\epsilon_0}{c} v.\tag{2.34}$$

By linearising Eqs. (2.15) to (2.17) and Eq. (2.5), with $e = r = d = G = 0$, which gives $H_* = 0$, the wave equation for velocity is found to be,

$$\frac{\partial^2 v}{\partial t^2} = \gamma(\gamma - 1)\epsilon_0 \frac{\partial^2 v}{\partial x^2},\tag{2.35}$$

which, when compared to Eq. (2.30), gives,

$$c = \sqrt{\gamma(\gamma - 1)\epsilon_0}.\tag{2.36}$$

Hence, Eqs. (2.33) and (2.34) become,

$$\hat{\rho}_1 = \frac{\rho_0}{\sqrt{\gamma(\gamma - 1)\epsilon_0}} v,\tag{2.37}$$

$$\hat{\epsilon}_1 = \sqrt{\frac{(\gamma - 1)\epsilon_0}{\gamma}} v,\tag{2.38}$$

which are shown in Table 2.1 with $v = A \sin(2\pi t)$.

2.4 Code Testing At Uniform Temperature Equilibrium

To ensure confidence and reliability of results, a uniform equilibrium temperature is initially modelled and compared to De Moortel and Hood (2003, 2004), the results of which are discussed in this section. Firstly an undamped sound wave travelling through an unstratified medium is considered (Section 2.4.1), before the complexity of the model is gradually increased by adding gravitational stratification (Section 2.4.2) and damping due to optically thin radiation (Section 2.4.3), compressive viscosity (Section 2.4.4) and thermal conduction (Section 2.4.6). Each extra effect is examined individually before the combined effects are investigated.

A five minute periodicity is used to represent p-modes and for consistency with De Moortel and Hood (2003, 2004). The velocity amplitude is chosen as $A = 0.001$ and 4800 grid points over a box length of $L = 16$ are used.

2.4.1 Ideal Medium

In an ideal medium, gravity, compressive viscosity, optically thin radiation and thermal conduction are neglected by setting, $G = e = r = d = 0$, respectively, which gives $H_* = 0$. Hence, Eqs. (2.15) to (2.17) become,

$$\frac{\partial \rho}{\partial t} = -\rho \frac{\partial v}{\partial x} - v \frac{\partial \rho}{\partial x}, \quad (2.39)$$

$$\frac{\partial v}{\partial t} = -v \frac{\partial v}{\partial x} - \frac{1}{\rho} \frac{\partial p}{\partial x}, \quad (2.40)$$

$$\frac{\partial \epsilon}{\partial t} = -v \frac{\partial \epsilon}{\partial x} - (\gamma - 1) \epsilon \frac{\partial v}{\partial x}, \quad (2.41)$$

with

$$\epsilon = \frac{p}{(\gamma - 1)\rho}. \quad (2.42)$$

Fig. 2.1(a) shows simulation results for an ideal medium with an equilibrium density, $\rho_0 = 1$ and an equilibrium energy, $\epsilon_0 = 1.5$, which corresponds to an equilibrium temperature, $T_0 = 1$ MK. v is plotted in black, ϵ_1 in red and $\frac{\rho_1}{\rho_0}$ in green. The wave in Fig. 2.1(a) is undamped, hence, the maximum and minimum amplitudes of the velocity and energy and density perturbations (dashed black, red and green lines, respectively) remain constant along x . These amplitudes were calculated using Eqs. (2.37) and (2.38) and agree with the simulation results shown in Fig. 2.1. The velocity perturbations are in phase with the energy and density perturbations.

Fig. 2.1(a) shows the full length ($x = 16$) of the numerical domain. We focus only on $0 \leq x \leq 8$ and essentially consider half of a coronal loop, from the coronal footpoint at $x = 0$ to the apex at $x = 8$. As we are only interested in the first half of the domain the simulation is stopped after the wave has travelled past $x = 8$, but before it reaches the upper boundary, so it cannot be reflected and affect the results at lower x .

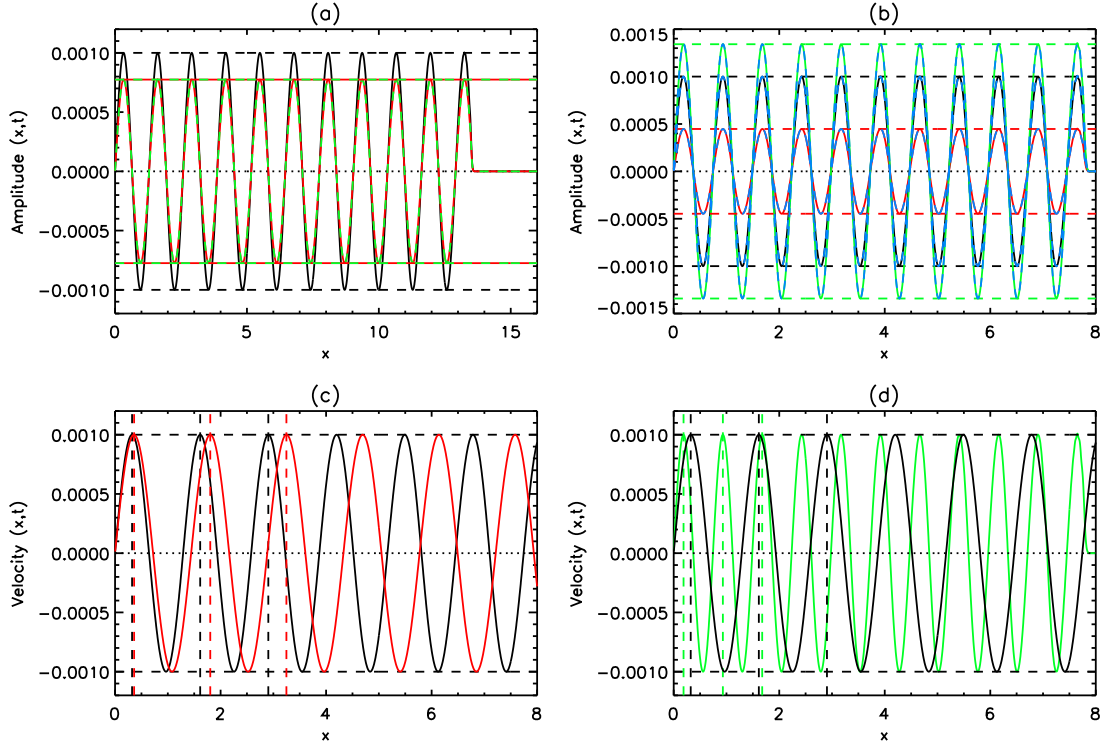


Figure 2.1: (a) v (black), ϵ_1 (red) and $\frac{\rho_1}{\rho_0}$ (green) for $\epsilon_0 = 1.5$ and $\rho_0 = 1$. (b) for $\epsilon_0 = 0.5$, v (black), ϵ_1 (red) and $\frac{\rho_1}{\rho_0}$ (green), with v , ϵ_1 and $\frac{\rho_1}{\rho_0}$ (dashed blue) for $\rho_0 = 8.5$. (c) and (d) v with $\epsilon_0 = 1.875$ (red in (c)), $\epsilon_0 = 1$ (black in both (c) and (d)) and $\epsilon_0 = 0.5$ (green in (d)) for $\rho_0 = 1$, with the first three wavelengths for each ϵ_0 calculated from Eq. (2.43) (vertical dashed). The horizontal dashed lines show the predicted maximum and minimum amplitudes of each perturbation. Snapshot taken at time $t = 10.5$.

Figs. 2.1(c) and (d) investigate the effects of different values of the equilibrium energy, ϵ_0 . The green line represents a lower equilibrium energy of $\epsilon_0 = 0.5$, corresponding to $T_0 = \frac{1}{3}$ MK, with the red line a higher value of $\epsilon_0 = 1.875$, corresponding to $T_0 = 1.25$ MK. These energies correspond to the minimum and maximum of the temperature profiles used in Section 2.5 and will be used for comparison later. The wavelength λ is found from Eq. (2.36) to be,

$$c_s = \sqrt{\gamma(\gamma - 1)\epsilon_0} = \frac{2\pi}{\omega}\lambda = \lambda, \quad (2.43)$$

which matches the wavelengths shown in Figs. 2.1(c) and (d), as shown by the vertical dashed lines. As the sound speed depends on $\sqrt{\epsilon_0}$ the waves at higher energy travel faster, as seen in Figs. 2.1(c) and (d).

Fig. 2.1(b) has equilibrium energy, $\epsilon_0 = 0.5$ with $\rho_0 = 1$ (green, black and red) and $\rho_0 = 8.5$ (dashed blue). It is clear from Fig. 2.1(b) that for an undamped wave in an unstratified medium changing the equilibrium density has no effect on v , ϵ_1 or $\frac{\rho_1}{\rho_0}$.

2.4.2 Gravitationally Stratified Medium

Gravitational stratification is included in the model with a value of $g_{00} = 274 \text{ m s}^{-2}$ chosen as the solar gravitational acceleration (Priest 1982), giving $H = 1.43$, which is calculated using,

$$H = \frac{p_0}{\rho_0 g_{00} L}, \quad (2.44)$$

corresponding to a gravitational scale height of 50.5 Mm. By including gravity, whilst neglecting viscosity, radiation and conduction, Eqs. (2.15) to (2.17) become,

$$\frac{\partial \rho}{\partial t} = -\rho \frac{\partial v}{\partial x} - v \frac{\partial \rho}{\partial x}, \quad (2.45)$$

$$\frac{\partial v}{\partial t} = -v \frac{\partial v}{\partial x} - \frac{1}{\rho} \frac{\partial p}{\partial x} - G g, \quad (2.46)$$

$$\frac{\partial \epsilon}{\partial t} = -v \frac{\partial \epsilon}{\partial x} - (\gamma - 1) \epsilon \frac{\partial v}{\partial x}, \quad (2.47)$$

with

$$\epsilon = \frac{p}{(\gamma - 1)\rho}. \quad (2.48)$$

Fig. 2.2(a) shows the equilibrium density profiles for a gravitationally stratified medium with $\epsilon_0 = 0.5$ (green), $\epsilon_0 = 1.5$ (black) and $\epsilon_0 = 1.875$ (red). The simulation results fit with that calculated from Eq. (2.29) as shown by the blue dashed lines. The initial equilibrium density, $\rho_0(0)$, is different in each case to be consistent with the results in Section 2.5. For the case of a uniform equilibrium temperature of 1 MK, the equilibrium density at $x = 0$ is normalised to unity (i.e. $\rho_0 = 1.67 \times 10^{-12} \text{ kg m}^{-3}$) and by including gravity it decreases exponentially with a value of $\rho_0 \approx 0.0284$ at $x = 8$. $\rho_0(x = 8) \approx 0.0002$ for $\epsilon_0 = 0.5$, $\rho_0(x = 8) \approx 0.0290$ for $\epsilon_0 = 1.875$.

Fig. 2.2(b) shows that the simulation is finished before the wave reaches the upper boundary and shows the velocity, energy and density perturbations for $\epsilon_0 = 1.5$ and $\rho_0(0) = 1$. It is clear that the amplitudes of v , ϵ_1 and $\frac{\rho_1}{\rho_0}$ all increase as ρ_0 decreases. This increase in amplitude is calculated using Eq. (2.51) (shown below) and agrees with the simulation results. The wavelength also agrees with the analytical solution given by Eq. (2.43), as indicated by the vertical dashed lines.

Following De Moortel and Hood (2004), the spatial dependence of v in Figs. 2.2(b) and (c) can be calculated, for an isothermal medium, such that c_s and H are constant, by linearising and taking spatial and temporal derivatives of Eqs. (2.45) to (2.47) and Eq. (2.5). These are combined to produce a wave equation,

$$\frac{\partial^2 v}{\partial t^2} = -\frac{\gamma(\gamma - 1)\epsilon_0}{H} \frac{\partial v}{\partial x} + \gamma(\gamma - 1)\epsilon_0 \frac{\partial^2 v}{\partial x^2}, \quad (2.49)$$

which, using Eq. (2.43) becomes,

$$\frac{\partial^2 v}{\partial t^2} = -\frac{c_s^2}{H} \frac{\partial v}{\partial x} + c_s^2 \frac{\partial^2 v}{\partial x^2}, \quad (2.50)$$

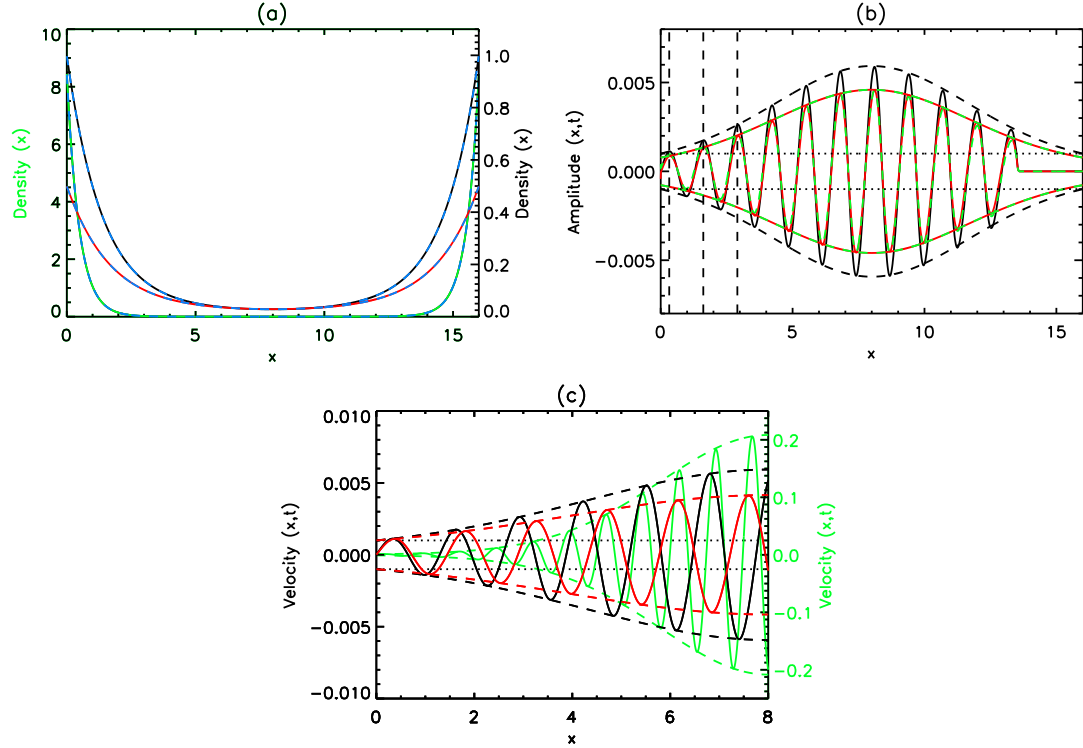


Figure 2.2: (a) ρ_0 with $\epsilon_0 = 0.5$ and $\rho_0(0) = 8.5$ (green), $\epsilon_0 = 1.5$ and $\rho_0(0) = 1$ (black) and $\epsilon_0 = 1.875$ and $\rho_0(0) = 0.5$ (red). The predicted ρ_0 from Eq. (2.29) is shown by dashed blue lines. (b) v (black), ϵ_1 (red) and $\frac{\rho_1}{\rho_0}$ (green) for $\epsilon_0 = 1.5$ and $\rho_0(0) = 1$, with the first three wavelengths calculated from Eq. (2.43) (vertical dashed). (c) v for the three ρ_0 profiles shown in (a). The maximum and minimum amplitudes of velocity for an unstratified medium are shown by dotted lines and the predicted amplitudes of v (black), ϵ_1 (red) and $\frac{\rho_1}{\rho_0}$ (green) are shown by dashed lines in (b) and (c). Snapshot taken at time $t = 10.5$.

where H is the constant stated above. Assuming v has the form $v(x, t) = \sin(\omega t) \sin(kx)$, gives,

$$v(x, t) = \sin(\omega t) e^{\frac{1}{2H} x} e^{ix\Omega}, \quad (2.51)$$

where $\Omega = \sqrt{\omega^2 - \omega_c^2}$ and $\omega_c = \frac{1}{2H}$, which is consistent with De Moortel and Hood (2004). Therefore, the velocity perturbations grow with height along the x-axis as $e^{\frac{1}{2H} x}$, where H (from Eq. (2.28)) is given by,

$$H = \frac{(\gamma - 1)\pi\epsilon_0}{L G \sin\left(\frac{\pi x}{L}\right)}. \quad (2.52)$$

The energy and density perturbations are given by the amplitude of the ideal D'Alembert solution, Eqs. (2.38) and (2.37), with the same gravitational dependence as velocity, giving $\epsilon_1 = \hat{\epsilon} \exp \frac{1}{2H} x$ and $\rho_1 = \hat{\rho} \exp \frac{1}{2H} x$, respectively. The calculated amplitudes of v , ϵ_1 and $\frac{\rho_1}{\rho_0}$ are shown by the dashed lines in Figs. 2.2(b) and (c) and agree with the simulation results. If $\omega_c > \omega$ then Ω is complex and $v \propto e^{-x}$, hence, the wave decays exponentially. Therefore, ω_c is the cut off frequency, below which no wave can propagate.

Fig. 2.2(c) shows the velocity with $\epsilon_0 = 0.5$ and $\rho_0(0) = 8.5$ (green), $\epsilon_0 = 1$ and $\rho_0(0) = 1$ (black) and $\epsilon_0 = 1.875$ and $\rho_0(0) = 0.5$ (red). As seen in Fig. 2.2(b), v , ϵ_1 and $\frac{\rho_1}{\rho_0}$ all increase as ρ_0 decreases. The

case of $\epsilon_0 = 0.5$ and $\rho_0(0) = 8.5$ shown in green has the largest decrease in ρ_0 , and therefore, the greatest increase in the wave amplitudes.

2.4.3 Optically Thin Radiation

Optically thin radiation is now included in the simulation whilst compressive viscosity and thermal conduction are still neglected (by setting $r \neq 0$ and $e = d = 0$), firstly in an unstratified medium and then including gravitational stratification (Section 2.4.3.1). Hence, Eqs. (2.15) to (2.17) become,

$$\frac{\partial \rho}{\partial t} = -\rho \frac{\partial v}{\partial x} - v \frac{\partial \rho}{\partial x}, \quad (2.53)$$

$$\frac{\partial v}{\partial t} = -v \frac{\partial v}{\partial x} - \frac{1}{\rho} \frac{\partial p}{\partial x} - G g, \quad (2.54)$$

$$\frac{\partial \epsilon}{\partial t} = -v \frac{\partial \epsilon}{\partial x} - (\gamma - 1) \epsilon \frac{\partial v}{\partial x} - r \rho \epsilon^\alpha + \frac{H_*}{\rho}, \quad (2.55)$$

with

$$\epsilon = \frac{p}{(\gamma - 1)\rho}, \quad (2.56)$$

where $G = 0$ for an unstratified medium. To include the effects of optically thin radiation, the radiation constants χ and α are required, taken from Priest (1982) and shown in Table 2.2. The χ values have been divided by $(2\tilde{\mu}m_p)^2$ as the radiation term in Lare1d uses density rather than number density ($\tilde{\mu}$ is the mean atomic weight of 0.6 and m_p is the proton mass of 1.673×10^{-27} kg).

Region	Temperature Range (K)	χ Values	α Values
1	$T_0 < 10^{4.3}$	0	0
2	$10^{4.3} \leq T_0 < 10^{4.6}$	3.50×10^{18}	0
3	$10^{4.6} \leq T_0 < 10^{4.9}$	2.48×10^9	2
4	$10^{4.9} \leq T_0 < 10^{5.4}$	1.57×10^{19}	0
5	$10^{5.4} \leq T_0 < 10^{5.75}$	9.88×10^{29}	-2
6	$10^{5.75} \leq T_0 < 10^{6.3}$	2.85×10^{18}	0
7	$10^{6.3} \leq T_0 < 10^{7.0}$	4.62×10^{22}	$-\frac{2}{3}$
8	$10^{7.0} < T_0$	0	0

Table 2.2: χ and α for optically thin radiation.

The equilibrium energy equation, from linearising Eq. (2.17) when $d = e = 0$ gives the coronal heating function, H_* to be,

$$H_* = r \rho_0^2 \epsilon_0^\alpha, \quad (2.57)$$

which is calculated from the density and energy at time $t = 0$ and added at every time step to maintain the correct equilibrium.

The simulation results shown in Fig. 2.3 show three different equilibrium energy values of $\epsilon_0 = 0.85$, $\epsilon_0 =$

1.5 and $\epsilon_0 = 1.875$, corresponding to $T_0 = 0.57$ MK, $T_0 = 1$ MK and $T_0 = 1.25$ MK, respectively. With $0.55 < T_0 < 2.0$ MK and a small perturbation, the temperature of the system remains within region 6 of Table 2.2, therefore, $\chi = 2.85 \times 10^{18}$ and $\alpha = 0$, giving a radiation coefficient, calculated from Eq. (2.12), of $r = 0.103$. Fig. 2.3(a) shows the velocity (black), energy (red) and density (green) perturbations of a wave damped by optically thin radiation in an unstratified medium with $\epsilon_0 = 1.5$ and $\rho_0 = 1$. Fig. 2.3(a) clearly shows a small amount of damping is present when optically thin radiation is included. The damping of the velocity is calculated using Eq. (2.64) (see below) and agrees with the simulation results. From this the energy and density perturbations are found using Eqs. (2.37) and (2.38), which also agree. Fig. 2.3(b) shows the velocity of a wave damped by optically thin radiation with $\epsilon_0 = 1.875$ and $\rho_0 = 0.5$ (black) and $\rho_0 = 1$ (red). The effects of radiation at $\epsilon_0 = 0.85$ (green in Fig. 2.3(d)), $\epsilon_0 = 1.5$ (black in Figs. 2.3(c) and (d)) and $\epsilon_0 = 1.875$ (red in Fig. 2.3(c)) are investigated. Figs. 2.3(c) and (d) clearly show that the velocity with the highest ϵ_0 of 1.875 (red in Fig. 2.3(c)) is damped the least. This can be seen in Eq. (2.64), where the damping due to optically thin radiation is proportional to $\epsilon_0^{-3/2}$. In contrast, damping due to optically thin radiation is proportional to ρ_0 , hence in Fig. 2.3(b) the case of $\rho_0 = 1$ (red) is damped more than $\rho_0 = 0.5$ (black).

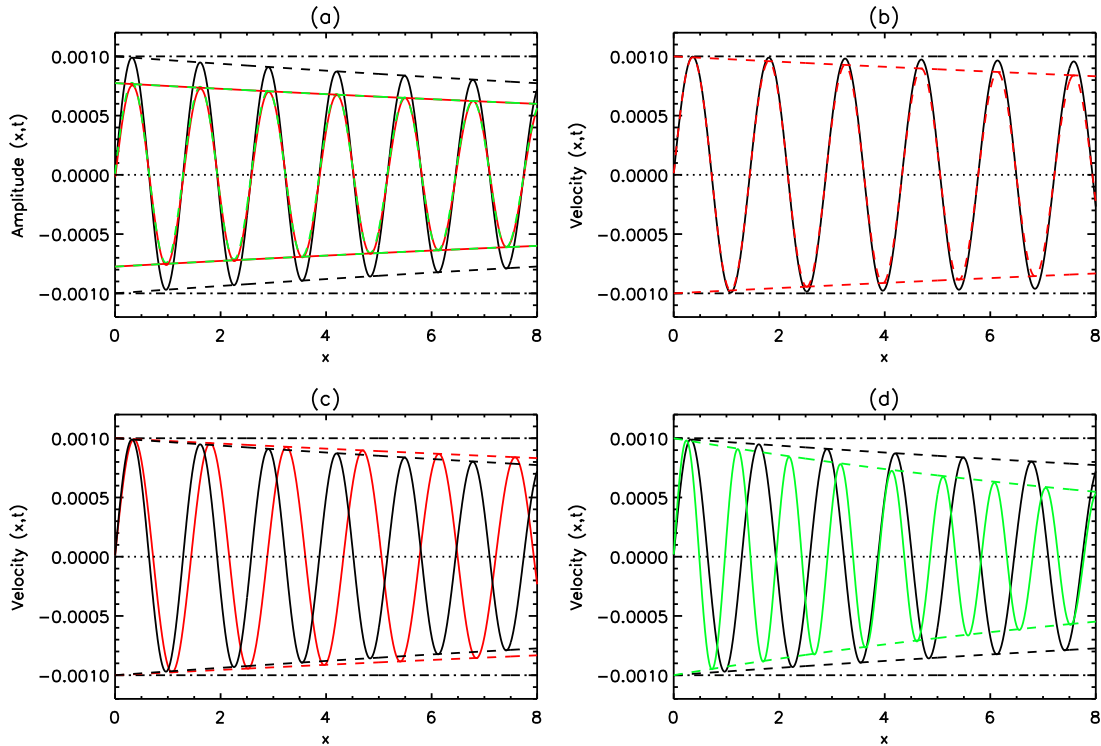


Figure 2.3: (a) v (black), ϵ_1 (red) and $\frac{\rho_1}{\rho_0}$ (green) for $\epsilon_0 = 1.5$ and $\rho_0 = 1$. (b) v for $\epsilon_0 = 1.875$ with $\rho_0 = 1$ (red) and $\rho_0 = 0.5$ (black). (c) and (d) v with $\epsilon_0 = 1.875$ (red in (c)), $\epsilon_0 = 1.5$ (black in (c) and (d)) and $\epsilon_0 = 0.85$ (green in (d)). The dashed lines show the predicted maximum and minimum amplitudes of each perturbation due to damping by optically thin radiation. The undamped maximum and minimum velocity amplitude are shown by horizontal dot-dashed lines. Snapshot taken at time $t = 10.5$.

Following De Moortel and Hood (2004), the predicted spatial dependence of velocity due to damping by optically thin radiation is found by linearising equations Eqs. (2.53) to (2.55) and Eq. (2.5) with $G = 0$, to

give,

$$\frac{\partial \rho_1}{\partial t} = -\rho_0 \frac{\partial v}{\partial x}, \quad (2.58)$$

$$\frac{\partial v}{\partial t} = -\frac{1}{\rho_0} \frac{\partial p_1}{\partial x}, \quad (2.59)$$

$$\frac{\partial \epsilon_1}{\partial t} = -(\gamma - 1)\epsilon_0 \frac{\partial v}{\partial x} - 2r\rho_1, \quad (2.60)$$

$$p_1 = (\gamma - 1)(\epsilon_0\rho_1 + \rho_0\epsilon_1), \quad (2.61)$$

which are combined to produce a wave equation,

$$\frac{\partial^3 v}{\partial t^3} = \gamma(\gamma - 1)\epsilon_0 \frac{\partial^3 v}{\partial x^2 \partial t} - 2(\gamma - 1)r\rho_0 \frac{\partial^2 v}{\partial x^2}. \quad (2.62)$$

Assuming v has the form $v(x, t) = e^{i(kx - \omega t)}$ gives,

$$k = \frac{\omega}{(\gamma(\gamma - 1)\epsilon_0)^{1/2}} + \frac{ir}{\gamma^{3/2}(\gamma - 1)^{1/2}} \frac{\rho_0}{\epsilon_0^{3/2}}, \quad (2.63)$$

which, considering only the spatial dependence, gives,

$$v(x, t) \propto \exp\left(-x \frac{r}{\gamma^{3/2}(\gamma - 1)^{1/2}} \frac{\rho_0}{\epsilon_0^{3/2}}\right), \quad (2.64)$$

as shown by the dashed lines in Fig. 2.3.

2.4.3.1 Optically Thin Radiation and Gravitational Stratification

Gravitational stratification is included, as described in Section 2.4.2, with damping due to optically thin radiation. Figs. 2.4(a) and (b) show the velocity, energy and density perturbations with the ρ_0 profiles given by the black and red lines, respectively, in Fig. 2.2(a).

The dashed lines in Fig. 2.4 show the wave amplitudes without damping. By comparing these with the solid lines which include damping due to radiation it is clear that damping due to optically thin radiation appears almost negligible in a gravitationally stratified plasma.

2.4.4 Compressive Viscosity

Compressive viscosity is included in the simulation using the coefficient of compressive viscosity, $\nu_{00} = 10^{-17} T_0^{5/2} = 0.01 \text{ kg m}^{-1} \text{ s}^{-1}$ to be consistent with De Moortel and Hood (2003), giving $e = 0.0019$. Eqs. (2.15) to (2.17) are solved, with optically thin radiation and thermal conduction neglected, by setting $r = d = 0$. Hence, Eqs. (2.15) to (2.17) become,

$$\frac{\partial \rho}{\partial t} = -\rho \frac{\partial v}{\partial x} - v \frac{\partial \rho}{\partial x}, \quad (2.65)$$

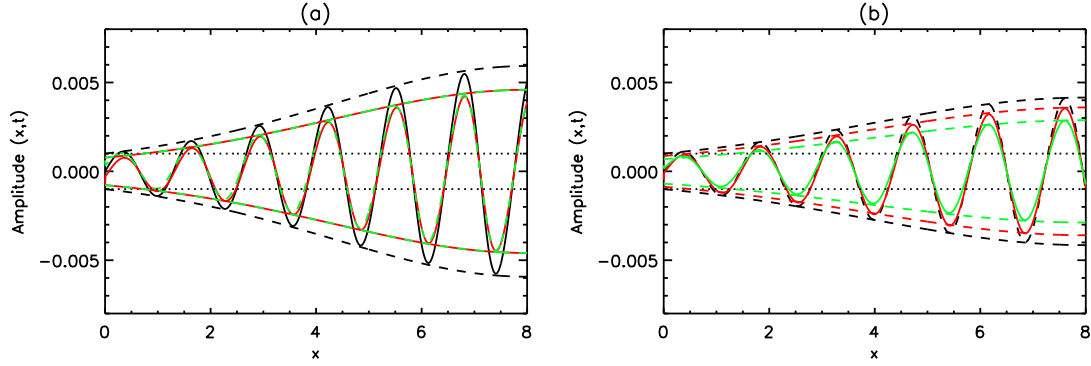


Figure 2.4: v (black), ϵ_1 (red) and $\frac{\rho_1}{\rho_0}$ (green) for (a) $\epsilon_0 = 1.5$ and $\rho_0(0) = 1$ and (b) $\epsilon_0 = 1.875$ and $\rho_0(0) = 0.5$. The maximum and minimum amplitudes for an undamped wave in a stratified medium are shown by dashed lines, with those for an unstratified medium (v only) shown by dotted lines. Snapshot taken at time $t = 10.5$.

$$\frac{\partial v}{\partial t} = -v \frac{\partial v}{\partial x} - \frac{1}{\rho} \frac{\partial p}{\partial x} - Gg + \frac{e}{\rho} \frac{\partial^2 v}{\partial x^2}, \quad (2.66)$$

$$\frac{\partial \epsilon}{\partial t} = -v \frac{\partial \epsilon}{\partial x} - (\gamma - 1) \epsilon \frac{\partial v}{\partial x}, \quad (2.67)$$

with

$$\epsilon = \frac{p}{(\gamma - 1)\rho}, \quad (2.68)$$

where $G = 0$ for an unstratified medium. The heating effects due to compressive viscosity are small in the linear regime as the term $\frac{e}{\rho} \left(\frac{\partial v}{\partial x}\right)^2$ in Eq. (2.17) is of order $O(v^2)$ and can, therefore, be neglected from Eq. (2.67).

Fig. 2.5 shows the results for an unstratified medium. From Fig. 2.5(a) it is clearly visible that compressive viscosity acts to damp the wave and by comparison with Fig. 2.3(a) the damping from compressive viscosity is roughly twice as strong as that of optically thin radiation for $\epsilon_0 = 1.5$ and $\rho_0 = 1$. Note that a small numerical effect causes the amplitude of the density to increase slightly at $x = 8$ in Figs. 2.5(b) and (d).

Damping due to compressive viscosity is greater at lower density, as shown in Figs. 2.5(c) and (d), where the green line of $\epsilon_0 = 0.5$ is damped considerably more than the red line of $\epsilon_0 = 1.875$. Including compressive viscosity does not affect the propagation speed of the wave, which agrees with Eq. (2.43), as shown by the vertical dashed lines in Figs. 2.5(c) and (d). As well as ϵ_0 , damping due to viscosity also increases as ρ_0 decreases. This can be seen in Fig. 2.5(b), where the black line is damped more than the red line. Both black and red lines have $\epsilon_0 = 1.875$, but with $\rho_0 = 0.5$ and $\rho_0 = 1$, respectively.

2.4.4.1 Compressive Viscosity and Gravitational Stratification

Gravitational stratification is included, as described in Section 2.4.2, with the results of damping due to compressive viscosity shown in Fig. 2.6. Comparing Fig. 2.6(a) with Fig. 2.4(a) it is clear that the effects of

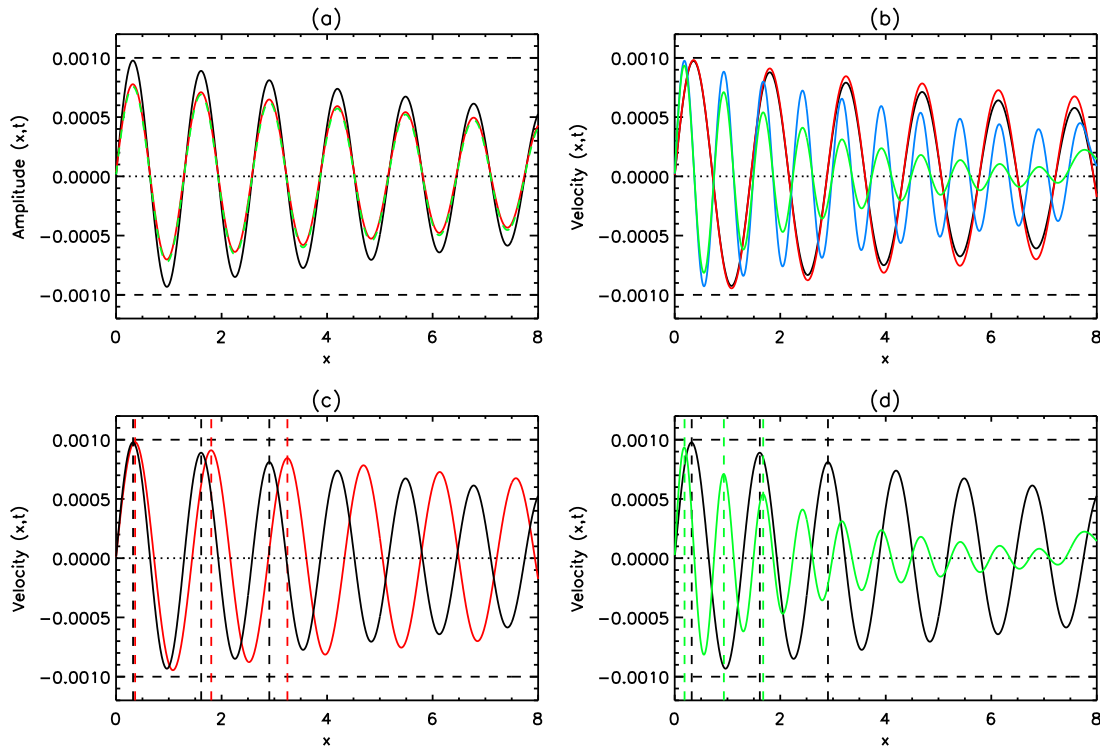


Figure 2.5: (a) v (black), ϵ_1 (red) and $\frac{\rho_1}{\rho_0}$ (green) for $\epsilon_0 = 1.5$ and $\rho_0 = 1$. (b) v for $\epsilon_0 = 0.5$ with $\rho_0 = 1$ (green) and $\rho_0 = 8.5$ (blue) and $\epsilon_0 = 1.875$ with $\rho_0 = 1$ (red) and $\rho_0 = 0.5$ (black). (c) and (d) v with $\epsilon_0 = 1.875$ (red in (c)), $\epsilon_0 = 1.5$ (black in (c) and (d)) and $\epsilon_0 = 0.5$ (green in (d)), with the first three wavelengths for each (vertical dashed). The horizontal dashed lines show the maximum and minimum amplitudes of the undamped v . Snapshot taken at time $t = 10.5$.

compressive viscosity are much stronger than those of optically thin radiation. In Fig. 2.4(a) there appears very little damping, whereas compressive viscosity in Fig. 2.6(a) has caused considerable damping, with the wave amplitudes at high x almost being reduced to below the level of an unstratified medium (dotted line).

The velocity is shown by the red ($\epsilon_0 = 1.875$ and $\rho_0(0) = 0.5$) and black ($\epsilon_0 = 1.5$ and $\rho_0(0) = 1$) lines in Fig. 2.6(b) with both oscillations experiencing similar levels of damping. The reason for this is that although ϵ_0 is higher for the black line (reducing the damping), ρ_0 is lower (increasing the damping), hence the damping remains similar in both cases. The amplitude of the red line is slightly lower than that of the black, however. This is a consequence of the smaller increase in wave amplitude due to gravity for the red line (Fig. 2.2(c) red dashed) compared to that of the black (Fig. 2.2(c) black dashed).

2.4.5 Optically Thin Radiation, Compressive Viscosity and Gravitational Stratification

The combined effects of optically thin radiation (Section 2.4.3.1) and compressive viscosity (Section 2.4.4.1) are investigated in a stratified medium with $\epsilon_0 = 1.5$ and $\rho_0(0) = 1$.

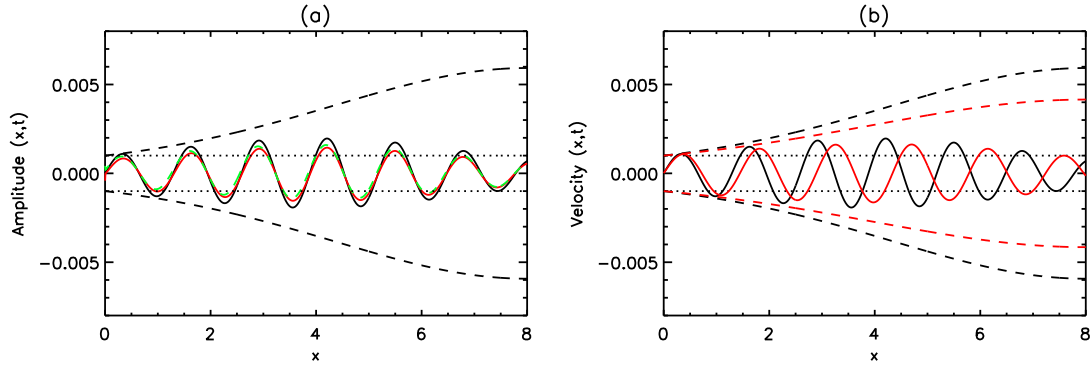


Figure 2.6: (a) v (black), ϵ_1 (red) and $\frac{\rho_1}{\rho_0}$ (green) for $\epsilon_0 = 1.5$ and $\rho_0(0) = 1$. (b) v for $\epsilon_0 = 1.5$ and $\rho_0(0) = 1$ (black and same as black line in (a)) and $\epsilon_0 = 1.875$ and $\rho_0(0) = 0.5$ (red). The maximum and minimum amplitudes of velocity for an undamped wave in a stratified medium are shown by dashed lines, with those for a stratified medium shown by dotted lines. Snapshot taken at time $t = 10.5$.

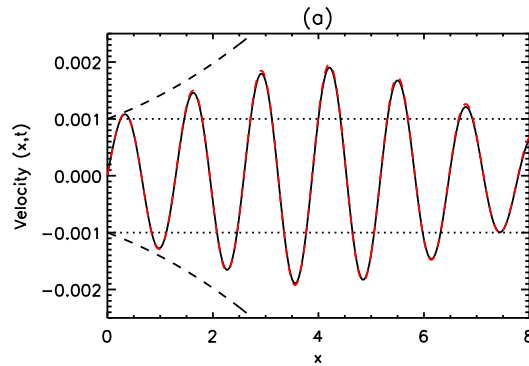


Figure 2.7: v with damping due to viscosity and radiation (black) and only viscosity (red) for $\epsilon_0 = 1.5$ and $\rho_0(0) = 1$. The maximum and minimum amplitudes of velocity for an undamped wave in a stratified medium are shown by dashed lines, with those for an unstratified medium shown by dotted lines. Snapshot taken at time $t = 10.5$.

The black line in Fig. 2.7 shows v with damping due to both compressive viscosity and optically thin radiation (black) compared to damping by viscosity alone (red). As seen in Fig. 2.6 there is considerable damping when viscosity is included, but removing radiation from the model has almost no effect. It is therefore clear that damping due to optically thin radiation is negligible compared to compressive viscosity in a gravitationally stratified medium at this temperature and density.

2.4.6 Thermal Conduction

Thermal conduction is included in the simulation with a coefficient of $d = 0.025$, whilst compressive viscosity and optically thin radiation are neglected ($e = r = 0$). Hence, Eqs. (2.15) to (2.17) become,

$$\frac{\partial \rho}{\partial t} = -\rho \frac{\partial v}{\partial x} - v \frac{\partial \rho}{\partial x}, \quad (2.69)$$

$$\frac{\partial v}{\partial t} = -v \frac{\partial v}{\partial x} - \frac{1}{\rho} \frac{\partial p}{\partial x} - G g, \quad (2.70)$$

$$\frac{\partial \epsilon}{\partial t} = -v \frac{\partial \epsilon}{\partial x} - (\gamma - 1) \epsilon \frac{\partial v}{\partial x} + \frac{d}{\rho} \frac{\partial}{\partial x} \left(\epsilon^{5/2} \frac{\partial \epsilon}{\partial x} \right) + \frac{H_*}{\rho}, \quad (2.71)$$

with

$$\epsilon = \frac{p}{(\gamma - 1)\rho}, \quad (2.72)$$

where $G = 0$ for an unstratified medium.

The equilibrium energy equation, from linearising Eq. (2.71), gives the coronal heating function, H_* to be,

$$H_* = d \left(\frac{5}{2} + \epsilon_0 \right) \epsilon_0^{3/2} \frac{\partial^2 \epsilon_0}{\partial x^2}, \quad (2.73)$$

which, if $\epsilon_0 = \text{const}$, becomes,

$$H_* = 0.$$

The thermal conduction term is calculated in the code using a Thomas Algorithm, which requires boundary conditions consistent with those in Table 2.1 (see Appendix A).

Fig. 2.8(a) shows the simulation results for an unstratified medium with $\epsilon_0 = 1.5$ and $\rho_0 = 1$. By comparing the amplitudes of v , ϵ_1 and $\frac{\rho_1}{\rho_0}$ (solid lines) with the amplitudes of the undamped wave (horizontal dashed lines) a large amount of damping is clearly present. Fig. 2.8(b) shows a close up of Fig. 2.8(a), where there is a phase shift between v , ϵ_1 and $\frac{\rho_1}{\rho_0}$ compared to the results without thermal conduction, where the extrema all occur at the same x . For clarity, the amplitudes of the energy and density perturbations in Fig. 2.8(b) have been normalised to that of the velocity.

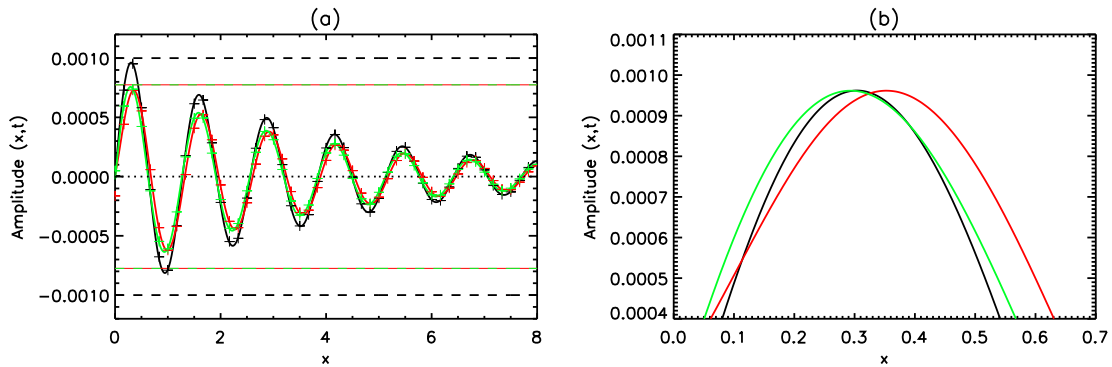


Figure 2.8: v (black), ϵ_1 (red) and $\frac{\rho_1}{\rho_0}$ (green) for $\epsilon_0 = 1.5$ and $\rho_0 = 1$. (a) Normal mode analysis prediction is shown by crosses and the maximum and minimum amplitudes of an undamped wave are shown as horizontal dashed lines. (b) part of (a) enlarged with ϵ_1 and $\frac{\rho_1}{\rho_0}$ amplitudes renormalised to illustrate the relative phase shift from v more clearly. Snapshot taken at time $t = 10.5$.

The amplitudes of the perturbed velocity, energy and density shown in Fig. 2.8(a) and the phase shift between them (enlarged in Fig. 2.8(b)) can be demonstrated analytically by a normal mode analysis. Without

gravity, linearising the dimensionless equations Eq. (2.69) to Eq. (2.71) gives,

$$\frac{\partial \rho_1}{\partial t} = -\rho_0 \frac{\partial v}{\partial x}, \quad (2.74)$$

$$\frac{\partial v}{\partial t} = -\frac{1}{\rho_0} \frac{\partial p_1}{\partial x}, \quad (2.75)$$

$$\frac{\partial \epsilon_1}{\partial t} = -(\gamma - 1)\epsilon_0 \frac{\partial v}{\partial x} + \frac{d}{\rho_0} \frac{\partial}{\partial x} \left(\epsilon_0^{5/2} \frac{\partial \epsilon_1}{\partial x} \right), \quad (2.76)$$

with

$$\epsilon_1 = \frac{p_0 + p_1}{(\gamma - 1)\rho_0} \left(1 + \frac{\rho_1}{\rho_0} \right)^{-1}. \quad (2.77)$$

Assuming v , ρ_1 and ϵ_1 have the form $e^{i(kx - \omega t)}$ and using Eq. (2.20) gives,

$$\omega \rho_1 - k \rho_0 v = 0, \quad (2.78)$$

$$\omega v - (\gamma - 1)k \frac{\epsilon_0}{\rho_0} \rho_1 - (\gamma - 1)k \epsilon_1 = 0, \quad (2.79)$$

$$\left(\omega + idk^2 \frac{\epsilon_0^{5/2}}{\rho_0} \right) \epsilon_1 - (\gamma - 1)\epsilon_0 k v = 0. \quad (2.80)$$

These equations can be expressed in matrix form as,

$$\begin{bmatrix} \omega & -k\rho_0 & 0 \\ -(\gamma - 1)k \frac{\epsilon_0}{\rho_0} & \omega & -(\gamma - 1)k \\ 0 & -(\gamma - 1)\epsilon_0 k & \omega + idk^2 \frac{\epsilon_0^{5/2}}{\rho_0} \end{bmatrix} \begin{bmatrix} \rho_1 \\ v \\ \epsilon_1 \end{bmatrix} = 0. \quad (A)$$

Setting the determinant = 0 gives,

$$i(\gamma - 1)d \frac{\epsilon_0^{7/2}}{\rho_0} k^4 + \left(\gamma(\gamma - 1)\epsilon_0 \omega - i\omega^2 d \frac{\epsilon_0^{5/2}}{\rho_0} \right) k^2 - \omega^3 = 0, \quad (2.81)$$

which is solved to give,

$$k = \pm \sqrt{-\frac{C}{2B} \pm \sqrt{\left(\frac{C}{2B}\right)^2 - \frac{D}{B}}} = \text{Re}\{k\} + i\text{Im}\{k\}, \quad (2.82)$$

where $\text{Re}\{k\}$ and $\text{Im}\{k\}$ are the real and imaginary parts of k and

$$B = i(\gamma - 1)d \frac{\epsilon_0^{7/2}}{\rho_0}, \quad (2.83)$$

$$C = \gamma(\gamma - 1)\epsilon_0 \omega - i\omega^2 d \frac{\epsilon_0^{5/2}}{\rho_0}, \quad (2.84)$$

$$D = -\omega^3. \quad (2.85)$$

Assuming $v = Ae^{i(kx-\omega t)}$ and considering only the spatial dependence, i.e. e^{ikx} gives,

$$\begin{aligned} v &= Ae^{i(\operatorname{Re}\{k\}x+i\operatorname{Im}\{k\}x)}, \\ &= Ae^{i\operatorname{Re}\{k\}x} e^{-\operatorname{Im}\{k\}x}. \end{aligned} \quad (2.86)$$

We can see that a phase shift is introduced to density with respect to velocity from Eq. (2.78) as k is complex. Indeed, we can write $k = re^{i\phi}$ where,

$$r = |k| = \sqrt{\operatorname{Re}\{k\}^2 + \operatorname{Im}\{k\}^2}, \quad (2.87)$$

$$\phi = \tan^{-1} \left(\frac{\operatorname{Im}\{k\}}{\operatorname{Re}\{k\}} \right), \quad (2.88)$$

and hence Eq. (2.78) becomes,

$$\rho_1 = \frac{\rho_0}{\omega} kv, \quad (2.89)$$

$$= \frac{\rho_0}{\omega} re^{i\phi} v. \quad (2.90)$$

Using Eq. (2.86) gives,

$$\rho_1 = A \frac{r\rho_0}{\omega} e^{i(\operatorname{Re}\{k\}x+\phi)} e^{-\operatorname{Im}\{k\}x}, \quad (2.91)$$

which can be written as,

$$\rho_1 = A \frac{r\rho_0}{\omega} e^{i\operatorname{Re}\{k\}(x+x_\rho)} e^{-\operatorname{Im}\{k\}x}, \quad (2.92)$$

where, x_ρ is the phase shift of ρ_1 from v , given by,

$$x_\rho = \frac{\phi}{\operatorname{Re}\{k\}}. \quad (2.93)$$

The phase shift in the energy perturbation is found from Eq. (2.79),

$$\epsilon_1 = \frac{\omega v}{(\gamma-1)k} - \frac{\epsilon_0}{\rho_0} \rho_1. \quad (2.94)$$

Substituting for k , ρ_1 and v gives,

$$\epsilon_1 = Ae^{i\operatorname{Re}\{k\}x} e^{-\operatorname{Im}\{k\}x} (\alpha e^{-i\phi} - \beta e^{i\phi}), \quad (2.95)$$

where,

$$\alpha = \frac{\omega}{(\gamma-1)r}, \quad (2.96)$$

$$\beta = \frac{\epsilon_0 r}{\omega}. \quad (2.97)$$

This can be written as,

$$\epsilon_1 = Ae^{i\text{Re}\{k\}x} e^{-\text{Im}\{k\}x} R e^{i\Phi}, \quad (2.98)$$

where,

$$R = \sqrt{(\alpha - \beta)^2 \cos^2 \phi + (\alpha + \beta)^2 \sin^2 \phi}, \quad (2.99)$$

$$\Phi = \tan^{-1} \left(-\frac{(\alpha + \beta) \sin \phi}{(\alpha - \beta) \cos \phi} \right). \quad (2.100)$$

Finally, we can rewrite this expression for ϵ as,

$$\epsilon_1 = A R e^{i\text{Re}\{k\}(x+x_\epsilon)} e^{-\text{Im}\{k\}x}, \quad (2.101)$$

where,

$$x_\epsilon = \frac{\Phi}{\text{Re}\{k\}}. \quad (2.102)$$

The black, red and green crosses on Fig. 2.8(a) are calculated using Eqs. (2.86), (2.101) and (2.90), respectively and show excellent agreement between the numerical results and the analytical approximations. The phase shifts, x_ρ and x_ϵ , can be estimated by using a small parameter approximation, where the thermal conduction constant, d , is assumed small and hence terms of order $O(d^2)$ can be neglected. Setting,

$$k = k_r + ik_i = \frac{\omega}{c_s} + id\Pi, \quad (2.103)$$

gives,

$$k^2 = \frac{\omega^2}{c_s^2} + 2id\frac{\omega}{c_s}\Pi + O(d^2), \quad (2.104)$$

$$k^4 = \frac{\omega^4}{c_s^4} + O(d). \quad (2.105)$$

Then substituting Eqs. (2.104) and (2.105) into Eq. (2.81) and solving for Π gives,

$$\Pi = \frac{\omega^2}{2\gamma^{5/2}(\gamma - 1)^{1/2}\rho_0} \frac{\epsilon_0}{c_s} + \frac{i\omega}{2c_s} \left(1 - \frac{1}{\epsilon_0 d} \right). \quad (2.106)$$

Note that in Eq. (2.81), k^4 is multiplied by d , so the $O(d)$ terms in Eq. (2.105) become $O(d^2)$ and are therefore neglected. By combining Eqs. (2.88) and (2.93), the phase shift for density, x_ρ , is given by

$$x_\rho = \frac{1}{k_r} \tan^{-1} \left(\frac{k_i}{k_r} \right), \quad (2.107)$$

$$= \frac{c_s}{\omega} \tan^{-1} \left(\frac{d\Pi c_s}{\omega} \right), \quad (2.108)$$

$$x_\rho \approx \frac{d\Pi c_s^2}{\omega^2}, \quad (2.109)$$

which, using the real part of Eq. (2.106), becomes

$$x_\rho \approx \frac{d\sqrt{(\gamma-1)}\epsilon_0^2}{2\gamma^{3/2}\rho_0}, \quad (2.110)$$

where $c_s^2 = \gamma(\gamma-1)\epsilon_0$ is used.

The energy perturbation is given by substituting k from Eq. (2.103), v from Eq. (2.86) and Ω from Eq. (2.106) in to Eq. (2.80) to give,

$$\epsilon_1 = \sqrt{\frac{(\gamma-1)\epsilon_0}{\gamma}} - i\frac{(\gamma+1)d\omega}{2\gamma^{5/2}(\gamma-1)^{1/2}}\frac{\epsilon_0^2}{\rho_0}. \quad (2.111)$$

The relative phase shift from velocity is then given by

$$x_\epsilon = \frac{1}{k_r} \tan^{-1} \left(\frac{\text{Im}\{\epsilon_1\}}{\text{Re}\{\epsilon_1\}} \right),$$

$$x_\epsilon \approx -\frac{(\gamma+1)d}{2\gamma^{5/2}(\gamma-1)^{1/2}}\frac{\epsilon_0^2}{\rho_0}. \quad (2.112)$$

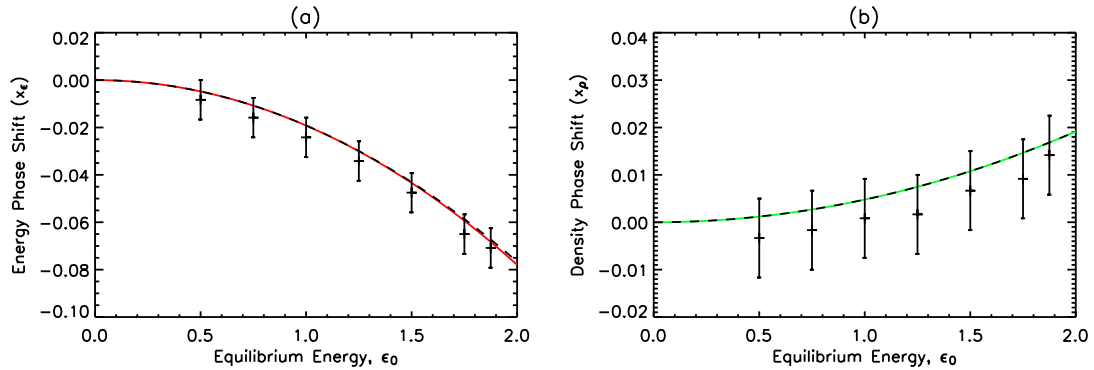


Figure 2.9: Relative phase shift from v of (a) ϵ_1 and (b) $\frac{d\epsilon_1}{\rho_0}$, as a function of ϵ_0 . Normal mode analysis shown in (a) red and (b) green with analytical approximation (dashed black) and the measured values shown with error bars.

From Eqs. (2.110) and (2.112) we can see that both x_ρ and x_ϵ have an $\frac{\epsilon_0^2}{\rho_0}$ dependence. This dependence of x_ϵ and x_ρ on ϵ_0^2 at constant ρ_0 can be seen in Figs. 2.9(a) and (b). Figs. 2.10(a) and (b) show the $\frac{1}{\rho_0}$ dependence of x_ϵ and x_ρ , respectively, for constant ϵ_0 . The values of x_ϵ and x_ρ are measured from the simulations and shown in Figs. 2.9 and 2.10 by symbols. These values are measured to the nearest grid cell, hence there is an associated error on x_ϵ and x_ρ of the order of the grid spacing. This is represented in Figs. 2.9 and 2.10 by vertical error bars. The analytical approximations are represented in Figs. 2.9 and 2.10 by dashed black lines and agree with x_ϵ and x_ρ from the normal mode analysis (red and green, respectively). Both calculated results agree with the measured results within the range of the error bars, except for the low density values of Fig. 2.10(b). At this point the analytical approximation diverges from the normal mode analysis. This is a consequence of the assumption of small d , which becomes invalid when density is very low, as seen in Eq. (2.11). From Eqs. (2.110) and (2.112), x_ρ is positive, whereas,

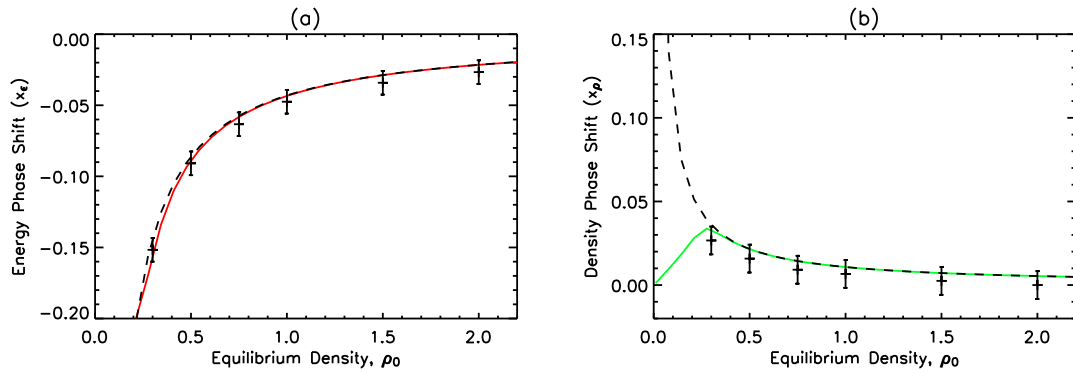


Figure 2.10: Relative phase shift from v of (a) ϵ_1 and (b) $\frac{\rho_1}{\rho_0}$, as a function of ρ_0 . Normal mode analysis shown in (a) red and (b) green with analytical approximation (dashed black) and the measured values shown with error bars.

x_ϵ is negative, as shown by Figs. 2.9 and 2.10. This implies that the density lags the velocity, whereas the energy leads and is in agreement with the simulation results shown in Fig. 2.8(b). This phase shift between v and the perturbations in ρ and ϵ occurs immediately after they are driven at the lower boundary. The propagation or sound speed (given by Eq. (2.43)) is constant in a region of uniform equilibrium energy. As a result, v , ϵ_1 and $\frac{\rho_1}{\rho_0}$ propagate at the same speed and hence, the initial phase shift is maintained as the perturbation travels through the numerical domain.

Fig. 2.11(a) shows the effects of thermal conduction for different values of ϵ_0 . As ϵ_0 increases from 0.5 (green), 1.5 (black) and to 1.875 (red), the damping caused by thermal conduction increases. The results of the normal mode analysis are also shown (blue dashed) and agree with the simulation results in that the amount of damping is proportional to ϵ_0 . However, the numerical boundary conditions at the upper boundary cause a slight deviation between the simulation results and the normal mode analysis of the $\epsilon_0 = 0.5$ results at $x = 8$. This phase shift may be a result of a difference between the phase and group speed.

The thermal conduction term in Eq. (2.71) is proportional to the inverse of the density and consequently, we can expect the behaviour of thermal conduction to be modified by the equilibrium density. This can be seen in Fig. 2.11(b) for $\epsilon_0 = 0.5$, where the damping is greater when $\rho_0 = 1$ (green) than for $\rho_0 = 8.5$ (blue). The same occurs at $\epsilon_0 = 1.875$, where the damping is greater when $\rho_0 = 0.5$ (black) than for $\rho_0 = 1$ (red). In the solar atmosphere the density decreases as the energy/temperature increases, both of which increase the damping due to thermal conduction. Consequently, perturbations higher in the atmosphere will experience more damping due to thermal conduction than those lower down.

Fig. 2.12 shows the effects of thermal conduction with $\epsilon_0 = 1.5$ for two uniform equilibrium densities (a) $\rho_0 = 1$ and (b) $\rho_0 = 0.03$. At low densities, the thermal conduction term in Eq. (2.71) becomes large and hence, the effects of thermal conduction become very strong. Thermal conduction acts to smooth temperature gradients, with heat flow from hot to cold regions, which, when density is low, it does very efficiently. This can be seen by the energy perturbation (red) in Fig. 2.12(b), which is damped far more than that seen in Fig. 2.12(a). As a result, if the density is sufficiently low, there is no longer an energy perturbation and the medium becomes isothermal. However, care must be taken when considering the

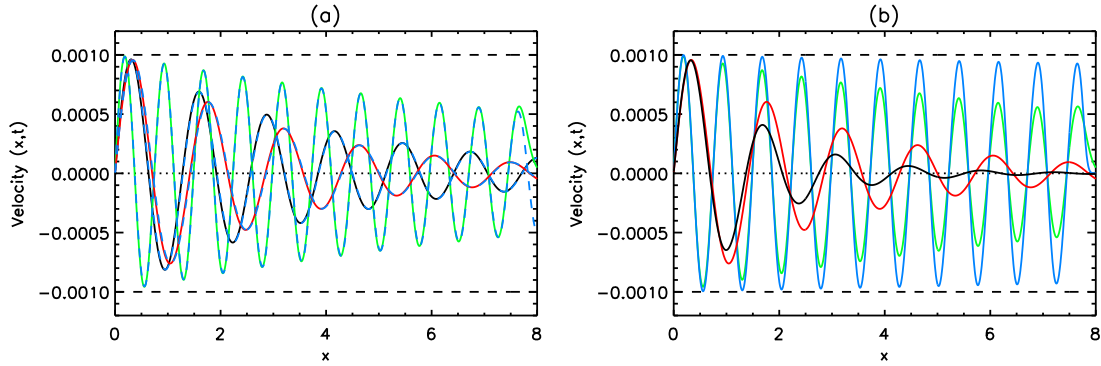


Figure 2.11: (a) v with $\rho_0 = 1$ and $\epsilon_0 = 0.5$ (green), $\epsilon_0 = 1.5$ (black) and $\epsilon_0 = 1.875$ (red), with normal mode analysis shown in blue dashed lines. (b) v with $\epsilon_0 = 0.5$ and $\rho_0 = 1$ (green) and $\rho_0 = 8.5$ (blue). With $\epsilon_0 = 1.875$ and $\rho_0 = 1$ (red) and $\rho_0 = 0.5$ (black) also shown. The horizontal dashed lines show the maximum and minimum of the undamped v . Snapshot taken at time $t = 10.5$.

effects of thermal conduction at such low densities. Luciani et al. (1983) questioned the validity of classical thermal conduction in this regime.

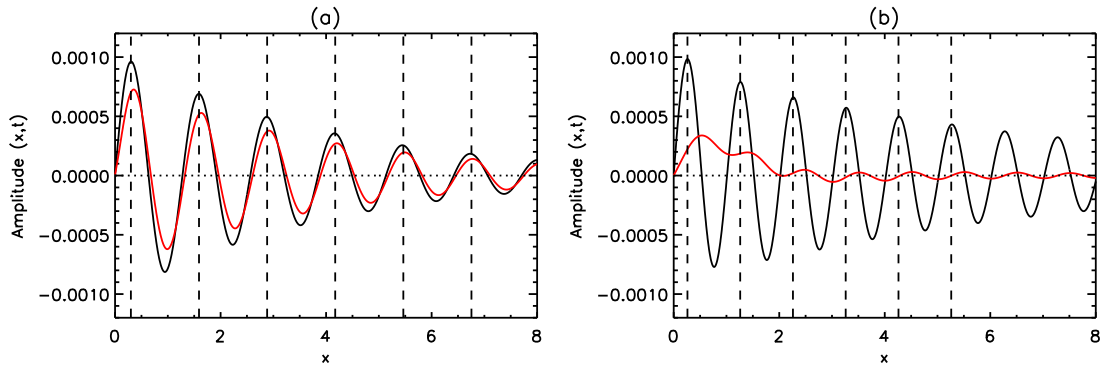


Figure 2.12: v (black) and ϵ_1 (red) for $\epsilon_0 = 1.5$ with (a) $\rho_0 = 1$ and (b) $\rho_0 = 0.03$. The vertical dashed lines show one wavelength when the wave is propagating at (a) the adiabatic sound speed and (b) the isothermal sound speed. Snapshot taken at time $t = 10.5$.

The wavelength of the propagating wave is given by Eq. (2.43). As a result, $\lambda = c_s$. In an isothermal medium the wave propagates at the isothermal sound speed, c_{si} , which is a factor of $\sqrt{\gamma}$ slower than the adiabatic sound speed, c_{sa} (De Moortel and Hood 2003). The vertical dashed lines in Fig. 2.12(a) have a spatial separation of one wavelength based on the adiabatic sound speed, whereas, in Fig. 2.12(b) the isothermal sound speed is used. The peaks in velocity match the vertical lines in both figures, which shows that the wave in Fig. 2.12(a) is travelling at the adiabatic sound speed, whilst the wave in Fig. 2.12(b) travels at the isothermal sound speed.

2.4.6.1 Thermal Conduction and Gravitational Stratification

Thermal conduction is included in the simulation with a coefficient of $d = 0.025$ and compressive viscosity and optically thin radiation are neglected.

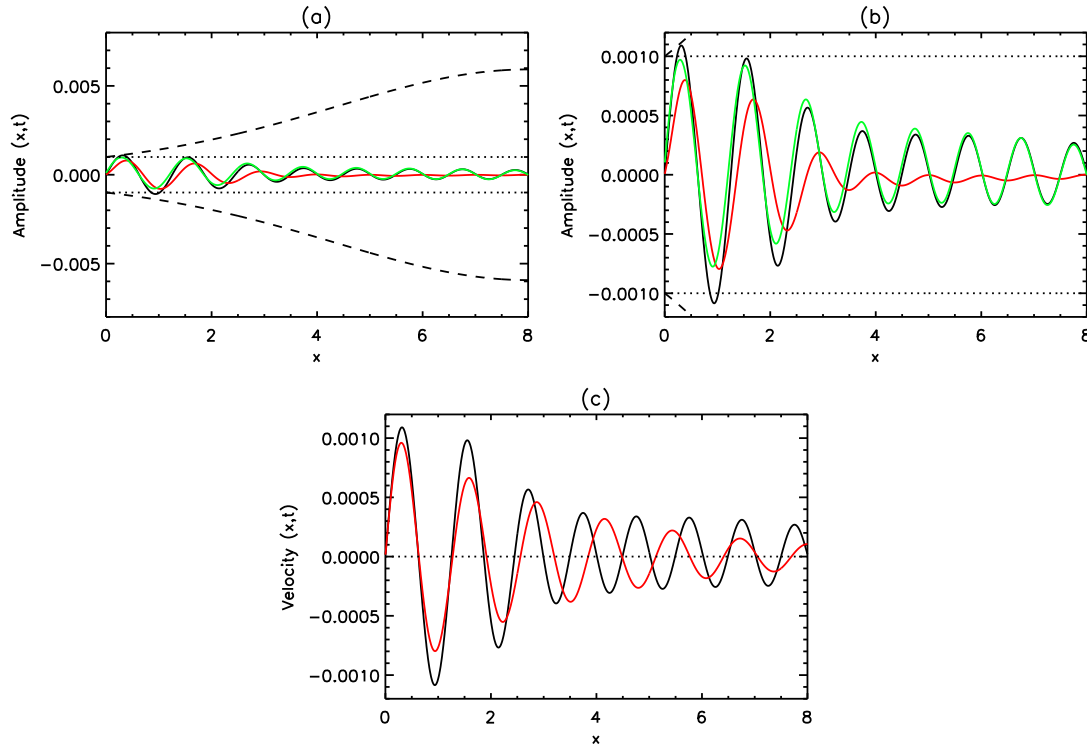


Figure 2.13: (a) v (black), ϵ_1 (red) and $\frac{\rho_1}{\rho_0}$ (green) for $\epsilon_0 = 1.5$ and $\rho_0(0) = 1$. The maximum and minimum amplitudes of v for a stratified medium without damping are shown by dashed lines, whilst those for an unstratified medium by dotted lines. (b) a close up of (a). (c) v for an unstratified medium with $\rho_0 = 0.9$ (red) plotted with v from (a) in black. Snapshot taken at time $t = 10.5$.

The results of the simulation shown in Fig. 2.13(a) include the effects of stratification, for $\epsilon_0 = 1.5$ and $\rho_0(0) = 1$. Fig. 2.13(b) is an enlarged version of Fig. 2.13(a) and Fig. 2.13(c) compares v from Fig. 2.13(b) (black) to that of an unstratified medium with $\rho_0 = 0.9$ (red). Figs. 2.13(a) and (b) show that a significant amount of damping is present when thermal conduction is introduced to the system, as seen in an unstratified medium (Fig. 2.8(a)). Comparing Fig. 2.13(a) with Fig. 2.6(a) it is clear that thermal conduction produces much greater damping than compressive viscosity. Additionally, Fig. 2.13(b) clearly shows that the damping due to thermal conduction dominates the increase in the amplitude of velocity caused by gravitational stratification by damping the velocity to an amplitude even smaller than that of the ideal case (dotted).

The inclusion of gravity produces a continually changing equilibrium density profile, which results in the effects of thermal conduction changing along the loop. Fig. 2.14(a) shows the damping length due to thermal conduction as a function of (a) ρ_0 and (b) x for a gravitationally stratified medium with $\epsilon_0 = 1.5$ and $\rho_0(0) = 1$. There is a clear minimum damping length, shown in Fig. 2.14(a), at $\rho_0 \approx 0.25$, which

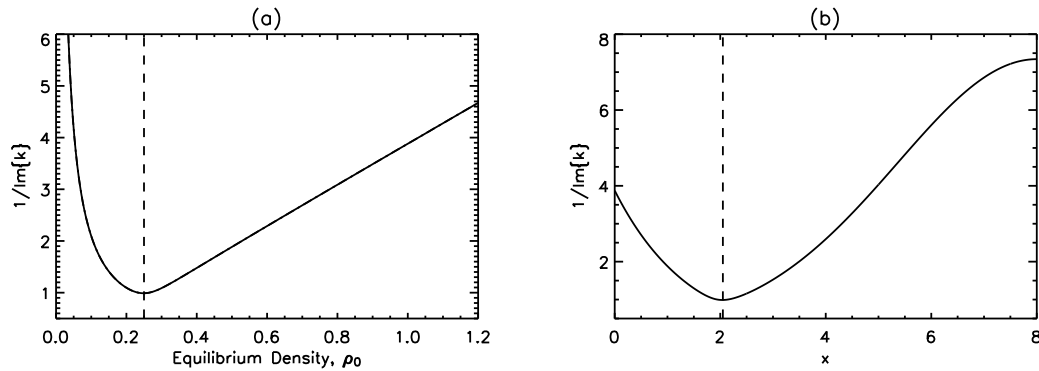


Figure 2.14: Damping length due to thermal conduction as a function of (a) ρ_0 and (b) x . The vertical dashed line represents the minimum damping length giving (a) the equilibrium density and (b) the position.

corresponds to $x \approx 2$ as seen in Fig. 2.14(b). As a result, either side of this density the damping due to thermal conduction is reduced. This result can be seen from the black line in Fig. 2.13(c) which shows the velocity damped by thermal conduction in a stratified medium. The velocity is moderately damped initially before the damping rate is increased between $x = 2$ and $x = 3$ after which it remains relatively undamped. This is shown more clearly in Fig. 2.14(b), where the damping length is plotted as a function of x . The fast reduction in damping is explained by the steep increase in damping length at densities lower than $\rho_0 \approx 0.1$, corresponding to $x \geq 3.5$. The red line in Fig. 2.13(c) shows the damping due to thermal conduction for a uniform equilibrium density of 0.9. The case with gravity (black) damps quicker than with $\rho_0 = 0.9$ (red) at $x \approx 2.5$ when thermal conduction is most efficient. However, the uniform density case damps quicker at both greater and lower x as a result of the reduced damping of the case with gravity. The peaks in velocity for the case with gravitational stratification in Fig. 2.13(c) (black) are seen to progressively lag the uniform density case (red). This demonstrates how the increase in thermal conduction causes the wave to no longer propagate at the adiabatic sound speed, but at the slower isothermal sound speed or an intermediate speed.

2.4.7 All Damping Mechanisms

The effects of optically thin radiation, compressive viscosity and thermal conduction are combined and compared to those of thermal conduction alone (dashed lines in Fig. 2.15). Fig. 2.15(a) shows v , ϵ_1 and $\frac{\rho_1}{\rho_0}$ (solid lines) damped due to all three mechanisms for $\epsilon_0 = 1.5$ and $\rho_0 = 1$. Comparison of the solid (all damping mechanisms) and dashed black (thermal conduction only) lines in Fig. 2.15(a) shows that most of the damping is caused by thermal conduction, however, there is extra damping from the inclusion of radiation and viscosity. This extra damping is almost entirely due to compressive viscosity, with optically thin radiation negligible, as discussed in Section 2.4.4.1 and shown by the comparison of Figs. 2.4(a) and 2.6(a). These results agree with the conclusions of De Moortel and Hood (2003, 2004).

Fig. 2.15(b) shows v from Fig. 2.15(a) in black with v for $\epsilon_0 = 1.875$ and $\rho_0 = 0.5$ in red. The maximum and minimum amplitudes of v when damped only by thermal conduction are again shown by the dashed lines. It is clear from the dashed red line in Fig. 2.15(b) that thermal conduction is more efficient for $\epsilon_0 = 1.875$ and $\rho_0 = 0.5$, as discussed in Section 2.4.6 and shown in Fig. 2.11. In addition, for $\epsilon_0 = 1.875$ and

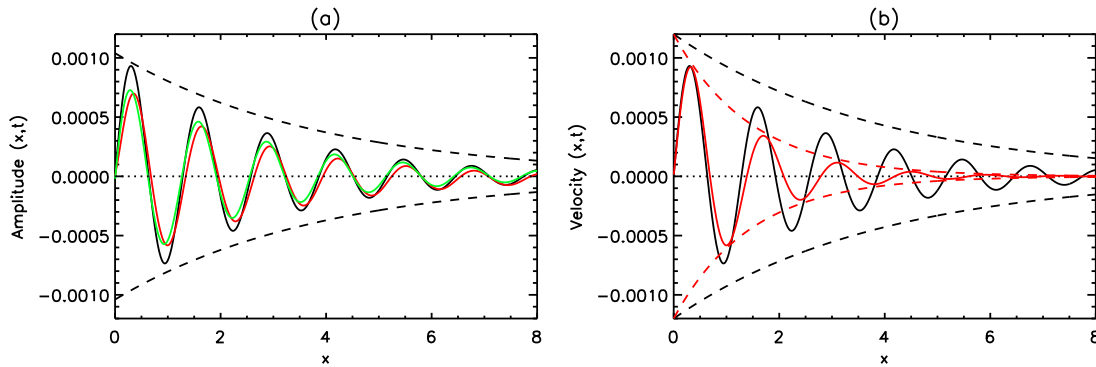


Figure 2.15: (a) v (black), ϵ_1 (red) and $\frac{\rho_1}{\rho_0}$ (green) for $\epsilon_0 = 1.5$ and $\rho_0 = 1$. (b) v for $\epsilon_0 = 1.875$ and $\rho_0 = 0.5$ (red) with v from (a) in black. The amplitude of v damped by thermal conduction alone are shown by the dashed lines. Snapshot taken at time $t = 10.5$.

$\rho_0 = 0.5$ the damping due to optically thin radiation and compressive viscosity is reduced and consequently the difference between damping due to radiation, viscosity and thermal conduction (red solid) compared to thermal conduction alone (red dashed) is almost negligible. Damping due to radiation is reduced as ϵ_0 increases and as ρ_0 decreases (as shown by Figs. 2.3(b) and (c)) and hence, is much weaker when $\epsilon_0 = 1.875$ and $\rho_0 = 0.5$ than $\epsilon_0 = 1.5$ and $\rho_0 = 1$. The effect of viscosity is reduced by the increase in ϵ_0 , but increased by the decrease in ρ_0 . However, the overall result is a small decrease in the damping, as shown by comparison of Figs. 2.5(b) and (c).

2.4.8 All Damping Mechanisms and Gravitational Stratification

The effects of gravitational stratification are added to the results from Section 2.4.7. The resulting perturbations in velocity, energy and density are shown in Fig. 2.16(a). Fig. 2.16(b) shows v from Fig. 2.16(a) (black) compared to v in a gravitationally stratified medium with damping due to radiation and viscosity (green) and thermal conduction alone (red).

Fig. 2.16(a) shows a large amount of damping, with the perturbation amplitudes far below that of an undamped wave in both a stratified (dot-dashed) and even an unstratified medium (dotted). The relative phase shift between the perturbed quantities produced by thermal conduction, discussed in Section 2.4.6, is still clearly visible.

2.5 Non-Uniform Temperature Equilibrium

Section 2.4 investigated the effects of optically thin radiation, compressive viscosity and thermal conduction for a uniform equilibrium temperature in both stratified and unstratified atmospheres. The uniform temperature equilibrium of 1 MK used in Section 2.4 and by De Moortel and Hood (2003, 2004) represents the solar corona. However, to model wave propagation through the lower regions of the solar atmosphere

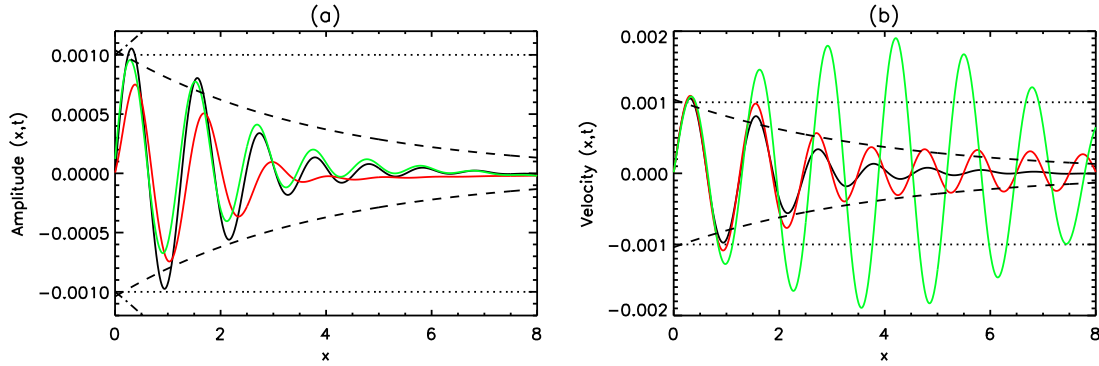


Figure 2.16: (a) v (black), ϵ_1 (red) and $\frac{\rho_1}{\rho_0}$ (green) for $\epsilon_0 = 1.5$ and $\rho_0(0) = 1$. (b) close up of v from (a) in black, with v due to damping by radiation and viscosity (green) and by conduction alone (red). The dashed black lines are taken from Fig. 2.15(a) of damping due to thermal conduction in a unstratified medium. The maximum and minimum amplitudes of v for a stratified medium without damping are shown by dot-dashed lines, whilst those for an unstratified medium are dotted. Snapshot taken at time $t = 10.5$.

into the corona, a non-uniform temperature profile is required. The model is therefore extended to a non-uniform equilibrium temperature (see Fig. 2.17) to investigate the effect of thermal conduction on wave propagation in a medium with changing background temperature and density. The temperature increases from 0.33 MK through a transition region to a coronal value of 1.25 MK.

In order to model wave propagation from the solar surface, a minimum temperature of around 6000 K is required. However, due to the high density below $10^{4.3}$ K the approximation of optically thin radiation becomes invalid i.e. the mean free path is shorter than typical length scales. Therefore, the model is restricted to propagation from the chromosphere into the corona. The minimum temperature used in the model (300,000 K) and the height and width of the transition region (≥ 14 Mm and ≥ 10 Mm, respectively) are limited due to numerical effects. A steeper temperature gradient over a greater temperature range requires an increased spatial resolution. In addition, the low coronal density, produced when the height of the temperature gradient is lower (this is due to the normalisation chosen and is discussed further in Section 2.5.2), reduces the numerical time step due to the Courant-Friedrichs-Lewy (CFL) condition. To ensure the accuracy of the numerical results the numerical time step must be shorter than the CFL condition. In Lare 1d, this condition is given by

$$\delta t \leq \frac{\delta x}{c} \approx \delta x \sqrt{\frac{\rho}{\gamma p + B^2}}, \quad (2.113)$$

which is proportional to $\sqrt{\rho}$.

Optically thin radiation has been neglected from the model due to the negligible effects found in Section 2.4. Despite this it still provides the lower temperature limit of $10^{4.3}$ K for the model, as below this temperature the assumption of the medium being optically thin becomes invalid and the effects of radiation may no longer be negligible. In addition, damping due to radiation will increase at lower temperatures and higher density. In contrast, damping due to thermal conduction will decrease at lower temperature and higher density, however, compressive viscosity is likely to remain similar as it will increase at lower temperature, but decrease at higher density.

2.5.1 Without Gravitational Stratification Or Damping

Initially an equilibrium temperature profile with a broad transition region is used, as shown in Figs. 2.17(a) and (c) (hereafter profile 1). The results from this are compared to a more realistically steep transition region given by Figs. 2.17(b) and (d) (hereafter profile 2). For long wavelength oscillations with periods of a few minutes, the steep transition region of profile 2 (Fig. 2.17(d)) approximates a discontinuity. By using the broad temperature profile, shown in Fig. 2.17(c), the effects of adding a non-uniform temperature profile can be investigated without the additional complexity of a discontinuity. The effects of the discontinuity are then ascertained by comparing the results using profile 1 with those of the steeper profile 2. For pressure to remain constant, the increase in temperature in the transition region is balanced by a decrease in density. Fig. 2.17(a) shows profile 1 for the full numerical domain with x in dimensional units and in Mm for comparison. As in Section 2.4, Figs. 2.17(c) and (d) and the results hereafter are only shown for the first half of the domain, from the footpoint to the loop apex. The vertical blue lines in Figs. 2.17(c) and (d) show the relative widths of the broad and steep transition regions, respectively. Profile 1 (Fig. 2.17(c)) has a shallow temperature gradient at $x = 1.7$ (60 Mm), with a width of 60 Mm, whereas, profile 2 (Fig. 2.17(d)) has a more realistically steep gradient at $x = 0.55$ (14 Mm), with a width of 10 Mm. The real transition region, where the temperature rises rapidly from 10^4K to 10^6K , has a width of 0.1-0.2 Mm at a height of around 2 Mm. The two profiles shown in Fig. 2.17 are normalised to coronal conditions at the edge of active regions. That is, for both profiles at an equilibrium temperature of 1 MK the equilibrium density is $1.67 \times 10^{-12} \text{ kg m}^{-3}$. This can be seen by the intersection of the dashed lines in Figs. 2.17(a) and (b).

Figs. 2.18(a) and (b) show the simulation results for the v , ϵ_1 and $\frac{\rho_1}{\rho_0}$ of an undamped sound wave, travelling in a medium without gravitational stratification and with non-uniform equilibrium energy and density profiles, as shown in Figs. 2.17(c) and (d), respectively. The maximum amplitude of v and ϵ_1 in both Figs. 2.18(a) and (b) are seen to increase at low x and subsequently stay constant with increasing x , as expected for an undamped wave with uniform equilibrium energy and density. The increase in amplitude is due to the change in the equilibrium conditions, with the maximum and minimum amplitudes only changing when the equilibrium energy and density are not constant, i.e. when $0.85 < x < 2.6$ for Fig. 2.18(a) and $0.4 < x < 0.68$ for Fig. 2.18(b). $\frac{\rho_1}{\rho_0}$ (green) decreases through this region to balance the increase in ϵ_1 and keep the perturbed pressure constant. Due to the steepness of the temperature gradient in profile 2, the density in Fig. 2.18(b) has a small spike, which is not seen in Fig. 2.18(a).

The amplitude of v in Fig. 2.18 has a $v \sim \rho_0^{-1/4}$ dependence, which was found for Alfvén waves by Wright and Garman (1998). It can be calculated for sound waves from the wave equation given by Eq. (2.35),

$$\frac{\partial^2 v}{\partial t^2} = c_s^2(x) \frac{\partial^2 v}{\partial x^2}, \quad (2.114)$$

using a WKB approximation. Assuming v has the form $v = \hat{v}e^{i\omega t}$ and taking temporal derivatives, Eq. 2.114 becomes,

$$\frac{\partial^2 v}{\partial x^2} + \frac{\omega^2}{c_s^2(x)} v = 0, \quad (2.115)$$

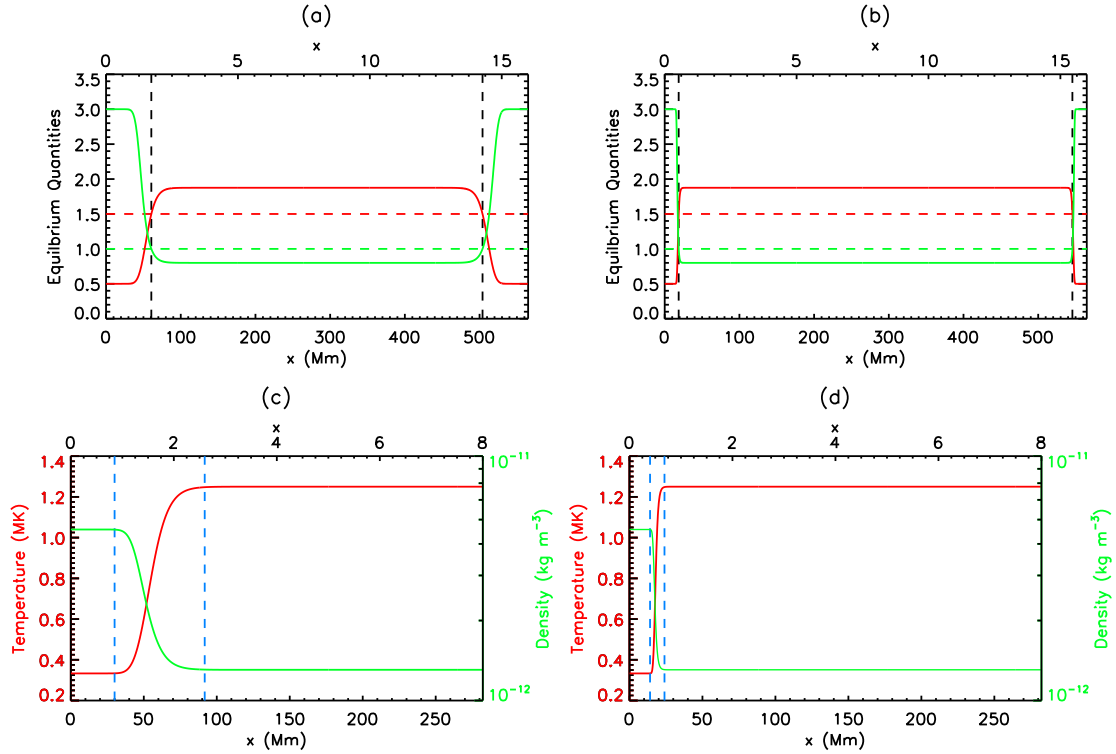


Figure 2.17: (a) equilibrium temperature (red) and density (green) profile in dimensionless units with a broad transition region (profile 1). (b) same as (a), but for profile 2. The red and green dashed lines mark a temperature of 1 MK and a density of $1.67 \times 10^{-12} \text{ kg m}^{-3}$, respectively, which occur at the positions marked by the dashed black lines. (c) same as (a), but for half the domain, with temperature and density in units of MK and kg m^{-3} , respectively. (d) same as (c), but for profile 2. The vertical dashed blue lines in (c) and (d) represent the transition region. The loop position is given in both Mm (below) and dimensionless units (above).

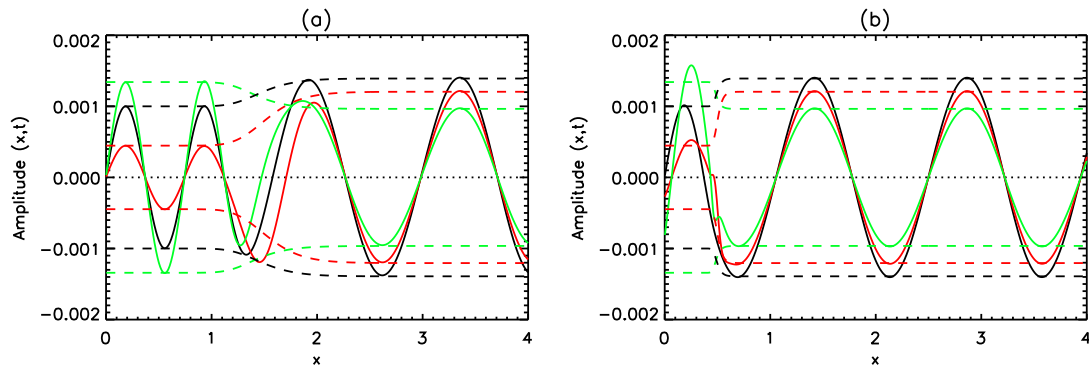


Figure 2.18: (a) v (black), ϵ_1 (red) and $\frac{\rho_1}{\rho_0}$ (green) for (a) profile 1 and (b) profile 2. The dashed lines show the predicted maximum and minimum amplitudes assuming no reflection in the transmission region. The figures are plotted for $0 \leq x \leq 4$ to show the change in amplitudes at low x more clearly. Snapshot taken at time $t = 10.5$.

which can be written as,

$$\frac{\partial^2 v}{\partial x^2} + \omega^2 f(x)^2 v = 0, \quad (2.116)$$

where $f(x) = \frac{1}{c_s(x)}$. Using a WKB approximation, v and its spatial derivatives can be written as,

$$v = e^{i\Omega\phi_0 + \phi_1}, \quad (2.117)$$

$$\frac{\partial^2 v}{\partial x^2} = \left(-\Omega^2 \left(\frac{\partial \phi_0}{\partial x} \right)^2 + 2i\Omega \frac{\partial \phi_0}{\partial x} \frac{\partial \phi_1}{\partial x} + i\Omega \frac{\partial^2 \phi_0}{\partial x^2} \right) v, \quad (2.118)$$

where ϕ_0 and ϕ_1 are to be determined. Substituting Eq. (2.118) into Eq. (2.35) gives,

$$\left(-\Omega^2 \left(\frac{\partial \phi_0}{\partial x} \right)^2 + 2i\Omega \frac{\partial \phi_0}{\partial x} \frac{\partial \phi_1}{\partial x} + i\Omega \frac{\partial^2 \phi_0}{\partial x^2} + \omega^2 f(x)^2 \right) v = 0. \quad (2.119)$$

By equating the real and imaginary parts of Eq. (2.119) and integrating with respect to x ,

$$\phi_0 = \pm \int f(x) dx, \quad (2.120)$$

$$\phi_1 = -\frac{1}{2} \ln f(x). \quad (2.121)$$

Substituting Eqs. (2.120) and (2.121) into Eq. (2.117) gives,

$$v = f^{-\frac{1}{2}} e^{\pm i\Omega \int f(x) dx}, \quad (2.122)$$

$$v = c_s(x)^{\frac{1}{2}} e^{\pm i\Omega \int \frac{1}{c_s(x)} dx}, \quad (2.123)$$

where v has a $c_s(x)^{\frac{1}{2}}$ dependence. Using Eqs. (2.43) and (2.20), $c_s(x)^{\frac{1}{2}} = \left(\frac{\gamma p_0}{\rho_0} \right)^{\frac{1}{4}}$, which as pressure is constant means, $v \sim \rho_0^{-\frac{1}{4}}$. This velocity dependence is plotted by dashed black lines in Fig. 2.18 and agrees with the simulation results. The amplitudes of the energy and density perturbations relative to that of velocity are found using Eqs. (2.38) and (2.37), respectively.

2.5.2 Gravitationally Stratified Medium

Gravitational stratification is now included in the model. Figs. 2.19(a) and (b) show profiles 1 and 2, respectively, with gravitational stratification (hereafter profiles 3 and 4, respectively). As discussed previously, the model is normalised so that the equilibrium density is $1.67 \times 10^{-12} \text{ kg m}^{-3}$ when the equilibrium temperature is 1 MK. As shown in Figs. 2.17(a) and (b) this position is determined by the temperature profile chosen ($x \approx 1.7$ and $x \approx 0.55$ for Figs. 2.19(a) and (b), respectively). The distance from the loop footpoint to where $\rho_0 = 1.67 \times 10^{-12} \text{ kg m}^{-3}$ is greater for profile 3 than 4, hence, the decrease in the equilibrium density over this distance, due to gravitational stratification, will be greater for profile 3 than 4. Therefore, in order to keep the same density at 1 MK, profile 3 requires a higher footpoint density than profile 4. This can be seen by comparing Figs. 2.19(a) and (b) and is a result of the temperature gradient and the normalisation method. The equilibrium density is reduced by around an order of magnitude at large x , due to the inclusion of gravity.

Profile 4, shown in Fig. 2.19(b), has a slightly lower equilibrium density than that of Fig. 2.19(a) at large x due to the lower density at $x = 0$, of $\rho_0(0) = 0.5$ compared to $\rho_0(0) = 8.5$. As a result, profile

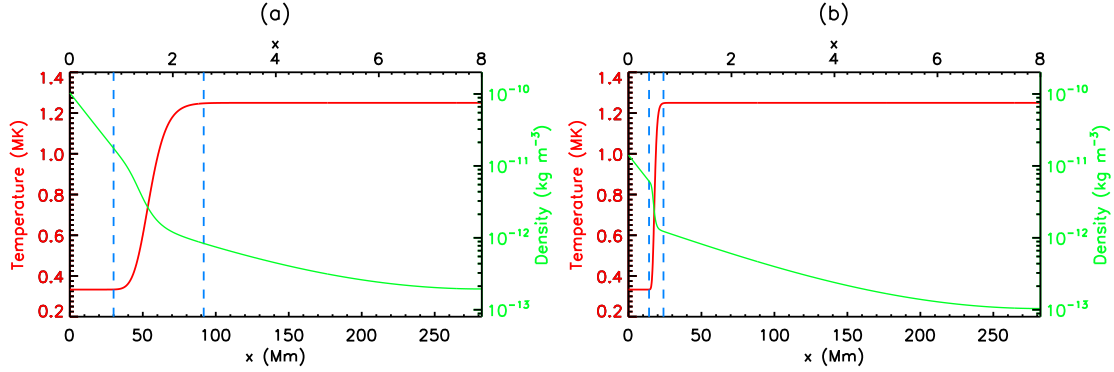


Figure 2.19: (a) equilibrium temperature (red) and density (green) profile units with a broad transition region. (b) same as (a), but with a steep transition region. The vertical dashed blue lines represent the transition region. The loop position is given in both Mm and dimensionless units.

3 has the largest reduction in equilibrium density, of almost three orders of magnitude across the box, compared with two orders of magnitude for profile 4. For both profiles the density at $T = 1$ MK is $\rho_0 = 1.67 \times 10^{-12} \text{ kg m}^{-3}$, which is consistent with the uniform equilibrium temperature results of Section 2.4 and the results of Section 2.5.1 without gravitational stratification.

The numerical results for v (black), ϵ_1 (red) and $\frac{\rho_1}{\rho_0}$ (green) are shown in Fig. 2.20(a) for profile 3 and in Fig. 2.20(b) for profile 4. The amplitude of the velocity without gravitational stratification is also plotted (dotted). The greater footpoint density of profile 3 compared to profile 4 causes the magnitude of the oscillation in Fig. 2.20(a) to become much greater than that of Fig. 2.20(b), despite having the same oscillation amplitude at the loop footpoint.

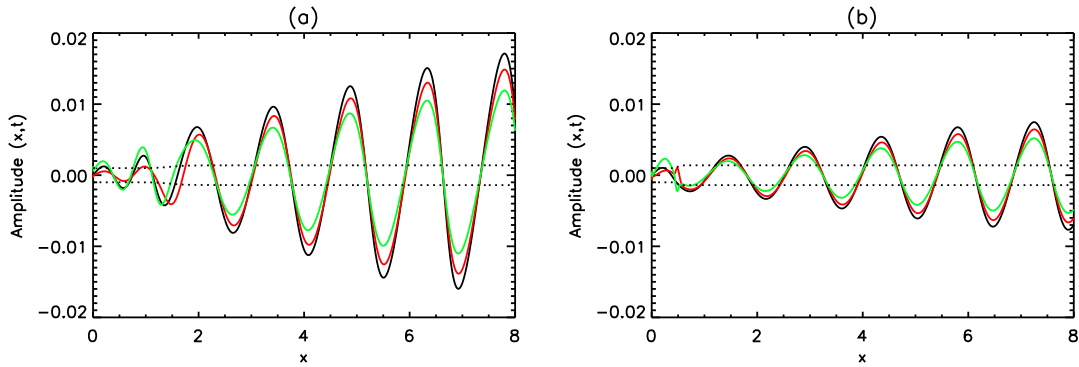


Figure 2.20: (a) v (black), ϵ_1 (red) and $\frac{\rho_1}{\rho_0}$ (green) for (a) profile 3 and (b) profile 4. The dotted lines show v without gravitational stratification. Snapshot taken at time $t = 10.5$.

2.5.3 Compressive Viscosity

The results for damping due to compressive viscosity in an unstratified medium with non-uniform equilibrium energy and density can be seen in Figs. 2.21(a) and (b) using profiles 1 and 2 from Figs. 2.17(c) and

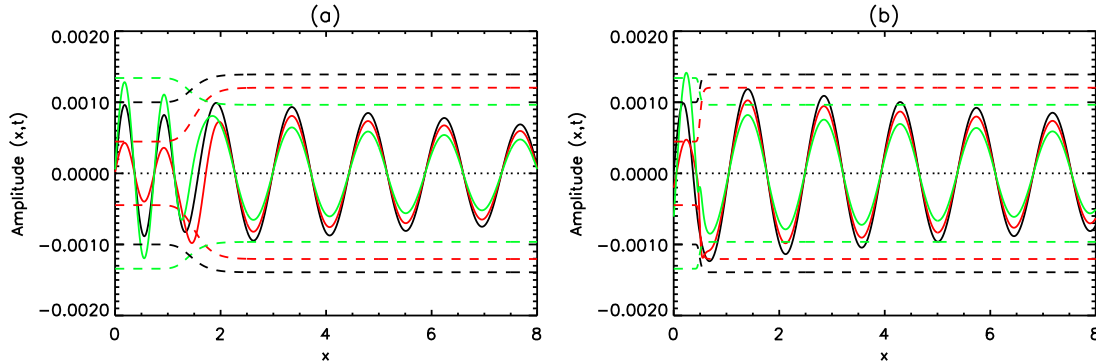


Figure 2.21: (a) v (black), ϵ_1 (red) and $\frac{\rho_1}{\rho_0}$ (green) for (a) profile 1 and (b) profile 2. The dashed lines show the predicted maximum and minimum amplitudes of an undamped wave assuming no reflection in the transition region. Snapshot taken at time $t = 10.5$.

(d), respectively. By comparing Fig. 2.21 with Fig. 2.18 it can be clearly seen that compressive viscosity acts to damp the wave in an unstratified medium. This is consistent with the results from Section 2.4.4 for uniform equilibrium energy and density. Both waves in Fig. 2.21 experience similar damping, with Fig. 2.21(a) damped slightly more. This is a consequence of damping due to compressive viscosity being greater at lower energies (see Figs. 2.5(c) and (d)). Due to the higher transition region of profile 1 compared to that of 2, the wave in Fig. 2.21(a) is at a lower energy for a greater distance than that of Fig. 2.21(b) and hence experiences greater damping.

2.5.3.1 Compressive Viscosity and Gravitational Stratification

Gravitational stratification is included with damping due to compressive viscosity. Figs. 2.22(a) and (b) show v , ϵ_1 and $\frac{\rho_1}{\rho_0}$ for profiles 3 and 4, respectively. As expected from Fig. 2.20, the inclusion of gravitational stratification has caused an increase in the wave amplitudes compared to those of an unstratified medium (Fig. 2.21). The amount of damping that occurs due to viscosity is again similar for both Figs. 2.22(a) and (b), however, Fig. 2.22(b) is damped slightly more compared to Fig. 2.22(a), which was not seen in Fig. 2.21 for an unstratified medium. This is a consequence of damping due to compressive viscosity being more efficient at lower densities (Fig. 2.5(b)), which therefore, suggests Fig. 2.21(b) should be damped more as profile 4 (Fig. 2.19(b)) has a slightly lower coronal density than profile 3 (Fig. 2.19(a)).

2.5.4 Thermal Conduction

In Section 2.4.6 the effects of thermal conduction were investigated for uniform equilibrium temperature in both stratified and unstratified atmospheres. It was found that thermal conduction can have a major effect on propagating slow waves. It causes rapid damping as well as a phase shift between the velocity and the perturbations in energy and density, as shown in Fig. 2.13(b). The effects of thermal conduction are now investigated for non-uniform equilibrium temperature profiles as shown in Figs. 2.17(c) and (d), the results of which are shown for v , ϵ_1 and $\frac{\rho_1}{\rho_0}$ in Figs. 2.23(a) and (b), respectively.

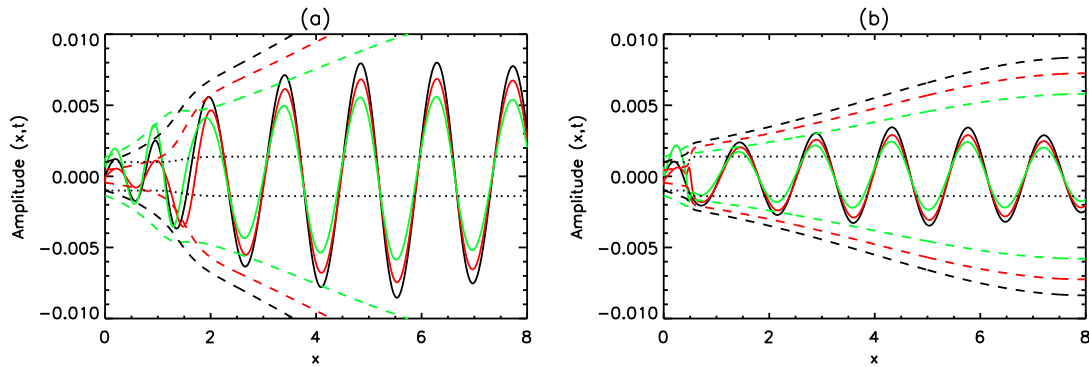


Figure 2.22: (a) v (black), ϵ_1 (red) and $\frac{\rho_1}{\rho_0}$ (green) for (a) profile 3 and (b) profile 4. The dashed lines show the predicted maximum and minimum amplitudes of the undamped v , ϵ_1 and $\frac{\rho_1}{\rho_0}$, assuming no reflection in the transition region, with v without gravitational stratification (dotted). Snapshot taken at time $t = 10.5$.

To maintain a non-uniform temperature equilibrium the coronal heating function, $d\left(\frac{5}{2} + \epsilon_0\right)\epsilon_0^{\frac{3}{2}}\frac{\partial^2\epsilon_0}{\partial x^2}$, in Eq. (2.73) must be balanced as $\frac{\partial\epsilon_0}{\partial x} \neq 0$. This term is a function of x , but is independent of t . It is, therefore, calculated at time, $t = 0$ and is added to the energy equation at every subsequent time step in order to maintain the equilibrium temperature gradient.

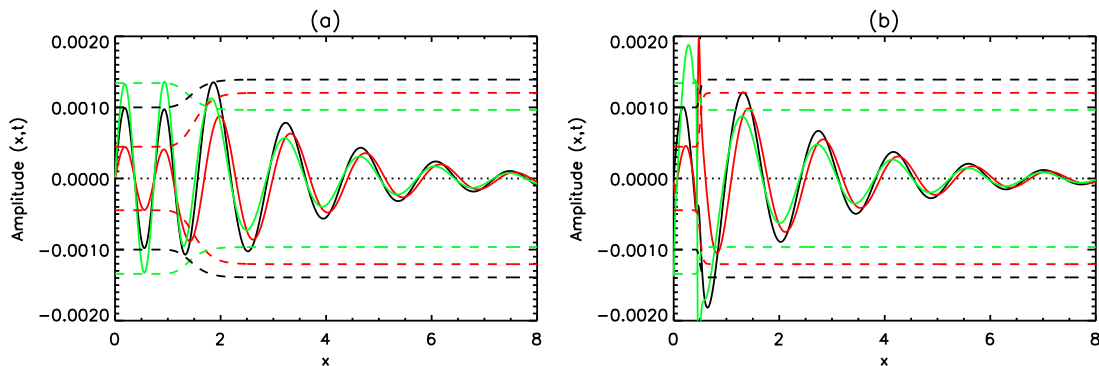


Figure 2.23: (a) v (black), ϵ_1 (red) and $\frac{\rho_1}{\rho_0}$ (green) for (a) profile 1 and (b) profile 2. The dashed lines show the predicted maximum and minimum amplitudes of an undamped wave assuming no reflection in the transition region. Snapshot taken at time $t = 10.5$.

As expected from Section 2.4.6, Figs. 2.23(a) and (b) both show that thermal conduction acts to significantly damp the wave. By comparing Fig. 2.23 with Fig. 2.21 for compressive viscosity it is clear that damping due to thermal conduction is again the dominant effect. A major contrast between Figs. 2.23(a) and (b) (enlarged for clarity in Figs. 2.24(a) and (b), respectively) are the spikes seen in the energy and density perturbations of Fig. 2.23(b) but not Fig. 2.23(a). The perturbed quantities, ϵ_1 and ρ_1 depend on the derivatives of the equilibrium quantities, ϵ_0 and ρ_0 , which can be seen by linearising Eqs. (2.69) and (2.71), respectively. As a result, the large gradient in the equilibrium quantities in Fig. 2.17(d) produce spikes in the density and energy perturbations which do not occur for the smaller derivatives of Fig. 2.17(c). The importance of the derivatives can be seen, for density for example, by linearising Eq. (2.69) and comparing the equation for a uniform equilibrium temperature (Eq. (2.124)) with that of a non-uniform temperature

equilibrium (Eq. (2.125)). For a uniform temperature equilibrium, Eq. (2.124) shows that changes in the density perturbation depend only on the derivative of the velocity:

$$\frac{\partial \rho_1}{\partial t} = -\rho_0 \frac{\partial v}{\partial x}. \quad (2.124)$$

However, for a non-uniform temperature equilibrium ρ_0 is not constant and Eq. (2.125) has an extra term,

$$\frac{\partial \rho_1}{\partial t} = -\rho_0 \frac{\partial v}{\partial x} - v \frac{\partial \rho_0}{\partial x}, \quad (2.125)$$

hence, the density perturbation is now also affected by the derivative of the equilibrium density. However, the spike in Fig. 2.23(b) is more likely to be a numerical effect caused by Gibbs overshoot.

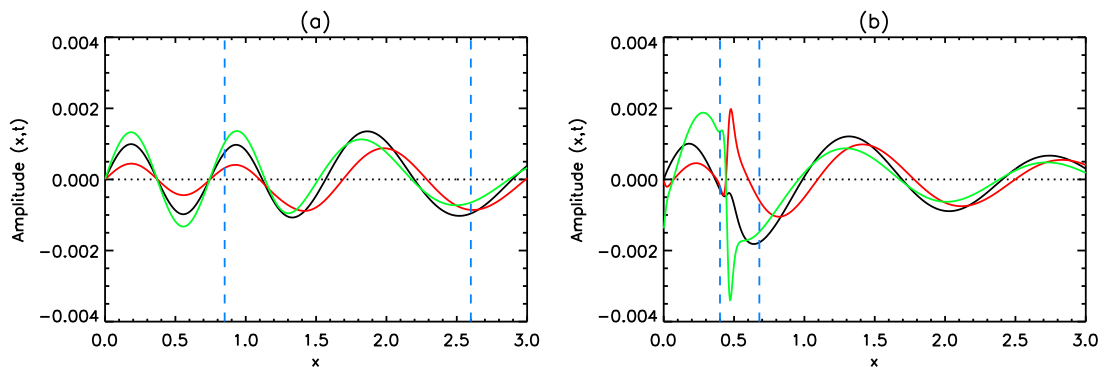


Figure 2.24: Close up of (a) Fig. 2.23(a) and (b) Fig. 2.23(b). The vertical dashed blue lines represent the transition region. Snapshot taken at time $t = 10.5$.

The inclusion of thermal conduction, as discussed in Section 2.4.6, introduces a phase shift near the lower boundary ($x \approx 0$), which is again seen in Fig. 2.24. Using either temperature profile shown in Fig. 2.17 gives a propagation speed (Eq. 2.43) that increases with x and hence, at any given instance in time, features at larger x will travel faster. Consequently, the initial phase shift will increase as, say a maximum of the energy perturbation will lead the corresponding velocity maximum and hence have a higher propagation speed. The increased phase shift between the perturbed quantities could provide a larger possibility of observation by comparing the relative position of perturbations in intensity with those from Doppler shifts.

2.5.4.1 Thermal Conduction and Gravitational Stratification

Figs. 2.25(a) and (b) show the simulation results for waves propagating in a gravitationally stratified medium with the equilibrium temperature and density profiles as shown in Figs. 2.19(a) and (b), respectively and damping due to thermal conduction.

Below the transition region ($x \leq 1.7$ for Fig. 2.25(a) and $x \leq 0.6$ for Fig. 2.25(b)) the equilibrium density is high and the equilibrium energy low, whereas above the transition region the equilibrium density is low and the equilibrium energy is high, as seen in Fig. 2.19. The damping due to thermal conduction depends on the equilibrium density and energy, as discussed in Section 2.4.6. Fig. 2.11 shows that damping due to

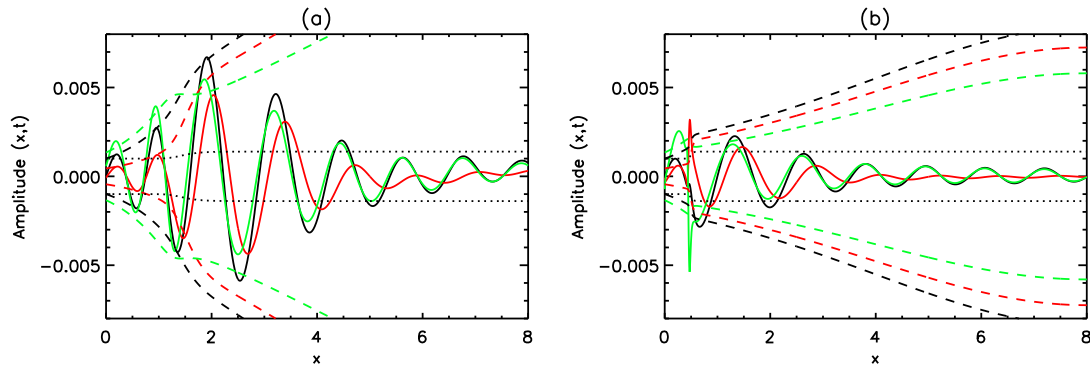


Figure 2.25: (a) v (black), ϵ_1 (red) and $\frac{\rho_1}{\rho_0}$ (green) for (a) profile 3 and (b) profile 4. The dashed lines show the predicted maximum and minimum amplitudes of the undamped v , ϵ_1 and $\frac{\rho_1}{\rho_0}$, assuming no reflection in the transition region, with v without gravitational stratification (dotted). Snapshot taken at time $t = 10.5$.

thermal conduction is less efficient at high density and low energy (i.e. below the corona in the transition region) and more efficient at high energy and low density (i.e. above the transition region in the corona). As a result, damping due to thermal conduction below the corona is inefficient. This, combined with the effect of gravity, causes the wave amplitude in both Fig. 2.25(a) and (b) to grow for small x . This growth continues until the increase in temperature and reduction in density increases the efficiency of thermal conduction. The wave then experiences a large amount of damping until at large x the wave amplitude is damped to below that of a wave in an unstratified medium (dotted).

The main difference between the oscillations in Figs. 2.25(a) and (b) is the magnitude of the maximum wave amplitude. Both are driven at $x = 0$ with the same amplitude of 0.001, yet the maximum amplitude in Fig. 2.25(a) is nearly three times that of Fig. 2.25(b). This difference occurs due to the position of the transition region. With a transition region at $x \approx 1.7$, the wave in Fig. 2.25(a) experiences a stronger decrease in density due to gravitational stratification than Fig. 2.25(b) where the transition region is at $x \approx 0.6$. Consequently, the wave amplitude in Fig. 2.25(a) grows larger before reaching the transition region where rapid damping due to thermal conduction begins. Another reason for the difference in amplitudes is due to reflection. The steep transition region of Fig. 2.25(b) reflects more of the wave amplitude than that of Fig. 2.25(a). As a result of these two effects, the amplitude of the wave in the coronal region ($x > 1$) of Fig. 2.25(b) is much less than Fig. 2.25(a) ($x > 1$) and hence, would be observable for a shorter length. The phase shift between the perturbations in velocity, energy and density, as well as the spikes in energy and density with the steep transition region are all still clearly visible in a stratified medium.

2.5.5 Compressive Viscosity and Thermal Conduction

The effects of damping due to compressive viscosity and thermal conduction which were investigated for a uniform equilibrium temperature profile in Section 2.4.7 are now combined with a non-uniform temperature equilibrium. Figs. 2.26(a) and (b) show the results for v , ϵ_1 and $\frac{\rho_1}{\rho_0}$ using equilibrium profiles 1 (Fig. 2.17(c)) and 2 (Fig. 2.17(d)), respectively.

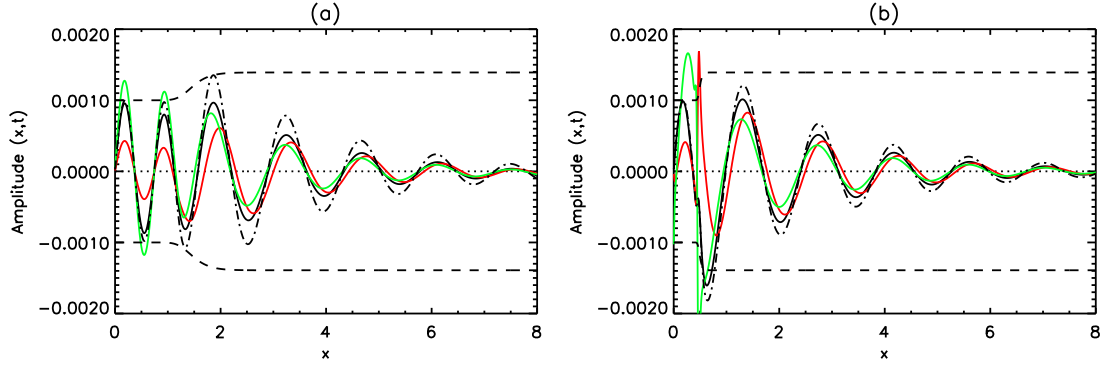


Figure 2.26: (a) v (black), ϵ_1 (red) and $\frac{\rho_1}{\rho_0}$ (green) for (a) profile 1 and (b) profile 2. The dot-dashed line shows v when damped only by thermal conduction, with the undamped amplitude shown by the dashed lines. Snapshot taken at time $t = 10.5$.

By comparing the velocity in both Figs. 2.26(a) and (b) damped by viscosity and conduction (solid) with that of the undamped v (dashed) and v damped only by thermal conduction (dot-dashed) it is clear that the main damping contribution is due to thermal conduction. However, as found for the uniform equilibrium case of Section 2.4.7, compressive viscosity does add a noticeable amount of extra damping to that of thermal conduction alone. The extra damping due to compressive viscosity compared to that of thermal conduction is slightly greater in Fig. 2.26(a) than Fig. 2.26(b) due to the higher transition region of profile 1. This causes the wave to propagate further in a low energy and high density region before reaching the high energy and low density corona. At low energy and high density, damping due to compressive viscosity is similar to that in the corona, however, damping due to thermal conduction is weaker than in the corona.

Fig. 2.26(b) shows the spikes in the perturbed energy and density that are produced with a steep temperature gradient but are not present for a shallow gradient (Fig. 2.26(a)). By comparing the spikes produced in Fig. 2.21(b) with those in Fig. 2.23(b) and Fig. 2.26(b), it is clear that the inclusion of thermal conduction increases the amplitude of the spikes produced compared to compressive viscosity. This can be seen analytically by linearising the energy equation with compressive viscosity included (Eq. (2.67), which gives,

$$\frac{\partial \epsilon_1}{\partial t} = -v \frac{\partial \epsilon_0}{\partial x} - (\gamma - 1) \epsilon_0 \frac{\partial v}{\partial x}, \quad (2.126)$$

and comparing it with that of thermal conduction (from Eq. (2.71)),

$$\frac{\partial \epsilon_1}{\partial t} = -v \frac{\partial \epsilon_0}{\partial x} - (\gamma - 1) \epsilon_0 \frac{\partial v}{\partial x} + \frac{d}{\rho_0} \frac{\partial}{\partial x} \left(\epsilon^{5/2} \frac{\partial \epsilon_1}{\partial x} + \frac{5}{2} \epsilon_0^{3/2} \epsilon_1 \frac{\partial \epsilon_0}{\partial x} \right). \quad (2.127)$$

Both equations contain the same first two terms on the right hand side, the first of which depends on the derivative of the equilibrium energy gradient. Eq. (2.127), however, has two extra terms, one of which also depends on the derivative of the equilibrium energy, hence sharp spikes are seen when thermal conduction is included.

2.5.6 Compressive Viscosity, Thermal Conduction and Gravitational Stratification

The combination of damping due to compressive viscosity and thermal conduction for a non-uniform equilibrium temperature is now investigated in a gravitationally stratified medium. Fig. 2.27(a) and (b) show the results of v , ϵ_1 and $\frac{\rho_1}{\rho_0}$ for equilibrium temperature profiles 3 and 4, respectively. The velocity damped by both compressive viscosity and thermal conduction (solid), is compared to that with thermal conduction alone (dashed).

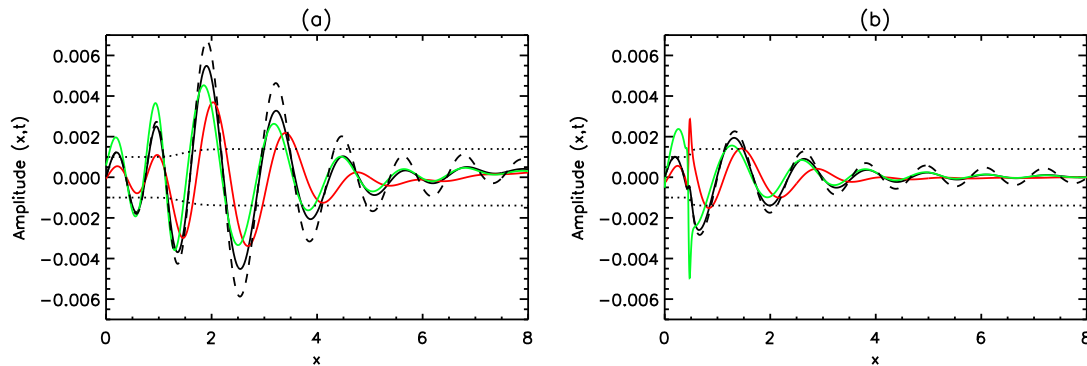


Figure 2.27: (a) v (black), ϵ_1 (red) and $\frac{\rho_1}{\rho_0}$ (green) for (a) profile 3 and (b) profile 4. The dashed black line shows v when damped only by thermal conduction. The predicted maximum and minimum amplitudes of the undamped v in an unstratified medium, assuming no reflection in the transmission region, is shown by the dotted lines. Snapshot taken at time $t = 10.5$.

Figs. 2.27(a) and (b) both show significant damping, with the wave amplitude at large x being damped to below the amplitude of an undamped wave without gravitational stratification. Thermal conduction again produces the largest amount of damping, with a small, but non-negligible contribution from compressive viscosity. As found with Fig. 2.26, Fig. 2.27(a) shows a greater contribution from compressive viscosity than Fig. 2.27(b), due to the higher transition region. The wave amplitude at large x in Fig. 2.27(b) is much less than Fig. 2.27(a) due to the lower transition region and hence the smaller increase in wave amplitude due to gravitational stratification.

2.6 Simulation Conclusions

The propagation of slow waves with a period of five minutes has been numerically simulated, in 1D, through the transition region and the corona. Initially loops were modelled at a range of uniform equilibrium temperatures and subsequently for a loop with non-uniform equilibrium temperature. The results of a uniform temperature equilibrium at 1 MK are consistent with previous work by De Moortel and Hood (2003, 2004). The effects of thermal conduction on the propagation of slow waves was investigated and the damping caused by this mechanism is consistent with previous work by De Moortel and Hood (2003). Beyond this, it was found that the inclusion of thermal conduction produces a phase shift between the perturbations in velocity, density and energy/temperature. This phase shift remains constant for waves propagating in a medium with uniform equilibrium temperature. However, the propagation speed depends

on the equilibrium temperature, hence for a non-uniform equilibrium temperature this phase shift varies along the loop. The phase shift is proportional to the equilibrium energy and inversely proportional to the density of the region. Intensity observations depend on the energy/temperature in contrast to Doppler shift observations, which depend on the velocity. Consequently, the phase shift between these three quantities may be observable as a phase shift between intensity and Doppler shift observations.

Damping due to optically thin radiation and compressive viscosity were also studied. At coronal temperatures (of order 1 MK), the damping due to optically thin radiation is negligible compared to that of thermal conduction. The inclusion of compressive viscosity, however, does show a clear, but small, amount of extra damping compared to that of thermal conduction alone. Below the corona, at lower temperature and higher density, the effects of thermal conduction are reduced, although it is still the dominant damping mechanism. Damping due to compressive viscosity remains similar as it increases at low temperature, but decreases at high density. Optically thin radiation is still negligible at the lowest temperature of our model (0.33 MK), but becomes increasingly important as the temperature falls and the density increases towards the solar surface.

The effects of non-uniform equilibrium temperature are investigated by the inclusion of a gradient from a transition region temperature of 0.33 MK to a coronal value of 1.25 MK. Two temperature profiles are modelled, the first with a shallow gradient and the second with a more realistically steep gradient. Without damping or gravitational stratification the perturbation amplitudes have a $\rho_0^{-1/4}$ dependence as calculated, for Alfvén waves, by Wright and Garman (1998). In addition, with gravitational stratification included the growth of the perturbation amplitudes agree with Roberts (2004). When thermal conduction, compressive viscosity and gravitational stratification are included, the wave amplitudes grow in the transition region and are damped in the corona. The steep transition region causes localised spikes in the energy and density perturbations where the temperature and density gradients are largest and the transition region also causes reflection of the wave. The steep temperature profile used has a transition region height of 14 Mm with a width of around 10 Mm. However, a more realistic height and width may be 2 Mm and 0.1-0.2 Mm, respectively. A narrower transition region width would increase the temperature and density gradients and may, therefore, increase the spikes produced. Whereas, a lower transition region height would reduce the growth of the perturbations by gravitational stratification and therefore result in lower oscillation amplitudes and hence reduced detection lengths.

The inclusion of an inclination angle for magnetic field lines, as shown by De Pontieu et al. (2005), allows leakage of five minute p-modes through the upper photosphere and the chromosphere. We consider only the transition region and the corona and hence leave the inclusion of an inclination angle at the solar surface to future study. Inclined magnetic field lines would reduce the effects of gravitational stratification on increasing the wave amplitude and hence may also reduce damping lengths.

Chapter 3

Forward Modelling

3.1 Introduction

In the previous chapter, numerical simulations were used to model the propagation of slow waves, damped by thermal conduction and compressive viscosity, in the solar atmosphere. The results from the numerical study presented in Chapter 2 give the plasma properties of the loop, such as energy, density and velocity. These quantities allow some understanding of the physics behind the model, but cannot readily be compared with EUV imaging observations. Velocities can be measured from Doppler shifts, however, the energy and density cannot be directly observed. Consequently, a method that allows a comparison between the simulated and observed quantities is required. This chapter uses the plasma properties of the loop from Chapter 2 with the technique of forward modelling. Forward modelling determines the observable quantities of theoretical models and, therefore, allows a better understanding of the observational consequences and signatures of the physical processes shown by the simulation results. In addition it allows a more direct comparison between numerical results and observational data. Forward modelling provides a valuable link between numerical simulations and observations, and can be performed for any observable quantity, for example Doppler velocity or intensity. This work, however, only considers intensity observations.

The intensity of a region can be calculated, with some assumptions, from the plasma density and temperature. The forward modelling of 3D MHD simulations of the corona is discussed in Peter et al. (2006). Forward modelling has been used to study acoustic waves in the sub-photosphere (Shelyag et al. 2006) as well as standing slow modes in hot coronal loops (Taroyan et al. 2007). Taroyan and Bradshaw (2008) compare forward modelling of a 1D loop model with observations from Hinode/EIS (Culhane et al. 2007) to investigate why standing slow modes have only been observed in hot coronal loops ($T > 6$ MK). De Moortel and Bradshaw (2008) used forward modelling of given temperature and density perturbations to investigate the resulting intensity perturbations for TRACE and Hinode/EIS. They found that determining the temperature and density perturbations from observations of coronal intensity oscillations was difficult and could easily lead to misinterpretation. De Moortel and Bradshaw (2008) did not model particular damp-

The work in this chapter is based on Owen et al. (2009)

ing mechanisms, but used simple analytical expressions for the temperature and density with oscillations that decay in time or space. Here, real plasma properties from the simulations in Chapter 2 are used to forward model and see how easily the resulting emission can be interpreted. This is undertaken for uniform equilibrium temperatures as in De Moortel and Bradshaw (2008), but then extended for the non-uniform equilibrium results of Section 2.5.

3.1.1 Forward Modelling Code

The forward modelling code used in this chapter is described in De Moortel and Bradshaw (2008). Forward modelling produces a synthesised emission that would be observed if a particular instrument (for example TRACE) was observing a region with conditions given by the model, in this case a coronal loop. Forward modelling for intensity observations requires the electron number density and the temperature in order to determine the synthesised emission along the loop ($\text{DN s}^{-1} \text{ pixel}^{-1}$). The electron number density, n_e (cm^{-3}) is calculated from the simulation density by,

$$n_e(s) = \frac{\rho_{00} \rho(s)}{2\tilde{\mu}m_p} \cdot 10^{-6}, \quad (3.1)$$

where, $\rho(s)$ is the simulation density (s can be a function of space or time), $\rho_{00} = 1.67 \times 10^{-12} \text{ kg m}^{-3}$, the proton mass, $m_p = 1.673 \times 10^{-27} \text{ kg}$ and the mean atomic weight, $\tilde{\mu} = 0.6$. This value of $\tilde{\mu}$ assumes that the solar plasma is not a fully ionised Hydrogen plasma, but contains heavier elements. The temperature, T (K) is calculated by,

$$T(s) = (\gamma - 1)T_{00}\epsilon(s), \quad (3.2)$$

where, ϵ is the simulation energy, $T_{00} = 10^6 \text{ K}$ and the ratio of specific heat capacities, $\gamma = 5/3$.

In addition to the electron number density and the temperature, the ability of forward modelling in calculating synthesised emission is heavily dependent on atomic data and chemical abundances. The appropriate instrument response function is required in addition to the emissivities of each element and ionisation state within the wavelength range of the instrument response function. The emissivities are obtained from the atomic data collaboration CHIANTI (Dere et al. 1997; Young et al. 2003). This information is stored for a range of temperatures, electron number densities and wavelengths and is linearly interpolated for the exact density and temperature from the simulation for each wavelength within the instrument response function. Solar abundances are taken from Feldman et al. (1992), equilibrium ionisation balances from Mazzotta et al. (1998) and a line of sight depth of 5 Mm is assumed. The use of equilibrium ionisation balances assumes that the timescale of the ionisation due to temperature changes is shorter than the period of the wave producing the temperature change. Otherwise, the population fraction of an ion species will not reach its equilibrium value and hence, non-equilibrium ionisation balances would be required. De Moortel and Bradshaw (2008) investigated the ionisation timescales of Fe X, which contributes to TRACE 171 Å emission and Fe XII which is used by the EIS 195 Å line, compared to different oscillation periods. For a period of five minutes, as used in this study, at coronal densities, De Moortel and Bradshaw (2008) found that both Fe X and Fe XII are within 2% of equilibrium ionisation balance within 20s. This timescale is clearly far

shorter than that of the five minute oscillation which causes the temperature change, hence, the use of equilibrium ionisation balances is justified. The emissivity data is converted into units of $\text{DN s}^{-1} \text{pixel}^{-1} \text{cm}^6$, using,

$$IU(IB, \lambda, s) = \frac{0.83 \times AB \times LOS \times IRF \times \lambda \times Em \times IB}{4\pi h c n_e}, \quad (3.3)$$

where IU is related to the emissivity, Em , IB is the ionisation balance, AB the atomic abundance normalised to that of hydrogen, LOS the line of sight depth and IRF the value of the instrument response function at the wavelength, λ . h is Plank's constant, n_e the electron number density and c the speed of light, where 0.83 is the proton/electron ratio (Bradshaw and Mason 2003). IU is then summed over all ionisation states and wavelengths to give $IU(s)$ as a function of loop position or time, which is multiplied by the number density squared to give intensity, $I(s)$ in units of $\text{DN s}^{-1} \text{pixel}^{-1}$.

As discussed in Section 2.3, small amplitude perturbations are required to ensure the simulations keep non-linear effects negligible. Consequently, the energy and density from the simulations have perturbations of around 1% of the equilibrium value. However, observed amplitudes of propagating slow waves are around 5% (De Moortel et al. 2002a), therefore, the perturbation amplitudes are multiplied by a factor of 5. This results in oscillations of around 5% in energy and density with the same equilibrium value. This multiplication assumes that the physical processes involved scale exactly linearly. However, other effects may become important when larger amplitudes are considered.

Forward modelling can be applied to both imagers and spectrometers. Imagers, such as TRACE, have broad instrument response functions (relative to spectrometers) covering a wide temperature range. In contrast, spectrometers have narrow instrument response functions and, therefore, observe spectral lines emitted at more specific temperatures. TRACE 171 Å has a wide spectral coverage, with the instrument response function covering wavelengths from around 160 Å to 190 Å, observing radiation emitted from a number of iron and oxygen lines. CDS and EIS lines, however, have narrower instrument response functions, observing emission from mainly a single line. For example, the CDS Mg x (624 Å) line has an instrument response function width of 5 Å, compared to 30 Å for TRACE 171 Å. Despite this narrow instrument response function, the CDS Mg x (624 Å) line observes weak contributions from O IV, Si x and Ar IV, which are sensitive to different temperatures to that of Mg x. This increases the complexity of interpreting observations. The CDS and EIS lines used in this section are not necessarily the strongest possible lines, but are lines which detect emission mainly from a single ion and therefore aid interpretation. The use of different spectral emission lines, which are formed at a range of temperatures, allows observations of different regions of the solar atmosphere. This allows analysis of, in this case, slow waves as they propagate through the solar atmosphere. The simulation results are modelled for the imager TRACE in the 171 Å passband in addition to the spectrometers SoHO/CDS Mg x (624 Å) and Ne VI (562 Å) and Hinode/EIS Fe XII (195 Å), Mg VI (269 Å) and Si VII (275 Å). These lines have been chosen to cover a temperature range from the transition region (Mg VI, $T \approx 0.4$ MK) to the corona (Fe XII, $T \approx 1.25$ MK), which corresponds to the temperature profile shown in Fig. 2.17(d).

3.2 Intensity along the Loop

Forward modelling as a function of position along the loop is initially undertaken as this provides a direct comparison with the results in Chapter 2. Forward modelling as a function of time, which allows a closer comparison with observations, is also undertaken and discussed later in Section 3.3.

3.2.1 Uniform Temperature Equilibrium

The intensity detected from any instrument passband depends on many different factors, as mentioned above and shown by Eq. (3.3). The total intensity in the passband is the sum of the intensities of all spectral lines that emit in the wavelength range of the instrument response function. The intensity of each line mainly depends on the loop density squared, as well as the ionisation balance and the emissivity of the spectral lines, both of which are temperature dependent (the emissivity is also density dependent). In order to understand how these quantities affect the resulting emission, the example of TRACE 171 Å is used and subsequently compared to several CDS and EIS lines. Firstly, the individual spectral lines that contribute to the TRACE 171 Å emission are examined. The ionisation balance and the emissivity for each line is then investigated. By comparing these quantities and the loop density we gain an understanding of how each factor contributes to the overall emission, as in De Moortel and Bradshaw (2008).

Each emission line is sensitive to a certain temperature range, outside of which no emission will be observed. By using a uniform temperature equilibrium with moderate temperature perturbations ($\sim 5\%$) the entire loop is at approximately the same temperature. Consequently, for a uniform temperature equilibrium, either the whole loop is observed by an instrument/emission line or none of the loop is. This is in contrast to the results for a non-uniform temperature equilibrium, which are discussed in Section 3.2.2.

3.2.1.1 Ideal Medium

To understand the observational consequences of propagating slow waves in a gravitationally stratified medium with an equilibrium temperature gradient (i.e. Fig. 2.27), we first need to understand the situation for a uniform equilibrium temperature and density. Hence we initially forward model the simulation results shown in Fig. 2.1(a) of an undamped slow wave propagating in an unstratified medium at a uniform equilibrium temperature of 1 MK and equilibrium density of $1.67 \times 10^{-12} \text{ kg m}^{-3}$. Fig. 3.1(a) shows the resulting synthesised emission that would be observed in the TRACE 171 Å passband. The black line in Fig. 3.1(a) gives the intensity from all the emission lines in the 171 Å passband, where the main contributions come from the Fe IX and Fe X ions. The intensities, by considering only Fe IX or Fe X, are shown by the purple and orange lines, respectively. For this example, at 1 MK, the other lines in the 171 Å passband make a negligible contribution to the emission. The black line shows an oscillation about a background of around $4.2 \text{ DN s}^{-1} \text{ pixel}^{-1}$, the total intensity of this line is the sum of the Fe IX and Fe X intensities. Clearly the Fe X line makes the largest contribution as it oscillates about a background of around $2.5 \text{ DN s}^{-1} \text{ pixel}^{-1}$, compared to only around $1.7 \text{ DN s}^{-1} \text{ pixel}^{-1}$ for Fe IX. From Fig. 3.1(a) it is difficult to determine the phase, amplitude and shape of the oscillations in each of the three cases. To bring out these quantities, the

constant background of each line has been subtracted, i.e. $\delta I = \frac{I - I(x=0)}{I(x=0)}$ and is plotted in Fig. 3.1(b).

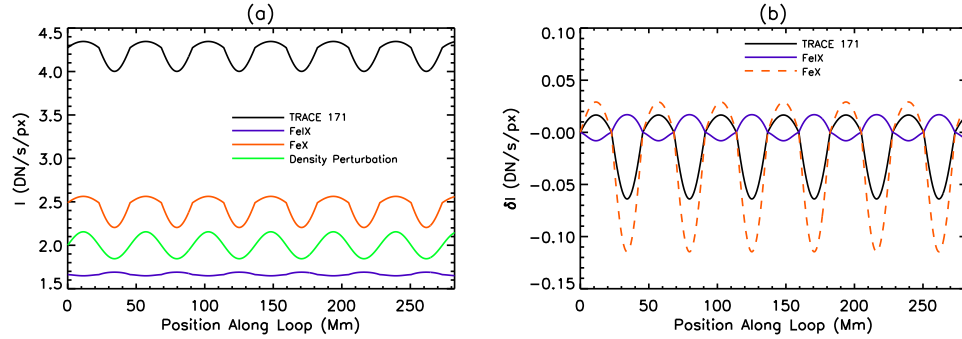


Figure 3.1: (a) intensity of TRACE 171 Å (black) with the intensity due to Fe IX (purple) and Fe X (orange) at 1 MK. (b) same as (a) but with the background subtracted to give the perturbed intensity. The density perturbation is renormalised and shown by the green line in (a).

From Fig. 3.1(b), it is again evident that Fe X (orange) is the dominant line, as the total oscillation (black) has a very similar shape, amplitude and phase. However, as shown by Fig. 3.1(a), Fe IX (purple) still contributes and has a very different shape of oscillation, which is in fact out of phase with the other intensities and the simulation density perturbation, which is renormalised and shown in Fig. 3.1(a) (green). As expected, the oscillations shown in Fig. 3.1(b) are clearly undamped throughout the entire loop. Both Fe IX and Fe X variations result from the same oscillation, i.e. they have the same input temperature and density. Therefore, any observed phase difference, etc, is a consequence of the atomic physics producing the observed radiation rather than the physical conditions (i.e. the temperature and density) of the loop. These effects are mainly due to the ionisation balance and the emissivity and must be understood in order to correctly interpret any observed intensity oscillations. The ionisation balance is a measure of the amount of each ion in a particular ionisation state. For example, at $T = 6 \times 10^5$ K, Fe is mainly in the form of Fe IX. However, at $T = 1 \times 10^6$ K there is more Fe X than Fe IX. Consequently, the ionisation balance fluctuates as the temperature of the loop oscillates. The emissivity is a measure of how much radiation is emitted by an ion species at a particular temperature, density and wavelength. Hence, it changes as the loop temperature and density oscillate and varies for each wavelength of the instrument response function, which is shown for TRACE 171 Å in Fig. 3.2.

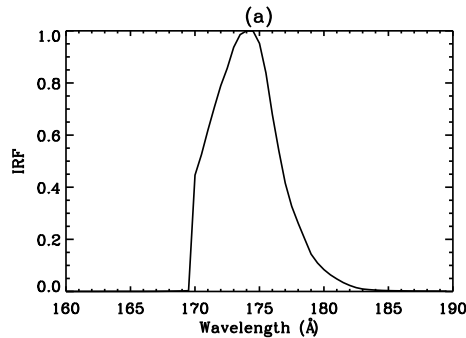


Figure 3.2: Instrument response function for TRACE 171 Å.

To understand the shape of the resulting oscillations in Fe IX and Fe X shown by Fig. 3.1(b) we examine

the ionisation balance and the emissivity individually for both Fe IX and Fe X. The ionisation balance for Fe IX (purple) and Fe X (orange) is shown in Fig. 3.3(a), with Fig. 3.3(b) showing the emissivity. The energy/temperature perturbation has been renormalised and is also shown in Fig. 3.3(a) (red). The emissivity for both Fe IX and Fe X show oscillations in phase with the temperature and density from the simulation results shown by the red line in Fig. 3.3(b) and the green line in Fig. 3.1(a), respectively. The emissivity is in phase with the simulation results mainly as a result of the density perturbation, which, when positive, means there are more ions to emit radiation and hence the emissivity is increased. The converse is true when the density perturbation is negative. For this example the emissivity is found to have little effect on the shape of the oscillation, merely the magnitude of the total emission, $I(x)$. It is the combination of the loop density squared and the ionisation balance which gives the oscillation its shape and phase. The ionisation balance depends on the temperature perturbation, as this changes the amount of each element that is in a particular ionisation state. Again, the more ions in a particular state, the more radiation is emitted, hence the stronger the intensity. Both the purple and orange lines in Fig. 3.3(a) are out of phase with the simulation results, shown as the temperature perturbation by the red line in Fig. 3.3(a). Fe IX is 180° out of phase with the temperature perturbation, whereas Fe X is more complicated with a very different shape. This behaviour is consistent with that found by De Moortel and Bradshaw (2008) who investigated the effects of the ionisation balance and the emissivity on intensity perturbations at uniform equilibrium temperature and density. De Moortel and Bradshaw (2008) also include the effects of non-linearity.

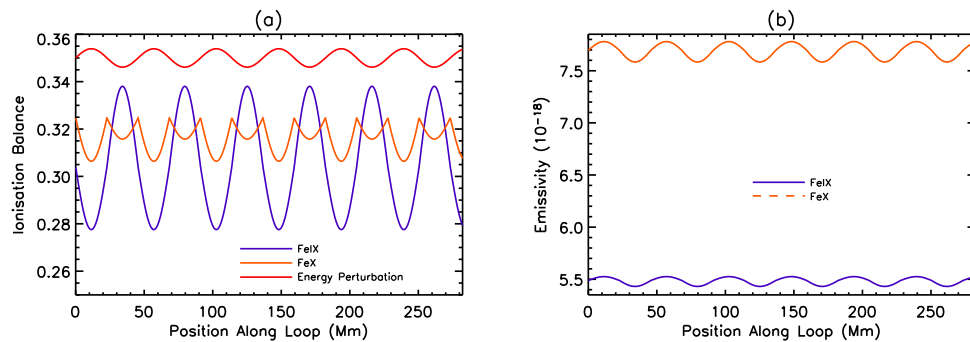


Figure 3.3: (a) Ionisation balance and (b) emissivity of Fe IX (purple) and Fe X (orange) at 1 MK. The energy perturbation is renormalised and shown by the red line in (a).

The ionisation balance of Fe IX (Fig. 3.3(a)) is 180° out of phase with the density which, as shown by Fig. 3.1(b), produces emission which is also 180° out of phase with the density. The ionisation balance of Fe X (Fig. 3.3(a)) is also out of phase with the density, but shows some asymmetry towards negative perturbation amplitudes (negative after the background is subtracted). This phase shift of the ionisation balance of Fe X is in contrast to the emission shown in Fig. 3.1(b), however, the asymmetry towards negative perturbations can clearly be seen. The emissivity of both Fe IX and Fe X (Fig. 3.3(b)) are in phase with the density perturbation. This suggests that it is the density that dominates the emission with the ionisation balance causing a slight asymmetry. The shape of these ionisation balances can be explained by looking at the formation temperatures of Fe IX and Fe X. These are shown by the purple and orange lines in Fig. 3.4(a) for Fe IX and Fe X, respectively, in addition to that of Fe XII in red and Mg X in green. The intersection of the vertical dashed line at $\log T = 6$ with the purple and orange lines gives the ionisation balance for Fe IX and Fe X, respectively at 1 MK (this is the equilibrium value from the simulations about which the

temperature oscillates). From Fig. 3.4(a) it is clear that the ionisation balances for both Fe IX and Fe X are comparable at this temperature. At 1 MK the ionisation balance of Fe IX, in Fig. 3.4(a), has a negative gradient, whereas it is at the peak of Fe X. Considering Fe IX, if the temperature increases the ionisation balance decreases (Fig. 3.4(a)), conversely, a decrease in temperature produces more Fe IX. This explains why the purple line in Fig. 3.3(a) has the opposite phase to the simulation results. Fe X peaks at 1 MK and therefore, any oscillation produces a decrease in Fe X. However, the gradient of the ionisation balance for temperatures above 1 MK is steeper than that below 1 MK (Fig. 3.4(a)). As a result, a negative perturbation in temperature reduces the ionisation balance less than a positive perturbation of the same amplitude, hence, the Fe X oscillation in Fig. 3.3(a) is asymmetric.

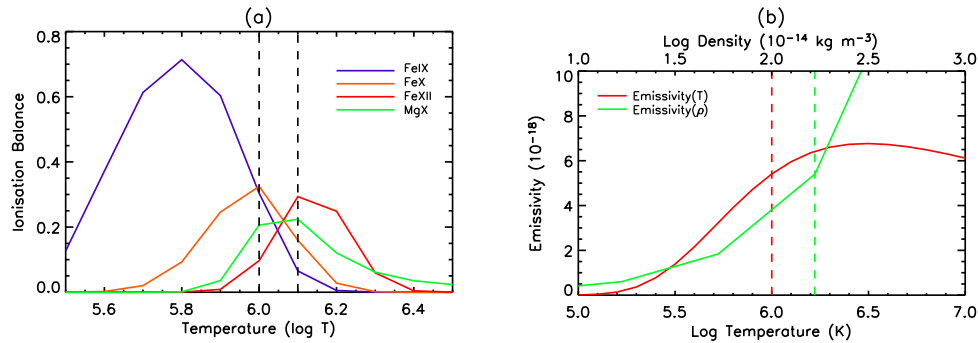


Figure 3.4: (a) Ionisation balance of Fe IX (purple), Fe X (orange), Fe XII (red) and Mg X (green). The vertical dashed lines represent T_0 of 1 MK and 1.25 MK. (b) emissivity of Fe X (at $\lambda = 174.53 \text{ \AA}$) as a function of temperature (red) with ρ_0 of $1.67 \times 10^{-12} \text{ kg m}^{-3}$ and as a function of density (green), with T_0 of 1 MK. The vertical dashed lines represent the equilibrium conditions of $T_0 = 1 \text{ MK}$ (red) and $\rho_0 = 1.67 \times 10^{-12} \text{ kg m}^{-3}$ (green).

As mentioned earlier, the emissivity of an ion species depends on the temperature, density and wavelength. The emissivity of Fe X is plotted in Fig. 3.4(b) at its peak wavelength of 174.53 \AA . The emissivity shown in Fig. 3.3(b) is summed over all the wavelengths that Fe X emits at, within the TRACE 171 \AA response function, hence the magnitude is slightly greater than that shown in Fig. 3.4(b). The red line in Fig. 3.4(b) gives the emissivity as a function of temperature at $\rho_0 = 1.67 \times 10^{-12} \text{ kg m}^{-3}$, with the green line as a function of density, where $T_0 = 1 \text{ MK}$. For a small temperature perturbation around 1 MK, the emissivity increases as both the temperature and density increase, hence, the emissivity shown in Fig. 3.3(b) is in phase with the temperature and density perturbations. The loop density, in addition to the ionisation balance and the emissivity of both Fe IX and Fe X, contributes to the magnitude of the full TRACE 171 \AA emission shown in Fig. 3.1(a). Note that the resolution of the ionisation and emissivity plots in Fig. 3.4 is limited by the data within the forward modelling code. Within the code, the data is linearly interpolated between these data points.

To complement the imager TRACE we examine the emission from the spectrometers CDS on SoHO and EIS on Hinode using the same temperature and density perturbations as used for Fig. 3.1, with equilibrium temperature of 1 MK. Figs. 3.5(a) and (b) give the emission for the CDS Mg X (624 \AA) line and the EIS Fe XII (195 \AA) line, respectively. The background emission is subtracted as described for Fig. 3.1(b). The CDS Ne VI (562 \AA), EIS Si VII (275 \AA) and EIS Mg VI (269 \AA) lines have peak formation temperatures of $T \approx 0.4 \text{ MK}$, $T \approx 0.63 \text{ MK}$ and $T \approx 0.4 \text{ MK}$, respectively, hence these lines are not shown here as the

equilibrium temperature of 1 MK is too hot.

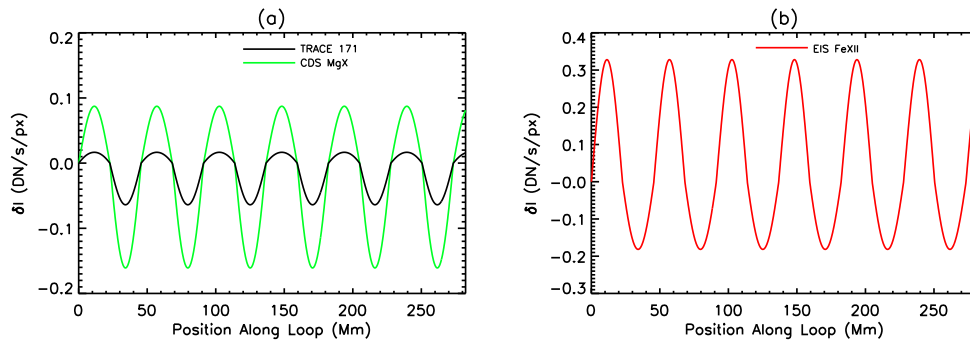


Figure 3.5: Perturbed intensity of (a) CDS Mg x (624 \AA) (green), with TRACE 171 \AA (black) and (b) EIS Fe XII (195 \AA) (red) at 1 MK.

The perturbed intensity from CDS Mg x, shown in green in Fig. 3.5(a), is similar to that of TRACE 171 \AA (black). The Mg x emission is also in phase with the temperature and density perturbations and is slightly asymmetric, having larger negative perturbations, although this effect is much less than seen for TRACE 171 \AA . The phase of the Mg x emission, as discussed for TRACE 171 \AA , mainly follows the loop density, hence both lines have the same phase. The asymmetries in the shape, however, are due to the ionisation balance. Unlike Fe x for TRACE 171 \AA , the Mg x ionisation balance at 1 MK is below its peak temperature, as shown by the green line in Fig. 3.4(a). As a result, the Mg x ionisation balance oscillates in phase with the temperature perturbation. The slight asymmetry is caused because the gradient of the ionisation balance is greater below 1 MK than above (see Fig. 3.4(a)), and hence, an increase in temperature causes a smaller change in emission than a corresponding decrease in temperature. The emission for EIS Fe XII shown in Fig. 3.5(b) is also in phase with the simulation perturbations. It too has a slight asymmetry, this time however, towards larger positive perturbations, but is more symmetric in shape than both Mg x and TRACE 171 \AA . Again, the asymmetry is caused by the ionisation balance. As with Mg x, at 1 MK, Fe XII is below its peak ionisation temperature, consequently, the ionisation balance and therefore, the emission oscillates in phase with the temperature. The slight asymmetry is due to the larger gradient in ionisation balance above 1 MK to that below. However, this difference is much less than for Mg x, hence the shape of the Fe XII emission shown in Fig. 3.5(b) is more symmetric than that of Mg x.

The effects of changing the equilibrium temperature, whilst keeping the same temperature and density oscillations are now investigated. Firstly, the maximum equilibrium temperature of the profile shown in Fig. 2.17(d) of 1.25 MK is used. This would correspond to observing the same wave propagating along a loop of different temperature. Looking at the same oscillation, but about an equilibrium temperature of 1.25 MK for TRACE 171 \AA , produces somewhat different results. The density is kept the same ($\rho_0 = 1.67 \times 10^{-12} \text{ kg m}^{-3}$) to allow easier comparison with the 1 MK results. The ionisation balances for Fe IX (purple) and Fe x (orange) oscillating about 1.25 MK are shown in Fig. 3.6(a) and are 180° out of phase with the temperature and density perturbations (shown by the red line in Fig. 3.3(a) and the green line in Fig. 3.1(a), respectively). The ionisation of both Fe IX and Fe x are lower than at 1 MK, as the temperature is further from the peak formation temperatures. At 1 MK, Fe IX is already above its peak formation temperature, hence, the Fe IX ionisation balance in Fig. 3.6(a) has the same phase as that in Fig. 3.3(a),

which is 180° out of phase with the temperature and density perturbations. Fe X is now also above the peak formation temperature, where the ionisation balance has a negative gradient (see Fig. 3.4(a)), hence it too has an ionisation balance that oscillates 180° out of phase with the temperature perturbation. The Fe X ionisation balance is symmetric as the gradient in Fig. 3.4(a) is constant just above and below 1.25 MK. Fe IX, however, is asymmetric towards larger positive perturbations, as the ionisation balance is steeper below 1.25 MK than above.

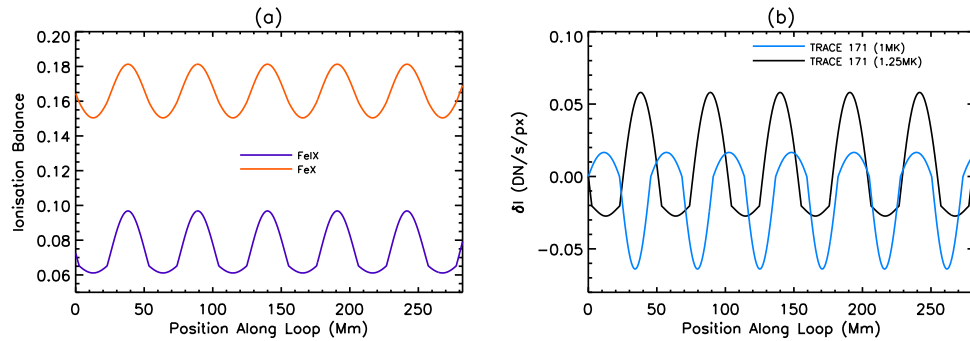


Figure 3.6: (a) Ionisation balance of Fe IX (purple) and Fe X (orange) at 1.25 MK. (b) Perturbed intensity of TRACE 171 Å at 1.25 MK (black) and at 1 MK (blue).

Fig. 3.6(b) shows the synthesised (background subtracted) emission for TRACE 171 Å at 1.25 MK in black, with the 1 MK case plotted for comparison in blue. For this case, when considering the shape and phase of the oscillation of the black line in Fig. 3.6(b), it is the ionisation balance that dominates the density and the emissivity. This results in emission for TRACE 171 Å at 1.25 MK which is out of phase with both the simulation oscillations and that of TRACE 171 Å at 1 MK. Due to the increase in temperature compared to the previous example, Fe IX has a much weaker contribution to the full 171 Å emission, compared to Fe X, due to a reduced ionisation balance, as seen in Fig. 3.4(a). However, it is the ionisation balance of Fe IX (purple line in Fig. 3.6(a)) that produces an asymmetry in the TRACE 171 Å emission (black line in Fig. 3.6(b)), where the troughs are flattened out. Such a case demonstrates the difficulties in correctly interpreting observational data, where for this example the observed intensity variation would appear out of phase with the density and temperature perturbations. This is discussed in more detail, using analytical functions, in De Moortel and Bradshaw (2008). The wavelengths of the two intensity perturbations in 3.6(b) are different, which is due to the difference in temperature, as expected from Eq. 2.43 in Chapter 2.

In Fig. 3.7 the perturbed intensity from CDS Mg X (624 Å) (green) and EIS Fe XII (195 Å) (red) at 1.25 MK are compared to the results of TRACE 171 Å (black). Comparisons are also made with the 1 MK results of Fig. 3.5. The intensity for CDS Mg X in Fig. 3.7(a) ($\approx 3.4 \text{ DN s}^{-1} \text{ px}^{-1}$) is similar to that at 1 MK from Fig. 3.5(a) ($\approx 3.2 \text{ DN s}^{-1} \text{ px}^{-1}$), with oscillations in phase with the temperature and density perturbations. The background emission of the Mg X line at 1.25 MK is greater than that of 1 MK due to an increase in the ionisation balance and emissivity due to the higher temperature. However, after subtracting the background, the oscillation shown in Fig. 3.7(a) has a smaller amplitude compared to that of 1 MK shown in Fig. 3.5(a). This is a result of the ionisation balance of Mg X, which peaks at 1.25 MK and hence is always reduced as the temperature oscillates. The emission shown in Fig. 3.7(a), unlike that of 1 MK, has flattened peaks. The cause is again the peak in ionisation balance, which results in a decrease in emission whether the

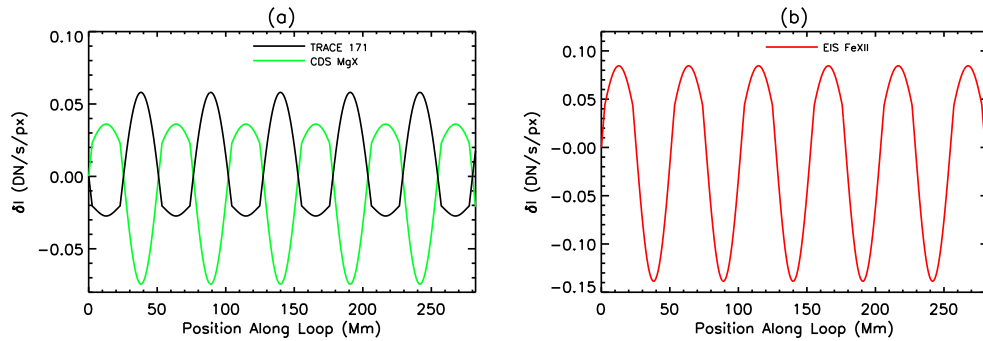


Figure 3.7: Perturbed intensity of (a) CDS Mg x (624 \AA) (green), with TRACE 171 \AA (black) and (b) EIS Fe XII (195 \AA) (red) at 1.25 MK.

temperature increases or decreases. This acts to deepen the troughs and suppress the peaks.

Unlike TRACE 171 \AA , CDS Mg x has not changed phase from the 1 MK to the 1.25 MK results. Consequently, for 1.25 MK, TRACE 171 \AA and CDS Mg x are now out of phase. The TRACE 171 \AA emission is also out of phase with the EIS Fe XII emission (shown in Fig. 3.7(b)), which has changed in a similar way to CDS Mg x. That is, the phase has remained the same, however, due to the peak in ionisation balance of Fe XII at 1.25 MK, the peaks have become flattened. Comparison between TRACE 171 \AA , CDS Mg x and EIS Fe XII for the 1 MK case show similar oscillations, however, for 1.25 MK the resulting oscillations appear substantially different, with the TRACE 171 \AA emission 180° out of phase with that of the two spectrometers. This highlights the importance of observing a range of emission lines for different instruments in order to correctly interpret observational data. In this case, if only the TRACE 171 \AA emission was observed, the resulting oscillation would be 180° out of phase, hence, the density and energy perturbations would be interpreted with this incorrect phase. By also analysing CDS Mg x and EIS Fe XII, however, the correct phase can be seen, with the flattening of the peaks suggesting that the loop is at the peak ionisation temperature of both Mg x and Fe XII of 1.25 MK. As shown in this Section, analysis of TRACE 171 \AA emission is often more complex than that of CDS Mg x and EIS Fe XII due to the contribution of both Fe IX and Fe X to the TRACE 171 \AA emission.

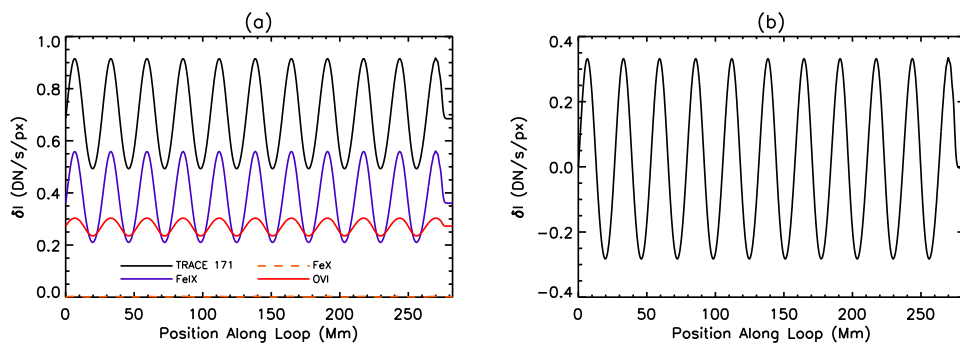


Figure 3.8: Perturbed intensity of TRACE 171 \AA (black) with the intensity due to Fe IX (purple), Fe X (orange dashed) and O VI (red) at 0.33 MK. (b) TRACE 171 \AA from (a) with the background subtracted.

The oscillation of a loop at the lowest temperature of the profile in Fig. 2.17(d) of $T_0 = 0.33 \text{ MK}$ is now

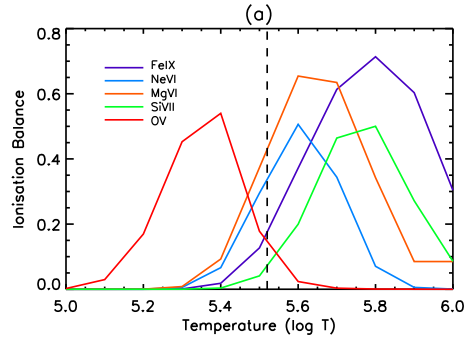


Figure 3.9: Ionisation balance of Fe IX (purple), Ne VI (blue), Mg VI (orange), Si VII (green) and O V (red). The vertical dashed line represents $T_0 = 0.33$ MK.

forward modelled for TRACE 171 Å and compared to cool CDS and EIS lines. As mentioned earlier, TRACE has wide instrument response function, which includes emission from many different ions and is therefore sensitive to a wide range of temperatures. Fig. 3.8(a) shows the perturbed intensity for TRACE 171 Å (black), Fe IX (purple), Fe X (orange dashed) and O VI (red) at 0.33 MK. Fig. 3.8(b) shows the TRACE 171 Å emission with the background subtracted. 0.33 MK is far below the peak ionisation balance and emissivity of Fe X, consequently, the contribution of Fe X emission is almost negligible. However, at this temperature the emission from the O VI line becomes important, although the main contribution is from Fe IX, as seen in Fig. 3.8(a). At 0.33 MK Fe IX is below its peak ionisation balance (see Fig. 3.9), as a result, the ionisation balance oscillates in phase with the temperature. Consequently, the Fe IX and therefore, TRACE 171 Å emission in Fig. 3.8 oscillates in phase with the temperature and density perturbations and is symmetric in intensity. This is in contrast to the 1 MK results and completely different to that found at 1.25 MK in Fig. 3.6(b). Fig. 3.9 shows the ionisation balance as a function of temperature for the Fe IX (purple) in addition to CDS Ne VI (blue) and O V (red) as well as EIS Si VII (green) and Mg VI (orange) for a range of temperatures around 0.33 MK (vertical dashed line). Fe X (see orange dashed line in Fig. 3.8(a)), Mg X and Fe XII are not included in Fig. 3.9 as the ionisation balance is too low at 0.33 MK. As a result the emission from these lines is negligible.

The emission for CDS Ne VI at 0.33 MK is shown by the blue line in Fig. 3.10(a), with that of TRACE 171 Å shown in black. The Ne VI emission has a much greater magnitude than TRACE 171 Å as 0.33 MK is close to the peak formation temperature of Ne VI (around 0.4 MK). However, both the phase and shape of the oscillations are very similar as the loop is below the peak formation temperature of both lines and the gradients of the ionisation balance are the same for positive and negative temperature changes. Fig. 3.10(b) shows the emission for EIS Si VII (green) and EIS Mg VI (orange), with that of TRACE 171 Å plotted in black. As with Ne VI and Fe IX, EIS Si VII and EIS Mg VI have peak formation temperatures above 0.33 MK (see Fig. 3.9), hence the intensity oscillates in phase with the simulation perturbations. In addition, the constant gradient of the ionisation balance either side of 0.33 MK results in symmetric oscillations. In contrast to the results in Figs. 3.10(a) and (b), which all appear symmetric and in phase with the simulation results, is the CDS O V line shown in Fig. 3.10(c) (red). The emission from this line is 180° out of phase with the temperature and density perturbations. This contrast is due to the difference in peak formation temperatures, which can be seen in Fig. 3.9, where O V is the only line which peaks below 0.33 MK.

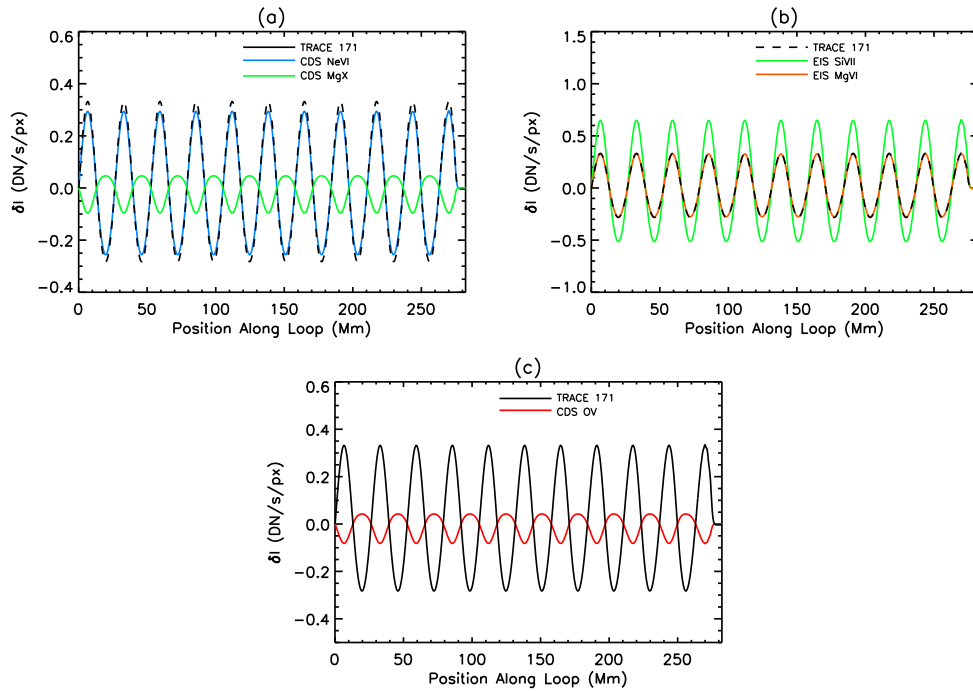


Figure 3.10: Perturbed intensity of (a) CDS Mg x (624 \AA) (green) and CDS Ne vi (562 \AA) (blue), (b) EIS Si vii (275 \AA) (green), EIS Mg vi (269 \AA) (orange) and (c) CDS O v (629 \AA) (red) at 0.33 MK . TRACE 171 \AA is shown in black.

Hence, the emission is out of phase with the temperature perturbations. The asymmetry is a result of the different gradients of the ionisation balance above and below 0.33 MK .

The peak formation temperature of Mg vi (0.4 MK) is closer to 0.33 MK than that of Si vii (0.6 MK) and yet the emission shown in Fig. 3.10(b) from Mg vi is lower than that of Si vii. This can be understood by examining the ionisation balance (shown in Fig. 3.11(a)) and the emissivity (Fig. 3.11(b)) of Mg vi (orange) and Si vii (green).

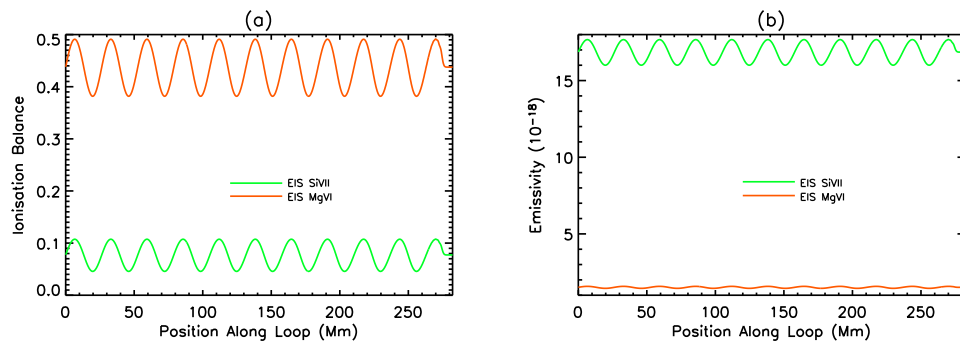


Figure 3.11: (a) Ionisation balance and (b) emissivity of EIS Si vii (275 \AA) (green) and EIS Mg vi (269 \AA) (orange) at 0.33 MK .

Fig. 3.11(a) shows that the ionisation balance of Mg vi is around five times higher than that of Si vii, as expected from Fig. 3.9, hence, at this temperature there is more Mg vi than Si vii to emit radiation (if

the amount of Mg and Si are the same). However, as seen in Fig. 3.11(b), the emissivity of Si VII at this temperature and density is an order of magnitude higher than that of Mg VI. Therefore, despite there being less Si VII, Si VII emits more radiation than Mg VI and hence the emission seen in Fig. 3.10(b) of Si VII is greater than that of Mg VI.

3.2.1.2 Gravitational Stratification

The effect of gravitational stratification is now investigated. Consequently, the simulation results shown in Fig. 2.2(b) of an undamped slow wave propagating in a gravitationally stratified medium at a uniform equilibrium temperature of 1 MK are forward modelled. The black line in Fig. 3.12(a) shows the resulting emission for the entire TRACE 171 Å passband. The synthesised emission by considering only Fe IX or Fe X is shown by the purple and orange lines, respectively.

As discussed earlier, the observed intensity depends on the loop density squared. Considering that the inclusion of gravity produces an exponential decrease in the background density (discussed in Section 2.4.2), the resulting intensity, therefore, also decreases exponentially. This can be clearly seen in Fig. 3.12(a). In order to detect oscillations we need to subtract the background intensity, however, this is no longer a constant value due to the inclusion of gravity. Consequently, the equilibrium conditions i.e. $\rho_0 = \rho(t = 0, x)$ and $\epsilon_0 = \epsilon(t = 0, x)$ are forward modelled and the subsequent emission is subtracted from Fig. 3.12(a). The results are plotted in Fig. 3.12(b) where the black line represents TRACE 171 Å and the purple and orange lines give the Fe IX and Fe X emission, respectively. As found in Section 3.2.1.1, at 1 MK, the TRACE 171 Å emission is mainly a combination of Fe IX and Fe X, with Fe X the larger contribution. The oscillation shown in Fig. 3.12(b) again shows that at 1 MK the shape and phase of the TRACE 171 Å emission strongly resembles that of Fe X, with Fe IX out of phase with Fe X and the simulation perturbations.

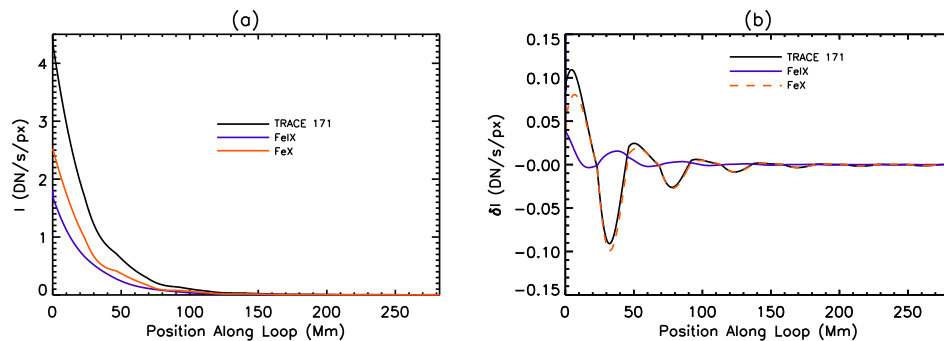


Figure 3.12: (a) intensity, in a gravitationally stratified medium, of TRACE 171 Å (black) with Fe IX (purple) and Fe X (orange) at 1 MK. (b) same as (a) but with the exponentially decreasing background subtracted to give the perturbed intensity.

The density and temperature at the loop footpoints of Fig. 3.1(b) and Fig. 3.12(b) are the same. The difference is that for Fig. 3.12(b) the density decreases exponentially along the loop. Therefore, as expected, the magnitude of the initial peak in both figures is similar as both results have the same combination of loop density, ionisation balance and emissivity. The most significant difference between the unstratified results shown in Fig. 3.1(b) and the results for a stratified medium shown in Fig. 3.12(b) is the apparent rapid

decay of the oscillation in a stratified medium. Fig. 3.1(b) clearly shows an undamped wave throughout the loop, yet in a gravitationally stratified medium the oscillation is only visible up to 100 Mm, despite no damping being present. 100 Mm is an upper limit considering that the effect of noise has been neglected. The simulation results, shown in Fig. 2.2(b), with gravity show oscillations at 200 Mm of five times the magnitude of those seen in Fig. 2.1(a) without gravity. Therefore, the decay of the oscillation in Fig. 3.12(b) is entirely an observational effect. The apparent damping is a result of the exponential decrease in density, which produces an exponential decrease in intensity along the loop. Therefore, despite the magnitude of the perturbations shown in Fig. 2.2(b) (ϵ_1 and $\frac{\rho_1}{\rho_0}$) increasing, the absolute change in the intensity is reduced due to the lower background value. Consequently, the intensity oscillation quickly falls away below the sensitivity of the instrument, hence, the wave appears to decay rapidly. This rapid decay of the oscillation along the loop also changes the shape of the wave, compared to that of the unstratified case, with the asymmetry of the emission shown in Fig. 3.12(b) much greater than that seen in Fig. 3.1(b).

The same simulation results forward modelled for TRACE 171 Å in Fig. 3.12(b) are now forward modelled for CDS Mg X (green) in Fig. 3.13(a) and for EIS Fe XII (red) in Fig. 3.13(b). The emission from both Mg X and Fe XII shows the same rapid decay along the loop as seen for TRACE 171 Å, confirming that this observational consequence of the exponential density decrease affects the emission of all lines. Apart from the rapid decay, the results for Mg X and Fe XII are very similar to those found in an unstratified medium (shown in Figs. 3.5(a) and (b), respectively). Both intensity oscillations are in phase with the temperature and density perturbations and with TRACE 171 Å. Unlike TRACE 171 Å, however, the unstratified emission of Mg X and Fe XII is very symmetric and this symmetry has been conserved in a stratified medium.

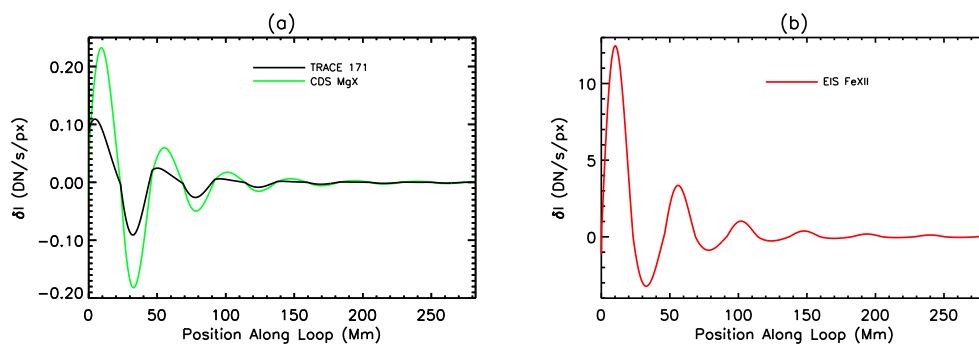


Figure 3.13: Perturbed intensity of (a) CDS Mg X (624 Å) (green), with TRACE 171 Å (black) and (b) EIS Fe XII (195 Å) (red) at 1 MK.

3.2.1.3 Damping due to Compressive Viscosity and Thermal Conduction

The effects of damping due to compressive viscosity and thermal conduction in the gravitationally stratified medium of the previous section are now investigated. As discussed in Chapter 2, damping due to optically thin radiation is negligible and is therefore not included. Fig. 3.14 shows the perturbed intensity for TRACE 171 Å, with the background subtracted, of a slow wave propagating in a gravitationally stratified loop at 1 MK, with no damping (orange), damping due to thermal conduction (purple) and damping due to thermal conduction and compressive viscosity (black).

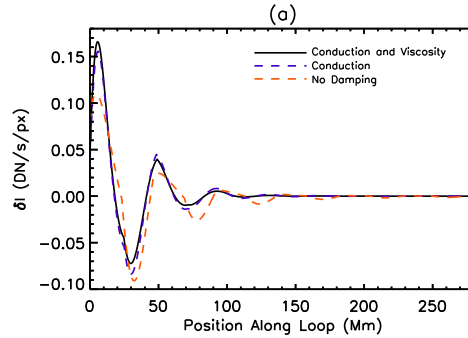


Figure 3.14: Perturbed intensity in a gravitationally stratified medium of TRACE 171 Å (black) with Fe IX (purple) and Fe X (orange) at 1 MK for a wave damped by thermal conduction and compressive viscosity.

Above around 70 Mm along the loop shown in Fig. 3.14 the oscillations behave as expected, with the wave damped by conduction and viscosity having the smallest perturbations. However, near the loop footpoint, the opposite effect occurs, with the amplitude of the first peak increasing as extra damping terms are included. This phenomenon can be understood from the emissivity and ionisation balance of Fe IX and Fe X which largely make up the TRACE 171 Å emission. Both the emissivity and the ionisation balance of Fe IX behave as expected and damp for the entire length of the loop. In addition, as expected, the damping due to thermal conduction and compressive viscosity is greater than that of just thermal conduction. However, Fe X has the dominant contribution and has more complicated behaviour. The ionisation balance and emissivity of Fe X are shown in Figs. 3.15(a) and (b), respectively for an unstratified medium. The emissivity of Fe X is shown in Fig. 3.15(b) for an undamped wave (orange) and with damping due to thermal conduction and compressive viscosity (black). When damping is included, the perturbed emissivity is seen to damp for the entire loop, as expected. The large initial peak of Fig. 3.14 when damping is included is due to the behaviour of the ionisation balance of Fe X, shown in Fig. 3.15(a). The ionisation balance for an undamped wave is shown in orange with that from damping by conduction and viscosity in black. As the ionisation balance of Fe X peaks at 1 MK the ionisation balance of the damped wave is always greater than that of the undamped wave. It is this effect which increases the magnitude of the first peak in Fig. 3.14. However, further along the loop, the damping of the loop density and the emissivity dominates the effect of the ionisation balance and the wave is damped as expected.

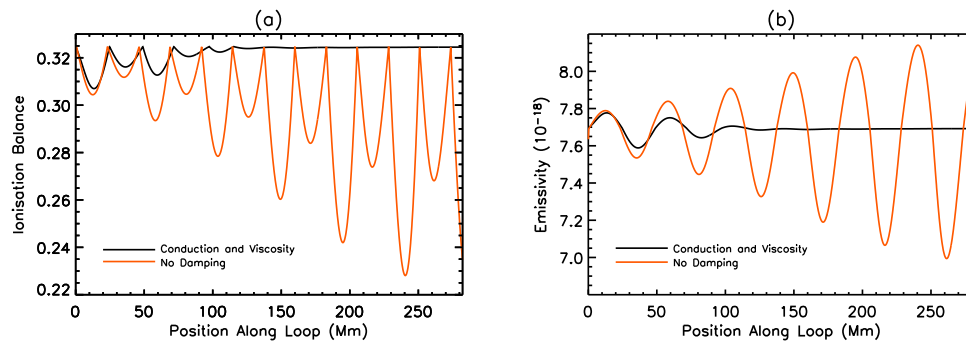


Figure 3.15: (a) Ionisation balance and (b) emissivity of Fe X for a wave damped by thermal conduction and compressive viscosity (black) and undamped (orange) at 1 MK in an unstratified medium.

Note that the phase shift which thermal conduction produces between the energy and density perturbations (as discussed in Section 2.4.6) can be seen in Fig. 3.14. The inclusion of thermal conduction and compressive viscosity decreases the observable oscillation length from that of the undamped wave (Fig. 3.14). The result for a slow wave propagating in a stratified medium at uniform temperature equilibrium of 1 MK with damping due to thermal conduction and compressive viscosity, as shown in Fig. 3.14 for TRACE 171 Å, is consistent with a rapidly decaying oscillation visible to the order of 50 Mm, as shown by observations (e.g. De Moortel et al. 2002a,b). Again, the complexity of interpreting the results has increased with the addition of damping. In addition to the phase of the emission depending on the equilibrium loop temperature and the particular emission line used, the inclusion of thermal conduction also affects the phase of the observed oscillation. As well as this, the inclusion of damping can affect the damping profile and may even increase the amplitude of the observed oscillation.

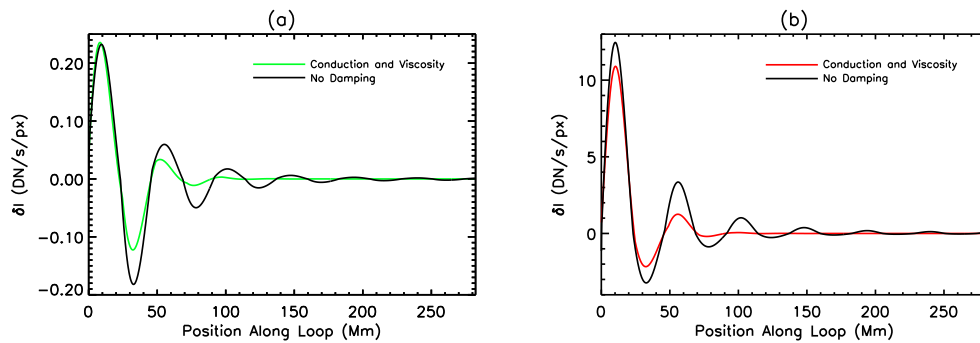


Figure 3.16: Perturbed intensity of (a) CDS Mg x (624 Å) (green) and (b) EIS Fe XII (195 Å) (red) for a wave damped by thermal conduction and compressive viscosity (coloured line) and undamped (black) at 1 MK.

Figs. 3.16(a) and (b) show the resulting perturbed intensity for CDS Mg x and EIS Fe XII, respectively, for an undamped wave (black) and with damping due to thermal conduction and compressive viscosity (coloured). Both Figs. 3.16(a) and (b) show more rapidly decaying oscillations when damping is included, which, away from the loop footpoint, are consistent with the results for TRACE 171 Å (Fig. 3.14). Near the loop footpoint, however, the results of TRACE 171 Å, CDS Mg x and EIS Fe XII differ slightly. The magnitude of the first peak of the TRACE 171 Å emission is greater for the damped oscillation than for the undamped oscillation. This is also seen, but to a much lesser degree, for CDS Mg x (Fig. 3.16(a)). In contrast, the EIS Fe XII emission (Fig. 3.16(b)) of the damped oscillation is less than that of the undamped case. As discussed earlier, for TRACE 171 Å, the increase in amplitude from damping is due to the peak in ionisation balance of Fe x at 1 MK. CDS Mg x shows similar, but less dramatic, behaviour as Mg x is close to its peak ionisation balance at 1 MK, whereas, Fe XII is far below its peak ionisation balance (as shown in Fig. 3.4(a)). In addition to the rapid damping, the small phase shift introduced by thermal conduction is also clear, particularly for Mg x in Fig. 3.16(a).

3.2.2 Non-Uniform Equilibrium Temperature

In this section the simulation results shown in Fig. 2.27(b), including damping from thermal conduction and compressive viscosity with a non-uniform equilibrium temperature profile, are forward modelled for a

range of instruments and emission lines. As seen in Section 3.2.1.1, TRACE 171 Å is sensitive to transition region and coronal temperatures and should detect emission along most of the loop length. In contrast, CDS Mg x (624 Å) and EIS Fe XII (195 Å) are sensitive to coronal temperatures of around 1.25 MK. EIS Si VII (275 Å) is sensitive to transition region temperatures of 0.6 MK and CDS Ne VI (562 Å) and EIS Mg VI (269 Å) are sensitive to cooler temperatures of 0.4 MK.

The equilibrium temperature profile used is given by the red line in Fig. 3.17, with the equilibrium density shown in green. The vertical dashed lines represent the transition region, where the temperature rises from 0.33 MK to 1.25 MK. To maintain constant pressure, the density decreases along the loop as the temperature increases. At an equilibrium temperature of 1 MK the density is chosen to be $1.67 \times 10^{-12} \text{ kg m}^{-3}$ (corresponding to the uniform ρ_0 value used in Section 3.2.1). However, as seen in Fig. 3.17, the density at the loop footpoint is much higher, conversely the coronal density is lower. The change in density with height is likely to affect the resulting emission, as intensity is proportional to the density squared.

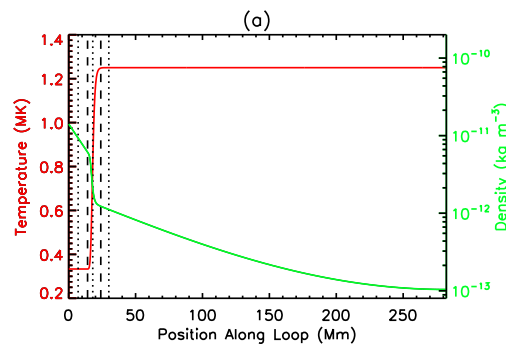


Figure 3.17: Equilibrium temperature (red) and density (green) profile. The vertical dashed lines mark the transition region where the temperature rises from 0.33 MK to 1.25 MK. The dotted vertical lines are at 7 Mm, 18 Mm and 30 Mm along the loop corresponding to temperatures of 0.33 MK, 0.8 MK and 1.25 MK, respectively. These positions are discussed in Section 3.3.

Fig. 3.18(a) shows the perturbed intensity for TRACE 171 Å (black), Fe IX (purple) and O VI (red) with the background subtracted. Fig. 3.18(b) shows the same as Fig. 3.18(a) for TRACE 171 Å, but plotted for a different scale of δI . It is clear from Fig. 3.18(b) that, as expected, TRACE 171 Å detects oscillations along the entire loop. However, it is the transition region emission which dominates, with the observed oscillation amplitude around two orders of magnitude greater than the coronal region. Comparison of Fig. 3.6(b) with Fig. 3.8(b) shows that the TRACE 171 Å intensity oscillation at 1 MK and 1.25 MK are of similar magnitude to that at 0.33 MK. This is in contrast to that seen in Fig. 3.18, where the transition region emission is much stronger. The reason for this increase is the much larger density near the loop footpoint from using the equilibrium profile of Fig. 3.17.

There is some observational evidence, from TRACE, SUMER and CDS, for larger amplitudes in the transition region. Marsh et al. (2003) detected propagating oscillations with a five minute periodicity with amplitudes of $9.8 \pm 3.1\%$ and $8.6 \pm 1.2\%$ in the chromosphere and the corona, respectively, compared to $12.4 \pm 2.1\%$ in the transition region. Brynildsen et al. (2003) detected three minute oscillations and found amplitudes of 7-16% in the transition region, compared to only 2.5-6% and 3-5% in the chromosphere and corona, respectively. O'Shea et al. (2002) also detected three minute oscillations and found the

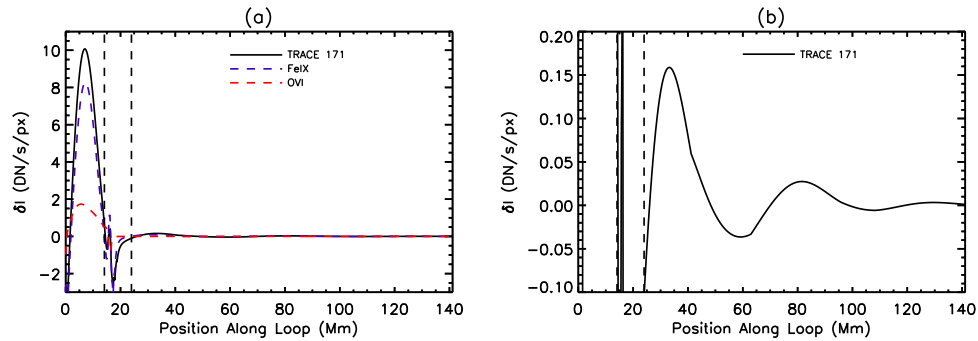


Figure 3.18: (a) perturbed intensity of TRACE 171 Å (black) with Fe IX (purple) and O VI (red). (b) TRACE 171 Å from (a) but plotted for $-0.1 \leq \delta I \leq 0.2$ to highlight the coronal oscillations.

amplitude to peak in the transition region. These observations are consistent with the model in that they do show higher oscillation amplitudes in the transition region than the corona. However, the difference in intensity is much less than predicted by our model. The reason for this discrepancy remains unclear, however, it is likely to be due to the equilibrium profile used. The real transition region has a much steeper temperature gradient (1-2 Mm compared to 10 Mm) and is at a lower altitude than that shown in Fig. 3.17 (2 Mm compared to 14 Mm). A steeper transition region would increase the reflection and thereby reduce the amplitudes seen in the transition region, however, this would also decrease the coronal amplitudes. Due to the normalisation of the model (discussed in Sections 2.5.1 and 2.5.2), the transition region amplitudes are likely to be reduced by reducing the height of the transition region. The density is always chosen to be $\rho_0 = 1.67 \times 10^{-12} \text{ kg m}^{-3}$ at $T_0 = 1 \text{ MK}$. Consequently, the density increases nearer to the loop footpoint to maintain constant pressure, as the temperature decreases. The density also increases towards the footpoint due to gravitational stratification. If the position of the transition region is closer to the loop footpoint then the density increase due to gravitational stratification is less, hence, as the density is fixed at $T_0 = 1 \text{ MK}$, the footpoint density is reduced compared to a transition region further from the footpoint. This results in a smaller density contrast (and therefore intensity contrast) between the loop footpoint and the corona (seen by comparing Figs. 2.19(a) and (b)), which may reduce the discrepancy of the transition region amplitudes found in the model compared to those observed.

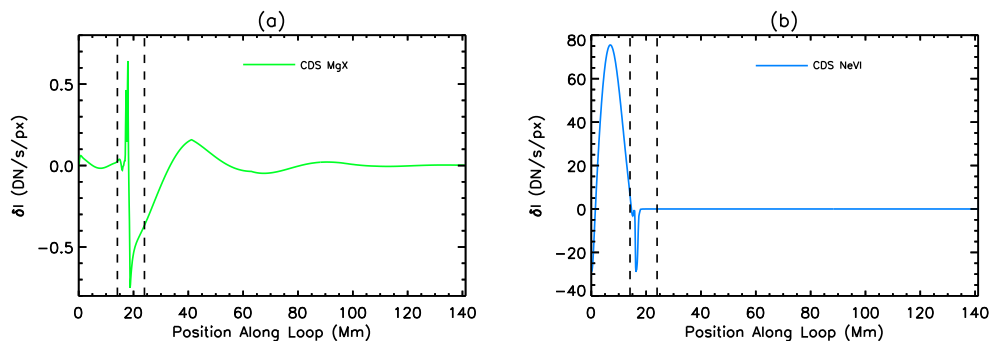


Figure 3.19: Perturbed intensity of (a) CDS Mg X (624 Å) (green) and (b) CDS Ne VI (624 Å) (blue).

The perturbed intensity of CDS Mg X and Ne VI are shown in Figs. 3.19(a) and (b), respectively. As

expected, Mg X emission (peak at $T = 1.25$ MK) shows a coronal oscillation. This oscillation is very weak due to the low density of the corona. Despite the reduction in emissivity and ionisation balance, the Mg X emission shows two strong spikes in the transition region. These spikes are a result of the spikes in the energy and density perturbations shown in Fig. 2.27(b), where the increase in these quantities in the transition region outweighs the decrease in ionisation balance and emissivity. No emission is expected at the loop footpoint due to the cool temperature, however, a small feature is seen. This is a result of a weak Si X line which exists in the CDS Mg X instrument response function. In contrast to Fig. 3.19(a), the Ne VI emission (peak at $T = 0.4$ MK) of Fig. 3.19(b) shows no coronal oscillations as the temperature is too high, hence the ionisation balance is very low (as is the loop density). Rather than two spikes in the transition region, Fig. 3.19(b) only shows one. The simulation results have a negative spike in the density perturbation which causes a negative spike in the intensity. However, the positive spike in the energy perturbation also causes a negative intensity spike, as the ionisation balance is reduced because the local temperature of the loop is above the peak formation temperature of Ne VI. As expected, due to its peak formation temperature of 0.4 MK, the emission of Ne VI is very strong near the loop footpoint at 0.33 MK. The magnitude of intensity is much greater in Fig. 3.19(b) than Fig. 3.10(a) due to the increased density near the footpoint.

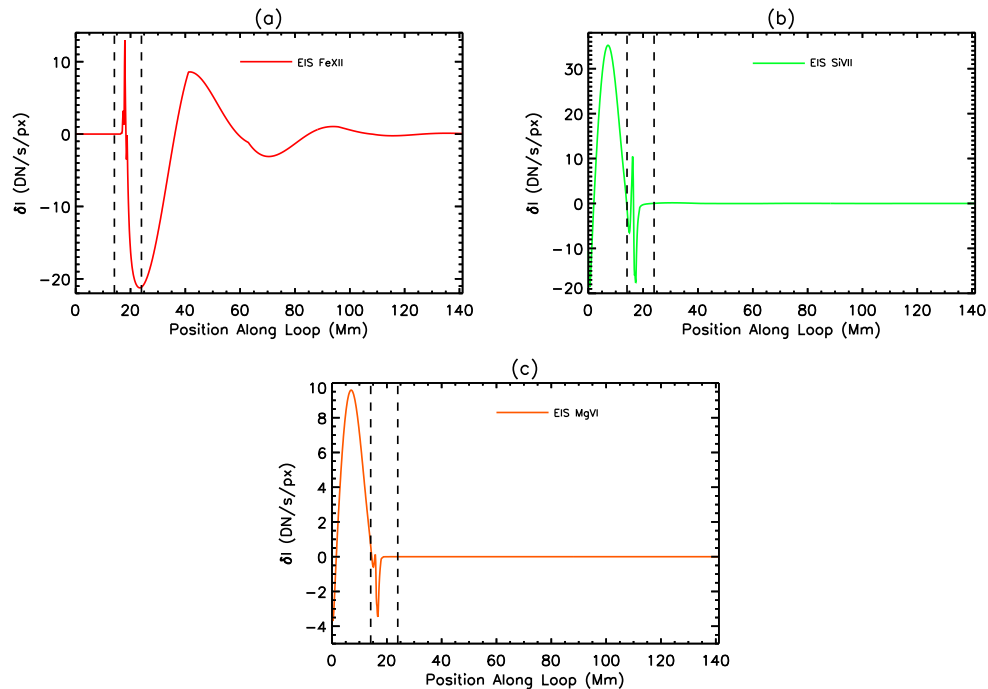


Figure 3.20: Perturbed intensity of (a) EIS Fe XII (195 \AA) (red), (b) EIS Si VII (275 \AA) (green) and (c) EIS Mg VI (269 \AA) (orange).

Figs. 3.20(a), (b) and (c) show the perturbed intensity for EIS Fe XII, EIS Si VII and EIS Mg VI, respectively. As expected from the results of Section 3.2.1.1, the Fe XII emission in Fig. 3.20(a) is very similar to that of CDS Mg X and shows a well defined coronal oscillation, but no emission near the cooler loop footpoint. The higher sensitivity of EIS compared to CDS produces a much clearer coronal oscillation in Fig. 3.20(a) than is seen in Fig. 3.19(a). The spike in the transition region is again due to the spike in the energy perturbation of Fig. 2.27(b). In contrast to Fe XII are the results for EIS Si VII and EIS Mg VI, which are both very

similar to each other with the maximum emission near the loop footpoint. Like CDS Ne VI, EIS Si VII and EIS Mg VI have no coronal part. Despite similar emission above and below the transition region, the results of EIS Si VII and EIS Mg VI are quite different in the transition region. Si VII in Fig. 3.20(b) has two spikes, the positive of which is a result of the positive energy perturbation which increases the ionisation balance, whereas the negative spike is caused by the negative spike in density. In contrast, Mg VI in Fig. 3.20(c) has only one spike. This is the same as seen in Fig. 3.19(b), where the positive energy spike produces a negative change in the ionisation balance because the temperature is above that of the peak formation temperature of Mg VI, and consequently the emission is reduced.

As expected, the spectrometers observe more localised parts of the loop compared to that of TRACE shown in Fig. 3.18. The CDS Ne VI and EIS Mg VI lines peak near the loop footpoint and show a spike in the transition region but no oscillation in the corona. EIS Si VII also peaks near the loop footpoint and has no coronal oscillation, however, it has two transition region spikes. Neither the CDS Mg X or the EIS Fe XII lines detect emission from the low transition region. However, both show spikes in the upper transition region/low corona followed by a rapidly decaying oscillation in the corona. This is consistent with TRACE 171 Å from Fig. 3.18. The oscillations in TRACE and EIS Fe XII are almost 180° out of phase with each other, with the CDS Mg X line showing a phase between the two. This demonstrates the difficulty in correctly interpreting the density and temperature perturbations along the loop from observations.

3.3 Intensity as a Function of Time

Spectrometers such as CDS and EIS resolve the spectra of observed radiation using narrow slits, leaving only a single spatial dimension for imaging. It is unlikely for a loop to be aligned directly along this slit, therefore, the slit would probably cut across the loop at one particular position along the loop. Successive images mean this position is observed as a function of time. Consequently, in order to allow a closer comparison with observations we now model a single position along the loop as a function of time.

Three different positions along the loop are chosen to show the emission from a range of equilibrium temperatures. The positions shown by the vertical dotted lines in Fig. 3.17, are in the corona at $x = 30$ Mm, where the equilibrium temperature is 1.25 MK, in the transition region at $x = 18$ Mm, where $T = 0.8$ MK and below the transition region at $x = 7$ Mm, where the temperature is 0.33 MK.

The coronal part of the loop at $x = 30$ Mm and $T = 1.25$ MK is initially examined (right hand vertical dotted line in Fig. 3.17). The initial time (i.e. $t = 0$ on Fig. 3.21) of the figures below for this position along the loop is $t = 6.8$ (34 min). This time is chosen to ensure that the travelling wave has reached this part of the loop and to aid interpretation by giving temperature perturbations that are in phase with those of Section 3.2. The temperature perturbation is shown by the red line in Fig. 3.21(b) and is initially zero before increasing to a positive peak, this is consistent with the temperature perturbation shown in Fig. 3.3(a).

Fig. 3.21(a) shows the perturbed intensity of TRACE 171 Å (black), of an oscillation in a gravitationally stratified medium damped by thermal conduction and compressive viscosity, at $x = 30$ Mm, as a function of time. The emission due to Fe IX (purple) and Fe X (orange) are also shown and the background emission has

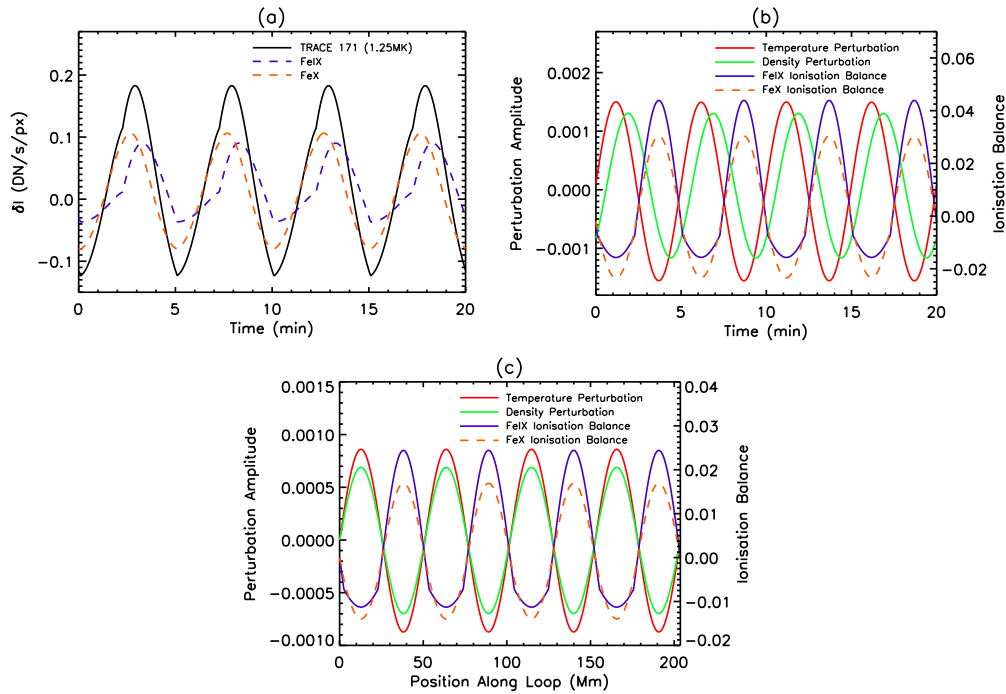


Figure 3.21: (a) perturbed intensity of TRACE 171 Å (black), Fe IX (purple) and Fe X (orange) in a gravitationally stratified medium damped by thermal conduction and compressive viscosity as a function of time, at 30 Mm, along the loop, where $T_0 = 1.25$ MK. The background emission has been subtracted. (b) Temperature (red) and density (green) perturbations used to calculate the intensity in (a) with the ionisation balance of Fe IX (purple) and Fe X (orange). (c) Temperature (red) and density (green) perturbations used to calculate the intensity along a loop of a uniform equilibrium temperature of 1.25 MK without damping (black line in Fig. 3.6(b)). The ionisation balance of Fe IX (purple) and Fe X (orange) are also shown.

been subtracted. The equilibrium temperature of the loop at this position is 1.25 MK, hence, the resulting emission should resemble that of Fig. 3.6 of intensity along a loop with a uniform equilibrium temperature of 1.25 MK. However, the results of Fig. 3.6 do not include gravitational stratification or damping. The Fe IX and Fe X ionisation balance are shown in Fig. 3.6(a) with the TRACE 171 Å emission shown in Fig. 3.6(b) (black line). Fig. 3.21(b) shows the temperature (red) and density (green) perturbations as well as the ionisation balance of Fe IX (purple) and Fe X (orange) that produce the emission of Fig. 3.21(a). For comparison, the temperature (red) and density (green) perturbations resulting in the emission of Fig. 3.6(b) (black line) are shown, as a function of loop position, in Fig. 3.21(c). The ionisation balance of Fe IX (purple) and Fe X (orange) are also shown.

Fig. 3.21(a) is consistent with Fig. 3.6 in that both Fe IX and Fe X have similar contributions to the TRACE 171 Å emission, with that of Fe X the largest. The TRACE 171 Å and Fe X emission are out of phase with the temperature and density perturbations (red and green lines, respectively in Fig. 3.21(b)). However, in contrast to the results of Fig. 3.6, the phase difference is no longer 180° . In addition, the oscillation in Fig. 3.21(a) appears far more symmetric than that of Fig. 3.6(b). These differences are a result of the inclusion of thermal conduction. From Fig. 3.21(c) it is clear that without thermal conduction the temperature and density oscillate in phase, producing, for this example, oscillations in the ionisation balance that are 180° out of phase with both the temperature and density perturbations. The inclusion of thermal conduc-

tion produces a phase shift between the temperature and density perturbations, as seen in Fig. 3.21(b). The ionisation balances of Fe IX and Fe X, which oscillate 180° out of phase with the temperature perturbation, are no longer 180° out of phase with that of the density. Consequently, the phase difference of the intensity in Fig. 3.21(a) with the simulation perturbations is no longer simply 180° . This change of phase introduced by thermal conduction produces a far more symmetric wave than that seen in Fig. 3.6(b).

The perturbed intensity of the CDS Mg X line is modelled for the same conditions as that described above for TRACE 171 Å and the resulting emission is shown in Fig. 3.22(a). Comparison of Fig. 3.22(a) with Fig. 3.7(a) shows very similar results to the TRACE 171 Å results described above. The oscillation of the Mg X emission has a different phase to that modelled along a loop at 1.25 MK and in addition, the oscillation in Fig. 3.22(a) again appears more symmetric than that of Fig. 3.7(a). Figs. 3.22(b) and (c) show the same for CDS Mg X as Figs. 3.21(b) and (c), respectively, show for TRACE 171 Å. By comparing the relative phase of the Mg X ionisation balance with the density perturbation in Figs. 3.22(b) and (c) it is again clear that the change in phase between Figs. 3.22(a) and 3.7(a) is produced by the phase shift between the temperature and density due to the inclusion of thermal conduction.

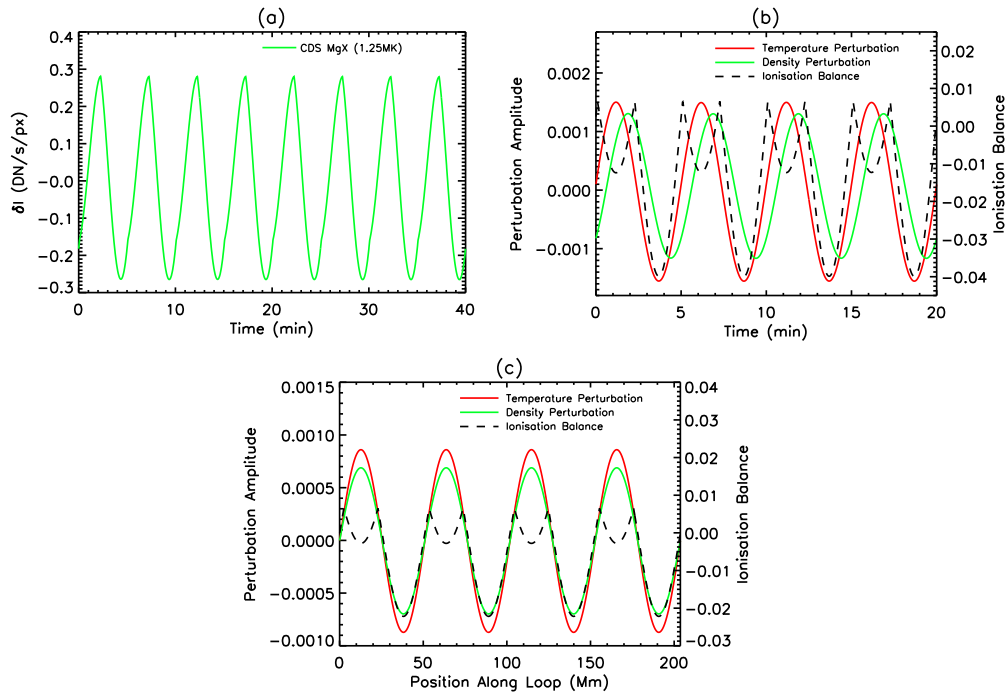


Figure 3.22: (a) perturbed intensity of CDS Mg X (624 \AA) in a gravitationally stratified medium damped by thermal conduction and compressive viscosity, as a function of time, at 30 Mm, along the loop, where $T_0 = 1.25 \text{ MK}$. The background emission has been subtracted. (b) Temperature (red) and density (green) perturbations used to calculate the intensity in (a) with the ionisation balance of Mg X (black). (c) Temperature (red) and density (green) perturbations used to calculate the intensity along a loop of uniform equilibrium temperature of 1.25 MK without damping (green line in in Fig. 3.7(a)). The ionisation balance of Mg X (black) is also shown.

The results for the EIS Fe XII emission, shown in Fig. 3.23, are consistent with TRACE 171 Å and CDS Mg X shown above, showing a slightly more symmetric wave with a small phase difference when compared to the results along a loop of 1.25 MK (see Fig. 3.7(b)). The background subtracted amplitudes for TRACE

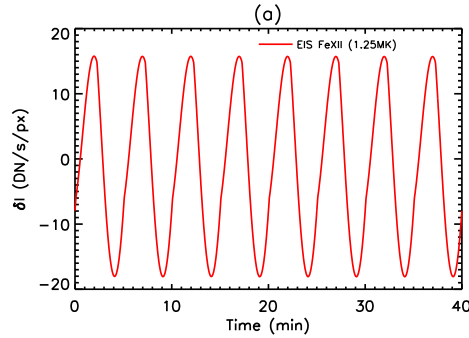


Figure 3.23: Perturbed intensity of EIS Fe XII (195 \AA) (red) as a function of time, at 30 Mm, along the loop, where $T_0 = 1.25 \text{ MK}$.

171 \AA , CDS Mg X and EIS Fe XII, shown in Figs. 3.21(a), 3.22(a) and 3.23, respectively are all similar, but slightly greater than those seen in Section 3.2.1. This is a result of the slightly greater magnitude of the density and energy perturbations at $x = 0.85$ (30 Mm) in Fig. 2.27(b) (with gravitational stratification and damping) than those used in Section 3.2.1.1 (without gravitational stratification or damping). The absolute magnitudes of the emission (i.e. without the background subtracted), however, are below those of Section 3.2.1.1 at 1.25 MK due to the lower coronal density (shown in Fig. 3.17) when gravitational stratification is included. The TRACE 171 \AA , CDS Mg X and EIS Fe XII emission, as a function of time, show similar oscillations, with a much smaller phase difference to the simulation perturbations, to those seen as a function of loop position (Figs. 3.6 and 3.7).

The emission is now modelled in the transition region, at $x = 18 \text{ Mm}$, where the loop temperature is 0.8 MK . The initial time of Fig. 3.24 is $t = 6.3$ (31 min), which is chosen to give a temperature perturbation that is in phase with the $x = 30 \text{ Mm}$ case (Fig. 3.21(b) red). All the emission lines previously discussed are included here as they all detect emission in the transition region (as discussed in Section 3.2.2).

The perturbed intensity of TRACE 171 \AA is given by the black line in Fig. 3.24(a), with the emission due to Fe IX and Fe X given by the orange and purple lines, respectively. The ionisation balance of Fe IX at 0.8 MK is much greater than that of Fe X, as shown in Fig. 3.4(a), hence the Fe IX emission makes the main contribution to the TRACE 171 \AA emission. 0.8 MK ($\log T = 5.9$) is above the peak formation temperature of Fe IX, hence the ionisation balance oscillates 180° out of phase with the temperature. The purple line in Fig. 3.24(a) shows that the intensity also oscillates, almost 180° out of phase with the temperature perturbation. Again, the presence of thermal conduction has produced a small change of phase from 180° . Thermal conduction is less efficient at lower temperatures (see Fig. 2.11(a)), hence, the phase shift produced by thermal conduction is reduced at 0.8 MK compared to 1.25 MK . The phase of the TRACE 171 \AA emission is between that of Fe IX and Fe X, but closer to Fe IX and is also between those found in the coronal part of the loop with and without thermal conduction (shown in Figs. 3.21(b) and (c), respectively).

Fig. 3.24(b) shows the emission of CDS Mg X (green) and CDS Ne VI (blue). Both lines show similar magnitudes of emission. At 0.8 MK , Mg X is below its peak ionisation balance, whereas, Ne VI is above its ionisation peak. Therefore, the oscillation in the ionisation balances of Mg X and Ne VI are 180° out of phase. It is this difference in the ionisation balance which causes the phase shift between the intensities

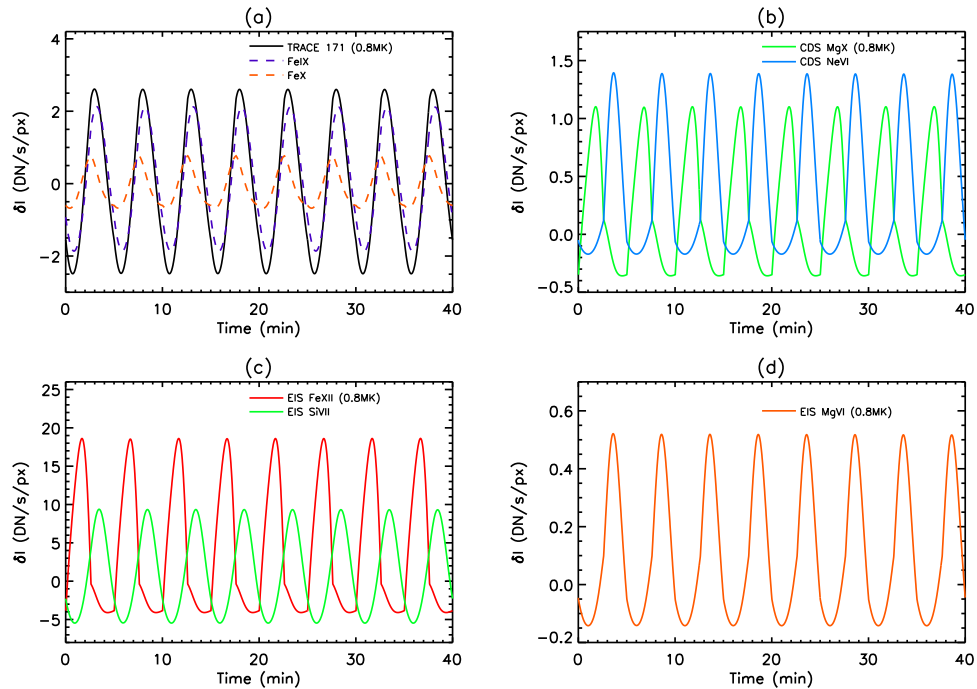


Figure 3.24: Perturbed intensity as a function of time, at 18 Mm, along the loop, where $T_0 = 0.8$ MK, with the background emission subtracted. (a) TRACE 171 Å (black) with Fe IX (purple) and Fe X (orange), (b) CDS Mg X (624 Å) (green) and CDS Ne VI (562 Å) (blue), (c) EIS Fe XII (195 Å) (red) and EIS Si VII (275 Å) (green) and (d) EIS Mg VI (269 Å) (orange).

of Mg X and Ne VI in Fig. 3.24(b). In contrast to the results found in Fig. 3.22(a), which show a very regular shape, the presence of thermal conduction has increased the asymmetry of the oscillation shown in Fig. 3.24(b). A similar effect has also occurred for the Ne VI line. The emission from the three EIS lines studied, namely Fe XII (195 Å) (red), Si VII (275 Å) (green) and Mg VI (269 Å) (orange) are shown in Figs. 3.24(c) and (d). The emission from Mg VI is very weak due to its low peak formation temperature of 0.4 MK and low emissivity (see Fig. 3.11(b)). A small oscillation can be seen, however, with a phase opposite to that of the temperature perturbation, which is due to the ionisation balance. Comparing the emission of Fe XII with that of the cooler Si VII line shows the same results as seen for CDS. That is, the hotter line is almost in phase with the temperature, whereas the cool line is 180° out of phase. This is again due to the ionisation balance and the effects of thermal conduction.

Finally, the emission closer to the loop footpoint is modelled, at $x = 7$ Mm, where the equilibrium loop temperature is 0.33 MK. The initial time in Fig. 3.25 is $t = 6.25$ (31.25 min), which gives a temperature perturbation in phase with the other results in this chapter. The perturbed intensity of TRACE 171 Å (black), Fe IX (purple) and O VI (orange) are shown in Fig. 3.25(a). Fig. 3.25(b) gives the emission of CDS Ne VI, with that of EIS Mg VI (orange) and EIS Si VII (green) shown in Fig. 3.25(c). The phase and shape of all the lines in Fig. 3.25 are consistent with those seen in Figs. 3.8(b), 3.10(a) and 3.10(b) at 0.33 MK without thermal conduction. This is a consequence of the inefficiency of thermal conduction at lower temperatures, hence there is little effect on changing the phase between the temperature and density perturbations. Therefore, the oscillations in Fig. 3.25 all appear very much as expected from the uniform

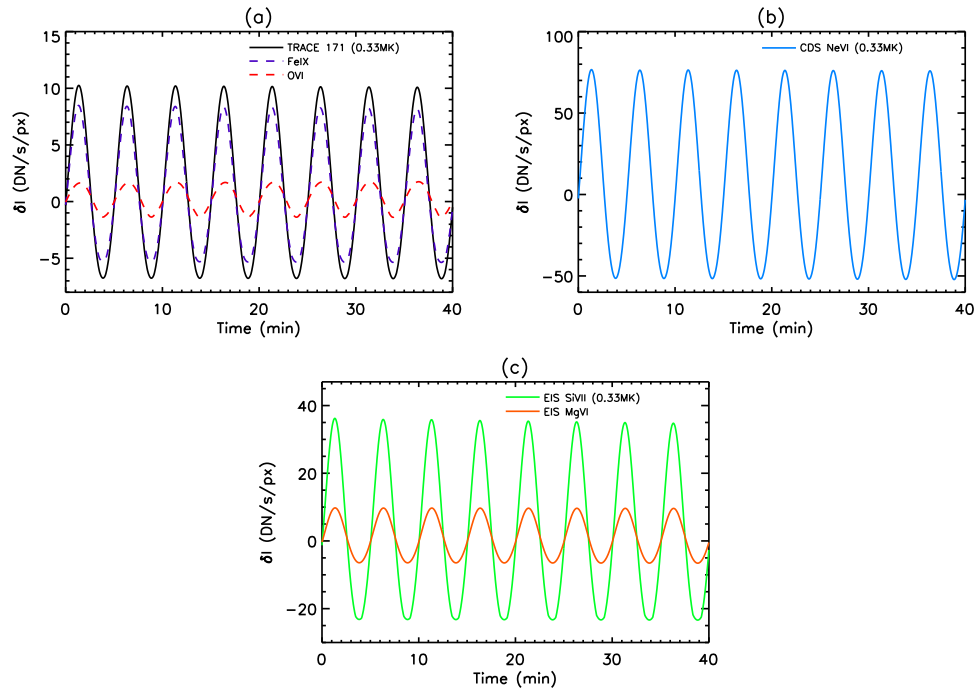


Figure 3.25: Perturbed intensity as a function of time, at 7 Mm, along the loop, where $T_0 = 0.33$ MK, with the background emission subtracted. (a) TRACE 171 Å (black) with Fe IX (purple) and O VI (orange), (b) CDS Ne VI (562 Å) (blue) and (c) EIS Mg VI (269 Å) (red) and EIS Si VII (275 Å) (green).

equilibrium temperature case, except that the intensities here are much higher. This is a result of the much larger density in this region using the non-uniform equilibrium conditions given by Fig. 3.17 compared to that of the uniform equilibrium conditions case used in Section 3.2.1.1.

3.4 Forward Modelling Conclusions

The synthesised emission for TRACE 171 Å and several CDS and EIS lines has been modelled along a loop of uniform and non-uniform equilibrium temperature as well as at a single position along the loop as a function of time. The resulting intensity depends in a complicated way on the emissivity, ionisation balance and the loop density. The emissivity depends on both the temperature and density of the loop, whereas the ionisation balance depends only on the temperature. Due to the temperature of the loop compared to the peak formation temperature of a particular ion, the ionisation balance can cause drastic phase changes in the intensity compared to the temperature and density oscillations. The shape of the intensity oscillation is often very anti-symmetric, with the maxima having significantly different magnitudes than the minima. The exact effects of the emissivity, the ionisation balance and the loop density vary for each example. However, certain cases show similar characteristics, for example, loops observed that are hotter than the peak formation temperature of the emission line used are often out of phase with the temperature and density of the loop, due to the ionisation balance. These effects demonstrate the difficulty in interpreting the density and temperature perturbations from observed oscillations. The comparison of many different

lines from different instruments is important to correctly interpret observations of such oscillations, as are simultaneous Doppler velocity observations. Observations of an oscillation along a loop from different emission lines with different peak formation temperatures are likely to show oscillations with different phases, shapes and amplitudes. By comparing many lines, and using knowledge of the ionisation balance and emissivity (and how they vary with temperature and density), the phase of the density and temperature perturbations and the temperature of the loop can be found more reliably. Doppler velocity observations (if sensitive enough) would reveal the phase and amplitude of the velocity perturbations, which would consequently aid the interpretation of the oscillation in intensity.

Investigating the emission from loops at uniform equilibrium temperature shows that the same waves propagating in loops at different uniform equilibrium temperatures can be observed with totally different phases and with asymmetries in the positive and negative magnitudes. This is most obvious when comparing the emission of TRACE 171 Å at 1 MK and 1.25 MK, shown in Fig. 3.6(b), which have very different shapes and are 180° out of phase.

Due to the dependence of intensity on the loop density, the inclusion of gravitational stratification for undamped waves along a uniform equilibrium temperature loop causes the intensity to decay rapidly, giving the appearance of damping. TRACE 171 Å, CDS Mg x and EIS Fe XII all show damped oscillations to around 100 Mm, despite undamped temperature and density perturbations. Damping due to thermal conduction and compressive viscosity increases this damping, with oscillations now observable to around 50 Mm. However, as a result of the ionisation balance, the inclusion of damping terms can actually increase the amplitude of some parts of the oscillation, as shown by Fig. 3.14.

By using a range of spectral lines, waves can be observed as they propagate through the solar atmosphere. With the addition of an equilibrium temperature gradient the forward modelling results vary more between imagers and spectrometers, with the emission detected by the spectrometers more localised than that of TRACE. TRACE 171 Å observes oscillations along the entire loop, however, the coronal part is weak with emission from the transition region dominant. The CDS Mg x and EIS Fe XII emission lines have similar peak formation temperatures of 1.25 MK and as a result detect similar coronal oscillations but nothing below the transition region. They are also consistent with the coronal part of TRACE 171 Å, despite small phase differences, which show rapidly decaying oscillations observable to around 50 Mm. CDS Ne VI, EIS Si VII and EIS Mg VI, however, which are sensitive to transition region temperatures, observe emission near the loop footpoint, but not in the corona. All the lines studied show intensity spikes in the transition region due to the spikes in the energy and density perturbations of the transition region. There is some observational evidence for dominant transition region emission, but not to the degree suggested by Fig. 3.18. The reason for the discrepancy is unclear, but may be due to the width and position of the transition region used in the model. A steeper transition region at lower altitude would reduce the density contrast between the transition region and the corona due to gravitational stratification and may therefore decrease the difference between the emission from the transition region and the corona.

The coronal sensitive lines of TRACE 171 Å, CDS Mg x and EIS Fe XII show oscillations visible to around 50 Mm, however, an exact detection length is difficult to determine. The levels of emission, particularly for TRACE and CDS are very low, with only fractions of data numbers, as seen in Figs. 3.18(b) and 3.19(a). These low data counts for TRACE have been found previously (e.g. De Moortel et al. 2002a;

McEwan and De Moortel 2006) where oscillations have been observed by spatial and temporal averaging. The oscillations are observed to around 50 Mm which is of the order of that observed for propagating slow waves (around 10 Mm, De Moortel et al. 2002a) but is still high. However, it is an upper limit in the detection length as observations have noise to consider which will reduce the detection threshold, especially considering the low data counts.

The synthesised emission at a single position of the loop as a function of time resembles that of a spectrometer, which having only one spatial dimension, is likely to detect emission from a single slice across a loop. At low transition region temperatures the phase of the emission, when damping is included, is consistent with that of a loop at uniform equilibrium temperature without damping. In contrast, at higher, coronal, temperatures the effects of thermal conduction are stronger and a phase shift is produced between the temperature and density perturbations. Consequently, the phase of the intensity oscillations are affected, adding further complexity to the interpretation of the data. In order to extend this work, and make the results more comparable with observations, the observational effects of slow waves which are only driven for a finite number of periods could be investigated.

Chapter 4

Data Analysis Techniques

4.1 Introduction

The previous chapter investigated the observational signatures of propagating slow waves. We now examine some of the techniques used to analyse observational data. The relative merits of each technique for the detection and interpretation of oscillations are discussed.

Fourier analysis has been widely used to analyse data and is particularly useful for coronal seismology as it is capable of determining the frequencies of oscillations. Fourier analysis allows the frequencies present in a time series to be determined. For example, Ofman et al. (1997) used Fourier analysis on SoHO UVCS data of polar coronal holes to detect six minute period oscillations, which have been interpreted as propagating slow waves. Three minute period slow waves propagating through the transition region into the corona were detected by Marsh and Walsh (2006) using a Fast Fourier Transform (hereafter FFT) of CDS and TRACE data. The FFT showed two distinct frequencies of oscillation of 5.9 mHz and 7.3 mHz. More recently, Yuan et al. (2011) analysed both EUV (TRACE) and radio (NoRH) data using Fourier analysis and detected three distinct frequencies of 0.22 mHz, 0.31 mHz and 0.57 mHz, in both the chromosphere and the corona. Kneer and Bello González (2011) used a Fourier transform of both intensity and velocity data to study the energy transport of propagating acoustic waves. Fourier analysis has also been used for many other solar purposes, for example by Tomczyk et al. (2007) to aid the detection of Alfvénic waves in the corona using CoMP data and in helioseismology by Kjeldsen et al. (2008).

In addition to Fourier analysis, a time series can also be evaluated using wavelet analysis, giving the power as a function of both frequency and time. A detailed description of wavelet analysis can be found in Farge (1992) and Torrence and Compo (1998). Like Fourier analysis, wavelet analysis has also been widely used for detecting solar oscillations. Wavelet analysis has been used extensively by many studies and a few examples are listed here by way of illustration. De Moortel et al. (2000) detected and examined the energy flux of a propagating slow wave, De Moortel et al. (2002a) found 38 oscillations using wavelet analysis on TRACE 171 Å data and De Moortel et al. (2002c) found three minute period oscillations above

sunspots and five minute periods above non-sunspot regions. With the aid of wavelet analysis McEwan and De Moortel (2006) detected and performed a statistical study of 25 propagating slow waves. In addition, Marsh et al. (2004) used wavelet analysis to analyse co-temporal and co-spatial CDS and TRACE data and found oscillations propagating through the solar atmosphere. Wavelet analysis has also aided the detection and separation of oscillations with similar or related periods. King et al. (2003) and Wang et al. (2009) both detected propagating slow waves along coronal loops and found two distinct periods of oscillation. Verwichte et al. (2004) detected multiple oscillation modes of a standing fast kink wave in a post-flare coronal loop. Wavelet analysis was also used to detect oscillations in active regions (O'Shea and Doyle 2009) and waves propagating in coronal holes (Gupta et al. 2009). Erdélyi and Taroyan (2008) detected two oscillation events by analysing EIS data from a selection of EUV emission lines. Wavelet analysis has also aided the detection of coronal oscillations using solar eclipse data. Oscillation periods of 20 s and 27 s were found by Singh et al. (2009) and were interpreted as fast magnetoacoustic waves. Williams et al. (2001) also found oscillations in coronal loops.

In addition to determining the period and duration of an oscillation, wavelet analysis can also give information about the damping of an oscillation. The use of wavelet analysis in determining the damping profile of an oscillation was investigated for Alfvén waves by De Moortel and Hood (2000) and for transverse oscillations of a coronal loop by De Moortel et al. (2002a) as well as Ireland and De Moortel (2002). Ireland and De Moortel (2002) showed the potential of wavelet analysis to determine the damping mechanism of an oscillation, although, the errors associated with this observation were too large for a specific mechanism to be determined. The potential of wavelet analysis in providing automatic detection of oscillations is discussed in De Moortel and McAteer (2004).

Observational data is often very complicated, containing information from a variety of physical processes. Appropriate data analysis is very important in order to extract the relevant signals from a data set and to allow these signals to be correctly interpreted. Of particular importance when observing oscillations, is the identification of the background trend about which the signal oscillates. An accurate determination of this background allows a more accurate extraction of the oscillation to be obtained and potentially the underlying physical mechanisms to be determined. The background trend is also required by wavelet analysis to give a confidence level.

Many different techniques are used to determine the background trend. Some of these techniques are intrinsic in that the background is determined from a self contained process. Most techniques, however, use arbitrary choices in order to determine the background. A common method of determining the background is by fitting a polynomial (of chosen degree) to the data and using this as the background. Linear fitting (i.e. polynomial degree 1) has been widely used in solar applications. Ofman et al. (2000b), De Moortel et al. (2002a), De Moortel et al. (2002b), McEwan and De Moortel (2006) and Erdélyi and Taroyan (2008) all used a linear fit to data in order to determine and subtract a background trend. A higher fitting degree of 4 was used by Singh et al. (2009) where oscillations were detected using a quadratic fitted to solar eclipse data. Marsh et al. (2004) determined a constant background using the mean value of the data. Another method often used to find a background is data averaging or smoothing (where the amount of smoothing or the timescale of the averaging is chosen). O'Shea et al. (2002) used a running average. Tian et al. (2008) and Wang et al. (2009) used 3.5 minute and 10 minute smoothing, respectively, whilst Gupta et al. (2009) took a 30 minute average. A Fourier filter was used to determine the background in O'Shea and Doyle

(2009) by isolating fluctuations with periods longer than a quarter of the duration of the time series.

A relatively new technique to determine oscillations in data is Empirical Mode Decomposition (hereafter EMD). It was proposed by Huang et al. (1998) and can be used to analyse non-linear and non-stationary time series and determine the background intrinsically. EMD splits a signal into a number of components each with variations on different timescales. The last of the components, with variations on the longest timescale, can be considered as the background trend of the data. The use of EMD to intrinsically determine background trends in climate data was studied by Wu et al. (2007). Huang et al. (2003) used EMD to analyse earthquake data and devised a confidence limit for the results and Lin et al. (2009) used EMD to analyse low signal to noise data. EMD was originally used and developed for geophysical research and a review of the development of the EMD technique for geophysical applications can be found in Huang and Wu (2008).

EMD has been used for solar research, firstly by Komm et al. (2001) to determine variations in the rotation rate of the solar convection zone. Terradas et al. (2004) used EMD to identify a wave with a period of five minutes propagating along a coronal loop. They isolated different frequencies of oscillation by splitting the time series into seven components and also found that EMD worked for noisy signals. More recently, EMD has been used to detect oscillations in sunspots (Chorley et al. 2010), in the photosphere (Morton et al. 2011) and generated by solar flares (Nakariakov et al. 2010).

Wu and Huang (2009) proposed Ensemble Empirical Mode Decomposition (hereafter EEMD) which is an extension to the EMD technique. EEMD uses white noise to provide a reference scale to aid the separation of components with similar timescales and uses ensemble averaging. Zhang et al. (2010) used simple analytical functions to study the effects of the white noise amplitude and the number of ensemble trials.

4.2 Techniques and Data Analysis

The uses, benefits and limitations of several analysis techniques for identifying and interpreting oscillations in data are investigated. A range of time series with known analytical components are used. The ability of these techniques to correctly determine the amplitude and the period of oscillations as well as the presence and strength of damping is examined. In addition the determination of the background trend is investigated. Initially a signal consisting of a single oscillation about a constant background (Section 4.2.1.1) is analysed. The complexity of the time series is increased by varying the background with time (Section 4.2.1.2) and by subsequently adding a second oscillation (Section 4.2.2.1) and damping (Section 4.2.2.2). The effects of beating (Section 4.2.3), a time dependent oscillation (Section 4.2.5) and reduced cadence (Section 4.2.6) are also examined. The data analysed in this chapter is one dimensional in order to be consistent with the treatment of observational data in Chapter 5, where spatial averaging has been performed.

4.2.1 Single Oscillation

4.2.1.1 Constant Background

The first time series to be analysed is that of a single undamped oscillation with a constant period oscillating about a constant background. An oscillation period of 300 s is chosen to be consistent with Chapters 2 and 3. Background and oscillation amplitudes of 2800 and 140 are chosen to give an oscillation of 5% of the background, again consistent with previous chapters. The length of the time series is chosen to be around 25 minutes with 1512 data points giving a cadence of 1 s. The duration of the time series and the amplitude of the background (A and B) are chosen to be broadly consistent with the TRACE data analysed in Chapter 5. In addition, the data is modelled in a single spatial dimension to be consistent with the spatially averaged observations of Chapter 5. An arbitrary phase shift of $\frac{\pi}{3}$ is added to the oscillation in order to give a more realistic time series. The time series, $X(t)$ is given by,

$$X(t) = A + B x_1(t), \quad (4.1)$$

where

$$x_1(t) = \sin\left(\frac{2\pi t}{\tau_1} + \phi_1\right), \quad (4.2)$$

with $A = 2800$, $B = 140$, $\tau_1 = 300$ s and $\phi_1 = \frac{\pi}{3}$, where t is the observation time. The signal, $X(t)$, is shown in black in Fig. 4.1(a) with the background in red. The oscillation is shown in Fig. 4.1(b).

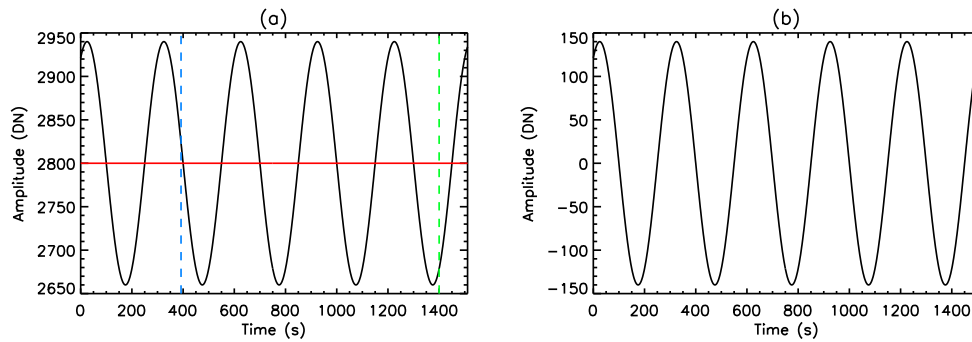


Figure 4.1: (a) signal (black) comprising of a constant amplitude background (red) and (b) an undamped oscillation with a period of 300 s. The blue and green lines in (a) mark $t = 392$ s and $t = 1400$ s, respectively.

Fast Fourier Transform (FFT)

The first technique to be examined is Fourier analysis, using the standard IDL FFT routine. An FFT is taken of the signal in Fig. 4.1(a) and shown in Fig. 4.2(a). The FFT in Fig. 4.2(a) clearly and correctly detects an oscillation with periodicity between 200 s and 400 s, with a very distinct peak at 300 s. No other periods are present, as expected considering the signal used. Although there is no information about the time of the oscillation the width of the peak does contain some information about the duration of the oscil-

lation. A broader peak means only a few periods are present, whereas a sharp peak represents many periods of oscillation (an infinite number of peaks would result in a delta function). The sharpening of the peak can be seen by the red line in Fig. 4.2(b) which is from a data set of twice the length as that of the black line (i.e. 3014 s), but is otherwise identical. The blue and green FFT's in Fig. 4.2(b) were taken for data sets of 392 s and 1400 s duration, respectively, as shown by the vertical dashed lines in Fig. 4.1(a). The blue FFT shows that the time series can be very short (392 s compared to the 300 s period) before the FFT can no longer resolve the oscillation. However, the green FFT shows that only a small shortening of the time series (1400 s compared to 1512 s) results in the FFT giving the wrong period (the peak of the green line is shifted slightly compared to the red and black peaks and is no longer at 300 s).

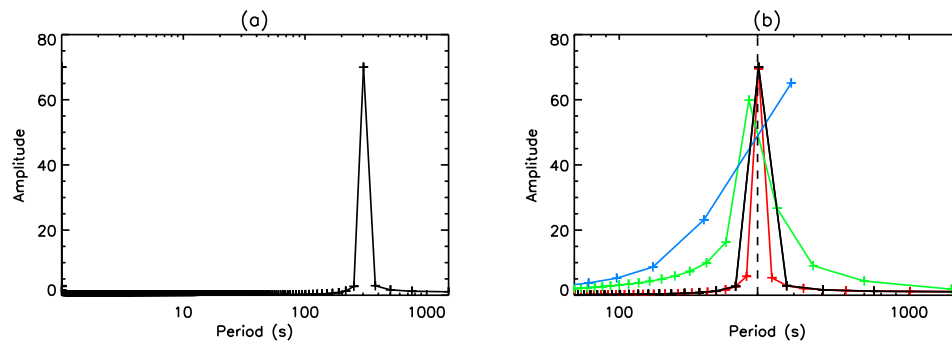


Figure 4.2: FFT of the signal in Fig. 4.1(a). (b) FFT from (a) (black) with FFT of 392 s time series (blue), 1400 s time series (green) and 3024 s time series (red).

Fourier analysis is a simple and effective way to identify periodicity in data. However, the information gained from a FFT alone is limited and therefore, other techniques are required to further aid interpretation.

Wavelet Analysis

The wavelet analysis code used here (available at <http://paos.colorado.edu/research/wavelets/>) is from Torrence and Compo (1998) who demonstrate the abilities of the code using El-Niño data. Wavelet analysis transforms a one dimensional time series (such as that in Fig. 4.1(a)) into a two dimensional time-frequency image (as seen in Fig. 4.3). The time from Fig. 4.1 is plotted against the oscillation period with the colour of the image representing the power. Bright colours correspond to high power. Hence, the bright feature in Fig. 4.3 at a period of around 300 s shows evidence of an oscillation for all time. Torrence and Compo (1998) include a significance test to ensure confidence in identifying oscillations. For this a background is required (i.e the red line in Fig. 4.1(a)) and the wavelet analysis is compared to that of a randomised signal about the same background. This gives a confidence level, which can be seen by the solid black lines in Fig. 4.3 that outline the bright feature at 300 s periodicity. The area enclosed by these lines is above the confidence level, hence the dark area below 100 s periodicity is below the confidence level and no periodicities can be reliably inferred. The confidence level for this study is chosen to be 99%.

The wavelet analysis assumes the time series data is periodic, which it is not. Consequently, edge effects produce errors at the boundaries (i.e. $t = 0$ s and $t = 1512$ s). This produces a cone of influence (hereafter COI) outside of which the results are unreliable and should not be used. The edge of the COI is marked

in Fig. 4.3 by the dot-dashed line, hence, only results below this line should be used. A longer time series is required to detect long period oscillations compared to short period oscillations. Consequently, the COI is particularly restrictive to the detection of long period oscillations (as seen by the COI in Fig. 4.3). The errors due to edge effects and the COI are discussed further in Torrence and Compo (1998) and De Moortel et al. (2004b).

Wavelet analysis is the convolution of a time series with an analysis function. The choice of this function, called the wavelet, affects the results of the wavelet analysis. The wavelet can be either real (e.g. DOG) or complex (e.g. Morlet or Paul). A real wavelet function can determine peaks or discontinuities, however, a complex wavelet is required in order to analyse oscillatory behaviour (Torrence and Compo 1998). For this work the Morlet wavelet is chosen as it has been commonly used to successfully detect oscillations in many other studies (e.g. De Moortel and Hood 2000; McEwan and De Moortel 2006; King et al. 2003; Erdélyi and Taroyan 2008; Wang et al. 2009; Singh et al. 2009; Gupta et al. 2009). The resolution of the wavelet is a balance between the time resolution and the frequency resolution, which depends on the shape of the wavelet function. The Morlet wavelet has high frequency resolution and therefore lower time resolution. Consequently, features in wavelet analyses using Morlet wavelets appear spread horizontally in time, but sharp in frequency (not to be confused with an oscillation present for all time as seen in Fig. 4.3). The Morlet wavelet, $\psi_0(\eta)$, is defined as,

$$\psi_0(\eta) = \pi^{-1/4} e^{i k \eta} e^{-\eta^2/2}, \quad (4.3)$$

where η is a non-dimensional time parameter and k is the non-dimensional frequency (Torrence and Compo 1998). This frequency parameter, k , affects the shape of the wavelet and hence the balance of time and frequency resolution. A value of $k = 6$ is used here as it gives the best balance of time and frequency resolution and is consistent with most of the previous studies mentioned above. The properties of different wavelets are discussed further in Farge (1992) and Torrence and Compo (1998) and a study of the basic wavelet parameters is covered in De Moortel et al. (2004b).

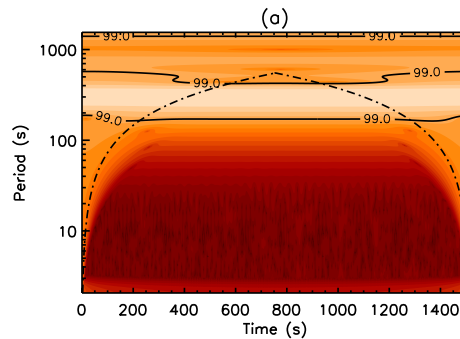


Figure 4.3: Wavelet analysis of the signal in Fig. 4.1(a), with the confidence level (solid) and the COI (dot-dashed).

The results of the wavelet analysis in Fig. 4.3 are consistent with that of the FFT in Fig. 4.2(a). A distinct band of periodicity can be seen between periods of 200s and 500s for the duration of the data set. The wavelet analysis has confirmed the periodicity of the FFT and shown it to be present throughout the time series, although the wavelet analysis has slightly reduced accuracy compared to the FFT in determining the

period. The wavelet analysis also shows that the oscillation is present above a 99% confidence level. The signal analysed here is well resolved, with a constant period of 300 s and a constant amplitude background and yet results of the FFT and the wavelet analysis find a range of periods from 200 s to 500 s, although both do show a well defined maximum at 300 s. These results, therefore, show that in using these techniques to determine any periodic signal there is an implicit uncertainty no matter how clear the observations are.

The wavelet analysis requires a background to give the confidence level. Here the constant value of $A = 2800$ from the analytical solution has been used, giving the most accurate possible results. However, the selection of an appropriate background for data in general is difficult and often involves arbitrary choices. Two methods of determining the background trend of a time series are now investigated.

Polynomial Fitting

One possible way to find the background trend of a time series is by fitting a polynomial of a chosen degree to the data. This polynomial then becomes the background, $r(t)$, and is subtracted from the data, $X(t)$ to give the oscillation or oscillations. The method of Fludra (2001) is often used where the oscillation is given by $X(t)/(r(t) - 1)$. However, here we use the simple subtraction method as this gives the analytical oscillation $x_1(t)$. The polynomial fitting technique is extrinsic as a choice of degree must be made. Data averaging and smoothing are often used instead, eliminating the arbitrary choice of fitting degree. However, these methods are still extrinsic as the degree of smoothing and the timescale of the averaging must be chosen.

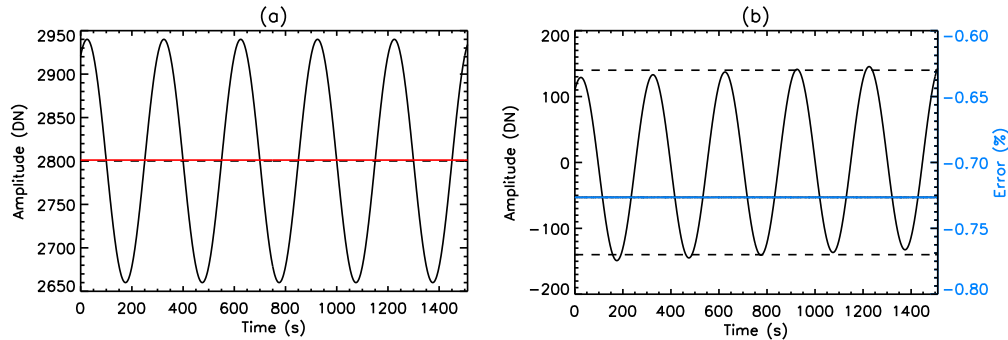


Figure 4.4: Polynomial fitting of the signal in Fig. 4.1(a). (a) signal (black) with the background fit (red) and the analytical background (dashed). (b) resulting oscillation after background subtraction (black) with the error compared to the analytical solution (blue).

The polynomial fitting is performed using the function `poly_fit` in IDL. For a time series with a constant background the only appropriate choice of degree is 0. Fig. 4.4(a) shows the constant background (red), with the data (black) and the resulting oscillation, after the subtraction of the background from the data, shown in Fig. 4.4(b). The polynomial fitting has separated an oscillation from a (chosen) background trend. The error, $Err(t)$, in percent, is defined as,

$$Err(t) = \frac{B_p(t) x_p(t) - B x_1(t)}{B} \times 100, \quad (4.4)$$

where $x_p(t)$ is the oscillation from the polynomial fitting (Fig. 4.4(b)) with maximum amplitude of $B_p(t)$.

As only a constant background has been subtracted the period of the oscillation will not be affected as shown in Figs. 4.5(a) and (b).

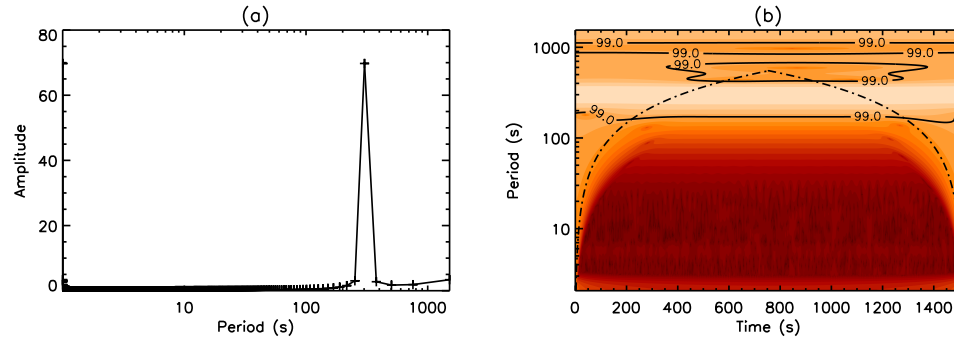


Figure 4.5: (a) FFT and (b) wavelet analysis of the oscillation in Fig. 4.4(b).

The FFT of the polynomial fitting oscillation gives a very similar result to the FFT of the original signal, shown in Fig. 4.2(a), with periods of 200 s to 400 s and a peak at 300 s. The power of the peak is very slightly reduced compared to that of Fig. 4.2(a), although the results within the COI of the wavelet are virtually identical to that of the original signal. The 300 s oscillation found here is clearly present in both the FFT and the wavelet analysis and is above the 99% confidence level.

Empirical Mode Decomposition (EMD)

A possible alternative method to determine a background trend is empirical mode decomposition (EMD). EMD allows the detection of oscillations by splitting a signal into several components called intrinsic mode functions (hereafter IMF's). Each of these IMF's contain variations with a different time scale. The original signal can then be recovered by summing all the IMF's together. This allows all/many of the physical timescales in a signal to be identified, not simply a single oscillation. The longest timescale IMF can be considered as the background trend and is therefore determined from the data intrinsically. This is in contrast to the methods discussed previously which require an arbitrary choice to determine the background trend.

The EMD technique of splitting a time series into IMF's is described in detail in Huang et al. (1998). Each IMF must be symmetric about its mean and have its own timescale of fluctuations. For this to be true each IMF must satisfy two conditions. Firstly, the number of extrema must be equal or differ by 1 to the number of zero crossings and secondly, the local mean of the IMF must be zero for all time. The extrema of a time series $X(t)$ are identified and an upper envelope, $e_u(t)$, is found by fitting a cubic spline to the maxima. A lower envelope, $e_l(t)$, is then found by fitting another spline to the minima of the data. The mean, $m_1(t)$, of these envelopes is found ($m_1(t) = (e_u(t) + e_l(t))/2$) and subtracted from the data to give the first component, $c_1(t) = X(t) - m_1(t)$. To satisfy the conditions of an IMF this process must be repeated with $c_1(t)$ becoming the new data, $c_{11}(t) = c_1(t) - m_{11}(t)$. This is called the sifting process and is discussed further in Huang et al. (1998). After the sifting process has been repeated k times the component $c_{1k}(t)$

will satisfy the condition for an IMF, hence, $IMF_1(t) = c_{1k}(t)$. The IMF is then subtracted from the data ($r_1(t) = X(t) - IMF_1(t)$), giving the residual, $r_1(t)$. $r_1(t)$ is then used as the new data and the process is repeated to find the other IMF's. The EMD process stops after l times when the residual $r_l(t)$ has less than two extrema. $r_l(t)$ is then the background trend, which can be a constant value or a function varying in time.

The sifting process helps to remove riding waves and to smooth fluctuation gradients making the oscillations more symmetric. However, this process can also create oscillations at the boundaries which propagate into the time series. Consequently, the sifting process should not be repeated more than necessary. Stopping criteria for the sifting process have been proposed by Huang et al. (1998), Huang et al. (1999) and Huang et al. (2003). The introduction of oscillations into the data during the sifting process depends on the boundary conditions of the cubic spline fitting. The splines are fitted to the extrema, hence, unless extrema occur very close to the boundaries the splines will not be well constrained at these boundaries. This can lead to large changes at the ends of the splines. The spline fitting is repeated for every sift of every IMF and therefore the boundary conditions are important. The EMD boundary conditions are discussed further in Section 4.2.4.

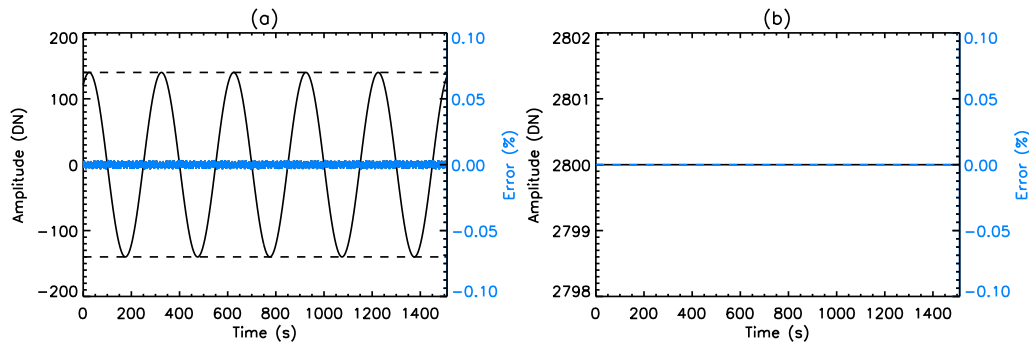


Figure 4.6: Results from the EMD of the signal in Fig. 4.1(a) with the error compared to the analytical solution (blue). (a) oscillation (IMF_1) (black) and (b) background (IMF_{10}) (black). All other IMF's (i.e. IMF_2 to IMF_9) are zero for all time.

The EMD code used here (available at <http://rcada.ncu.edu.tw/>) is the EMD/EEMD code of Wu and Huang (2009), where the code is used in EMD mode by setting the noise amplitude, $n_{amp} = 0$ and the ensemble number, $n = 1$ (this is discussed further in Section 4.2.5.1). The code uses the linear fit boundary conditions for the cubic spline fitting as described in Wu and Huang (2009). A graphical representation of the linear fit boundary conditions can be seen in Fig. A.3 of Wu and Huang (2009). To give reliable envelopes the splines fitted to the extrema must be constrained at the boundaries. Either the value of the data at the boundary is used or the value of a linearly fitted line. This value is found, for the lower boundary, by a linear fit to the first two maxima (or minima) which is then extended to the lower boundary. If the value of this fitted line is greater (or lower) than the value of the data at the boundary then the fitted value is used to constrain the spline, otherwise the value of the data is used. The same process is repeated at the upper boundary using the final two maxima or minima.

The signal in Fig. 4.1(a) is analysed using the EMD code which has identified an oscillation (shown in Fig. 4.6(a)) and a constant background (Fig. 4.6(b)). Like the polynomial fitting method, the EMD has

successfully separated the oscillation from the background. The EMD gives a symmetric oscillation with constant amplitude of 140, in agreement with the analytical solution. The time between the individual extrema gives a period of around 300 s showing that the original oscillation has been preserved during the EMD process. In addition, the constant background of 2800 has been correctly determined. The errors of the EMD in determining both the background trend and the oscillation are very small demonstrating the use and success of the technique.

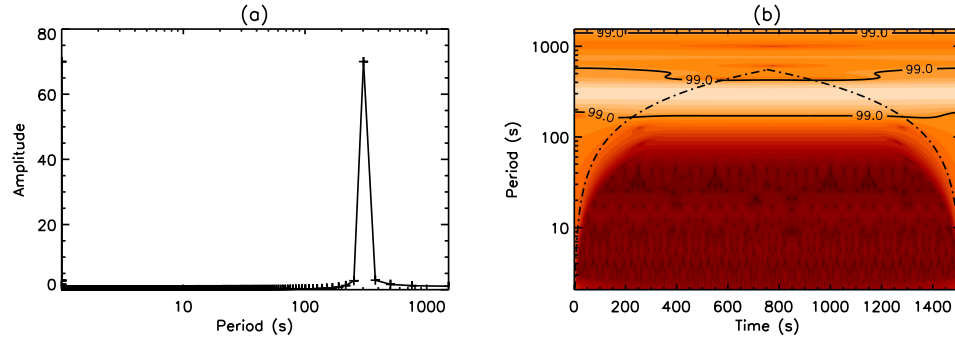


Figure 4.7: (a) FFT and (b) wavelet analysis of the oscillation in Fig. 4.6(a).

A FFT and a wavelet analysis of the EMD oscillation (Fig. 4.6(a)) are performed and shown in Figs. 4.7(a) and (b), respectively. Both analyses clearly show an oscillation with a period of around 300 s. As before, there is a limit to the precision of the determined period, which is around 200 s to 400 s for the FFT and 200 s to 500 s for the wavelet analysis. The EMD technique has correctly and intrinsically determined the constant background. For this simple example the extrinsic determination of the background by the polynomial fitting technique is relatively simple and as shown by Figs. 4.4(b) and 4.5(a) the errors are likely to be small. However, the ability of the EMD to determine the background accurately and intrinsically is increasingly important for more complex data sets.

4.2.1.2 Non-Constant Background

The constant background of Section 4.2.1.1 is replaced by a more realistic non-constant background. This background is oscillatory with a period of 5000 s, a phase of $\frac{\pi}{5}$ and the same maximum background value used previously of 2800. The time series is given by,

$$X(t) = Ax_0(t) + Bx_1(t), \quad (4.5)$$

where

$$x_0(t) = \sin\left(\frac{2\pi t}{\tau_0} + \phi_0\right), \quad (4.6)$$

with $\tau_0 = 5000$ s and $\phi_0 = \frac{\pi}{5}$ and is shown in Fig. 4.8. All the other quantities remain the same as stated in Section 4.2.1.1.

A FFT and wavelet analysis of the signal in Figs. 4.8(a) are shown in Fig. 4.9(a) and (b), respectively. The

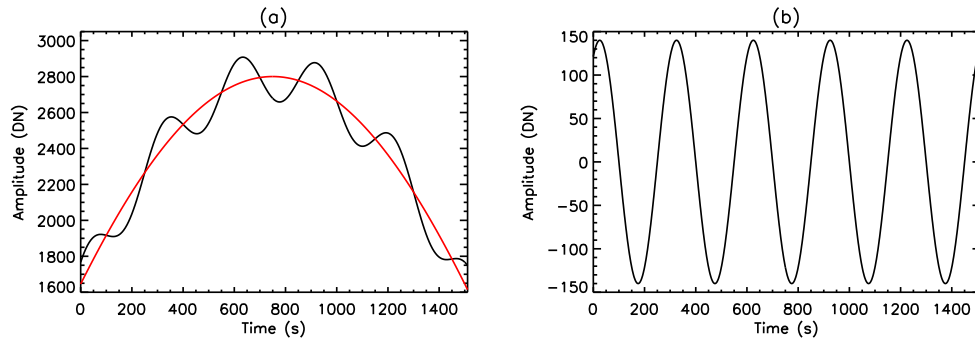


Figure 4.8: (a) signal (black) comprising of a non-constant amplitude background (red) and (b) an undamped oscillation with a period of 300 s.

FFT in Fig. 4.9(a) shows a peak at around 300 s, but in contrast to Fig. 4.5(a), there is greater power at larger periods. The exact periodicity of these larger periods, however, cannot be resolved. The larger periods are caused by the background which has a period of 5000s. This period is too long to be determined from a timescale of only 1512 s as the FFT requires several periods of oscillation in order to accurately determine the period (shown in Fig. 4.2(b)). The wavelet analysis in Fig. 4.9(b) also detects periodicity from 200 s and above, although the COI is more restrictive in determining larger periods than the FFT, consequently no isolated period can be seen.

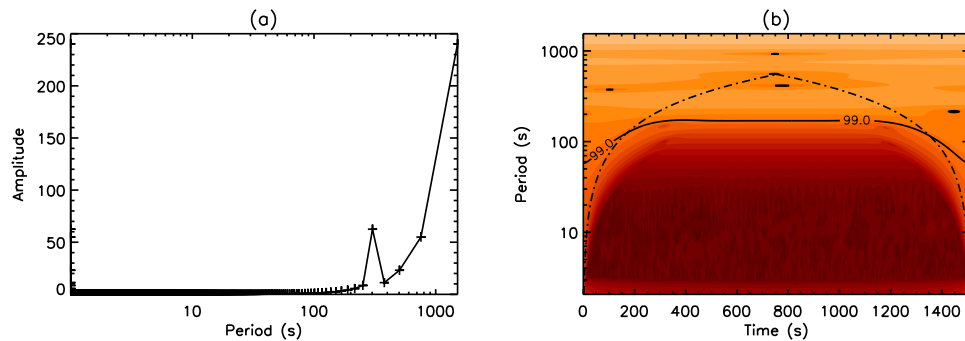


Figure 4.9: (a) FFT and (b) wavelet analysis of the signal in Fig. 4.8(a), with the confidence level (solid) and the COI (dot-dashed).

The polynomial fitting of the signal in Fig. 4.8(a) is shown in Fig. 4.10. The red line in Fig. 4.10(a) gives the linear fit of the background as used in the previous section. In this case the linear fit is clearly not appropriate for determining the background trend. The resulting oscillation from this choice of polynomial degree simply gives the same shape as the original signal, but with a reduced amplitude. The background and oscillation are not separated and any FFT or wavelet analysis gives the same results as those of Fig. 4.9 without the polynomial fitting. These do show the peak at 300 s period, but add nothing new.

For the polynomial technique to be of use in this case a higher degree of fitting is required. A higher degree will allow the polynomial to fit the general shape of the data, however, too high a degree will cause the polynomial fit to oscillate about the background and thereby produce spurious oscillations. Therefore, the lowest possible degree that fits the background should be used. For this data set, a degree of 4 is the

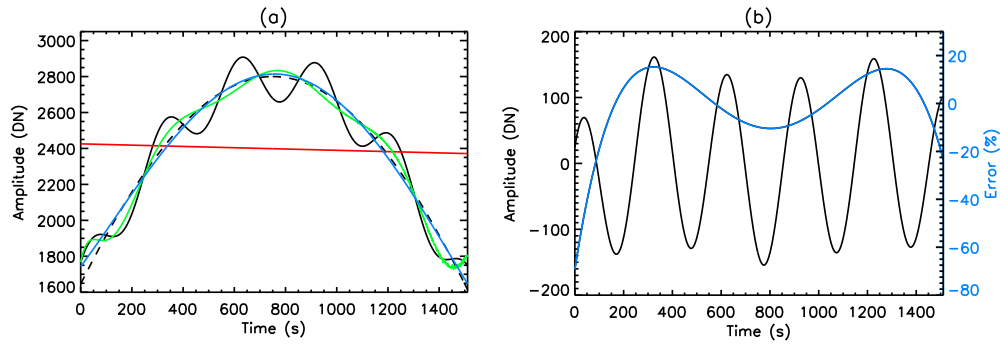


Figure 4.10: Polynomial fitting of the signal in Fig. 4.8(a). (a) signal (black), resulting background with polynomial degree 1 (red), degree 4 (blue) and degree 10 (green) with the analytical background (dashed). (b) resulting oscillation from polynomial degree 4 (black) with the error compared to the analytical solution (blue).

closest fit to the analytical solution, however, without the analytical solution this choice is more difficult as a degree of 2 would be the most likely choice. Fig. 4.10(a) shows the background determined using a fitting degree of 4 (blue) and by a degree of 10 (green). The choice of polynomial degree 4 successfully separates the background and the oscillation as shown in Fig. 4.10(b). A clear periodic oscillation can be seen with a period of around 300 s. The maximum amplitude of the oscillation is around 160, compared to that of 140 for the analytical solution. However, in complete contrast to the original oscillation, the amplitude in Fig. 4.10(b) is not constant, but increases rapidly before then decreasing. This gives the appearance of growth and damping which is simply not present.

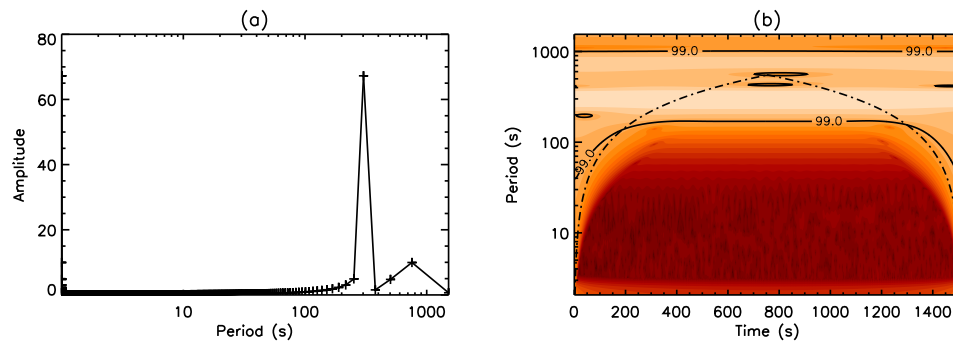


Figure 4.11: (a) FFT and (b) wavelet analysis of the oscillation in Fig. 4.10(b).

The polynomial fitting has produced an oscillation with a periodic error (blue in Fig. 4.10(b)) which is generally less than 15%, but is as large as 70% at the lower boundary. This error (by comparing the positions of the extrema) has a period of around 800 s, hence, this period has been introduced into the oscillation by the polynomial fitting. This is investigated by a FFT and a wavelet analysis.

The FFT of Fig. 4.10(b) is shown in Fig. 4.11(a) and does give a peak at 300 s in agreement with the analytical solution. The larger periods, however, have only been partially removed by the polynomial fitting, with a clear secondary peak at 700 s to 800 s corresponding to the error in Fig. 4.10(b). The peak at 300 s in the FFT is as sharp as that of Fig. 4.9(a), suggesting that the oscillation period has not been affected

by the fitting, as expected from the long periodicity of the error. This is in contrast to the degree 10 result which has a peak at 400 s and all the longer periodicity removed. The wavelet analysis in Fig. 4.11(b) also shows the clear band of 300 s periodicity throughout the time series, however, the period of 700 s to 800 s from the error is above the COI and therefore can not be reliably inferred.

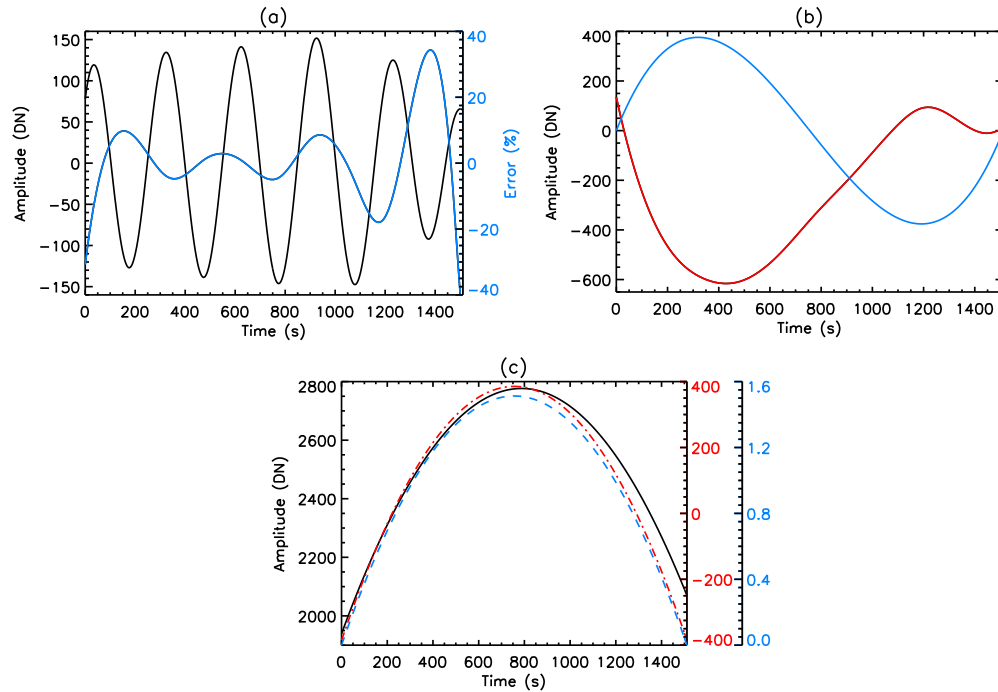


Figure 4.12: EMD of the signal in Fig. 4.8(a). (a) IMF_1 (black) with the error compared to the analytical solution (blue). (b) IMF_2 (red) and IMF_3 (blue). (c) IMF_4 (blue - identical to IMF's 5 to 8), IMF_9 (red) and IMF_{10} (black).

The signal in Fig. 4.8(a) is now analysed using EMD. This process splits the data into close to $\log_2 N$ data sets (Wu et al. (2007)) where N is the number of data points in the time series. Therefore, the EMD produces 10 IMF's with gradually increasing period for this time series of 1512 points and can be reproduced by summing all the IMF's together. The results are shown in Fig. 4.12. The number of IMF's produced depends only on the number of data points and is therefore the same for each time series (with the same number of data points) no matter how simple or complex the signal is. If the time series contains variations on many physical timescales then each IMF will contain a different physically relevant timescale. However, if there are more IMF's than timescales then the components of the signal become extracted over many IMF's, rather than being solely contained in a single IMF. Often the redundant IMF's are simply zero for all time and are therefore ignored (this was the case in the previous section). In addition, some IMF's are identical to each other and can simply be summed together. However, the extraction of the IMF's is not always so simple and it is often difficult to determine which IMF's contain physically relevant information.

IMF_1 has the shortest period (shown in Fig. 4.12(a)) and represents the 300 s period oscillation of Fig. 4.8(b). The EMD has clearly isolated the 300 s period oscillation with amplitude of around 140. The amplitude is not constant, however, particularly at the boundaries where the error is around 40%. Away from the boundaries the amplitude is much closer to 140, although still not constant, but the error is always below

10%. As seen for the polynomial case the error has a periodic nature, this suggests either a slight change in period during the analysis process or a periodic change in the amplitude. Fig. 4.12(b) shows IMF_2 (red) and IMF_3 (blue), both with similar periods of 800 s, which are not present in the original signal. IMF_2 shows evidence of a shorter period after 1000 s, which coincides with a sharp decrease in IMF_1 . This suggests possible timescale mixing between IMF_1 and IMF_2 , where part of the 300 s period oscillation of IMF_1 has been missed near the boundary and extracted into IMF_2 . A fuller discussion of boundary conditions can be found in Section 4.2.4.

The FFT and wavelet analysis of IMF_1 (black) are given in Figs. 4.13(a) and (b), respectively. They show a clear period around 300 s, with the FFT in particular having the same sharp peak as the polynomial degree 4 result, but without the secondary peak. The FFT of IMF_2 (red) and IMF_3 (blue) are also shown in Fig. 4.13(a). Both IMF's have long periods over 800 s, suggesting they may form part of the background. IMF_2 , however, has a small peak at around 400 s (marked by the vertical dashed line in Fig. 4.13(a)), which confirms the presence of a shorter period oscillation. This is most likely part of the original oscillation of Fig. 4.8(b), that has been extracted from IMF_1 into IMF_2 , producing the error in Fig. 4.12(a). This is confirmed by plotting the FFT of the error in Fig. 4.12(a) on Fig. 4.13(a) (green), which shows a small peak at 400 s matching that of IMF_2 . This oscillation in IMF_2 towards the end of time series is outside the COI of the wavelet analysis.

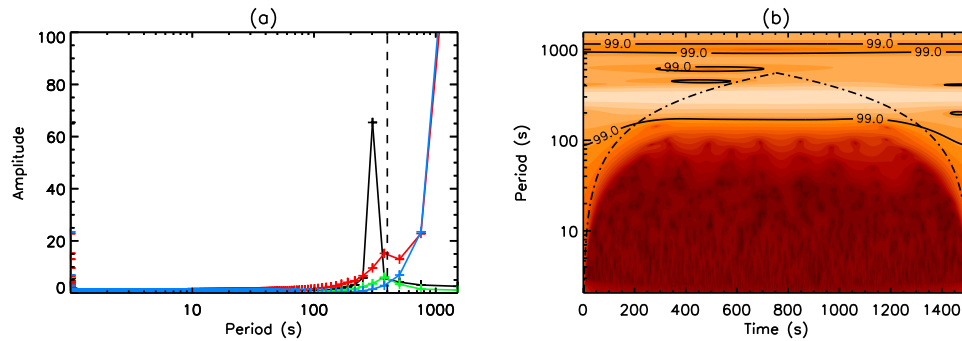


Figure 4.13: (a) FFT of the oscillation in Fig. 4.12(a) (black) and of the red and blue oscillations in Fig. 4.12(b) (red and blue, respectively). The green line shows the FFT of the error in Fig. 4.12(a) with the vertical dashed line at a period of 400 s. (b) wavelet analysis of the oscillation in Fig. 4.12(a).

Fig. 4.12(c) shows IMF's 4 to 10, which all have virtually the same shape, but different amplitudes. IMF's 4 to 8 are all identical and are shown in blue. IMF_9 , shown in red and IMF_{10} in black have much larger amplitudes. These IMF's show no evidence of shorter periods, consequently they can clearly be summed together to make up the total background. It is unclear, however, how IMF_2 and IMF_3 fit with the original background or the oscillation. Fig. 4.14(a) shows the summation of IMF's 4 to 10 in black and IMF's 2 to 10 in red, compared to the analytical background (dashed). It is clear that the inclusion of IMF_2 and IMF_3 produces a far more accurate background fit. This is shown quantitatively in Fig. 4.14(b) where the error of each summation compared to the analytical background is plotted. The error when IMF_2 and IMF_3 are included is always less than 1%, except for close to the boundaries, particularly the upper boundary, but even here the error is less than 3%. The error of the background without the inclusion of IMF_2 and IMF_3 is as large as 15%. The EMD technique successfully separates the oscillation (IMF_1) from the background when the summation of IMF's 2-10 is taken as the background trend. For a real signal the background can

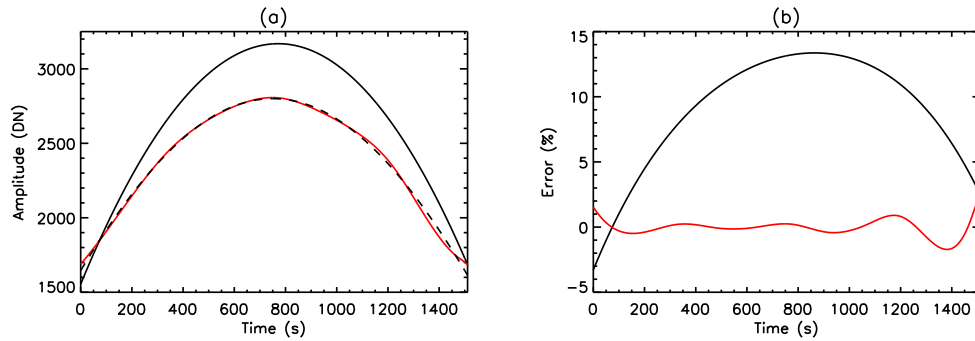


Figure 4.14: Background determined from the EMD. (a) sum of IMF's 4 to 10 (black) and IMF's 2 to 10 (red) with analytical background (dashed). (b) error of the backgrounds in (a) compared to the analytical solution.

be determined by comparing an FFT of the signal with FFT's of the various summations of the IMF's. The IMF's which combine to match the longer periods in the FFT of the signal are then used as the background trend. Using this method, the background trends of real data are found in Chapter 5.

4.2.2 Multiple Oscillations

The complexity of the time series is now increased by adding a second oscillation. Whether the original oscillation can still be identified and separated from the second oscillation and if this oscillation can also be correctly identified is now investigated. The ability of the polynomial fitting and the EMD to determine the correct background is also examined.

4.2.2.1 No Damping

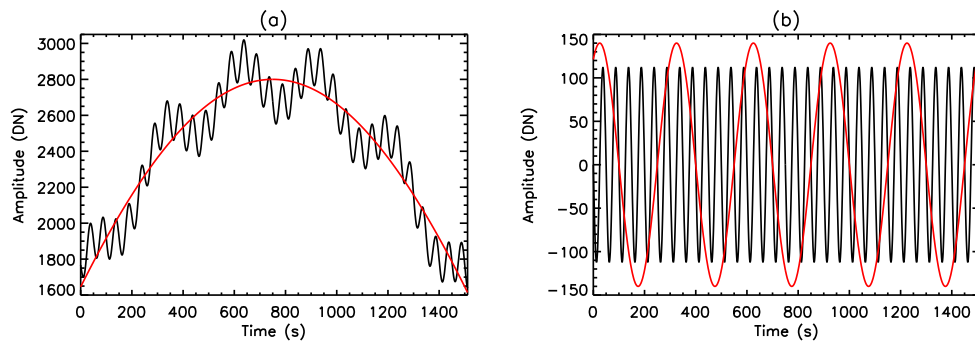


Figure 4.15: (a) signal (black) comprising of a non-constant amplitude background (red) and (b) two un-damped oscillations with periods of 50 s (black) and 300 s (red).

A second, higher frequency oscillation with amplitude 112 and period 50 s is added to the signal in Sec-

tion 4.2.1.2. The time series of two oscillations with a non-constant background is given by,

$$X(t) = Ax_0(t) + Bx_1(t) + Cx_2(t), \quad (4.7)$$

where

$$x_2(t) = \sin\left(\frac{2\pi t}{\tau_2} + \phi_2\right), \quad (4.8)$$

with $C = 112$, $\tau_2 = 50$ s and $\phi_2 = \pi$ and is shown in Fig. 4.15. All the other quantities remain the same as stated in Section 4.2.1.2. Unlike the previous two cases the signal here is not simply an oscillation about the background, but a combination of two oscillations. This makes the determination of the background more difficult, which is essential to accurately separate the two oscillations or the oscillations from the background.

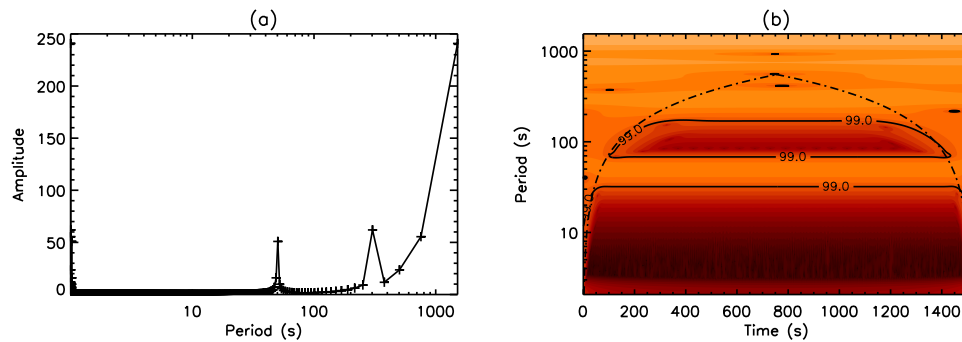


Figure 4.16: (a) FFT and (b) wavelet analysis of the signal in Fig. 4.15(a), with the confidence level (solid) and the COI (dot-dashed).

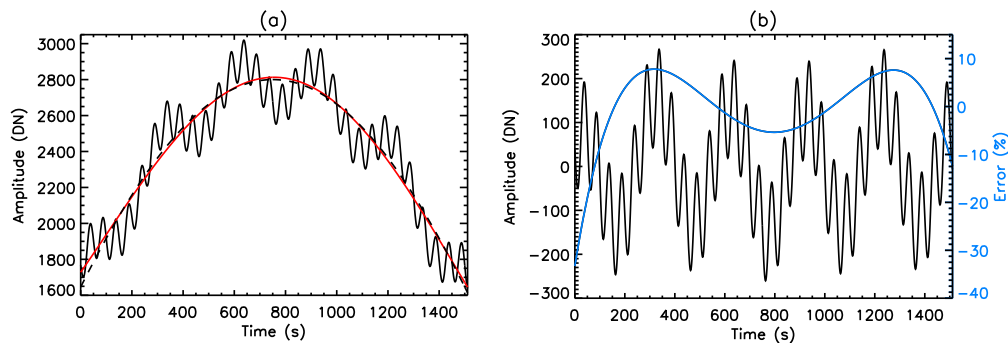


Figure 4.17: Polynomial fitting of the signal in Fig. 4.15(a). (a) signal (black), resulting background from fitting (red) and the analytical background (dashed). (b) resulting oscillation (black) with the error compared to the analytical solution (blue).

The FFT and the wavelet analysis of the signal in Fig. 4.15(a) are shown in Figs. 4.16(a) and (b), respectively. Both the FFT and the wavelet analysis can detect and separate the oscillations and show evidence of the larger period background as seen previously. The precision of the FFT and of the wavelet analysis are similar for the 300 s period oscillation, but the FFT is far superior for the 50 s oscillation, with a much narrower peak than the wavelet analysis. The wavelet analysis gives the period between 30 s to 70 s,

whereas the FFT clearly shows a sharp peak at 50 s. The FFT has more data points at short periods which increases the resolution at 50 s compared to 300 s. This resolution is higher than the wavelet analysis, which sacrifices some frequency resolution for time resolution. However, only the wavelet analysis can confirm that the periodicity is present for all time.

As in the previous section, a polynomial of degree 4 is used, with the results shown in Fig. 4.17. Comparison of the red and dashed black lines in Fig. 4.17(a) shows that the polynomial fit of the background matches the analytical solution well. The resulting oscillation shown in Fig. 4.17(b) has separated the two oscillations from the background, albeit with large errors of up to 30% at the lower boundary, however, the oscillations have not been separated from each other.

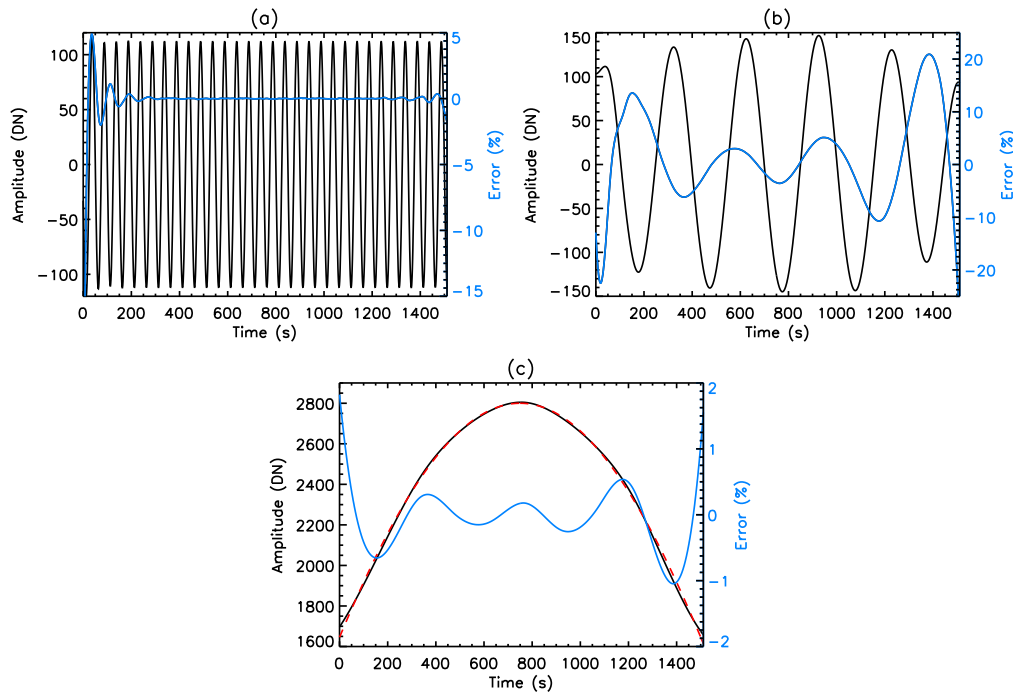


Figure 4.18: EMD of the signal in Fig. 4.15(a) with the error compared to the analytical solution (blue). (a) IMF_1 (black), (b) IMF_2 (black) and (c) background (black) and analytical background (red).

The results of the EMD of the signal in Fig. 4.15(a) are shown in Fig. 4.18. IMF_1 is shown in (a), IMF_2 in (b) and the summation of IMF's 3 to 10 forming the background is shown in (c). Clearly the EMD has successfully separated each oscillation and the background. The errors are generally low, especially away from the boundary, although IMF_2 has errors of up to 20%. The amplitude of IMF_1 (Fig. 4.18(a)) is 112, in agreement with the analytical solution and has a period of around 50 s as expected. IMF_2 (Fig. 4.18(b)) has a period of around 300 s with amplitude of 80 to 140, again with the largest error at the upper boundary. The error of the background (Fig. 4.18(c)), despite being small, appears to be periodic suggesting either the oscillations have not been completely separated or an anomalous oscillation has been introduced. Despite this, the background has been determined intrinsically with an error of less than 2%, even at the boundaries. The high frequency of the 50 s period oscillation increases the EMD accuracy as there are more extrema to fit the splines to compared to the 300 s period case. Unlike the polynomial fitting technique, the EMD can separate multiple oscillations and intrinsically determine the background trend. For a real, observed signal,

it will not necessarily be clear what physical relevance each IMF has and whether, or how, they should be summed.

4.2.2.2 Damping

Many observed oscillations show signs of damping. Here, the ability of the analysis techniques to identify and quantify damped oscillations is investigated. Damping is added to the oscillations considered in the previous section and the time series is given by Eq. (4.7) with,

$$x_1(t) = \sin\left(\frac{2\pi t}{\tau_1} + \phi_1\right) e^{-d_1 t}, \quad (4.9)$$

$$x_2(t) = \sin\left(\frac{2\pi t}{\tau_2} + \phi_2\right) e^{-d_2 t}, \quad (4.10)$$

where the damping coefficients are $d_1 = 0.0005 \text{ s}^{-1}$ and $d_2 = 0.001 \text{ s}^{-1}$. All the other quantities remain the same as stated in Section 4.2.2.1. Fig. 4.19 shows the signal and its components, which, as seen in Fig. 4.19(b), are clearly damped.

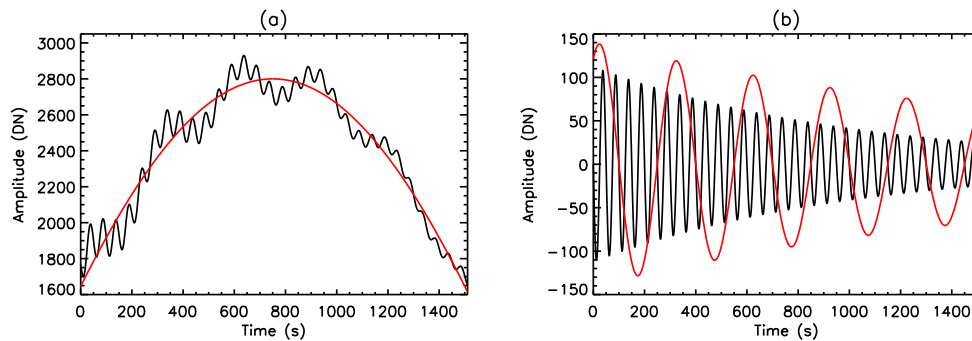


Figure 4.19: (a) signal (black) comprising of a non-constant amplitude background (red) and (b) two damped oscillations with periods of 50 s (black) and 300 s (red).

A FFT and a wavelet analysis of the signal in Fig. 4.19(a) are shown in Fig. 4.20(a) and (b), respectively. The FFT detects both oscillations and the longer period background, as expected from Section 4.2.2.1. By direct comparison with the FFT of the undamped oscillation (Fig. 4.16(a)) evidence of damping can be seen, as the amplitudes of the two peaks in Fig. 4.20(a) are lower than those of Fig. 4.16(a), particularly for the 50 s period oscillation, which has the strongest damping. In theory it should be possible to see the evidence of damping from the FFT in Fig. 4.20(a) alone. The peak of an undamped oscillation with an infinite number of periods has no width (i.e. a delta function). However, when the oscillation is damped the peak of the FFT gains a natural width, no matter how many periods are present. The presence of damping is then easily inferred by the width of the peak. As shown in Fig. 4.2(b), however, a finite number of periods in the oscillation also affects the width of the peak. It is, therefore difficult, without direct comparison to the undamped case to see evidence of damping in Fig. 4.20(a) alone. The wavelet analysis, however, does show clear evidence of damping. The width of the period band around 50 s reduces with time, as the amplitude of the detected oscillation decreases. This is also the case with the 300 s period oscillation, but the lower

damping in this case and the presence of the COI make the narrowing less obvious. A cross section of the wavelet power shows the power decreasing as a function of time (Fig. 4.23(a)).

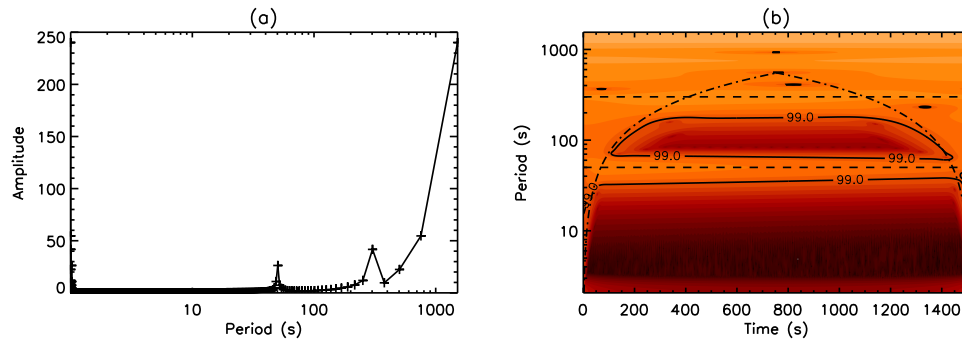


Figure 4.20: (a) FFT and (b) wavelet analysis of the signal in Fig. 4.19(a), with the confidence level (solid) and the COI (dot-dashed).

The results of the polynomial fitting are shown in Fig. 4.21 and as expected from Section 4.2.2.1, the two oscillations have not been separated. Despite this the amplitudes of the oscillations in Fig. 4.21(b), in particular the 50 s period oscillation, can be seen to damp with time.

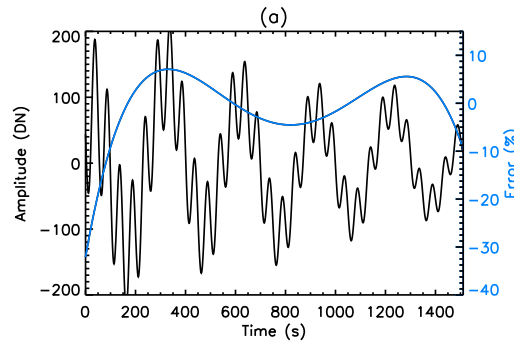


Figure 4.21: Resulting oscillation from subtracting the polynomial fit to the signal in Fig. 4.19(a) with the error compared to the analytical solution (blue).

The results of the EMD are shown in Fig. 4.22, with IMF_1 in (a) and IMF_2 in (b). Figs. 4.22(a) and (b) clearly show that the EMD process has determined two distinct oscillations with the correct periods of 50 s and 300 s, respectively. Both oscillations are clearly damped, with the higher frequency oscillation having the most damping, in agreement with the analytical solution. IMF_1 is very close to the analytical oscillation, except for an error of up to 15% very close to the lower boundary. IMF_2 has larger errors, particularly at both boundaries. The damping is still clear, but the boundary error produces the appearance of growth which is not present in the real oscillation. As seen in the previous case, the EMD accurately determines the background which allows better determination of the oscillations and the periodicities of both IMF_1 and IMF_2 are clear using FFT's and wavelet analyses.

The damping rate can be determined from the wavelet analyses following the method of De Moortel and Hood (2000) and Ireland and De Moortel (2002). The amplitude of the wavelet analysis of IMF_2 is shown in Fig. 4.23(a). From this the damping coefficient (Fig. 4.23(b) dashed) can be calculated by assuming an

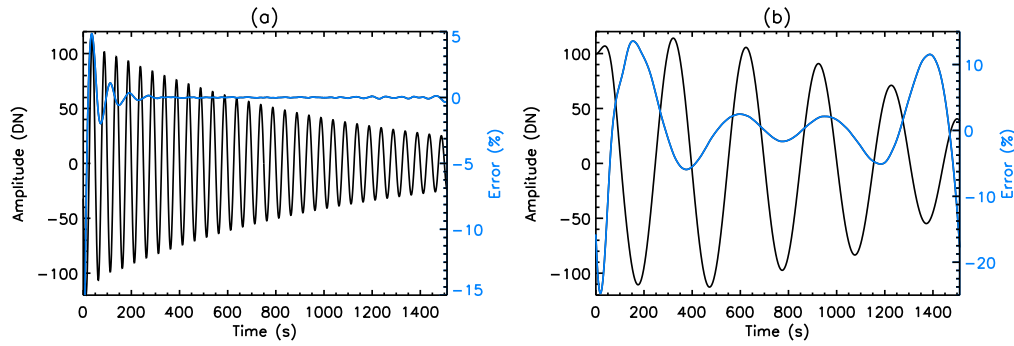


Figure 4.22: EMD of the signal in Fig. 4.19(a) with (a) IMF_1 (black), (b) IMF_2 (black) and the error compared to the analytical solution (blue).

exponential form, $x(t) = De^{-dt}$, where $x(t)$ is the amplitude of Fig. 4.23(a) at time t , D is a constant and d is the damping coefficient. D is calculated using the two points furthest from the boundaries (and therefore furthest from boundary condition errors and edge effects), where the wavelet analysis is assumed to be the most reliable. The damping coefficient is also calculated directly from the extrema of IMF_2 (shown by symbols in Fig. 4.23(b)) by fitting the exponential form defined above. The results of Fig. 4.23(b) are only plotted within the COI with the horizontal dotted line giving the true damping coefficient which is constant for all time.

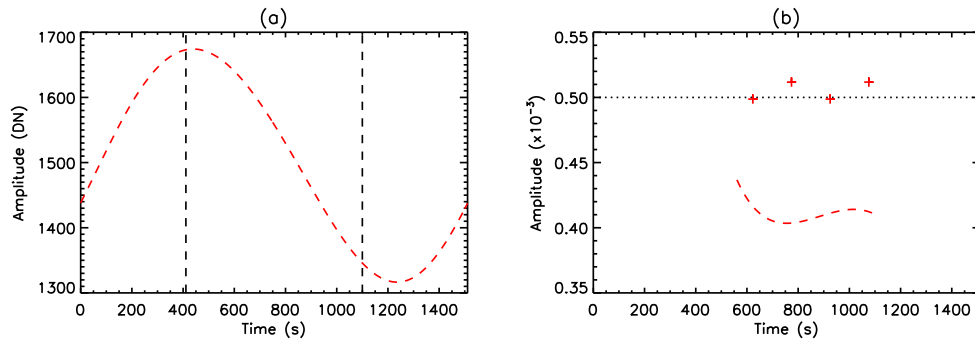


Figure 4.23: Damping of the 300 s period oscillation. (a) amplitude of the wavelet analysis of IMF_2 (logarithmic scale) and (b) damping coefficient calculated from (a) (red) and from the extrema of IMF_2 (symbols), with the analytical value (dotted).

For the 50 s period oscillation the damping coefficients calculated following the method of De Moortel and Hood (2000) are close to the analytical value of $d_2 = 0.001 \text{ s}^{-1}$ (within the COI). Generally the results from the 300 s period oscillation are less accurate due to the larger COI of the wavelet analysis and the boundary errors of the EMD. Despite this, Fig. 4.23(b) gives values of $d = 0.00041 \text{ s}^{-1}$ from the wavelet analysis and $d = 0.000505 \text{ s}^{-1}$ directly from IMF_2 , which agree well with the analytical value of $d_1 = 0.0005 \text{ s}^{-1}$, albeit only at the very centre of the data set. Using this method for the polynomial fitting gives very similar results.

4.2.3 Beat Wave

In Section 4.2.2.2 we showed how two oscillations with different periods can be separated and the periods, amplitudes and damping coefficients determined. The effect of two oscillations with similar periods are now investigated to see if the oscillations can still be resolved and the oscillation properties correctly determined. This depends on the length of the time series and how close together the two periods are. The 50 s period of oscillation of the previous section has been changed to 250 s to produce beating with the 300 s period oscillation and for clarity the non-constant background is replaced with the constant background of Section 4.2.1.1. The time series is given by Eq. (4.7) with, $x_0(t) = 1$ and $\tau_2 = 250$ s and is shown in Fig. 4.24. All the other quantities remain the same as stated in Section 4.2.2.1, including $B = 140$, $C = 112$, $\tau_1 = 300$ s, $\phi_1 = \frac{\pi}{3}$ and $\phi_2 = \pi$. The beat wave produced by the oscillations $x_1(t)$ and $x_2(t)$ is given by,

$$x_b(t) = B x_1(t) + C x_2(t), \quad (4.11)$$

$$= B \sin \Lambda_1 + C \sin \Lambda_2, \quad (4.12)$$

$$= B (\sin \Lambda_1 + \sin \Lambda_2) + (C - B) \sin \Lambda_2, \quad (4.13)$$

where

$$\Lambda_1 = \frac{2\pi t}{\tau_1} + \phi_1, \quad (4.14)$$

$$\Lambda_2 = \frac{2\pi t}{\tau_2} + \phi_2. \quad (4.15)$$

Using,

$$\sin \Lambda_1 + \sin \Lambda_2 = 2 \sin \left(\frac{\Lambda_1 + \Lambda_2}{2} \right) \cos \left(\frac{\Lambda_1 - \Lambda_2}{2} \right), \quad (4.16)$$

Eq. (4.13) becomes,

$$x_b(t) = 2B \sin \left(\frac{\Lambda_1 + \Lambda_2}{2} \right) \cos \left(\frac{\Lambda_1 - \Lambda_2}{2} \right) + (C - B) \sin \Lambda_2, \quad (4.17)$$

and is shown in blue in Fig. 4.24(b).

The FFT and the wavelet analysis of the signal in Fig. 4.24(a) are shown in Figs. 4.25(a) and (b), respectively. In contrast to Fig. 4.16(a), the FFT in Fig. 4.25(a) (black) has only one peak instead of two. This peak covers periods from 200 s to 400 s, with a maximum amplitude from 250 s to 300 s matching the analytical solution. The two periods cannot be separated and therefore without prior knowledge it could not be determined that two oscillations exist. If the oscillations have lower periods, where the FFT has greater resolution, separation is possible. The red line of Fig. 4.25(a) shows the FFT when the oscillations have periods of 150 s and 200 s, which are partially resolved. When the period is even lower (75 s and 100 s) the two oscillations can be completely separated, as shown by the green line. The wavelet analysis, which as seen earlier cannot resolve periods as well as the FFT, appears to show only one oscillation, with a period of 180 s to 400 s.

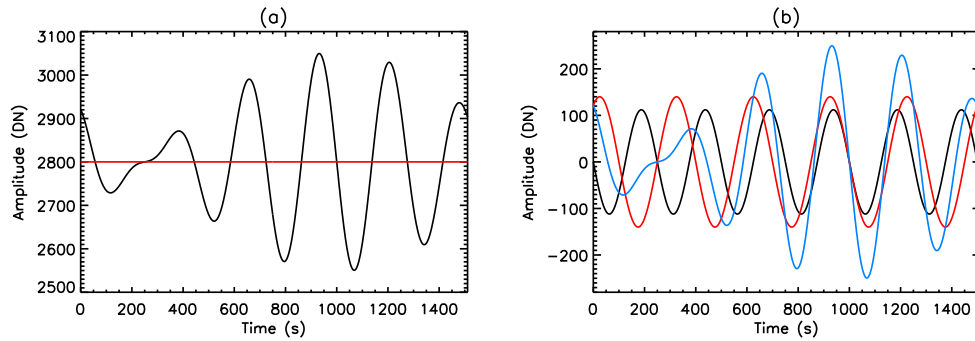


Figure 4.24: (a) signal (black) comprising of a constant amplitude background (red) and (b) two undamped oscillations with periods of 250 s (black) and 300 s (red) with the beat wave (blue).

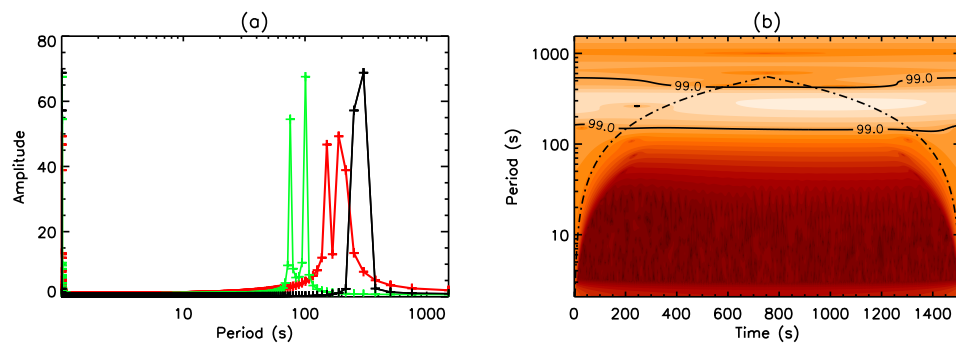


Figure 4.25: (a) FFT and (b) wavelet analysis of the signal in Fig. 4.24(a), with the confidence level (solid) and the COI (dot-dashed). (a) also shows the FFT's of signals with oscillation periods of 150 s and 200 s (red) and 100 s and 75 s (green).

The resulting oscillation from a linear polynomial fitting is shown in Fig. 4.26(a) (black), with the results from the EMD (IMF_1) shown in Fig. 4.26(b) (black). Neither technique can separate the two oscillations and hence both results produce a single oscillation. However, the shape of the oscillations appear as a wave packet, giving the suggestion of beating or multiple timescales. On the other hand, this wave packet shape could be interpreted as a single quasi-periodic oscillation and consequently, it is difficult to draw confident conclusions from this result. The error of IMF_1 is generally below 5% of the analytical beat wave, except for the first third of the data set and close to the upper boundary. This is likely to be a result of the boundary conditions and the increased distance between the extrema of the beat wave at around 300 s (as seen in Fig. 4.24(b)) due to the destructive interference of the two oscillations.

The damping coefficients of $d_1 = 0.0005 \text{ s}^{-1}$ and $d_2 = 0.001 \text{ s}^{-1}$ are added to the oscillations in Fig. 4.24 to make a new signal. The resulting oscillations are shown in red in Fig. 4.26. For both the polynomial fitting and the EMD, damping is clear when compared to the undamped black lines, however, the shape is very similar and the presence of damping is again difficult to determine without direct comparison.

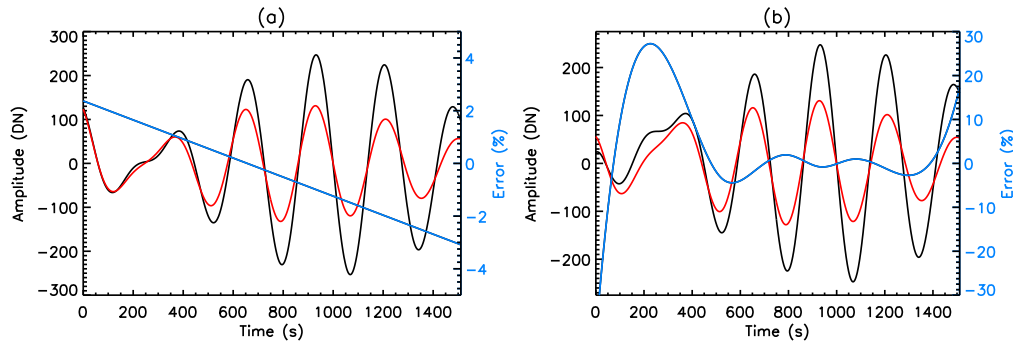


Figure 4.26: Resulting oscillation (black) from the signal in Fig. 4.24(a) using (a) linear polynomial fitting and (b) EMD (IMF_1). The error compared to the analytical beat wave (blue) and the result with damping (red) are also shown.

4.2.4 EMD Boundary Conditions

The boundary conditions for the spline fitting of the EMD are examined for the case of two damped oscillations with beating and a non-constant background. The idea of extending a data set to give boundary conditions for EMD was proposed by Huang et al. (1998), whereas Huang and Wu (2008) and Wu and Huang (2009) suggest boundary conditions can be found without extending the data. Three different boundary conditions are compared, free, extended and linear fit. The linear fit boundary conditions (from Wu and Huang (2009)) are explained in Section 4.2.1.1 and used in all other sections. The free boundary conditions only fix the splines at the extrema, however, both the linear fit and the extended boundary conditions fix the splines to a certain value at each boundary. For the extended boundary conditions (similar to Huang et al. (1998)) the data set is extended at each boundary for three minima and three maxima (by reflecting the data set about each boundary). The splines are then fitted to the extrema of the new data set, as shown in Fig. 4.27(a). The blue and red lines show the splines fitted to the maxima and minima, respectively.

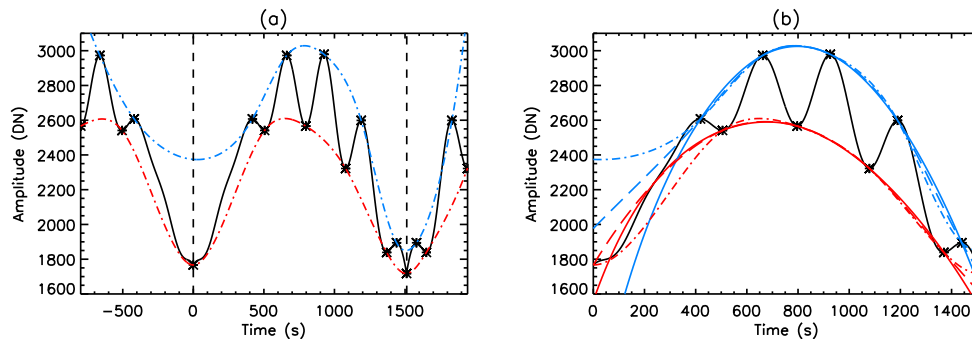


Figure 4.27: Spline fitting of the extrema for the EMD. (a) extension of the data set with spline fitting for the extended boundary conditions. (b) fitting of the extrema with free (solid), extended (dot-dashed) and linear fit (dashed) boundary conditions. The positions of the extrema to which the splines are fitted are shown by the stars and the splines fitted to the maxima and minima are shown in blue and red, respectively.

Fig. 4.27(b) shows the spline fitting to the maxima (blue) and minima (red) for each of the three boundary conditions at the first time of fitting. The splines are repeatedly fitted to the data throughout the sifting

process for each IMF. The free boundary conditions are shown by solid lines, extended by dot-dashed and linear fit by dashed with the stars showing the extrema to which the splines are fitted. For shorter periods of oscillation the extrema are more likely to be near the boundaries and hence the end of the splines are better constrained. All three methods give very similar spline fittings in the centre of the time series (Fig. 4.27(b)) and are also quite similar at the upper boundary ($t = 1512$ s) where there are extrema close to the boundary. The difference in the splines produced by the different boundary conditions is much greater at the lower boundary ($t = 0$ s) where there are no extrema nearby. Here the free boundary conditions are clearly inappropriate as the maximum spline actually has a lower value than that of the minimum spline for a fifth of the data set. The extended boundary conditions have the opposite problem, in that the maximum spline is far too high. This is a consequence of the lack of a maximum near the boundary in the extended data set of Fig. 4.27(a), resulting in the spline missing the sharp decrease in amplitude near this boundary. In contrast, the linear fit splines remain close to the amplitude of the data at the lower boundary, albeit slightly too high, underestimating the sharp decrease in amplitude at that boundary.

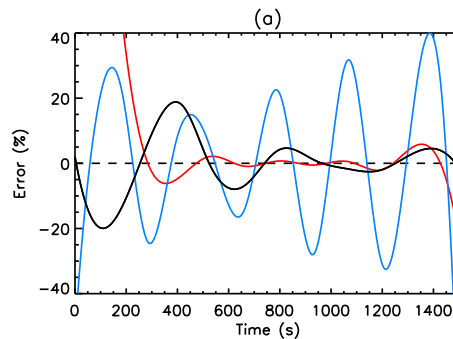


Figure 4.28: Error of IMF_1 compared to the analytical solution using free (red), extended (blue) and linear fit (black) boundary conditions.

Fig. 4.28 shows the error of the EMD in determining the damped beat wave oscillation for each of the three boundary conditions compared to the analytical solution. The red line of the free boundary conditions gives the smallest error for most of the data set, of below 5%, with the linear fit (black) conditions giving similar but generally slightly larger errors. The extended (blue) boundary conditions are generally the worst with error around 20% and rising to over 40% at the boundaries. This is a consequence of the maximum spline being too high, as mentioned above. Despite low error throughout the centre of the data set the free boundary conditions give an error of over 20% at the upper boundary and over 100% at the lower boundary, which is expected as the maximum spline has a lower amplitude than the minimum spline at the lower boundary. The error of the linear fit conditions is always below 20%, even at the left boundary, hence it is the clear choice for this case.

Every data set is different and each set of boundary conditions have advantages and disadvantages. Each of these three boundary conditions is the most suitable for a particular shape of data, however, the linear fit conditions are always robust in avoiding the large errors seen in Fig. 4.28 and is often the most accurate solution. The spline fitting is repeated many times for each IMF and so a different boundary condition may be best for each fitting. In this case the choice of boundary conditions becomes very arbitrary and difficult to draw comparison from, consequently the linear fit conditions are always used.

All three results show periodic errors, with similar, but clearly different periods, suggesting care must be taken when identifying oscillations in order to rule out anomalous results. More work is required to improve the boundary conditions and reduce the end effects of the spline fitting in order to increase the accuracy of the EMD results and in particular reduce periodic errors. In general, however, most data sets are well treated by the spline fitting and the errors are far reduced from those seen here. This data set was chosen to highlight problems with the boundary conditions due to its shape and the low number of extrema near the boundaries. Constraining the ends of the splines is also improved by using the EEMD technique, which is discussed in Section 4.2.5.1.

4.2.5 Time Dependent Oscillation

The previous two sections have investigated oscillations that were constant or damped for all time. Here a signal including an oscillation that only exists for a short duration is examined. This replicates the situation where a physical process changes the oscillation or the oscillation is only present for part of the data set.

The time series for a constant background with an undamped oscillation present for all time and a time dependent oscillation which only exists for a short duration is given by,

$$X(t) = A + B x_1(t) + C x_2(t), \quad (4.18)$$

where

$$x_1(t) = \sin(\alpha t), \quad (4.19)$$

$$x_2(t) = \sin(\beta t) e^{-((t-\tau)^2/\sigma)}, \quad (4.20)$$

with $A = 20$, $B = 1$, $C = 0.04$, $\alpha = 160\pi$, $\beta = 3200\pi$, $\sigma = 10^{-6}$ and $\tau = t_{max}/2$, where t_{max} is the length of the time series (Zhang et al. 2010). 1000 data points are used. Zhang et al. (2010) use this time series to investigate the effects of EEMD, which we will also study (Section 4.2.5.1.) and compare to the EMD results of this section. Therefore, we use the same time series as Zhang et al. (2010) in order to ensure consistency with their EEMD results. However, we add a constant background of $A = 20$ in order to make $x_1(t)$ an oscillation of 5% of the background amplitude. Fig. 4.29 shows the signal and its components.

Fig. 4.30 shows the FFT and the wavelet analysis of the signal in Fig. 4.29(a). The blue line in Fig. 4.30(a) clearly shows a peak at a period of 0.0125, matching that of the oscillation shown in blue in Fig. 4.29(b), however, there is no evidence of a shorter period oscillation. This can only be seen by plotting the FFT on a smaller scale, but a period of 0.000625 is then evident (black line in Fig. 4.30(a)). The FFT can detect the low period oscillation, despite its low amplitude, however from the FFT it is impossible to see the time dependent nature of the oscillation. The wavelet analysis (Fig. 4.30(b)) also shows the 0.0125 period oscillation throughout the signal, however, it is beyond the COI and therefore cannot be trusted without other evidence, for example the FFT. The short period oscillation can also be seen in the wavelet analysis, but is below the 99% confidence level due to the short amplitude of the oscillation. Despite this, the wavelet analysis correctly shows that the oscillation only exists for a short period of time in the middle of the signal from 0.01 to 0.015. This can be seen more clearly in Fig. 4.30(c) which shows the cut along the dashed

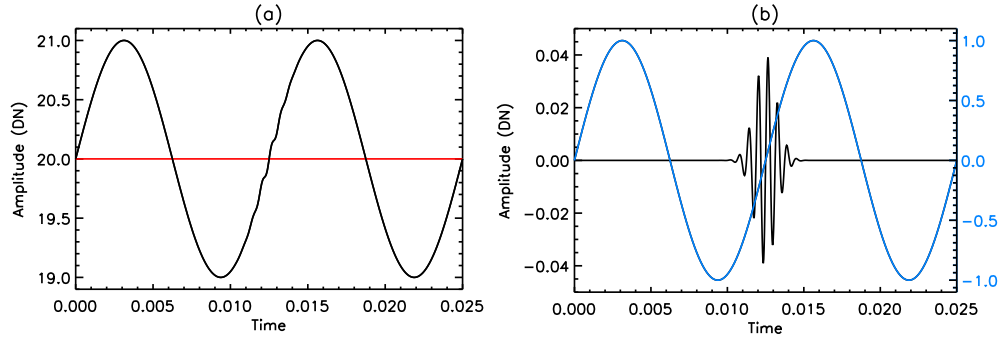


Figure 4.29: (a) signal (black) comprising of a constant amplitude background (red) and (b) two oscillations which are present for all (blue) and part (black) of the time series.

line of the wavelet analysis in Fig. 4.30(b). This clearly demonstrates the use of wavelet analysis, however, drawing reliable conclusions from these results below the confidence level with real data is unlikely. The ability of wavelet analysis to identify time dependent oscillations is discussed further in De Moortel et al. (2004b). Neither the polynomial fitting or the EMD (as found in Zhang et al. 2010) can separate these two oscillations, however the EMD does accurately determine the constant background.

4.2.5.1 Ensemble Empirical Mode Decomposition

As discussed above, the EMD technique cannot separate some oscillations with very low amplitudes, which can lead to mode mixing where the same IMF contains variations with two distinct timescales. The technique of EEMD was proposed by Wu and Huang (2009) as an extension of EMD in order to eliminate the problem of mode mixing. White noise of finite amplitude is added to the time series to make a noisy signal, although the correct determination of the noise amplitude is difficult, as discussed later. This process is repeated n times with different random white noise added to the original signal each time, resulting in an ensemble of n noisy time series, each consisting of the original signal plus random white noise. The EMD process is then applied to each of the n time series individually and IMF's are obtained. This results in n number of IMF_1 's and n number of IMF_2 's, etc, all of which are noisy. The final IMF's are given by the ensemble mean, for example, $IMF_1 = \frac{1}{n} \sum_{i=1}^n IMF_{1i}$. If the ensemble number, n , is sufficiently high then the white noise cancels and only the original signal remains.

The added noise creates reference scales and acts as a filter allowing the EEMD method to eliminate or seriously reduce the mode mixing (Wu and Huang 2009). The noise also produces lots of extrema to which the splines are fitted, consequently, the ends of the splines are far better constrained than without the noise. Wu and Huang (2009) used a noise amplitude of $n_{amp} = 0.1 \times SD$, where SD is the standard deviation of the original signal. However, Zhang et al. (2010) investigated the effects of the noise amplitude on the EEMD results and found that n_{amp} should be defined using the signal to noise ratio, SNR ,

$$SNR = 10 \log_{10} \left(\frac{P_s}{P_n} \right), \quad (4.21)$$

where P_s is the power of the original signal and P_n is the power of the noise ($P_n = n_{amp}^2$). Eq. (4.21) is

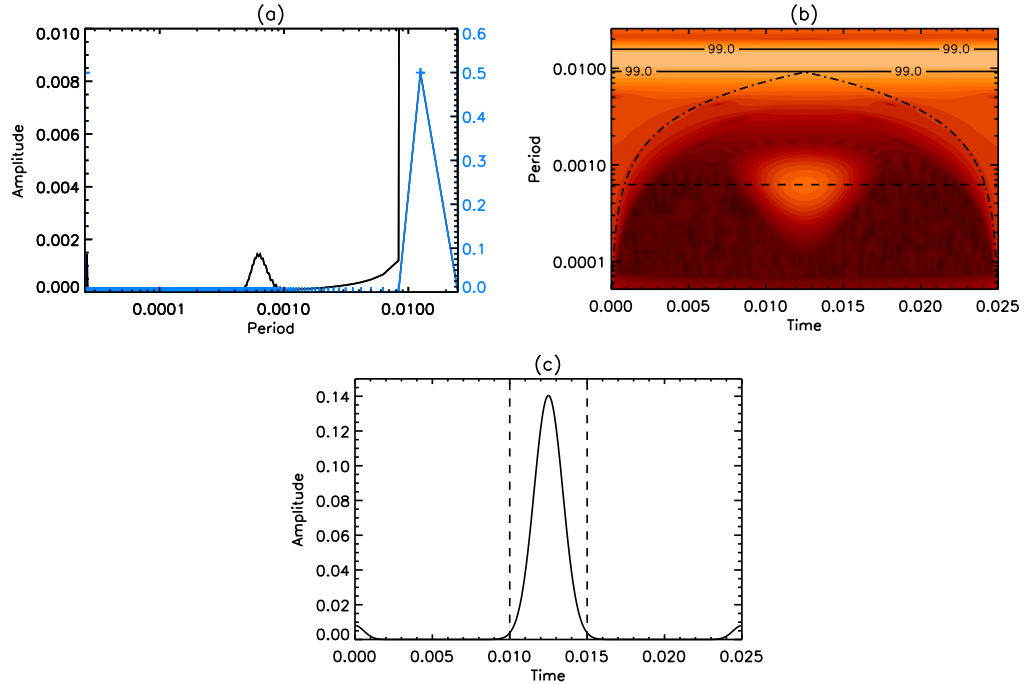


Figure 4.30: (a) FFT (plotted on two different amplitude scales) and (b) wavelet analysis of the signal in Fig. 4.29(a) with the confidence level (solid) and the COI (dot-dashed), with (c) a cut along the dashed line of (b).

rearranged to give the noise amplitude,

$$n_{amp} = \sqrt{\frac{P_s}{10^{SNR/10}}}, \quad (4.22)$$

which is calculated after a signal to noise ratio is chosen (consistent with Zhang et al. 2010).

The same EMD/EEMD code (from Wu and Huang 2009) used for the EMD results above is used here by setting $n \neq 1$ and $n_{amp} \neq 0$. The results for the EEMD of the signal in Fig. 4.29(a) are shown in Fig. 4.31. The signal to noise ratio is chosen to be 85 (giving $n_{amp} = 0.001$) and the ensemble number 100, the choice of which is discussed below. Fig. 4.31(a) shows IMF_1 in black and IMF_2 in blue with the analytical solutions in red. The EEMD clearly separates the constant period oscillation from the time dependent oscillation and the background. This is a big advantage over the EMD technique and the polynomial fitting method, neither of which could separate the oscillations. The error in determining the background is also small.

This demonstrates the potential of EEMD, however, the choice of the signal to noise ratio and the ensemble number used is rather arbitrary and the results are very sensitive to these choices. The main uncertainty is with the correct choice of the signal to noise ratio. With the right value, EEMD can correctly separate even small, short lived oscillations. However, if the signal to noise is too high then the noise introduced is too low and the separation of the modes and the EEMD results are no better than those of EMD. This is demonstrated in Fig. 4.32, with a signal to noise ratio of 115 ($n_{amp} = 3.6 \times 10^{-5}$) and the same ensemble

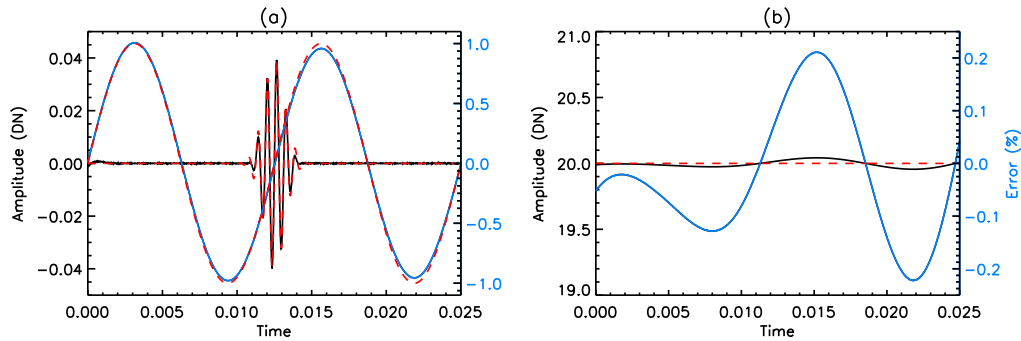


Figure 4.31: EEMD of the signal in Fig. 4.29(a) with a signal to noise ratio of 85 and an ensemble number of 100. (a) IMF_1 (black) and IMF_2 (blue) with the analytical oscillations (red). (b) resulting background (black) and analytical background (red) with the error compared to the analytical solution (blue).

number of 100. By changing only the signal to noise ratio the results of Fig. 4.31(a) have become the same as those of the EMD (shown in Fig. 4.32 by symbols) where the two oscillations cannot be separated.

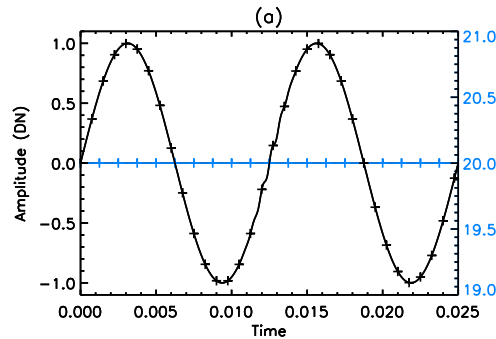


Figure 4.32: EEMD of the signal in Fig. 4.29(a) with a signal to noise ratio of 115 and an ensemble number of 100, with the resulting oscillation (black) and the background (blue). The EMD results are shown by the symbols.

In addition, a signal to noise ratio that is too low can also cause problems. In this case the noise level is too high and the noise introduced cannot be completely separated from the signal being analysed. This is demonstrated by the results in Fig. 4.33 where the ensemble number is again 100, but the signal to noise ratio is now 40 ($n_{amp} = 0.2$). The EEMD has determined the background (Fig. 4.33(d)), with a very low error, in addition to the longer period oscillation (Fig. 4.33(c)), although the error here is more noisy than that seen previously. The time dependent signal, however, is visible (Fig. 4.33(b)) but is heavily masked by noise and could no longer be determined above a reliable confidence level. In addition to these IMF's there is also an IMF consisting entirely of noise (Fig. 4.33(a)), all of which is artificial.

The appropriate summing of the individual IMF's is also less clear in this case. In Fig. 4.31 the two oscillations are given by IMF_1 and IMF_2 , with all the rest summed together to make the background, which is consistent with our treatment of the EMD results throughout this chapter. In contrast, however, in Fig. 4.33 IMF_1 and IMF_2 are summed together to make (a), IMF_3 and IMF_4 are summed for (b), IMF's 5 to 7 for (c) and IMF_8 and IMF_9 for the background in (d). Without the analytical solution, which would

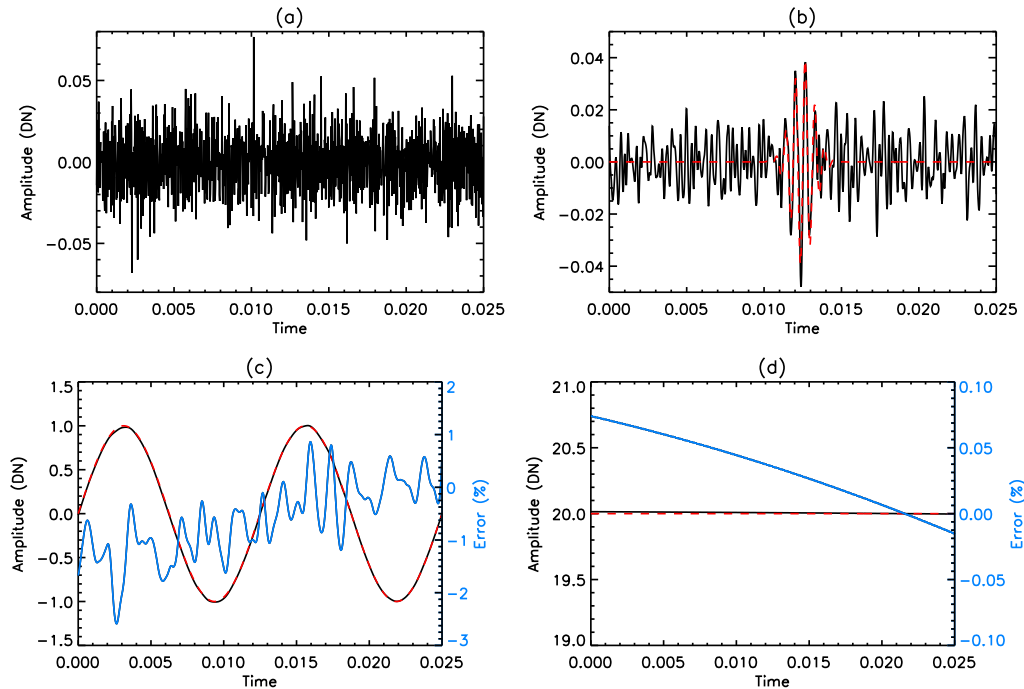


Figure 4.33: EEMD of the signal in Fig. 4.29(a) with a signal to noise ratio of 40 and an ensemble number of 100. (a) IMF_1 and (b) IMF_2 with the time dependent oscillation (red). (c) IMF_3 (black) and the longer period oscillation (red) and (d) the resulting background (black) and the analytical background (red). In (c) and (d) the error compared to the analytical solution is shown (blue).

not exist for real data, it is difficult to know how to reliably sum the IMF's together, or how to interpret each one individually.

The ensemble number must also be chosen, however, this solution is much simpler than that of the signal to noise ratio. The white noise is removed by averaging each IMF over the ensemble, consequently, the greater the ensemble number the greater the averaging of the noise, hence the better the removal of that noise. Therefore, the ensemble number should be as large as possible. The results of Fig. 4.31 ($SNR = 85$ and $n = 100$) are repeated varying the value of the ensemble number. The correlation coefficients between IMF_1 and the analytical solution are shown in Fig. 4.34. The correlation between the EEMD and the analytical solution is above 99% when the ensemble number is greater than 20. This threshold may vary for different cases, but a value of 100 is likely to always be high enough, as suggested by Zhang et al. (2010).

The maximum amplitude of the time dependent oscillation in Fig. 4.29(b) of 0.04 ($C = 0.04$) is unlikely to be detectable through real observations. By increasing the amplitude to just 0.075 ($C = 0.075$), which is still less than 0.5% of the background, the EMD can separate the time dependent oscillation from the longer period oscillation. Fig. 4.35(a) shows the new signal (black) with the increased amplitude time dependent oscillation (blue). IMF_1 and IMF_2 from the EMD of the signal in Fig. 4.35(a) are shown in Fig. 4.35(b), with the two oscillations clearly separated. This result shows that the EMD process is capable of reliably analysing the more realistic case of Fig. 4.35(a). Therefore, due to the simpler nature of the EMD and the difficult choice of a signal to noise ratio for the EEMD, the EMD process is preferred.

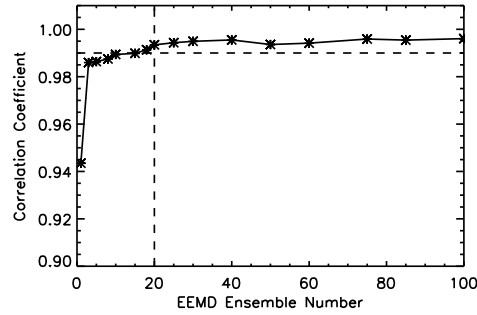


Figure 4.34: Correlation of EEMD IMF_1 with the analytical solution for varying ensemble numbers and a signal to noise ratio of 85.

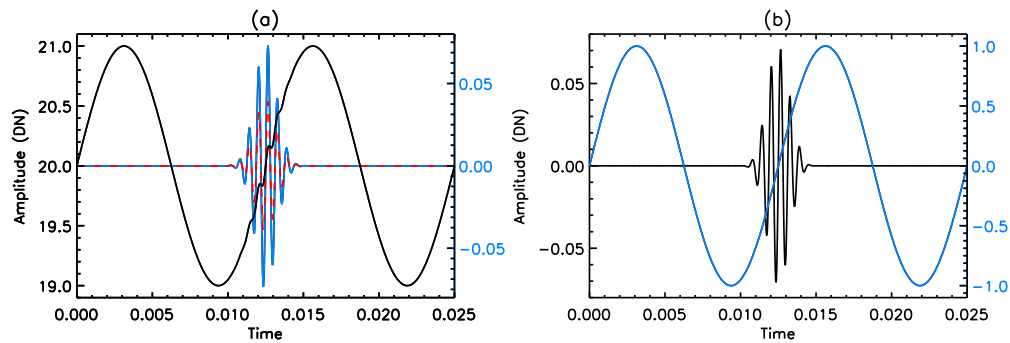


Figure 4.35: Signal with increased amplitude of the time dependent oscillation ($C = 0.075$ compared to $C = 0.04$ previously). (a) signal (black) with the time dependent oscillation (blue) and the previous oscillation (red). (b) EMD of the signal in (a) with IMF_1 (black) and IMF_2 (blue).

4.2.6 Reduced Cadence

As discussed in Section 4.2.1.1, for a real finite signal length there is an inherent uncertainty in the ability of the FFT and the wavelet analysis to determine the period of an oscillation, even when the signal is well resolved. Real observations are unlikely to be so well resolved. Therefore, the sampling rate is reduced and the effects of a longer more realistic cadence are investigated.

4.2.6.1 Single Oscillation

The cadence of the data in Fig. 4.8 is reduced from 1 s to 56 s to be comparable to the cadence of the temporally averaged TRACE data in Chapter 5 and is shown in Fig. 4.36. The FFT and the wavelet analysis of the signal in Fig. 4.36(a) are shown in Figs. 4.37(a) and (b), respectively. The reduced cadence has had little effect on the FFT resolving the 300 s period oscillation, as shown by the peak in Fig. 4.37(a). The same is seen for the wavelet analysis, although, note the change in the period scale compared to all previous wavelet analyses. The reduced cadence, however, has affected the ability of the FFT to detect lower period oscillations. Comparing the reduced cadence (black) with the high cadence (red) case in Fig. 4.37(a), it is clear that the FFT's differ below periods of 100 s. The low cadence FFT has a peak at around 69 s which was

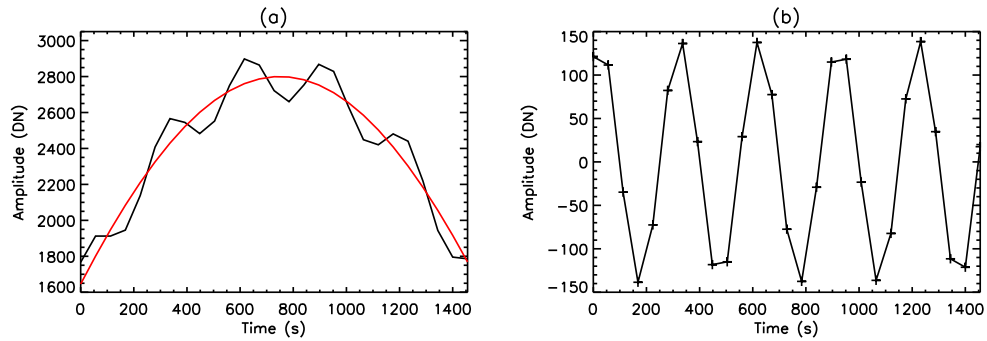


Figure 4.36: (a) signal (black) comprising of a non-constant amplitude background (red) and (b) an undamped oscillation with a period of 300 s, sampled at 56 second intervals.

not previously seen. This is a result of the FFT identifying periodicity due to the sampling interval of 56 s. By comparing the FFT period with the sampling interval such anomalies are easily discounted. The wavelet analysis, however, simply does not calculate results below periods twice that of the sampling interval, i.e. 112 s, as shown by the white space on Fig. 4.37(b) between periods of 100 s and 112 s. In this way errors at low periods due to the sampling rate are avoided. For the 300 s period, the results of the FFT and wavelet analysis are virtually unaffected and a 56 s cadence would be enough to allow confident detection. The reduction in cadence has only had a small effect on both the polynomial and the EMD results.

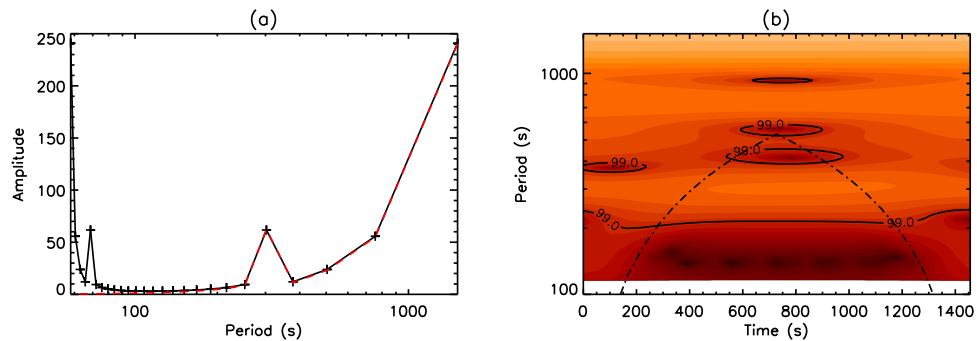


Figure 4.37: (a) FFT and (b) wavelet analysis of the signal in Fig. 4.36(a), with the confidence level (solid) and the COI (dot-dashed). (a) also shows the FFT of the high cadence signal from Fig. 4.9(a) (red).

4.2.6.2 Multiple Oscillations

A signal with the 50 s and 300 s period oscillations of Section 4.2.2.1 and the constant background of Section 4.2.1.1 is now reduced to a 56 s cadence and analysed. A 56 s sampling rate obviously cannot resolve a 50 s period oscillation, therefore, aliasing occurs. This can be seen in Fig. 4.38(b) where the red line of the 50 s period oscillation appears to have a greater period than that of the 300 s period (black). For clarity, the red line in Fig. 4.38(b) is always referred to as the 50 s period oscillation even though it has been aliased to a different period.

As shown in the previous section, the 300 s period is relatively unaffected by the lower sampling rate. The

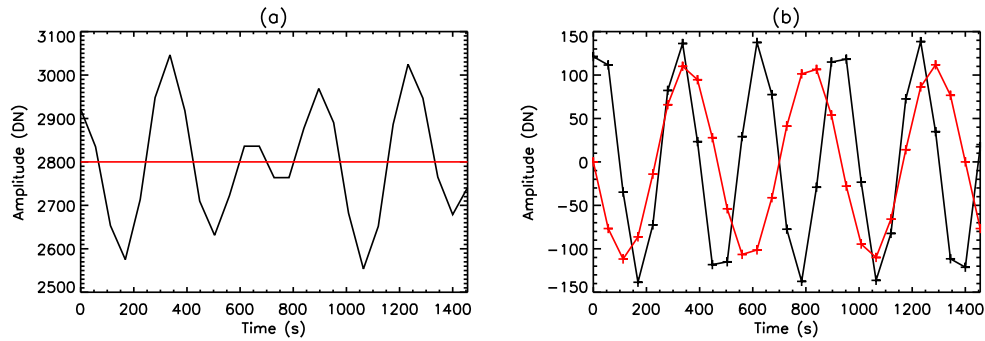


Figure 4.38: (a) signal (black) comprising of a constant amplitude background (red) and (b) two undamped oscillations with periods of 50 s (red) and 300 s (black), sampled at 56 second intervals.

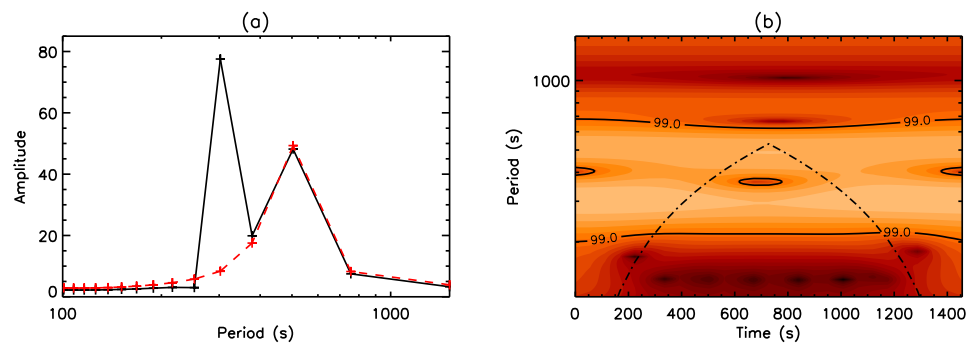


Figure 4.39: (a) FFT and (b) wavelet analysis of the signal in Fig. 4.38(a), with the confidence level (solid) and the COI (dot-dashed). (a) also shows the FFT of the red line in Fig. 4.38(b) (red).

aliasing, however, has resulted in a 500 s period oscillation. The FFT of the signal in Fig. 4.38(a) (shown in black in Fig. 4.39(a)), shows peaks at 300 s period and at 500 s. The red line in Fig. 4.39(a) gives the FFT of just the 50 s period oscillation (red line in Fig. 4.38(b)), which confirms that the lower sampling rate has produced a 500 s period oscillation. However, this is only possible using the analytical solution. The FFT is only plotted for periods above 100 s in order to avoid anomalous peaks at low periods produced by the lower sampling rate. The wavelet analysis in Fig. 4.39(b) finds periodicity at all periods between 200 s and 700 s, however, two slightly higher bands at 300 s and 500 s are dominant. However, the amplitude at 300 s period appears to decrease and then increase again with time, as shown by the slight darkening at time of 700s. The extrema of the full cadence oscillation have constant amplitude, whereas the magnitudes of the minimum at 500 s and the maximum at 900s of the black line in Fig. 4.38(b) have been reduced. This may account for the change in the amplitude of the wavelet analysis.

The danger of aliasing is that it leads to the interpretation that the 50 s period oscillation is actually a 500 s period oscillation, which is then used to incorrectly interpret physical mechanisms or parameters. It is only possible to be confident about periods if analysed with two different cadences, i.e. two different instruments. Once aliasing has occurred nothing can be done to retrieve the 50 s period. All that can be investigated is the ability of the analysis techniques to separate the 300 s period oscillation and the 500 s period and see whether the 500 s period oscillation would be interpreted as a real oscillation.

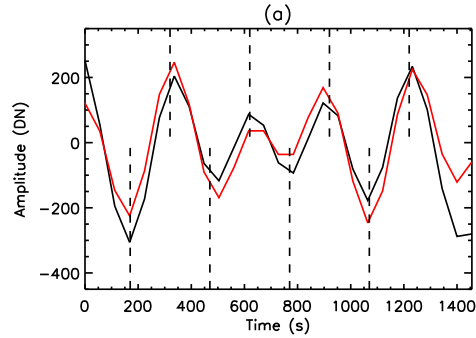


Figure 4.40: EMD of the signal in Fig. 4.38(a). IMF_1 (black) with the analytical solution (red). The vertical dashed lines are 150 s apart.

IMF_1 from the EMD is shown in Fig. 4.40, with the analytical summation of both oscillations given in red. The EMD cannot separate the two oscillations and can only reliably detect the 300 s period oscillation. However, using an FFT and wavelet analysis, IMF_1 strongly suggests the presence of another oscillation with a period of 500 s to 700 s.

4.3 Data Analysis Conclusions

The use of several techniques to identify and determine the properties of oscillations in a range of time series has been investigated. Fourier and wavelet analysis were both used to determine the frequencies present in the time series, whilst polynomial fitting and EMD were used to determine the background trends and separate the oscillations from these trends, thus allowing the properties of the oscillations to be seen more clearly. The use of each technique was initially demonstrated for a single oscillation about a constant background. The complexity of the signal was then increased by adding a non-constant background and multiple oscillations. The effects of damping, wave beating and a reduced cadence were also investigated in addition to an oscillation which is only present for part of the time series.

The FFT was found to be very accurate at identifying the periods present in the time series, particularly at low period. The accuracy of the period determined by the FFT depends on the duration and cadence of the time series and the oscillation period. Despite relatively short time series, the FFT determined the peaks accurately and generally showed distinct peaks for each oscillation. However, this was not possible for the background trend as the time series was too short compared to the period of the background. The FFT was not capable of determining two distinct periods of oscillation when beating occurred between the 250 s and 300 s period oscillations in a 1500 s time series. However, when these periods were decreased the increased resolution of the FFT made possible a partial separation for periods around 150 s and a complete separation for periods of around 100 s. The periods determined by the wavelet analysis are always consistent with those from the FFT, giving confidence in the results. The period resolution of the wavelet analysis at short periods is particularly reduced compared to the FFT and the COI is very restrictive for longer periods. However, the time resolution given by the wavelet analysis gives information that cannot be determined from the FFT alone. Despite the low amplitude of the time dependent oscillation examined, the wavelet

analysis determined the duration of the oscillation very accurately, although this result was below the chosen confidence level (as the amplitude of the oscillation was extremely small).

Determining the background trend of the data is very important in order to allow the oscillation or oscillations to be separated from the background and therefore correctly identified (or to show no oscillations exist). Two methods of determining the background trend and isolating the oscillations were investigated, namely polynomial fitting and EMD. The polynomial fitting method is extrinsic, in that, the degree of the polynomial must be arbitrarily chosen for each data set. This choice is sometimes clear, such as a linear fit for a constant background, but is often far more difficult. Using a linear fit for a non-constant background cannot isolate the oscillations as this requires a higher degree. However, unless the background is fitted extremely accurately, the higher degree polynomial will introduce spurious oscillations into the data. The higher the fitting degree the shorter the period of the oscillations introduced. In addition to, or instead of, polynomial fitting the background could be determined by averaging or smoothing the data, however, this method still requires an arbitrary choice of timescale or smoothing degree. An inappropriate background determination by polynomial fitting, smoothing or averaging will result in variations already in the data to be mixed between components and hence the physical relevance might be lost.

The EMD technique is capable of separating a time series into all of its different timescales. This is particularly important for time series containing multiple oscillations. Another advantage of EMD is that it is an intrinsic analysis method that is robust in separating the oscillations of different time series without first making arbitrary choices. However, the extraction of IMF's that often occurs can make the interpretation of each IMF difficult. Throughout this chapter we have found consistently reliable results by assuming that IMF_1 is the highest frequency oscillation, IMF_2 the next highest and all other IMF's are summed together to give the background, although this assumes two distinct modes of oscillation are present. By performing FFT's on each IMF a clearer picture can be gained of whether an IMF truly contains a separate timescale or has been extracted from another IMF or whether mode mixing has occurred. With a cadence of 1 s EMD was capable of separating two oscillations from each other and the background, however, when this cadence was reduced to 56 s the EMD could no longer separate the oscillations. This is a consequence of the loss in sharpness of the extrema to which the splines were fitted, thereby reducing the accuracy of the EMD. However, the reduced number of data points decreases the number of IMF's and therefore the extraction of one IMF into another is also reduced allowing the IMF's to be interpreted more confidently. In addition, a noisy signal will result in at least one IMF containing this noise, which again limits the extraction of each signal component over more than one IMF. EMD is a very strong and robust technique for extracting oscillations from a wide range of data sets.

EEMD was also examined, which is an extension to the EMD technique. The potential of EEMD to identify even extremely low amplitude and short lived oscillations has been demonstrated. By using EEMD some of the intrinsic nature of EMD is lost as the noise amplitude and the ensemble number must be chosen. The choice of ensemble number is simple, namely as high as possible, and anything above 100 is likely to be sufficient for most data sets. The choice of the noise amplitude, in this case by choosing a signal to noise ratio, is far more difficult. It is not clear whether the same value of the signal to noise ratio should be used for all data sets or a different value chosen each time. The interpretation of each IMF can also be more difficult if the wrong noise amplitude is chosen. Despite this, EEMD is a very powerful technique to extract oscillations from complex data sets. Many observations of slow waves propagating along coronal

loops have required data to be summed in both time and space (e.g. De Moortel et al. 2002a; McEwan and De Moortel 2006) to increase the data counts and the signal to noise ratio. However, EEMD may allow these oscillations to be identified from this noisy data despite the low data counts.

Damping can be seen by the width of an FFT although for the short time series used here the width of the peak produced from the finite number of periods of the signal was difficult to distinguish from the width due to damping. Wavelet analysis can show evidence of damping by a reduction in amplitude with time at a certain period. The polynomial fitting and the EMD also allow damping to be identified by separating the oscillations from the background, showing the oscillation as a function of time. The damping coefficients of two oscillations of period 50 s and 300 s were determined using wavelet analyses and directly from IMF_1 (50 s) and IMF_2 (300 s) of the EMD. The coefficient for the 50 s period was calculated more accurately than the 300 s period coefficient, although even this was still within 20% of the analytical solution. The 300 s period suffers from greater edge effects and boundary condition errors than the 50 s period and therefore the damping coefficient could only be determined for a short duration at the centre of the time series.

This work could be extended to include the observational effects of a gravitationally stratified medium. As discussed in Chapters 2 and 3, the effects of gravitational stratification cause an exponential decay in the density and therefore the observed intensity. Consequently, determining an appropriate background for a stratified medium, in order to reliably extract oscillations, will be more difficult than for the examples in this chapter. A polynomial fitting will not follow the exponential decay and the extrema on which the EMD rely may also be affected.

Chapter 5

Slow Wave Observations

5.1 Introduction

In previous chapters propagating slow waves have been studied theoretically using numerical modelling and the observational properties of these waves have been examined using forward modelling. In addition to this, the analysis techniques used to detect such oscillations were investigated. In this chapter observational data is analysed for evidence of propagating slow waves and some properties of those waves are derived. An overview of previous work on propagating disturbances can be found in De Moortel (2009) and De Moortel and Nakariakov (2012).

Before the 1990's, the observation of waves and oscillations in the solar atmosphere was limited by poor spatial and temporal resolution, but this changed with the launch of the satellites SoHO (Domingo et al. 1995) and TRACE (Handy et al. 1999). A large number of MHD waves have been observed in the solar atmosphere including both fast and slow mode oscillations. Overviews of the waves observed are extensive and can be found in Erdélyi et al. (2003); Aschwanden (2004); Wang (2004); Nakariakov and Verwichte (2005); De Moortel (2005, 2006) and more recently in Banerjee et al. (2007).

Propagating intensity oscillations have been detected in the corona, firstly in polar plumes by Ofman et al. (1997) using SoHO/UVCS (Kohl et al. 1995) and by DeForest and Gurman (1998) with SoHO/EIT (Delaboudinière et al. 1995). These intensity oscillations have been interpreted as propagating slow waves (Ofman et al. 1999, 2000b). Such oscillations have also been observed along coronal loops with SoHO/EIT (Berghmans and Clette 1999) as well as by TRACE (Nightingale et al. 1999; Schrijver et al. 1999; De Moortel et al. 2000). Two statistical studies with many detections of such oscillations are given in De Moortel et al. (2002a,b) and McEwan and De Moortel (2006), where the former found intensity oscillations of $4.1 \pm 1.5\%$ with average propagation speeds of $122 \pm 43 \text{ km s}^{-1}$. They also found that such oscillations are quickly damped and are only detected $8.9 \pm 4.4 \text{ Mm}$ along the loop from one footpoint and are never detected between the loop apex and the other footpoint. De Moortel et al. (2002c) used wavelet analysis to determine the period of such oscillations. They found two distinct bands of periodicity of around three

and five minutes. The three minute periodicities were predominately found above sunspots, whereas the five minute periodicities were found on the edge of active regions. McEwan and De Moortel (2006) suggested that the oscillations they observed are driven by leakage into the corona from the global five minute p-modes. Oscillations above sunspots have also been observed by O'Shea et al. (2002) and Brynildsen et al. (2003).

Oscillations with a periodicity of five minutes have been observed simultaneously with SoHO/EIT and TRACE 171 Å (Robbrecht et al. 2001) as well as with TRACE 171 Å and TRACE 195 Å (King et al. 2003). Marsh et al. (2003, 2004) and Marsh and Walsh (2006) detected oscillations with periodicity of five minutes using co-temporal and co-spatial observations from TRACE 171 Å and SoHO/CDS. Oscillations were detected over a temperature range of 35,000 K to 1 MK, covering the chromosphere, the transition region and the corona. From the CDS O v (629 Å) data of Marsh and Walsh (2006), Marsh et al. (2008) used Bayesian analysis to identify four distinct oscillation periods.

More recently propagating slow waves have been observed in both intensity and Doppler shift observations of Hinode/EIS data (Wang et al. 2009). Analysis of Fe XII (195 Å) data detected oscillations with relative amplitudes of 3% to 5% propagating at 100 km s^{-1} to 120 km s^{-1} with two distinct periods of 12 minutes and 25 minutes. Slow waves with longer periods of around 10 to 30 minutes have also been detected propagating in coronal loops using STEREO/EUVI (Marsh et al. 2009) and in polar coronal holes using SoHO/SUMER (Gupta et al. 2009) and SUMER and EIS (Banerjee et al. 2009).

In this chapter TRACE, SoHO/CDS (Harrison et al. 1995) and Hinode/EIS (Culhane et al. 2007) data is analysed. All three of these instruments use EUV emission lines and are therefore ideal to observe the solar atmosphere which contains many features and regions which emit radiation in the EUV range. The spectrometers, CDS and EIS, can observe both intensity and Doppler shift, however, in this Chapter only intensity is discussed.

TRACE produces two dimensional images of the intensity of a region. It has a typical field of view of $512''$ in solar x by $512''$ in solar y and can therefore observe large solar features or many small features, such as coronal loops. In order for CDS to resolve wavelengths and hence give spectroscopic information one of the two spatial dimensions is lost. Therefore, the CDS slit has a narrow field of view in solar x (e.g. $4''$) and a larger field of view in solar y (e.g. $200''$) compared to TRACE (e.g. $512''$). Consequently, unless a feature lies directly along the field of view of the CDS slit (i.e. in solar y) only part of the feature can be observed at any time. The small CDS field of view is overcome by producing rasters, where multiple images are taken using the slit with the slit position adjusted each time to produce a single image with a larger field of view. However, the multiple images required to make a raster significantly reduces the cadence of the data, which for the rasters discussed here is 16 minutes for a $240''$ field of view in solar x with a resolution of $4''$ in x and $1.68''$ in y. As a result these rasters cannot be used to detect oscillations with periods of a few minutes and the CDS slit must be used, either in sit and stare mode or by tracking features on the Sun over time. Operating in sit and stare mode, the CDS slit observes the same absolute position of the Sun with features moving through the field of view of the slit due to solar rotation. In addition to narrow slits the EIS instrument uses a $40''$ slot, with a field of view of $40''$ in solar x and $504''$ in solar y, with a resolution of $40''$ in x and $1''$ in y, which has the spectroscopic ability of a slit, but also has a much larger field of view in which entire loops can be observed with a high cadence.

The propagation of slow waves through the solar atmosphere can be seen by observing regions at different temperatures. This is possible using data from many different emission lines. The radiation emitted by each emission line depends on the temperature (and density) of the region, consequently, with the use of atomic physics (from CHIANTI (Dere et al. 1997)) the temperature of the region can be determined. By comparing TRACE, CDS and EIS observations, data from a wide range of emission lines can be analysed, allowing the detection, and more accurate determination of the properties of propagating slow waves throughout the atmosphere.

5.2 TRACE and CDS Observations

Co-spatial and co-temporal TRACE and CDS data have been analysed to find evidence of slow waves propagating along coronal loops. The data sets were taken over a period from 21st April 2003 to 3rd May 2003. The TRACE 171 Å data has been analysed previously by McEwan and De Moortel (2006) who found 25 examples of propagating slow waves. The addition of the CDS data allows the loop to be observed in many more emission lines and therefore at different temperatures in order to observe the propagation of the waves through the solar atmosphere. Due to the narrow field of view of the CDS 4" slit, joint CDS and TRACE observations are only possible for one of the examples found by McEwan and De Moortel (2006). This loop is discussed in Section 5.2.1 and two other examples of propagating slow waves have been identified and are discussed in Section 5.2.2. The oscillation signatures are identified using running differences in addition to EMD, polynomial fitting, wavelet analysis and FFT, as discussed in Chapter 4, and the data is analysed using Solarsoft IDL (Freeland and Handy 1998).

5.2.1 30th April 2003

The first data sets examined are from 30th April 2003. TRACE 171 Å data is initially examined and is subsequently compared to CDS slit data from several emission lines. The methods used to analyse both the TRACE and CDS data are consistent for all the examples, but are outlined below for 30th April data.

5.2.1.1 TRACE

TRACE 171 Å data is cleaned and prepared using the `trace_prep` routine in Solarsoft IDL. Firstly, missing pixels are filled and saturated pixels are replaced, then the dark pedestal and dark current are subtracted and the flat field is corrected for. In addition, cosmic ray hits are removed using the `unspike` option, cosmic ray streaks are removed using `destreak`, read out noise is removed using the `deripple` command and the `wave2point` command is used to correct the pointing values for the `trace_align_cube` routine, which de-jitters, aligns and accounts for solar rotation.. Finally, the images are normalised for exposure times to DN per second, which gives consistent oscillation amplitudes between images, but reduces the signal to noise ratio.

After reducing the length of the data set to avoid radiation effects, a data cube of 110 clean images of

TRACE 171 Å with consistent cadence of 13 to 14 seconds is identified. The images have a field of view of 512'' in solar x and solar y and a resolution of 1'' in both x and y. To detect oscillations with periods of around five minutes a cadence of at least 60 seconds is required in order to avoid aliasing. Higher cadences allow oscillations to be more clearly resolved in time or alternatively to sum the data over time in order to increase the signal to noise ratio. Here the data is summed in time to increase the signal to noise ratio. The wavelet analysis used to identify oscillations requires a constant cadence.

Fig. 5.1 shows the selected loop from the data set, which was also analysed by McEwan and De Moortel (2006). Broad loops are also chosen to allow summing across the loop in order to increase the number of data counts for an oscillation along the loop. Propagating slow waves have only been detected up to around 20Mm from the loop footpoint (De Moortel et al. 2002a), it is therefore important to pick loops with a clear isolated footpoint.

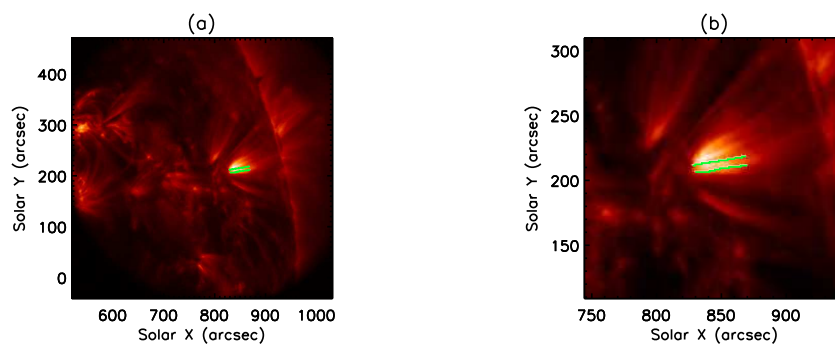


Figure 5.1: (a) loop position shown in TRACE 171 Å with (b) the same as (a) but enlarged.

Propagating slow waves typically produce oscillations of less than 5% of the background (e.g. De Moortel et al. 2002b). The brightest pixel of the loop highlighted in Fig. 5.1 has an intensity of around 60 DN per second, which for a 5% oscillation gives a maximum amplitude of only 3 data counts. This is too low to reliably detect an oscillation, hence the data must be summed to increase the number of data counts. Note that the total number of data counts would be increased if the images were not normalised. To increase the signal to noise ratio, the same procedure as in De Moortel et al. (2000) is followed. The data is summed across the loop so that the 2D loop is collapsed to a 1D loop. Pixels are also summed slightly along the loop, with the resolution of the TRACE data reduced from 1'' to 2''. This halves the data points and spatial resolution along the loop, but increases the data counts for each remaining macro-pixel allowing oscillations to be identified more easily. To further aid the identification of any oscillations, before the spatial averaging is performed, temporal averaging is performed over every four images to give a final cadence of 54 s, reducing the time resolution, but increasing the signal to noise ratio in return. Reducing the loop to 1D has the benefit of allowing more direct comparison with both the results from the CDS slit, which has only one spatial dimension, and with the 1D forward modelling simulations discussed in Chapter 3.

Summing the data in time gives a data set of 27 images with 54 second cadence. The loop is identified in the first image of the data set and the loop position is assumed to stay constant throughout the course of the 25 minute time sequence. The loop position moves up to 2'' (1 pixel), depending on the latitude, in this time due to solar rotation, but this is accounted for by the trace_align_cube routine. A running difference is performed to remove the background intensity of the loop and hence show any oscillations more clearly.

The running difference is performed on each image of the data set, except the first, by subtracting the previous image. This leaves a 1D running difference along the loop at 26 constant time intervals, as shown in Fig. 5.2(a). Bright regions of the loop (as outlined by the green dashed lines in Fig. 5.2(a)) show where the intensity has increased from the previous image, i.e. the oscillation is growing in intensity. Conversely dark regions (pink dashed lines in Fig. 5.2(a)) show where the intensity has reduced since the previous image, i.e. where the oscillation intensity has a negative gradient. Propagating features in the running difference are diagonal with a positive gradient for upward propagation and a negative one for downward propagation. These features are outlined by the dashed green and pink lines in Fig. 5.2(a) and are used to determine the oscillation period and the propagation speed of the wave. The time difference between the green and pink lines is 150 s (e.g. the time between the lowest green line and the lowest pink line), consequently, an oscillation period of 300 s is ascertained. The propagation speed is determined from the gradient of the green and pink lines. An average propagation speed of 115 km s^{-1} is found, with a possible minimum and maximum speed of 75 km s^{-1} and 240 km s^{-1} , respectively. As discussed in Chapter 3, TRACE 171 Å mainly comprises of contributions from Fe IX and Fe X, which are at peak ionisation balance at temperatures of roughly 0.6MK and 1MK, respectively. Assuming the temperature of the loop in Fig. 5.1 is within this range, the sound speed along the loop is therefore 120 km s^{-1} to 150 km s^{-1} , which is consistent with the propagation speed of the wave calculated from Fig. 5.2(a). Hence, the speed of the wave is consistent with an interpretation in terms of a slow magnetoacoustic wave.

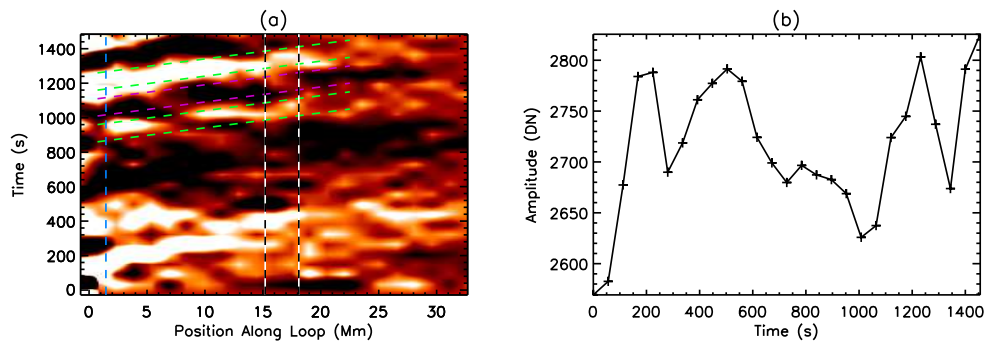


Figure 5.2: (a) running difference along the loop outlined in Fig. 5.1. (b) loop intensity as a function of time at the position marked by the blue vertical dashed line in (a). The green and pink dashed lines in (a) highlight a propagating feature with periodic nature and the black/white lines mark the position of the CDS slit (see Section 5.2.1.2) at the beginning of the observation (i.e. $t = 0$ s in (b)).

Fig. 5.2(b) shows the loop intensity as a function of time (hereafter referred to as the signal) at the position marked by the blue vertical dashed line in Fig. 5.2(a), which is at 1.5 Mm along the loop. This signal, which consists of at least one oscillation about a non-constant background, is now analysed using the techniques discussed in Chapter 4. In order to isolate the oscillation and hence determine its properties more confidently, the background must be determined and removed. The signal consists of few data points over a relatively short time series, hence, the changes in the background intensity are difficult to determine. Fig. 5.3(a) shows the signal (black) with several background trends determined using different methods. A linear trend (i.e. polynomial degree 1) is fitted to the data, as shown by the dashed blue line in Fig. 5.3(a), which is consistent with the method used in McEwan and De Moortel (2006). The advantage of a linear trend is that it will not introduce spurious oscillations into the data set, however, it may not give the most

accurate solution to the background. A polynomial fitting of degree 3 (purple) and a data smoothing of degree 5 (green) using the IDL smooth function are also shown. The background trends obtained using various polynomial fitting degrees and different degrees of smoothing are shown in Fig. 1 of Appendix B. Due to the low number of data points, a smoothing degree higher than 5 causes sharp changes in the background (see the red line in Fig. 1(b) of Appendix B) and is therefore inappropriate. These methods all require an arbitrary choice of either polynomial degree or smoothing degree. In contrast, the empirical mode decomposition (hereafter EMD) determines the background intrinsically and the resulting trend is shown in red in Fig. 5.3(a).

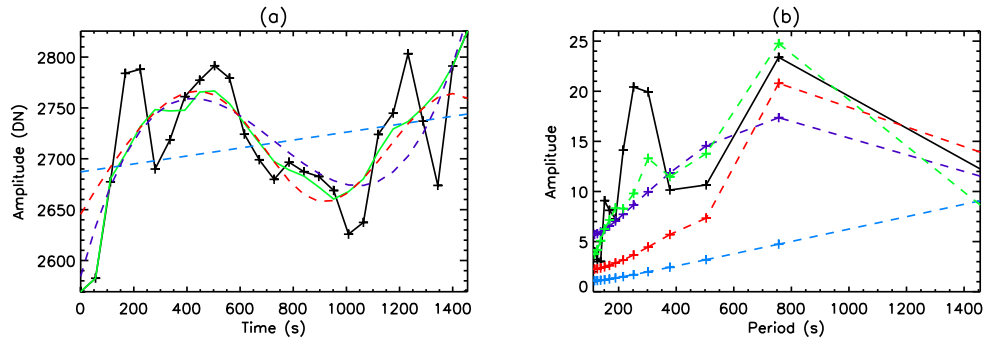


Figure 5.3: Background trend determination of the signal in Fig. 5.2(b). (a) background trends and (b) FFT's of the trends in (a). Signal (black), EMD (red), polynomial fitting degree 1 (blue) and degree 3 (purple) and smoothing degree 5 (green).

The aim of determining the background trend is to remove the longer periods and isolate the shorter periodicity without introducing spurious oscillations. FFT's can be used to help determine whether a background fitting is appropriate, and contains the longer periodicity of the background without any of the shorter periodicity, by comparing the periodicity present in the background fit to those in the signal itself. Fig. 5.3(b) shows the FFT of the signal (black) and the FFT's of the background trends in Fig. 5.3(a), which are plotted from a period of twice the cadence (i.e. 108 s) to avoid errors at low period. This is consistent with the low cadence treatment in Section 4.2.6. The FFT of the signal shows two peaks, firstly between 200 s and 400 s period, which corresponds to the oscillation, and also at longer periods between 500 s and 1450 s, which is interpreted as the background.

An accurate and appropriate background trend must fit the signal in Fig. 5.3(a) and contain the longer periods seen in the FFT in Fig. 5.3(b) of 500 s and above, whilst it must not contain the shorter periodicity of the oscillation. Consequently, when the background is removed from the signal only the oscillation will remain, which will have accurate periodicity and amplitude. The FFT's of the EMD (red), polynomial degree 3 (purple) and the smoothing (green) all show peaks between 500 s and 1450 s periodicity, which is consistent with the background periods of the signal, although the peak in the polynomial degree 3 FFT is far less pronounced than that of the EMD and the smoothing. However, the polynomial fitting and the smoothing FFT's show a high amplitude for periods of 300 s, corresponding to the oscillation. The smoothing FFT even has a peak at 300 s. Therefore, these backgrounds clearly contain some of the 200 s to 400 s periodicity of the oscillation, which would be lost if either of these backgrounds were removed. In contrast the FFT of the EMD background has a low amplitude at short periods, which increases greatly above periods of around 500 s, and is therefore a good choice of background trend. The FFT from the linear

fitting does not show a peak at any period, but instead shows increasing amplitude as the period increases. The linear fit, therefore, does not match the peak in periodicity at 800 s that is seen in the FFT of the signal. Consequently, this background will not remove all of the longer periodicity of the signal. However, the linear fit produces the lowest amplitude of FFT at low periods and therefore, using this background has the least effect on the periodicity of the oscillation. From this evidence the most appropriate background is that of the EMD, however, the oscillation periods obtained from the linear fitting results should also be used.

The oscillation produced by subtracting the linearly fitted background (Fig. 5.3(a) blue) from the signal (Fig. 5.3(a) black) is shown in Fig. 5.4(a) (blue). The oscillation determined from the EMD, given by IMF_1 , is shown in red. The EMD produces 4 IMF's for the 27 data points of the signal, which are shown in Fig. 2 of Appendix B. Determining which IMF's to use for the oscillation and for the background is discussed in more detail in Chapter 4. However, the choice of background and the FFT's of each are shown in Fig. 3 of Appendix B. Fig. 5.4(b) shows the FFT of the signal (black) and the FFT's of the oscillations in Fig. 5.4(a) (IMF_1 red and linear fit blue). All three FFT's give a clear peak between periods of 200 s to 400 s, with a maximum at 250 s to 300 s. This is consistent with the 300 s period determined from the running difference and with previous results on propagating disturbances (De Moortel 2009; McEwan and De Moortel 2006). The broad peak in Fig. 5.4(b) between periods of 250 s and 300 s may suggest that the oscillation period varies slightly, which would be a result of a change in sound speed. This is consistent with the non-constant background intensity of Fig. 5.3(a), which is caused by changes in temperature and density, and therefore the sound speed, as discussed in Chapter 2. Despite a clear peak in all three FFT's corresponding to the oscillation only the EMD results contain a clear dominate peak, with little evidence of the longer period background. There is also evidence of a peak in all three FFT's at around 150 s, although this peak is too small to determine reliably.

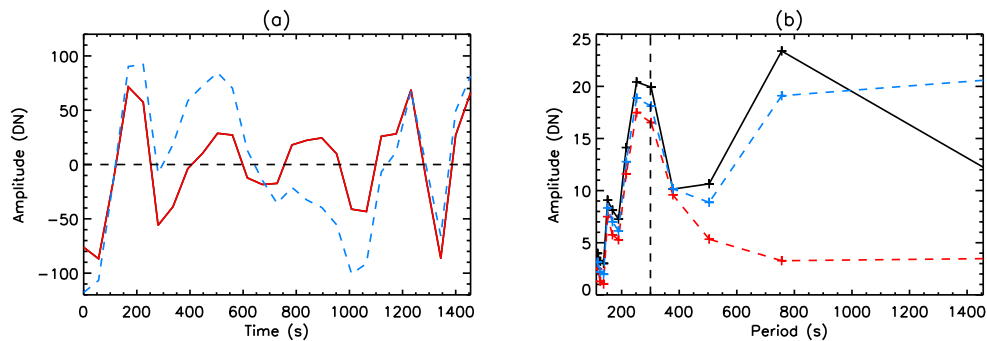


Figure 5.4: (a) oscillations and (b) FFT's of the oscillations in (a). IMF_1 (red) and linear fit (blue) with the FFT of the signal (black).

The relative amplitude of the oscillations in Fig. 5.4(a) can be found by comparison to the backgrounds in Fig. 5.3(a). The maximum, A_{max} , and the minimum, A_{min} , amplitude estimate of the oscillation relative to the background is given by,

$$A_{max} = \frac{|x(t)|_{max} - \overline{x(t)}}{\overline{r(t)}}, \quad (5.1)$$

$$A_{min} = \frac{\overline{|x(t)|}}{\overline{r(t)}}, \quad (5.2)$$

where $|x(t)|_{max}$ is the maximum value of the modulus of the oscillation, $\overline{x(t)}$ is the mean of the oscillation, $\overline{|x(t)|}$ is the mean of the modulus of the oscillation and $\overline{r(t)}$ is the mean of the background. From IMF_1 the oscillation is calculated to have a relative amplitude of 1.4% to 3.2%, which is consistent with the value of 1.9% to 4.3% from the linear fit.

Wavelet analysis is also performed on the two oscillations in Fig. 5.4(a) in order to determine the oscillation period. The Morlet wavelet is used here as it is especially accurate at calculating the periods present. A disadvantage with wavelet analysis and FFT's are that they cannot differentiate between stationary and propagating oscillations. They must be used in conjunction with the running difference which clearly shows propagating structures as diagonal features moving along the loop in time.

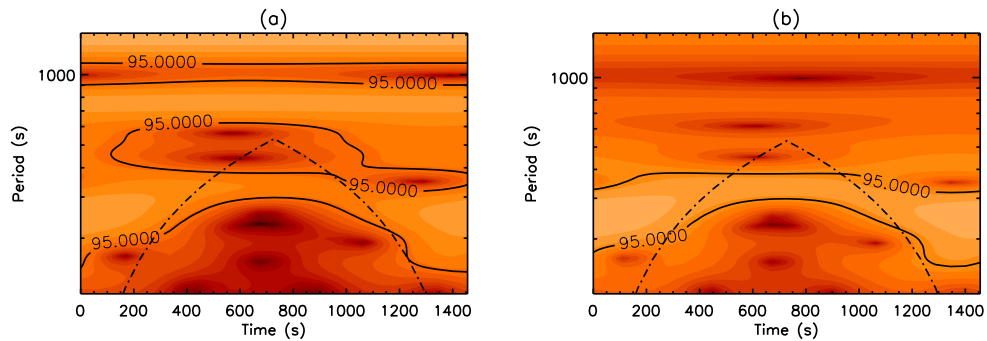


Figure 5.5: Wavelet analyses of the oscillations in Fig. 5.4(a) for (a) linear fit and (b) IMF_1 .

The wavelet analyses of the linear fit (Fig. 5.5(a)) and the EMD (Fig. 5.5(b)) oscillations both show periods from 300 s to 380 s that are above the 95% confidence level for the duration of the observation. There is evidence of shorter periods at the start and end of the time sequence, but this is outside of the COI and therefore unreliable. An oscillation period between 300 s to 380 s is consistent with both the 300 s period determined by the running difference and with the peak marked in the FFT's of Fig. 5.4(b). However, the FFT's also show a peak at 250 s, which the wavelet analysis suggests only exists at the start and end of the time series. An oscillation period of 300 s is found in the running difference, the FFT's and for all time in the wavelet analyses, and hence can be confidently inferred as the oscillation period. Following De Moortel et al. (2000, 2002a,b), a detection length was found by performing the wavelet analyses of the EMD results at each position along the loop until the oscillations were no longer above the confidence level. The oscillation is only above the 95% confidence level of the wavelet analyses for 3 Mm along the loop although the running difference does seem to suggest it continues much further and the FFT's shows evidence of the same 300 s periodicity for around 7 Mm. In agreement with the FFT, the wavelet analysis of the linear fit oscillation does show evidence of longer periods, albeit outside of the COI, whereas the EMD results do not. For comparison, the oscillations, FFT's and wavelet analyses using both the polynomial degree 3 and data smoothing degree 5 backgrounds are shown in Figs. 4 and 5 of Appendix B. The periods and relative amplitudes are consistent with those discussed above.

As mentioned earlier, the coronal loop discussed here has also been analysed in TRACE 171 Å by McEwan and De Moortel (2006). The results given here are consistent with those from McEwan and De Moortel (2006), who found a propagation speed of order 100 km s^{-1} , a range of periods from 175 s to 450 s, and a relative amplitude of 1.5% to 3.9%. However, the detection length of 11.2 Mm in McEwan and De

Moortel (2006) differs from the 3 Mm found here, which is most likely due to the treatment of the data in the trace_prep routine. As the cadence varies slightly between 13 s and 14 s, each image is normalised for exposure time to ensure that the oscillation amplitudes remained consistent. However, this results in lower data counts than McEwan and De Moortel (2006).

5.2.1.2 CDS

The coronal loop discussed above for TRACE 171 Å is also observed at the same time by CDS. The CDS data consists of a raster taken with the 4" slit a few minutes before the TRACE data and a sit and stare observation with the 4" slit for the duration of the TRACE data. This allows a direct comparison of the loop for co-temporal and co-spatial CDS slit and TRACE 171 Å data. Both raster and slit data are cleaned and prepared using Solarsoft IDL. Missing pixels are replaced using the command `cds_fill_missing`, cosmic ray hits are removed using `cds_new_spike` and `nis_rotate` is used to align the two normal incident spectrometers. In addition, the data is summed for each wavelength to give the total intensity for each emission line and is converted to photons per second per pixel using the `vds_calib` command.

The CDS raster is made from 60 images of the 4" slit over a 16 minute period. The raster has a field of view of 240" in solar x and solar y with a resolution of 4" in x and 1.68" in y. The field of view allows alignment of the CDS and TRACE data as well as giving a visual perspective of the loop's position and of the surrounding features. The 16 minute cadence, however, does not allow oscillations with periods of a few minutes to be observed. The raster data was taken using six emission lines, He I (584 Å), O V (629 Å), Mg IX (367 Å), Si X (347 Å), Si X (356 Å) and Fe XVI (360 Å). As discussed above and in Chapter 3, TRACE 171 Å mainly comprises of Fe IX and Fe X which are at peak ionisation balance at around 0.6 MK and 1 MK, respectively. Therefore, the best raster to use for alignment is from the emission line closest to this temperature range. He I and O V have temperatures (0.05 MK and 0.2 MK, respectively) far below TRACE 171 Å and Fe XVI has a temperature which is far too high (2.5 MK). Mg IX and the two Si X lines have peak temperatures of around 1 MK. The Mg IX (367 Å) line was chosen as it was found to give the easiest comparison with the TRACE data and was also used for the sit and stare observations.

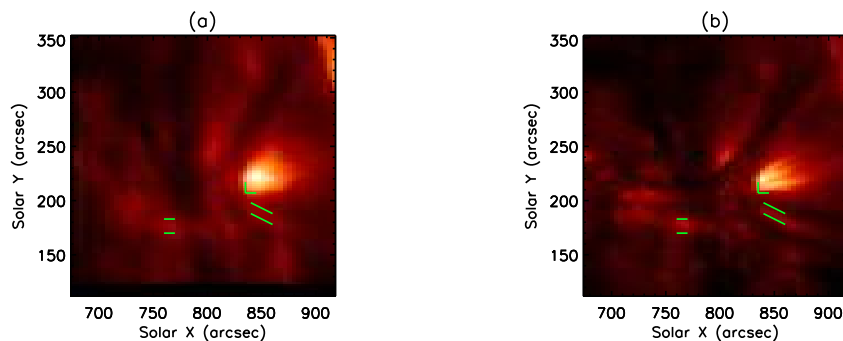


Figure 5.6: Alignment of (a) CDS Mg IX (367 Å) raster with (b) TRACE 171 Å. The resolution of the TRACE image has been reduced to match that of the CDS raster.

The closest raster to the TRACE data was taken 15 minutes before the data set discussed in Section 5.2.1.1. i.e. 16:10 UT to 16:26 UT. The Solarsoft IDL routine `rot_xy` was used to determine the distance in solar x

and solar y that a feature in the raster would have moved over this 15 minute period. The position of the Mg IX (367 \AA) raster was then adjusted by this distance and the raster was compared to the first image of the TRACE 171 \AA data set. CDS is aligned to TRACE using the IDL routine `c_correlate` and then manually adjusted if required. The offsets between the CDS and TRACE pointing were found ($28''$ in x and $3.8''$ in y) by comparing features in the Mg IX (367 \AA) raster and the TRACE 171 \AA data. Fig. 5.6 shows a cutout of (a) the Mg IX (367 \AA) raster and (b) the first image of the TRACE 171 \AA data. The TRACE resolution has been reduced to that of the CDS raster to allow easier comparison and several features have been highlighted to confirm the alignment. The CDS slit is then aligned to the raster using the CDS pointing.

Fig. 5.7(a) shows the first image of the TRACE 171 \AA data with the position of the CDS raster and the $4''$ slit outlined in green. The white lines show the position of the slit without the data alignment. Once the data is aligned, the true position of $4''$ slit is found, this is shown in more detail in Fig. 5.7(b) (green) with the loop selected in the TRACE 171 \AA data also shown. With CDS operating in sit and stare mode the slit scans across the Sun due to solar rotation. This can be seen in Fig. 5.7(b), where the white line marks the position of the slit relative to the loop at the end of the TRACE data set. Note that the coordinates of the white line in Fig. 5.7(b) are not correct, it is the coordinates of the loop that change in time not the slit, but the section of the loop that intersects the slit is correct. Consequently, a particular feature can only be observed for a short period of time, until that feature has rotated past the field of view of the slit, or a different part of the feature is being observed.

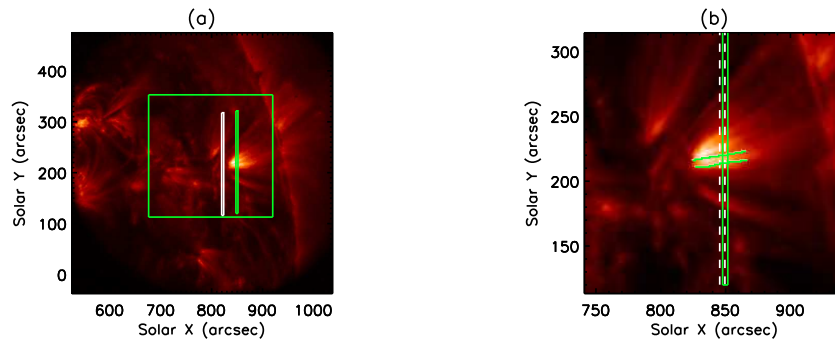


Figure 5.7: (a) position of TRACE, CDS raster and CDS $4''$ slit (green). (b) same as (a) but enlarged with the selected loop shown. The position of the slit without alignment (white) is also shown in (a) and the position of the slit relative to the loop at the end of the TRACE data (white) is shown in (b).

The sit and stare observations have a field of view of $4''$ in x and $200''$ in y with a resolution of $4''$ in solar x and $3.36''$ in solar y and a cadence of 16 s for 135 minutes. The sit and stare observations were taken using five emission lines over a range of coronal and transition region temperatures. The emission lines used are He I (584 \AA), O IV (554 \AA), O V (629 \AA), Mg IX (367 \AA) and Fe XVI (360 \AA) which are sensitive to temperatures of around 0.05 MK , 0.2 MK , 0.2 MK , 1 MK and 7.5 MK , respectively. The 135 minutes of the CDS slit observations are reduced in time to match the TRACE 171 \AA data set. The loop position relative to the CDS slit is assumed to stay constant throughout the 25 minutes, which considering Fig. 5.7(b) is a reasonable assumption.

Unlike TRACE, the CDS $4''$ slit cannot observe the entire loop, only where the slit crosses the loop. This position can be seen by the intersection of the green lines in Fig. 5.7(b), which is 6 CDS pixels in solar

y, and is 17 Mm along the loop. This gives the loop intensity as a function of time for this fixed position, giving a time series comparable to that of TRACE 171 Å in Fig. 5.2(b). The position of the loop along the CDS slit is assumed to remain constant for the duration of the 25 minute data. The time series for He I (584 Å), O IV (554 Å), O V (629 Å) and Mg IX (367 Å) of the section of the slit which intersects the loop are shown in Figs. 5.8(a), (c), (e) and (g), respectively. No evidence of any oscillations was found in the Fe XVI (360 Å) data, most likely due to its high peak ionisation temperature and hence the Fe XVI results are not shown. The time series are analysed using the same method as the TRACE 171 Å signal. The background trend of the data is found using EMD and is shown in blue in Figs. 5.8(a), (c), (e) and (g). The linear fit is given in red. The higher cadence of the CDS data (16 s compared to 54 s for TRACE) produces 6 IMF's rather than 4. IMF_1 and IMF_2 were found to contain high frequency noise, with IMF_3 representing the periodicities found in the TRACE 171 Å analysis. IMF_3 is shown for the He I, O IV, O V and Mg IX data in Figs. 5.8(b), (d), (f) and (h), respectively. The oscillations produced using a linear fit are shown for comparison in red. These oscillations are seen to generally follow the EMD results but have variations with much higher frequencies than the smooth EMD results.

IMF_2 (blue) of the O IV results are also shown in Fig. 5.8(d) as mode mixing occurred, where some of the periodicity of IMF_3 can be found in IMF_2 . This can be easily seen at around 300 s where the linear fit results follow IMF_2 and not IMF_3 . As discussed in Chapter 4 the EMD does suffer from boundary errors which for short time series such as these may affect the results. Consequently, the apparent growth and rapid damping near the boundaries cannot be used to reliably infer damping or growth of the oscillation. The relative amplitudes of the oscillation in Fig. 5.8 are calculated using the same method as the TRACE 171 Å results. With peak emission at a temperature of around 1 MK the Mg IX line should give the closest results to that of TRACE 171 Å. A relative amplitude of 0.6% to 1.6% was found, which is slightly different to the TRACE results of 1.4% to 3.2%, however, the TRACE results are far nearer to the loop footpoint. The cooler lines of He I, O IV and O V have similar amplitudes to each other of 2.3% to 6.0%, 3.4% to 7.5% and 1.8% to 6.3%, respectively which are all greater than the coronal values. These higher transition region amplitudes, as previously discussed, are broadly consistent with the theoretical results of Chapter 3 and have previously been reported by other authors (e.g. Marsh et al. 2003).

FFT's are performed on both the data and the oscillations in Fig. 5.8. The results for each emission line can be found in Fig. 6 of Appendix B. The FFT's of just the oscillations are shown in Fig. 5.9. O IV (red) and O V (green) both show a peak at 300 s period, in agreement with the TRACE 171 Å results. The He I (black) FFT gives a peak at longer periods of 350 s to 400 s, however, the FFT of the original data (Fig. 6(a) of Appendix B) does show a clear peak at 300 s. This period has been lost due to boundary errors of the EMD, where IMF_3 in Fig. 5.8(b) clearly has longer period variations at the start of the data set than at the end. The Mg IX (blue) FFT does not show a peak at 300 s period, but instead at 250 s. It therefore might not correspond to the blue 300 s period oscillation detected in the TRACE 171 Å data. This could explain why the oscillation amplitudes above vary for Mg IX and TRACE 171 Å. In addition, the amplitude of the Mg IX peak is too low to reliably infer a periodic oscillation. Wavelet analyses were also performed on the oscillations in Fig. 5.8 and are shown for all four emission lines in Fig. 6 of Appendix B. As expected from the FFT, the wavelet analysis of Mg IX does suggest a periodicity at 250 s, but it is below the 95% confidence level. The wavelet analyses of the He I, O IV and O V all show periodicity between 200 s and 320 s which are above the confidence level for all time. These periods are consistent with those of TRACE 171 Å.

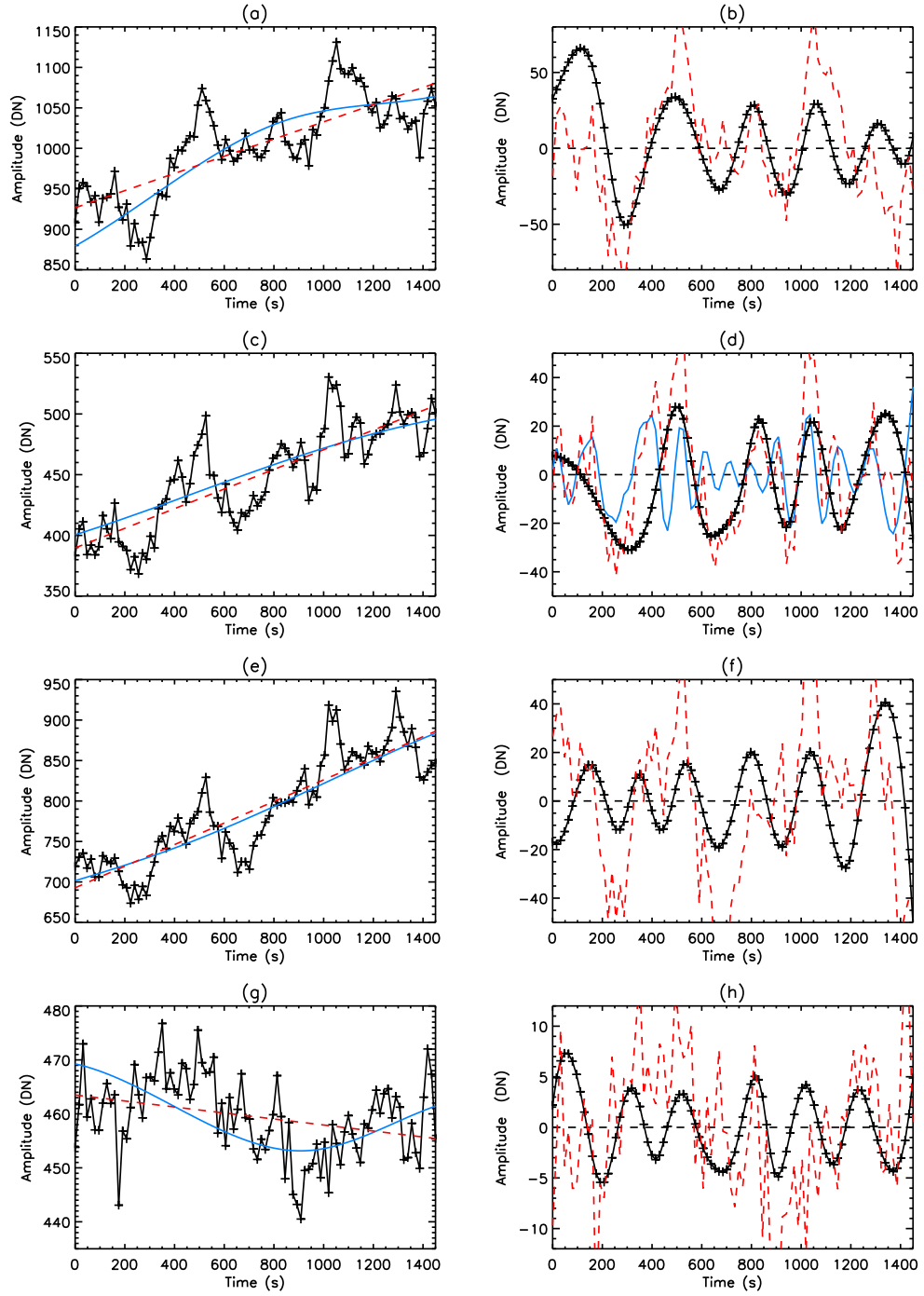


Figure 5.8: (left) signal (black) with a background of $IMF_5 + IMF_6$ (blue) and from linear fitting (red). (right) IMF_3 (black) and the oscillation from linear fit (red). (a) and (b) He I (584 Å), (c) and (d) O IV (554 Å), (e) and (f) O V (629 Å) and (g) and (h) Mg IX (367 Å). IMF_2 (blue) is also shown in (d).

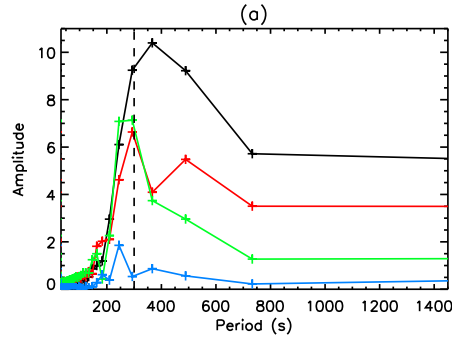


Figure 5.9: FFT of IMF_3 for He I (584 Å) (black), O IV (554 Å) (red), O V (629 Å) (green) and Mg IX (367 Å) (blue).

An oscillation with a period of around 300 s propagating along a coronal loop at around the sound speed with a relative amplitude of 1.5% in the corona and a higher value of around 5% in the transition region is theoretically consistent with a propagating magnetoacoustic wave. The lack of confident detection of this oscillation in Mg IX is not unexpected due to the position of the CDS slit along the loop. The oscillation was only detected to around 3 Mm to 7 Mm in TRACE 171 Å which is sensitive to a similar temperature to that of Mg IX and therefore a detection at 17 Mm along the loop in Mg IX is unlikely.

The multiple emission lines of CDS allow the oscillations to be observed throughout the solar atmosphere. However, the single spatial dimension of the slit does not allow propagating signatures to be seen directly as in the diagonal bands of the TRACE running difference in Fig. 5.2(a).

5.2.2 29th April 2003

5.2.2.1 22:06 UT

A data set is now analysed at 22:06 UT on 29th April 2003. The data is cleaned and prepared as discussed in Section 5.2.1.1 giving 131 clean TRACE 171 Å images with 7 s to 8 s cadence. The images have a field of view of 512" in solar x and solar y and a resolution of 1" in both x and y. The same summing across and along the loop is performed as discussed in Section 5.2.1.1. Every 6 images are summed together in time to give a final data set of 21 images with a 48 s cadence.

The coronal loop of interest is shown in Fig. 5.10(a) with the CDS slit position also marked. As discussed in Section 5.2.1.1 a running difference along the loop is performed and the resulting image is shown in Fig. 5.10(b). The green and pink lines in Fig. 5.10(b) show a periodic feature that propagates along the loop, although this is not obvious above 10 Mm along the loop. From this running difference an oscillation period of around 220 s is determined. In addition, an average propagation speed of 100 km s^{-1} is found, with a possible minimum and maximum speed of 70 km s^{-1} and 150 km s^{-1} , respectively. Comparing the propagation speed to the sound speed of the loop, which is 120 km s^{-1} to 150 km s^{-1} , gives a propagation speed that is consistent with a slow wave.

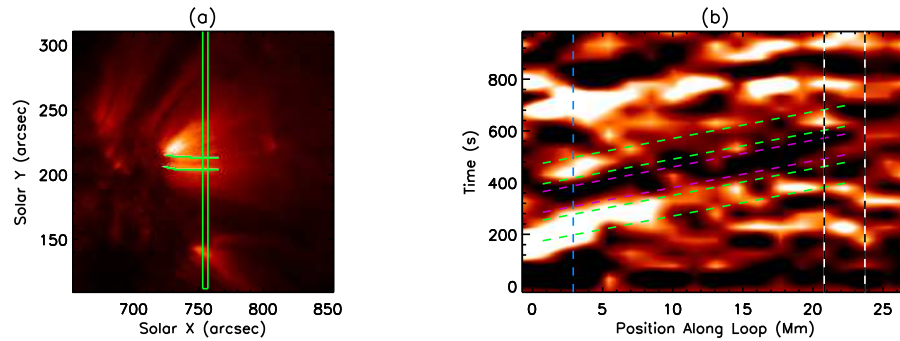


Figure 5.10: (a) loop position in TRACE 171 Å with the CDS slit location also shown. (b) running difference along the loop outlined in (a). The green and pink dashed lines in (b) highlight a propagating feature with periodic nature and the black/white lines mark the position of the CDS slit.

Following the method used in Section 5.2.1.1 the intensity at a single position along the loop (marked by the blue vertical dashed line in Fig. 5.10(b)) is shown as a function of time in Fig. 5.11(a). The background trend of this signal is determined using a linear fit (blue) and EMD (red), both of which are shown in Fig. 5.11(a). The EMD produces 4 IMF's which are shown in Fig. 7 of Appendix B. The background trends produced by summing the different IMF's are also shown in Appendix B (Fig. 8(a)) along with FFT's of these trends (Fig. 8(b)). The red line in Fig. 5.11(a) is given by $\sum_{i=2}^4 IMF_i$ and was found to be the most suitable background, which is consistent with the previous example and with the low cadence results of Chapter 4.

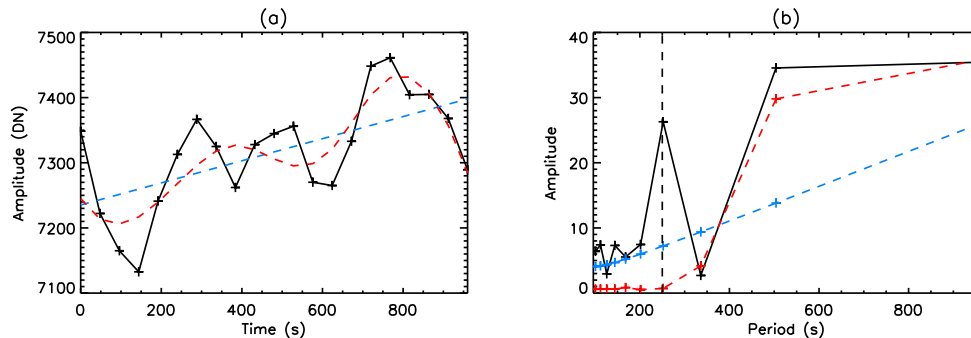


Figure 5.11: Background trend determination of the signal along the blue vertical dashed line in Fig. 5.10(b). (a) background trends and (b) FFT's of the trends in (a). Signal (black), EMD (red) and linear fit (blue).

Fig. 5.11(b) shows the FFT's of the signal (black) and the linear fit (blue) and EMD (red) background trends from Fig. 5.11(a). The FFT of the signal shows two peaks, firstly representing an oscillation with periodicity of 250 s, and secondly of a longer periodicity background above periods of 400 s. As discussed in Section 5.2.1.1 the linear fit background shows higher amplitude at longer period, but does not have the rapid increase above periods of 400 s that the FFT of the signal suggests. Therefore, the linear fit will produce an oscillation with the correct periods, but the amplitude may be incorrect due to the presence of a residual background. The EMD background, however, shows virtually no evidence of low periods and rises steeply at 400 s period to match the background trend very well.

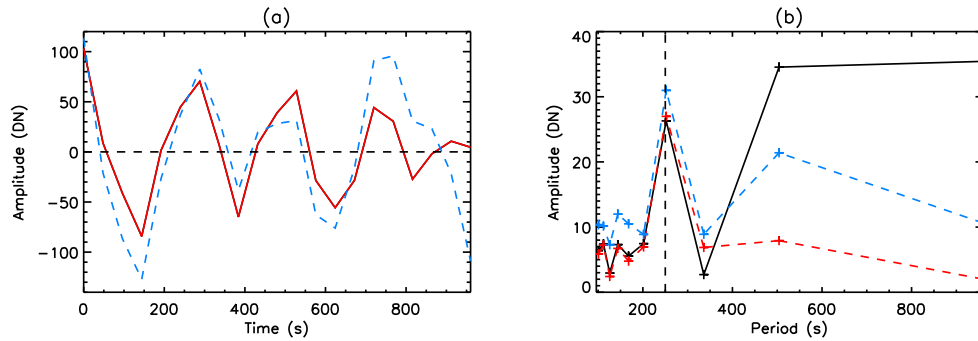


Figure 5.12: (a) oscillations and (b) FFT's of the oscillations in (a). IMF_1 (red) and linear fit (blue) with the FFT of the signal (black).

The oscillations obtained from the EMD (IMF_1 red) and the linear fitting (blue) are shown in Fig. 5.12(a). Both oscillations show consistent periodic behaviour, but with slightly differing amplitudes, particularly towards the end of the data set. This is likely to be a consequence of either the linear fit not removing all of the background periodicity or the EMD removing too much of the oscillation near the upper boundary. IMF_1 shows evidence of a possible damped oscillation. The oscillation period is found using FFT's, which are shown in Fig. 5.12(b) and wavelet analyses which are shown in Figs. 5.13(a) and (b) for the linear fit and the EMD results, respectively. The FFT's of both oscillations show a clear peak at 250 s period matching that of the FFT of the signal. The EMD results again show that the longer period background has been removed far better than by using the linear fitting. Both wavelet analyses show periods between 210 s and 275 s that are above the confidence level for all time. This period range is consistent with the peak at 250 s of the FFT and the 220 s period obtained from the running difference in Fig. 5.10(b). The oscillation is detected to around 4.5 Mm along the loop. The relative amplitude of the oscillation is calculated using the method described previously, giving an amplitude of 0.5% to 2.3% from the EMD results, which is consistent with 0.8% to 1.7% from the linear fit.

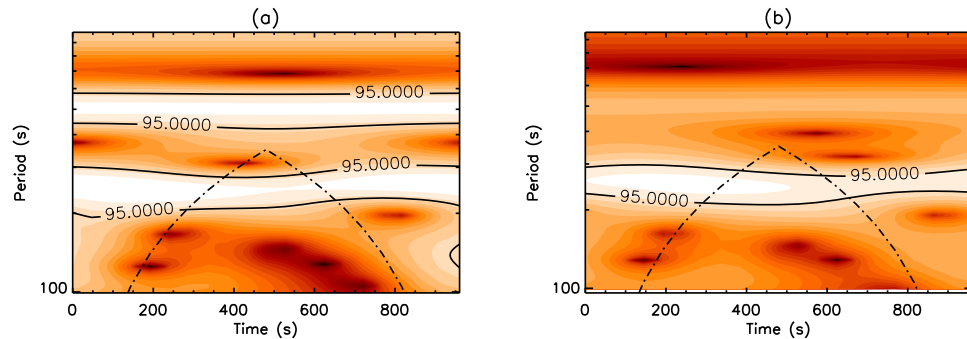


Figure 5.13: Wavelet analyses of the oscillations in Fig. 5.12(a) for (a) linear fit and (b) IMF_1 .

The damping of the oscillation in Fig. 5.12(a) is investigated further using the method of De Moortel and Hood (2000) described earlier in Section 4.2.2.2. The amplitude of the wavelet analysis in Fig. 5.13(b) at a period of 250 s is shown on a logarithmic scale in Fig. 5.14(a). The edges of the COI are marked by the vertical dashed lines. Within this COI and away from the boundary errors the amplitude of the wavelet

analysis decreases linearly, i.e. shows exponential damping.

The damping coefficient can be calculated from Fig. 5.14(a) by assuming an exponential form, $x(t) = De^{-dt}$, where $x(t)$ is the amplitude of the signal at time t , D is a constant and d is the damping coefficient. D is calculated using the two points furthest from the boundaries (and therefore furthest from boundary condition errors and edge effects), where the wavelet analysis is assumed to be the most reliable. d is then calculated at each point of Fig. 5.14(a) and the results are shown by the black line in Fig. 5.14(b), which is only plotted within the COI. The damping coefficient is also calculated directly from the extrema (red) of the oscillation in Fig. 5.12(a) using the same equation and is shown by the symbols in Fig. 5.14(b). The horizontal red line marks a constant exponential damping coefficient of $d = 0.00063$, which agrees well with the results of both the wavelet analysis and the extrema calculations. This decay of the signal was only seen in the EMD results and not those of the linear fit. This may be a consequence of the linear fit not sufficiently isolating the oscillation from the background. However, the appearance of damping may be artificial, caused by the EMD background in Fig. 5.11(a) following the signal too closely after a time of around 700 s, resulting in a reduced oscillation amplitude.

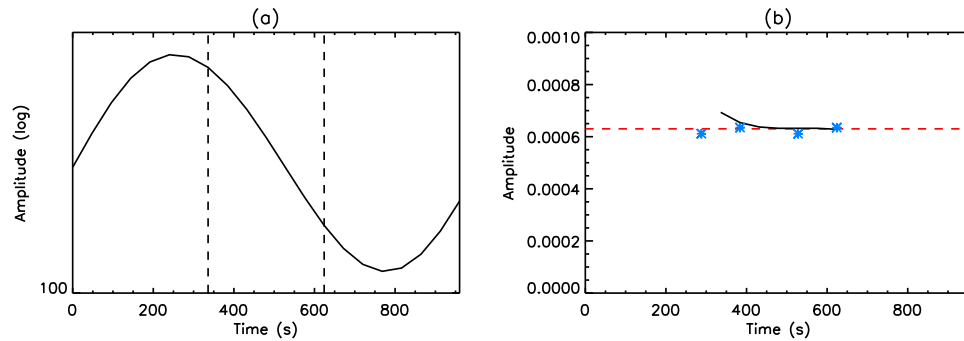


Figure 5.14: (a) amplitude of the wavelet analysis shown in Fig. 5.13(b) at a period of 250 s. (b) damping coefficient calculated from (a) (black) and from the extrema in Fig. 5.12(a) (symbols), with a constant value of 0.00063 marked in red. The vertical dashed lines in (a) mark the COI and the results in (b) are only shown within this region.

Co-spatial and co-temporal CDS data is also analysed. Mg IX (367 Å) rasters are used to align the CDS and TRACE 171 Å data as discussed in Section 5.2.1.2. The position of the CDS 4" slit (which operates in sit and stare mode) relative to the loop is shown in Fig. 5.10 and crosses at 22 Mm along the loop. The position of the slit relative to the loop is again assumed to stay constant for the duration of the 20 minute TRACE data set. The 4" slit data is cleaned and prepared as discussed in Section 5.2.1.2 and reduced to the same time period as the TRACE 171 Å data. This gives a data set of 61 data points with a 16 s cadence which is shown for O IV (554 Å), O V (629 Å) and Mg IX (367 Å) in Figs. 5.15(a), (c) and (e). The background trends determined using linear fit (blue) and EMD (red) are also shown. The resulting oscillations are shown in Figs. 5.15(b), (d) and (f) for O IV, O V and Mg IX, respectively for EMD (black) and linear fit (red). The linear fit results in O IV and O V clearly agree with IMF_3 , albeit with additional higher frequency variations. The agreement between the Mg IX results is less clear, however, and the presence of a periodic oscillation cannot be reliably inferred. This is most likely due to the distance of the CDS slit from the loop footpoint (22 Mm), where, as discussed in Chapters 2 and 3, the decrease in density due to gravitational stratification has reduced the intensity of the oscillation below a level that can be detected.

The He I and Fe XVI lines do not show any sign of this periodic oscillation, which could be because the peak temperatures of the lines are too cold (He I 0.05 MK) and too hot (Fe XVI 7.5 MK), respectively.

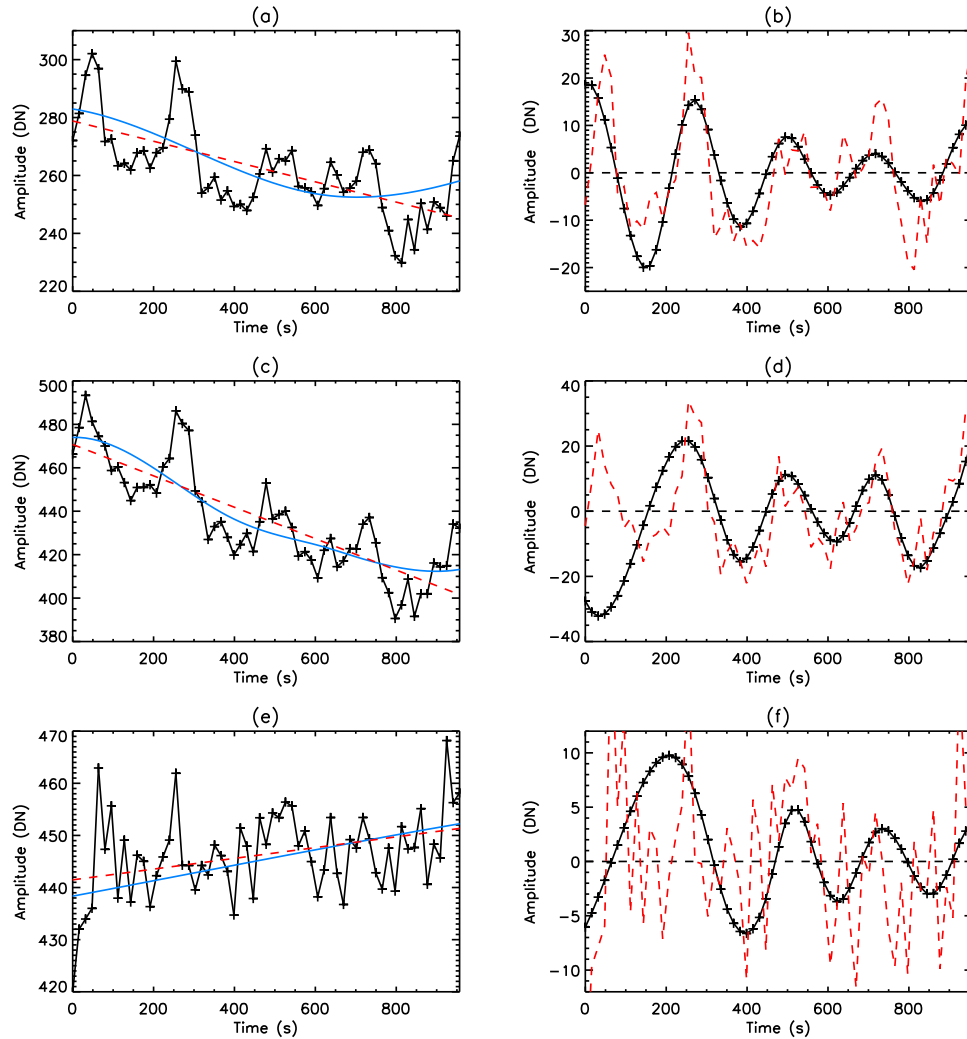


Figure 5.15: (left) signal with a background of $IMF_5 + IMF_6$ (blue) and from linear fitting (red). (right) IMF_3 (black) and oscillation from linear fit (red). (a) and (b) O IV (554 Å), (c) and (d) O V (629 Å) and (e) and (f) Mg IX (367 Å).

FFT's and wavelet analyses of the O IV, O V and Mg IX results are shown in Fig. 9 of Appendix B. The FFT's of the Mg IX signal and oscillation differ greatly, which suggests the EMD process has produced mode mixing and the IMF shown in Fig. 5.15(f) is therefore not a true IMF and hence cannot be confidently interpreted. The FFT's of IMF_3 from the O IV and O V emission lines are shown in Fig. 5.16, along with Mg IX for comparison. Both Oxygen lines clearly show a peak at a period of 250 s, which is also seen in the wavelet analyses of Fig. 9 in Appendix B, with periods between 220 s and 260 s above the confidence level for all time. These periods are consistent with the TRACE 171 Å results. The relative amplitudes of the oscillation in the O IV and O V lines are 2.7% to 7.4% and 2.7% to 7.9%, respectively. These amplitudes are consistent with each other and agree with the values found in Section 5.2.1.2.

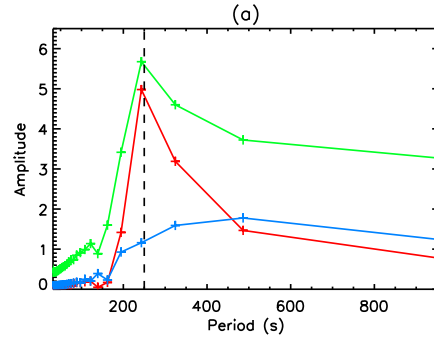


Figure 5.16: FFT of IMF_3 for O IV (554 Å) (red), O V (629 Å) (green) and Mg IX (367 Å) (blue).

5.2.2.2 23:02 UT

TRACE 171 Å and CDS 4" slit data are now analysed for a loop at 23:02 UT on 29th April 2003. The data is cleaned, prepared and summed, as discussed in Section 5.2.1, giving 20 minute data sets with 27 TRACE 171 Å images of 48 s cadence and CDS data with 79 data points and a 16 s cadence.

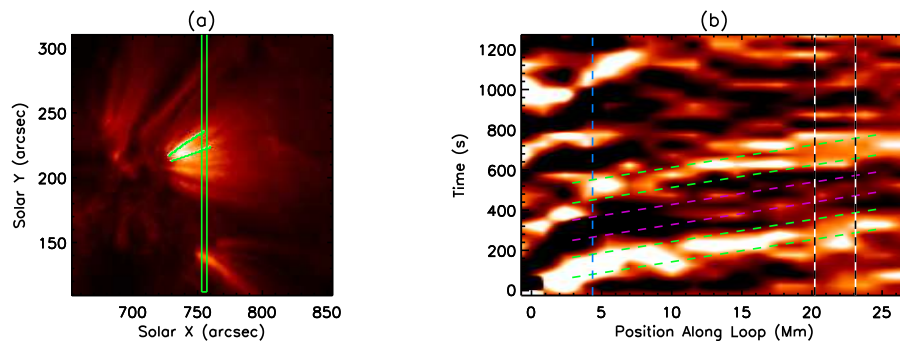


Figure 5.17: (a) loop position in TRACE 171 Å with the CDS slit location also shown. (b) running difference along the loop outlined in (a). The green and pink dashed lines in (b) highlight a propagating feature with periodic nature and the black/white lines mark the position of the CDS slit.

The selected loop is shown in the first image of the TRACE 171 Å data in Fig. 5.17(a) and the position of the CDS slit, at 22 Mm along the loop, is also marked. The running difference along the loop of the TRACE 171 Å data is shown in Fig. 5.17(b). The green and pink lines highlight a propagation feature with periodic nature. From this running difference an oscillation period of 370 s is determined with an average propagation speed of 90 km s^{-1} . The maximum and minimum propagation speeds are found to be 65 km s^{-1} and 155 km s^{-1} , respectively, which, for TRACE 171 Å data, is consistent with propagation at the sound speed of the loop, as expected for slow waves.

The intensity of the loop at the position marked by the blue vertical dashed line in Fig. 5.17(b) is shown as a function of time by the black line in Fig. 5.18(a). The background trend obtained from the EMD is shown in red and is very similar to a linear fit for this signal. The resulting oscillation is given by $IMF_1 + IMF_2$ (as some mode mixing has occurred) and is shown in Fig. 5.18(b). All of the EMD IMF's are shown in Fig. 10 of Appendix B and the background trends from summing these IMF's are shown with FFT's in

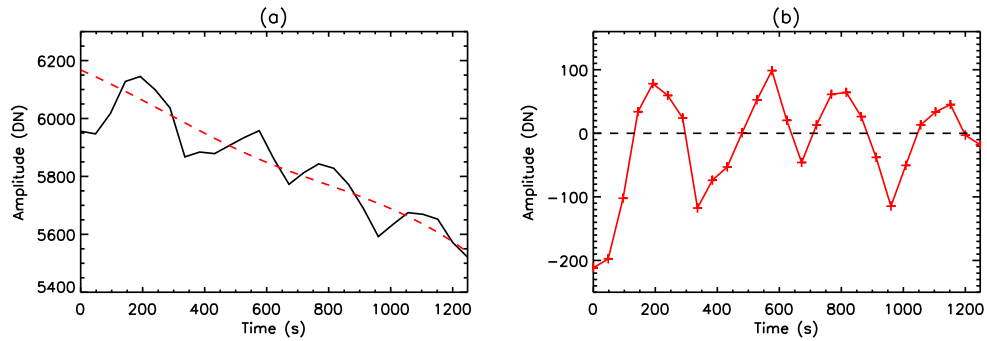


Figure 5.18: (a) Signal (black) along the blue vertical dashed line in Fig. 5.17(b) and $IMF_3 + IMF_4$ (red) with (b) $IMF_1 + IMF_2$ (red).

Fig. 11 of Appendix B.

The oscillation shown in Fig. 5.18(b) has a relative amplitude of 1% to 3.9% with periodicity determined from the FFT and wavelet analyses in Figs. 5.19(a) and (b), respectively, of 200 s to 400 s, which is in agreement with the running difference. The oscillation is detected up to 5 Mm along the loop in the wavelet analysis, but the FFT and the running difference show evidence of an oscillation for much further.

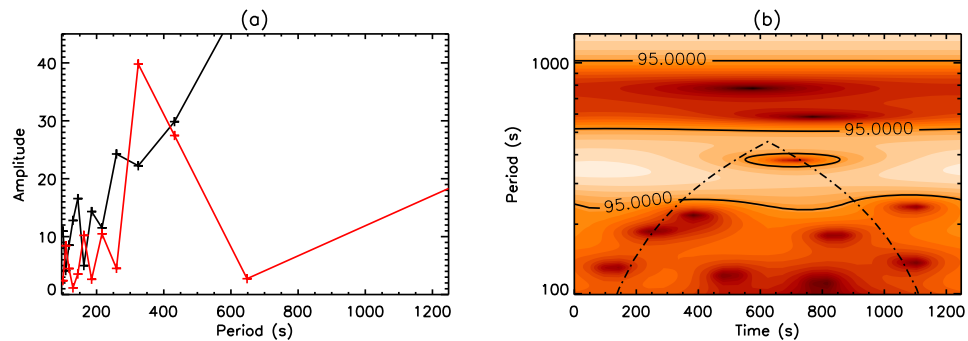


Figure 5.19: (a) FFT (red) and (b) wavelet analysis of $IMF_1 + IMF_2$. The FFT of the signal (black) is also shown in (a).

There is no evidence of this periodicity in the CDS He I (584 Å), O IV (554 Å), O V (629 Å) or Fe XVI (360 Å) data. However, the Mg IX (367 Å) data does suggest an oscillation may be present (Fig. 5.20(a)), but the amplitudes of the FFT (Fig. 5.20(b)) as well as the wavelet analysis are too low to determine this with confidence. The lack of detection in the CDS emission lines is likely to be due to the slit position, which only just catches the very edge of the loop. The limited field of view of the CDS slit makes co-temporal and co-spatial observations of loop footpoints in CDS and TRACE very difficult.

5.3 TRACE, CDS and EIS Observations

In the previous section co-spatial and co-temporal TRACE and CDS data was analysed to find evidence of propagating slow waves. The large field of view of TRACE allows loops to be analysed along their

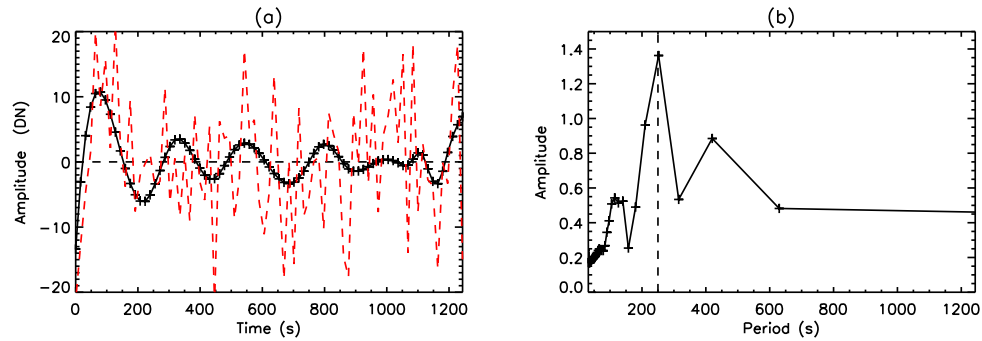


Figure 5.20: (a) oscillation in CDS Mg IX (367 \AA) using EMD (black) and linear fit (red) and (b) FFT of the black oscillation in (a).

entire length. This is also possible using CDS rasters, however, the low cadence (16 minutes in the previous section) means that oscillation periods of a few minutes cannot be observed. This is overcome by the CDS sit and stare observations which in the previous section had a cadence of 16 s. The use of CDS also allows the loop to be observed in many different emission lines and hence possibly propagation through the atmosphere. A disadvantage of the sit and stare observations, however, is the small field of view in the solar x direction. Unless the loop is orientated vertically, only a small section of the loop will be within the field of view of the slit. This is the case in Section 5.2.2 where oscillations are observed at the loop footpoint in TRACE, but the CDS slit observes 22 Mm along the loop. Sit and stare observations can be made using the EIS $40''$ slot, which allows the same high cadence observations but with a much larger field of view and with the correct pointing an entire loop can be observed. As discussed in Chapter 3, EIS also has a higher sensitivity than CDS and hence could show oscillations more clearly.

Joint TRACE, CDS and EIS observations were undertaken on 15th and 16th December 2007 with an aim to observe coronal loops and identify slow waves propagating through the solar atmosphere. Co-temporal and co-spatial observations using all three instruments was not possible, however, due to pointing errors between CDS and EIS. Fig. 5.21(a) shows the position, after alignment, of the CDS slit and the EIS slot within the TRACE field of view for (a) 15th December 2007 and (b) 16th December 2007. The EIS slot was repositioned after each exposure to give two adjacent images. In this way the $40''$ slot with a 20s cadence produced images with an $80''$ field of view and a 40s cadence.

Despite the lack of co-spatial and co-temporal CDS and EIS data, the CDS and EIS data can still be analysed and compared to TRACE separately. The CDS and TRACE data were aligned and analysed using the techniques described in Section 5.2. The EIS data is cleaned and prepared using `eis_prep` in Solarsoft IDL. The larger field of view of the EIS slot compared to the CDS slit means that the EIS slot can be used to align to the TRACE data without the need for a raster. Firstly, each EIS emission line is aligned to the He II (256 \AA) line. This alignment depends on the position of the emission line on the CCD and therefore the wavelength of the line. Each emission line is aligned in solar y using the Solarsoft `eis_ccd_offset` routine. In addition the emission lines in the short wavelength band (170 \AA to 211 \AA) are adjusted by $4''$ in solar x to match those of the long wavelength band. The data is now adjusted for the solar y pointing error of $-13.7''$ (Mariska 2010) and the jitter is removed using the Solarsoft `eis_jitter` routine. This broadly aligns the TRACE and EIS data in both solar x and solar y , however, the pointing values do vary between the

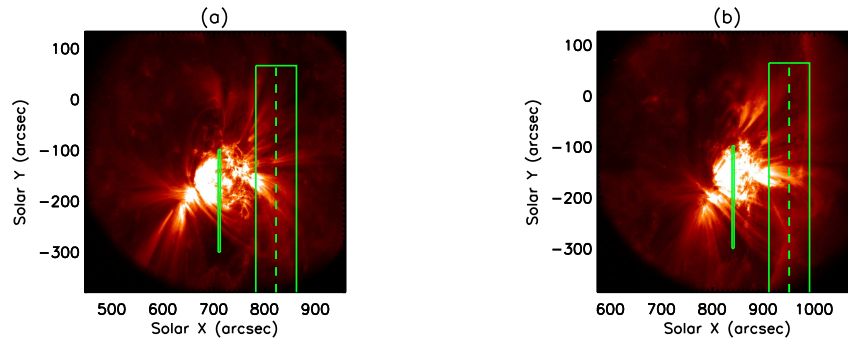


Figure 5.21: Position of the CDS slit and the EIS slot compared to TRACE for (a) 15th December 2007 and (b) 16th December 2007.

instruments.

In addition, the jitter is not completely removed by the `eis_jitter` routine and shifts of up to $5''$ in both x and y are still seen. The jitter can be removed and the TRACE and EIS data aligned using the `c_correlate` routine in IDL. Aligning the TRACE and EIS data requires only a single image to be aligned as the pointing difference between the instruments remains constant for the duration of the observation. The jitter, however, affects every EIS image and therefore `c_correlate` must be used to align every image of the EIS data to the first image, which is then aligned to TRACE. In this case the EIS Si VII (275 \AA) and Fe XII (195 \AA) lines were used. However, for the data sets discussed here the timescale of the jitter is very similar to the intensity variation of the features in the images. Consequently, `c_correlate` cannot be used to reliably remove the jitter as changes in loop intensity are often mistaken for movement of the image by jitter. In addition, the field of view of the observations was kept small to allow a higher cadence, but this removes other background features that may have slower intensity variations that could therefore be used to align the images. In this case, in order to remove the jitter every image of the EIS data must be aligned manually.

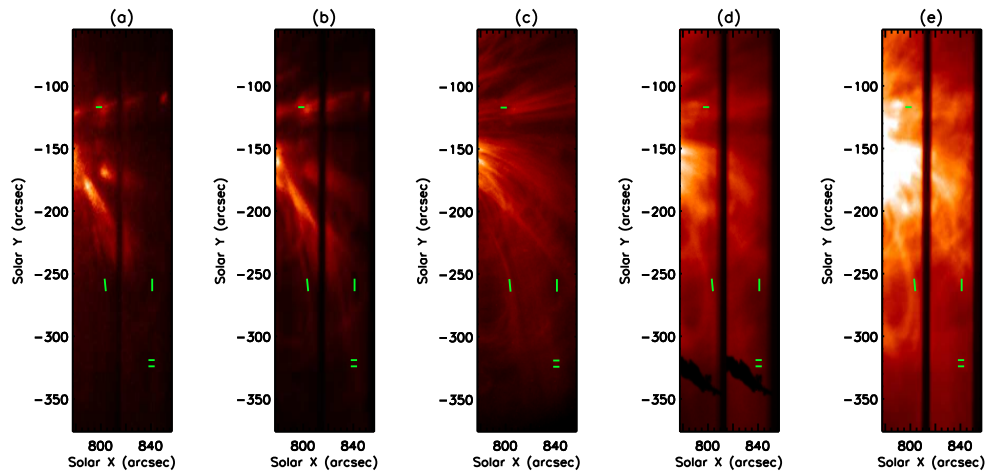


Figure 5.22: Alignment of (a) EIS Mg VI (269 \AA), (b) EIS Si VII (275 \AA), (c) TRACE 171 \AA , (d) EIS Fe XI (188 \AA) and (e) EIS Fe XII (195 \AA) at the beginning of the data sequence.

Fig. 5.22 shows the aligned EIS data for (a) Mg VI (269 \AA), (b) Si VII (275 \AA), (d) Fe XI (188 \AA) and (e)

Fe XII (195 Å) compared to the TRACE 171 Å data in (c), with the TRACE field of view reduced to that of the EIS slot. The slot data has 11 emission lines covering temperatures from 0.05 MK (He II (256 Å)) to 5 MK (Ca XVII (192 Å)). The images in Fig. 5.22 cover a temperature range of 0.4 MK (Mg VI (269 Å)) to 1.25 MK (Fe XII (195 Å)). The dark vertical bands in the centre of the EIS images mark where two slot exposures have been joined and show that the images have been shifted during the alignment process causing some data to be lost.

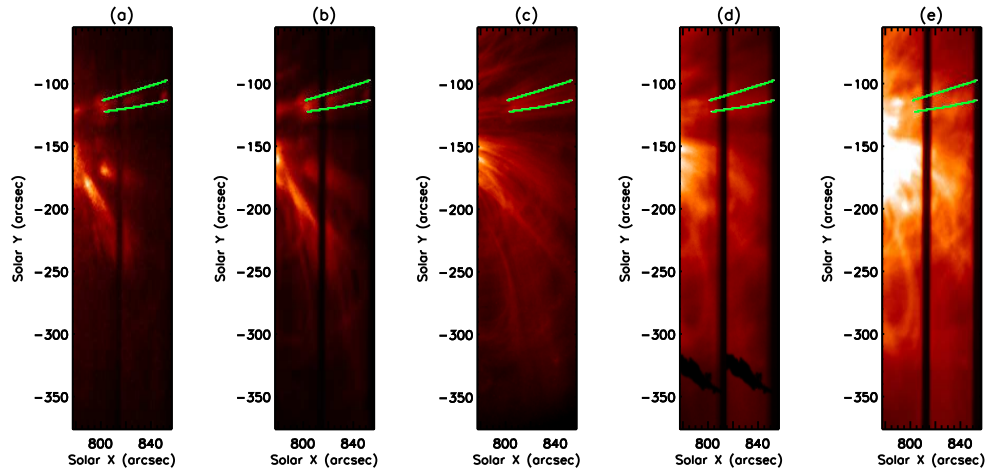


Figure 5.23: Position of a loop in (a) EIS Mg VI (269 Å), (b) EIS Si VII (275 Å), (c) TRACE 171 Å, (d) EIS Fe XI (188 Å) and (e) EIS Fe XII (195 Å).

A loop is selected from the TRACE 171 Å data and shown in Fig. 5.23(c). The same loop is highlighted (green lines) in the EIS slot data of (a) Mg VI, (b) Si VII, (d) Fe XI and (e) Fe XII. Unlike the CDS data the two spatial dimensions of the EIS slot allow the entire loop to be observed. In addition, the slot data allows the same running difference along the loop to be produced as seen previously in TRACE 171 Å data. This allows propagating features and speeds to be identified and determined throughout the solar atmosphere. The running difference along the loop highlighted in Fig. 5.23 is shown in Figs. 5.24(a) and (b) for EIS Si VII and TRACE 171 Å, respectively. Both images show similar features as the Si VII line is sensitive to temperatures around 0.63 MK and TRACE 171 Å to temperatures between 0.6 MK and 1 MK. The vertical band in Fig. 5.24(a) between 4 Mm and 8 Mm in which no bright or dark regions are seen is an artificial feature and shows where this section of the loop in Fig. 5.23(b) has not been observed due to the alignment of the emission lines on the CCD.

Both data sets, on the 15th and 16th December 2007, were analysed for all the loops that had co-spatial and co-temporal TRACE and EIS data and no evidence of propagating slow waves was found, which may be the result of the difficulty in reliably determining low amplitude oscillations when the EIS jitter is not fully removed. No evidence of propagating slow waves was found for the CDS and TRACE data either, however, in this case there were very few distinct isolated loops within the CDS field of view that could be confidently analysed.

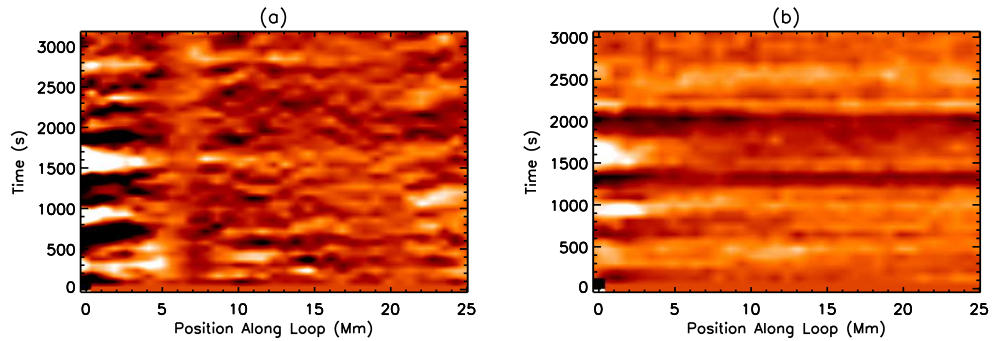


Figure 5.24: Running difference along the loop outlined in Fig. 5.23 for (a) EIS Si VII (275 Å) and (b) TRACE 171 Å.

5.4 Observations Conclusions

Co-spatial and co-temporal TRACE and CDS data have been analysed to find evidence of slow waves propagating along coronal loops. The data sets were taken over a period from 21st April 2003 to 3rd May 2003. The TRACE 171 Å data has been analysed previously by McEwan and De Moortel (2006) who found 25 examples of propagating slow waves. The addition of the CDS data allows the loop to be observed in many more emission lines and therefore at different temperatures in order to observe the propagation of the waves through the solar atmosphere. The narrow field of view of the CDS slit means that joint CDS and TRACE observations are only possible for one of the examples found by McEwan and De Moortel (2006).

The TRACE 171 Å data has been analysed using FFT's, wavelet analyses and EMD, in addition to a linear fitting as used by McEwan and De Moortel (2006). The results of the TRACE analysis for 30th April 2003 found a propagating oscillation with a relative amplitude of 1.4% to 3.2% and a period of around 300 s, propagating at the coronal sound speed of around 120 km s^{-1} . These properties agree with McEwan and De Moortel (2006) and are consistent with a propagating slow magnetoacoustic wave. The oscillation is detected for a greater length along the loop in McEwan and De Moortel (2006) (11.2 Mm) than found here (3 Mm), which is likely to be a consequence of the normalisation of the data. The CDS data was analysed using the same techniques and evidence of an oscillation with the same period of around 300 s was found in the He I (584 Å), O IV (554 Å) and O V (629 Å) emission lines. The relative amplitude of the oscillation was found to be greater in the transition region (2.3% to 6.0%) than in the corona (1.4% to 3.2%). This is consistent with the theoretical work of Chapters 2 and 3 and with previous observations (e.g. Marsh et al. 2003). However, a more rigorous treatment of errors in this chapter is required in order to reliably determine, in particular, the periodicity of the detected oscillations.

A slow wave with a period of 210 s to 275 s and a relative amplitude of 0.5% to 2.3% propagating in the corona at around 100 km s^{-1} was observed. After using the EMD method to extract the oscillatory signal, the amplitude of this signal was found to decay with time. The damping was determined using the method described in Section 4.2.2.2 and a constant exponential damping rate was found with a damping coefficient of 0.00063. However, the presence of damping is only seen using the EMD technique and may therefore be an artificial feature produced by errors in determining the background near the boundary. Again, higher amplitudes were observed in the transition region than in the corona.

A third propagating wave was found in the TRACE 171 Å data with a period of 370 s, amplitude of 1% to 3.7% and a propagation speed of around 90 km s^{-1} . No clear evidence of this wave was found in the CDS data, except for a small peak in the FFT and the wavelet analysis of the Mg IX (367 Å) data. The lack of a detection in CDS is most likely due to the position of the CDS slit, which was 22 Mm from the loop footpoint.

Co-spatial and co-temporal TRACE, CDS and EIS observations for 15th and 16th December 2007 were not possible due to a pointing error between CDS and EIS. The co-spatial and co-temporal TRACE and EIS data were analysed, but no clear evidence of propagating slow waves was found. This may be a consequence of the lack of large diffuse loops within the EIS field of view in which propagating slow waves are commonly observed, in addition to, the difficulty of removing the EIS jitter sufficiently to allow low amplitude oscillations to be reliably detected. No evidence of slow waves was found in the co-spatial and co-temporal CDS and TRACE data either due to the lack of isolated loops within the CDS field of view.

Chapter 6

Conclusions

The propagation and damping of slow magnetoacoustic waves has been studied theoretically using numerical modelling and the observational properties of these waves have been examined using forward modelling. In addition to this, the analysis techniques used to detect such oscillations were investigated and observational data analysed for evidence of propagating slow waves.

The propagation of slow waves with a period of five minutes has been numerically simulated, in 1D, through the transition region and the corona. Loops were modelled at a range of uniform equilibrium temperatures and with a non-uniform equilibrium temperature from a transition region temperature of 0.33 MK to a coronal value of 1.25 MK. The results of a uniform temperature equilibrium at 1 MK are consistent with previous work by De Moortel and Hood (2003, 2004). Without damping the perturbation amplitudes have a $\rho_0^{-1/4}$ dependence as calculated, for Alfvén waves, by Wright and Garman (1998) and with gravitational stratification included the growth of the perturbation amplitudes agrees with Roberts (2004).

The effect of thermal conduction on the propagation of slow waves was investigated and found to produce a phase shift between the perturbations in velocity, density and energy/temperature which may be observable as a phase shift between intensity and Doppler shift observations. Damping due to optically thin radiation and compressive viscosity were also studied. At all temperatures of the model (0.33 MK to 1.25 MK) the damping due to optically thin radiation is negligible compared to that of thermal conduction, but would become increasingly important as the temperature falls and the density increases towards the solar surface. The inclusion of compressive viscosity, however, does show a clear, but small, amount of extra damping compared to that of thermal conduction alone.

With thermal conduction, compressive viscosity and gravitational stratification included, the wave amplitudes grow in the transition region and are damped in the corona with a detection length of order 50 Mm. Localised spikes in the energy and density perturbations are seen in the transition region, where the temperature and density gradients are largest. This is caused by a temperature profile with a transition region height of 14 Mm and a width of around 10 Mm. However, a more realistic height and width may be 2 Mm and 0.1-0.2 Mm, respectively. A narrower transition region width would increase the temperature and density gradients and may, therefore, increase the spikes produced. On the other hand, a lower transition region

height would reduce the growth of the perturbations by gravitational stratification and therefore result in lower oscillation amplitudes and hence reduced detection lengths.

The synthesised emission for TRACE 171 Å and several CDS and EIS lines has been modelled along a loop of uniform and non-uniform equilibrium temperature and at a single position along the loop as a function of time. By using a range of spectral lines, waves can be observed as they propagate through the solar atmosphere. The resulting intensity depends in a complicated way on the emissivity, ionisation balance and the loop density. The ionisation balance can cause drastic phase changes in the intensity compared to the temperature and density oscillations, where the shape of the intensity oscillation is often very anti-symmetric. The exact effect of the emissivity, ionisation balance and the loop density varies for each example, however, certain cases show similar characteristics. For example, loops observed that are hotter than the peak formation temperature of the emission line used are often out of phase with the temperature and density of the loop, due to the ionisation balance.

Due to the dependence of intensity on the loop density, the inclusion of gravitational stratification for undamped waves causes the intensity along a loop to decay rapidly, giving the appearance of damping. TRACE 171 Å, CDS Mg x and EIS Fe XII all show damped oscillations to around 100 Mm, despite undamped temperature and density perturbations. Damping due to thermal conduction and compressive viscosity increases this damping, with oscillations now observable to around 50 Mm. However, as a result of the ionisation balance, the inclusion of damping terms can actually increase the amplitude of some parts of the oscillation. The phase shift produced between the temperature and density perturbations by thermal conduction affects the phase of the intensity oscillations, adding further complexity to the interpretation of the data. In addition, the strength of thermal conduction is greater in the corona than the transition region, hence this phase shift changes as the wave propagates through the atmosphere.

Observations of an oscillation along a loop from different emission lines with different peak formation temperatures are likely to show oscillations with different phases, shapes and amplitudes. These effects demonstrate the difficulty in deducing the density and temperature perturbations from observed oscillations. However, by comparing many emission lines, and using knowledge of the ionisation balance and emissivity, the phase of the density and temperature perturbations and the temperature of the loop can be found more reliably. Doppler velocity observations (if sensitive enough) would reveal the phase and amplitude of the velocity perturbations, which would consequently aid the interpretation of the oscillation in intensity. All of the emission lines studied show intensity spikes in the transition region due to the spikes in the energy and density perturbations of the transition region. There is some observational evidence for dominant transition region emission, but not to the degree suggested here. The reason for the discrepancy is unclear, but may be due to the width and position of the transition region used in the model.

The use of several techniques to identify and determine the properties of oscillations in a range of time series with known analytical components has been investigated. The use of each technique has been demonstrated for a single oscillation about a constant background and with multiple oscillations about a non-constant background. The effects of damping, wave beating and a reduced cadence were investigated in addition to an oscillation which is only present for part of the time series. Fourier and wavelet analysis were both used to determine the frequencies present in the time series. The FFT was found to be very accurate at identifying the periods present in the time series, particularly at low period, however, this was not possible for the

background trend as the time series was too short compared to the period of the background. The periods determined by the wavelet analysis are always consistent with those from the FFT, giving confidence in the results. The period resolution of the wavelet analysis at short periods is particularly reduced compared to the FFT and the COI is very restrictive for longer periods. However, the time resolution given by the wavelet analysis gives information that cannot be determined from the FFT alone.

Polynomial fitting and EMD were used to determine the background trends and separate the oscillations from these trends, thus allowing the properties of the oscillations to be seen more clearly. The choice of polynomial fitting degree is sometimes clear, such as a linear fit for a constant background, but is often far more difficult. An inappropriate background determination by polynomial fitting, or smoothing/averaging, will result in variations already in the data to be mixed between components and hence the physical relevance might be lost. EMD is a more robust technique for extracting oscillations from a wide range of data sets and is capable of separating a time series into all of its different timescales. This is particularly important for time series containing multiple oscillations. However, the extraction of extra, unphysical, IMF's that often occurs can make the interpretation of each IMF difficult. By performing FFT's on each IMF a clearer picture can be gained of whether an IMF truly contains a separate timescale or has been extracted from another IMF. EEMD was also examined, which is an extension to the EMD technique and the potential of EEMD to identify even extremely low amplitude and short lived oscillations has been demonstrated. By using EEMD some of the intrinsic nature of EMD is lost as the noise amplitude and the ensemble number must be chosen. It is not clear whether the same value of the signal to noise ratio should be used for all data sets or a different value chosen each time. The interpretation of each IMF can also be more difficult if the wrong noise amplitude is chosen. Despite this, EEMD is a very powerful technique to extract oscillations from complex data sets. Unlike the wavelet analyses, the EMD and EEMD results in this chapter do not contain confidence levels, however, this work could be extended by using a statistical significance test to give a confidence level to any oscillations identified. This would ease the interpretation of each IMF and give more reliable results.

Damping can be seen in an FFT by the width of a peak, in wavelet analysis by a reduction in amplitude with time and with polynomial fitting and EMD by separating the oscillations from the background, showing the oscillation as a function of time. The damping coefficients of two oscillations were determined using wavelet analyses and directly from EMD to within 20% of the analytical solution. For the short time series used here the width of the FFT peak produced from the finite number of periods of the signal was difficult to distinguish from the width due to damping.

TRACE, CDS and EIS data have been analysed to find evidence of slow waves propagating along coronal loops. Co-spatial and co-temporal TRACE, CDS and EIS observations were not possible due to a pointing error between CDS and EIS. The co-spatial and co-temporal TRACE and EIS data were analysed, however, no clear evidence of propagating slow waves was found. This may be a consequence of the lack of large diffuse loops within the EIS field of view in which propagating slow waves are commonly observed, in addition to the difficulty of removing the EIS jitter sufficiently to allow low amplitude oscillations to be reliably detected. Co-spatial and co-temporal TRACE and CDS data were analysed, where the TRACE 171 Å data was analysed previously by McEwan and De Moortel (2006). They found 25 examples of propagating slow waves, however, the narrow field of view of the CDS 4" slit meant that joint CDS and TRACE observations were only possible for one of the examples found. The addition of the CDS data allows the loop to

be observed in many more emission lines and therefore at different temperatures in order to observe the propagation of the waves through the solar atmosphere.

The results of the TRACE analysis found a propagating oscillation with a relative amplitude of 1.4% to 3.2% and a period of around 300 s, propagating at the coronal sound speed of around 120 km s^{-1} . These properties agree with McEwan and De Moortel (2006) and are consistent with a propagating slow magnetoacoustic wave. The oscillation is detected for a greater length along the loop in McEwan and De Moortel (2006) (11.2 Mm) than found here (3 Mm), which is likely to be a consequence of the normalisation of the data. The CDS data shows evidence of an oscillation with the same period of around 300 s in the He I (584 Å), O IV (554 Å) and O V (629 Å) emission lines. The relative amplitude of the oscillation was found to be greater in the transition region (2.3% to 6.0%) than in the corona (1.4% to 3.2%), which is consistent with the numerical simulations and the forward modelling as well as with previous observations (e.g. Marsh et al. 2003). Evidence of a decaying oscillation was found in TRACE 171 Å data using EMD, with a period of 210 s to 275 s and a relative amplitude of 0.5% to 2.3%. A constant exponential damping rate was found with a damping coefficient of 0.00063, however, the presence of damping is only seen using the EMD technique and may therefore be an artificial feature produced by errors in determining the background near the boundary.

Future Work

The inclusion of an inclination angle for magnetic field lines, as shown by De Pontieu et al. (2005), allows leakage of five minute p-modes through the upper photosphere and the chromosphere. As only the transition region and the corona were considered in the model the inclusion of an inclination angle at the solar surface is left to future study. Including an inclination angle and reducing the minimum temperature of the model to that of the solar temperature minimum (from 0.33 MK to 4400 K) would allow the propagation of slow waves from the surface to be modelled. In addition to lowering the minimum temperature of the model, the height and width of the transition region could be reduced to more realistic values. A steeper transition region at lower altitude would reduce the density contrast between the transition region and the corona due to gravitational stratification and may therefore decrease the difference between the emission from the transition region and the corona and give a value closer to that of observations. However, due to the high density below $10^{4.3} \text{ K}$ the approximation of optically thin radiation used in the model would become invalid.

The detection length of 50 Mm found from the forward modelling is much greater than that observed for propagating slow waves, which is around 10 Mm (De Moortel et al. 2002a). Inclined magnetic field lines would reduce the effects of gravitational stratification on increasing the wave amplitude and hence may reduce detection lengths. Also, this is an upper limit in the detection length as observations have noise to consider which would reduce the detection threshold. A more accurate detection length could be found from forward modelling by adding noise to the simulation results, in addition to using spatial and temporal summing of the synthesised emission results as used to analyse real signals. The signatures of the phase shift produced by thermal conduction could be investigated further by extending the forward modelling code to include Doppler velocity observations. The required sensitivity to detect this phase shift could then

be quantified.

Many observations of slow waves propagating along coronal loops have required data to be summed in both time and space (e.g. De Moortel et al. 2002a; McEwan and De Moortel 2006) to increase the data counts and the signal to noise ratio. However, EEMD may allow these oscillations to be identified from this noisy data despite the low data counts. Noise levels are routinely calculated for data, however, the extraction of IMF's by the EEMD technique is particularly sensitive to the noise level, making appropriate noise determination difficult. Consequently, more work is required in order to determine a reliable and consistent method of calculating the noise across a wide range of data sets. In addition, the ability to confidently interpret the importance and relevance of each IMF and disregard artificial features is essential. Applying FFT's to each IMF to determine the success of timescale separation is very useful and for data sets longer than those analysed here the use of wavelet analysis may be particularly beneficial. The significance test of the EMD/EEMD code (Wu and Huang 2009) could be used to give a confidence level to the results, thereby greatly increasing the reliability of oscillations determined using EMD.

Appendix A: Thomas Algorithm in Lare1d

Heat Conduction Subroutine For Lare1d

The subroutine `heat_conduct` in `Lare1d` calculates the thermal conduction term in Eq. (2.71), which requires the use of a Thomas Algorithm, implemented by C.S. Brady (Centre for Scientific Computing, University of Warwick), with line-tied boundary conditions consistent with Table 2.1. Considering only the thermal conduction term, Eq. (2.71) becomes,

$$\begin{aligned}\frac{\partial \epsilon}{\partial t} &= -\frac{1}{\rho} \frac{\partial}{\partial x} \left(d \epsilon^{5/2} \frac{\partial \epsilon}{\partial x} \right), \\ &= -\frac{1}{\rho} \frac{\partial}{\partial x} \left(\kappa_{\parallel} \frac{\partial \epsilon}{\partial x} \right),\end{aligned}$$

where $\kappa_{\parallel} = d \epsilon^{5/2}$ and d is given in Eq. (2.11) (note the change of sign to be consistent with `Lare1d`). This gives,

$$\frac{\partial \epsilon}{\partial t} = -\frac{\kappa_{\parallel}}{\rho} \frac{\partial^2}{\partial x^2} - \frac{1}{\rho} \frac{\partial \kappa_{\parallel}}{\partial x} \frac{\partial \epsilon}{\partial x},$$

which in finite difference terms becomes,

$$\begin{aligned}\frac{\partial \epsilon}{\partial t} &= \frac{\epsilon_{ix}^{n+1} - \epsilon_{ix}^n}{\delta t}, \\ &= -\frac{\kappa_{\parallel ix}^n}{\rho_{ix}^n} \left(\frac{\epsilon_{ix+1}^n - 2\epsilon_{ix}^n + \epsilon_{ix-1}^n}{\delta_{xcix}^2} \right) - \frac{1}{\rho_{ix}^n} \left(\frac{\kappa_{\parallel ix+1}^n - \kappa_{\parallel ix-1}^n}{2\delta_{xcix}} \right) \left(\frac{\epsilon_{ix+1}^n - \epsilon_{ix-1}^n}{2\delta_{xcix}} \right), \\ \epsilon_{ix}^{n+1} &= \epsilon_{ix}^n - \frac{\delta t \kappa_{\parallel ix}^n}{\delta_{xcix}^2 \rho_{ix}^n} (\epsilon_{ix+1}^n - 2\epsilon_{ix}^n + \epsilon_{ix-1}^n) - \frac{\delta t}{4\delta_{xcix}^2 \rho_{ix}^n} (\kappa_{\parallel ix+1}^n - \kappa_{\parallel ix-1}^n) (\epsilon_{ix+1}^n - \epsilon_{ix-1}^n).\end{aligned}$$

In `Lare1d` parameters A_1 and A_2 (shown in the code below) are defined as,

$$\begin{aligned}A_1 &= \frac{\delta t}{4\delta_{xcix}^2 \rho_{ix}^n} (\kappa_{\parallel ix+1}^n - \kappa_{\parallel ix-1}^n), \\ A_2 &= \frac{\delta t \kappa_{\parallel ix}^n}{\delta_{xcix}^2 \rho_{ix}^n},\end{aligned}$$

which gives,

$$\begin{aligned}\epsilon_{ix}^{n+1} &= \epsilon_{ix}^n - A_2(\epsilon_{ix+1}^n - 2\epsilon_{ix}^n + \epsilon_{ix-1}^n) - A_1(\epsilon_{ix+1}^n - \epsilon_{ix-1}^n), \\ &= \epsilon_{ix-1}^n(-A_2 + A_1) + \epsilon_{ix}^n(1 + 2A_2) + \epsilon_{ix+1}^n(-A_2 - A_1).\end{aligned}$$

The heat_conduct subroutine in which the thermal conduction term is calculated is shown below:

```

SUBROUTINE heat_conduct(set_h_cond)
  REAL(num),DIMENSION(:),ALLOCATABLE :: a,b,c,d,kappa_par
  REAL(num) :: m,A1,A2
  REAL(num) :: pow=5.0_num/2.0_num
  LOGICAL, INTENT(IN) :: set_h_cond
  ALLOCATE(a(-1:nx+1),b(-1:nx+1),c(-1:nx+1),d(-1:nx+1),kappa_par(-2:nx+2))

  DO ix = 0,nx+1
    kappa_par(ix)=kappa*energy(ix)**pow
  ENDDO

  DO ix = 0,nx+1
    A1=(dt/((2.0_num*dxc(ix))**2*rho(ix)))*(kappa_par(ix+1)-kappa_par(ix-1))
    A2=(dt/(dxc(ix)**2*rho(ix))) * kappa_par(ix)
    a(ix) = -A2+A1
    b(ix) = (1.0_num+2.0_num*A2)
    c(ix) = -A2-A1
    d(ix) = energy(ix) - h_cond(ix) * dt / rho(ix)
  ENDDO

  !Boundary Conditions
  b(0)=1.0_num
  c(0)=0.0_num
  a(nx+1)=0.0_num
  b(nx+1)=1.0_num

  !Thomas Algorithm
  DO ix = 1,nx+1
    m=a(ix)/b(ix-1)
    b(ix)=b(ix)-m*c(ix-1)
    d(ix)=d(ix)-m*d(ix-1)
  ENDDO

  DO ix=nx,1,-1
    energy(ix)=(d(ix)-c(ix)*energy(ix+1))/b(ix)
  ENDDO

  DEALLOCATE(a,b,c,d,kappa_par)
END SUBROUTINE heat_conduct

```

Appendix B: TRACE and CDS Observations

30th April 2003 - 16:33 UT

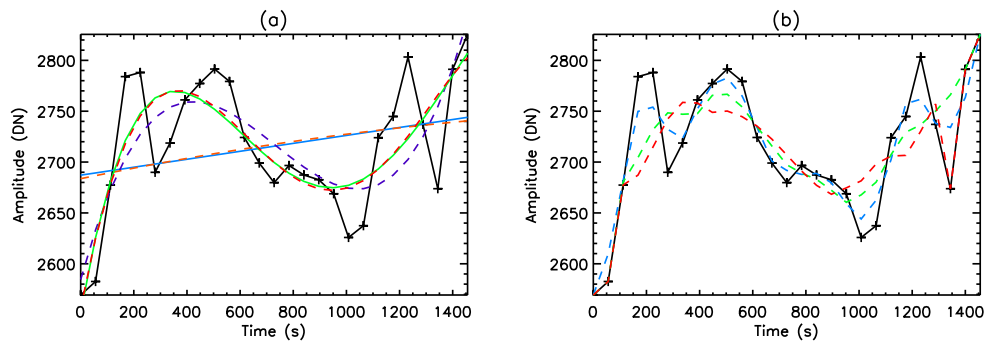


Figure 1: Background trend determination of the signal in Fig. 5.2(b) (shown here in black). (a) polynomial fitting with degree 1 (blue), 2 (orange), 3 (purple), 4 (green) and 5 (red). (b) data smoothing with degree 3 (blue), 5 (green) and 7 (red).

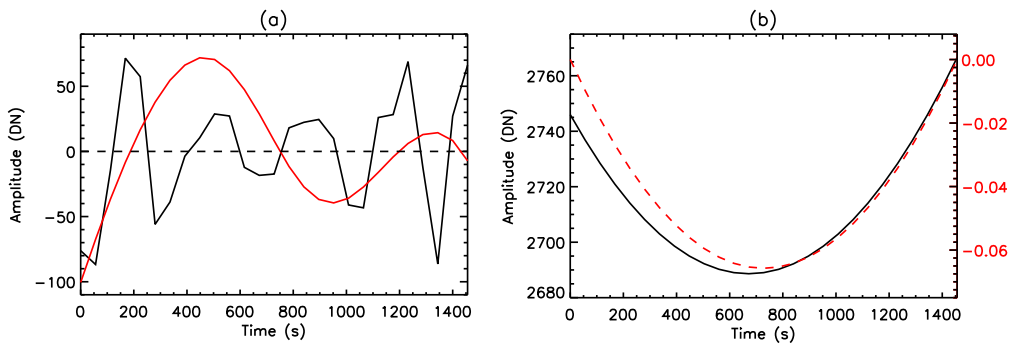


Figure 2: EMD IMF's. (a) IMF_1 (black) and IMF_2 (red) with (b) IMF_3 (red) and IMF_4 (black).

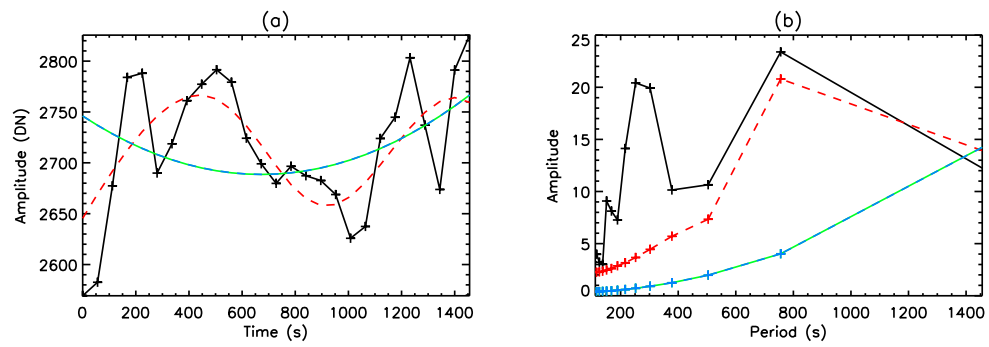


Figure 3: EMD background trends. (a) background trends and (b) FFT's of the trends in (a). Signal (black), $\sum_{i=2}^4 IMF_i$ (red), $IMF_3 + IMF_4$ (green) and IMF_4 (blue).

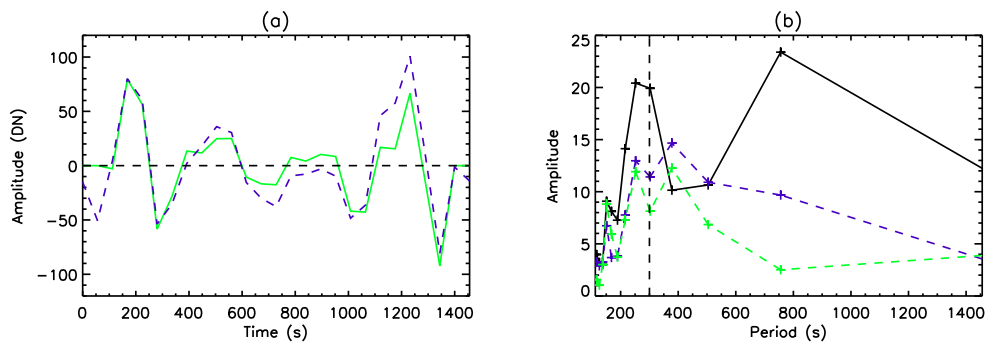


Figure 4: (a) oscillations and (b) FFT's of the oscillations in (a). Polynomial degree 3 (purple) and smoothing degree 5 (green) with the FFT of the signal (black).

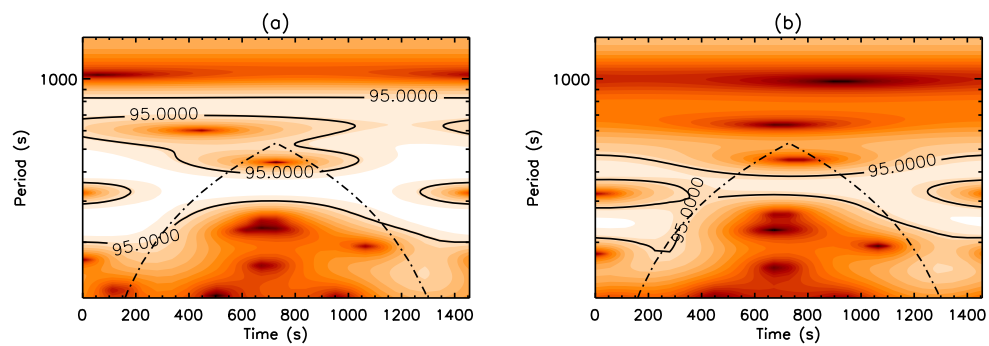


Figure 5: Wavelet analyses of the oscillations in Fig. 4(a) for (a) polynomial fitting degree 3 and (b) data smoothing degree 5.

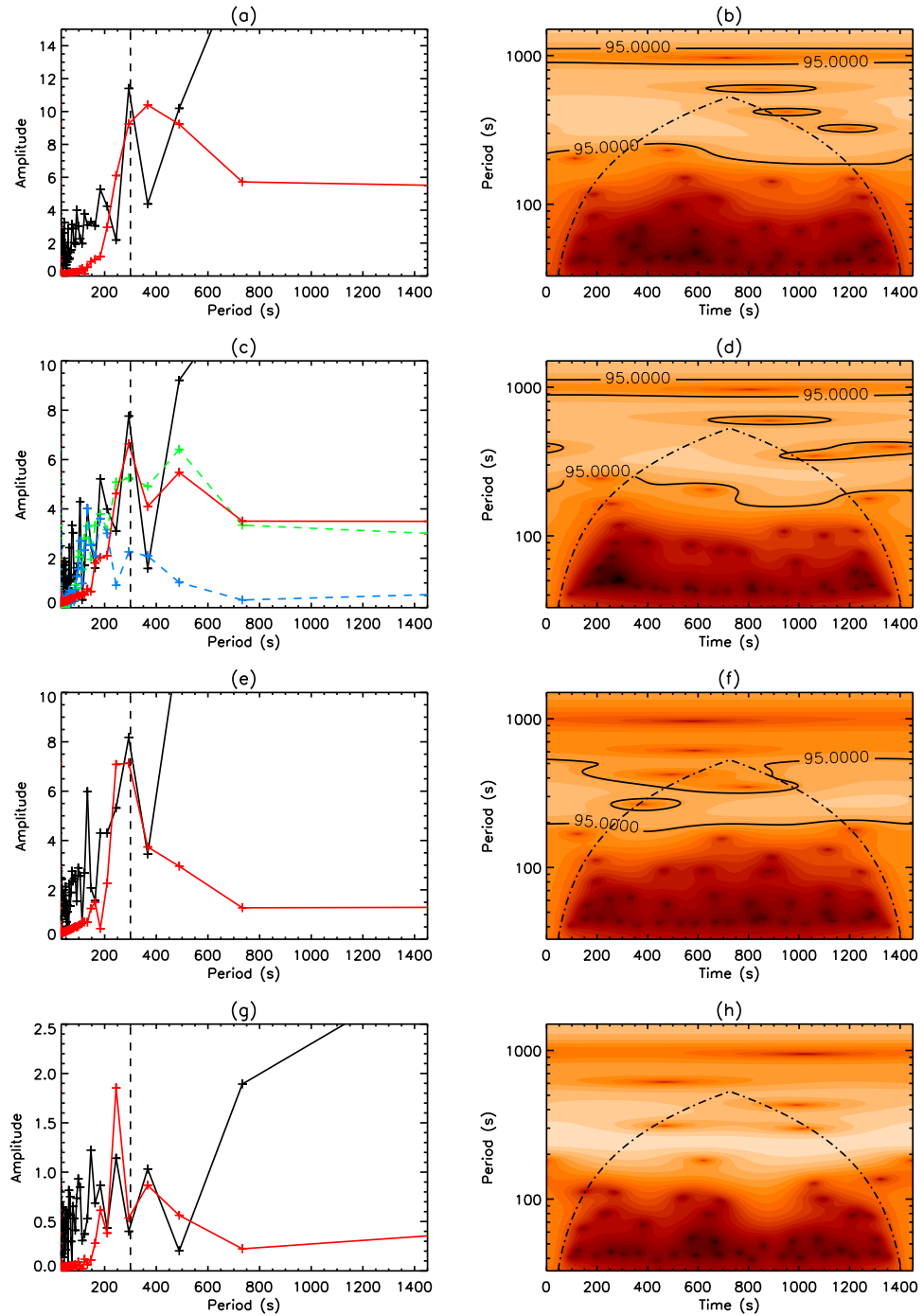


Figure 6: (left) FFT and (right) wavelet analysis of IMF_3 . (a) and (b) He I (584 Å), (c) and (d) O IV (554 Å), (e) and (f) O V (629 Å) and (g) and (h) Mg IX (367 Å). The FFT's of IMF_2 (blue) and $IMF_2 + IMF_3$ (green) are also shown in (c).

29th April 2003 - 22:06 UT

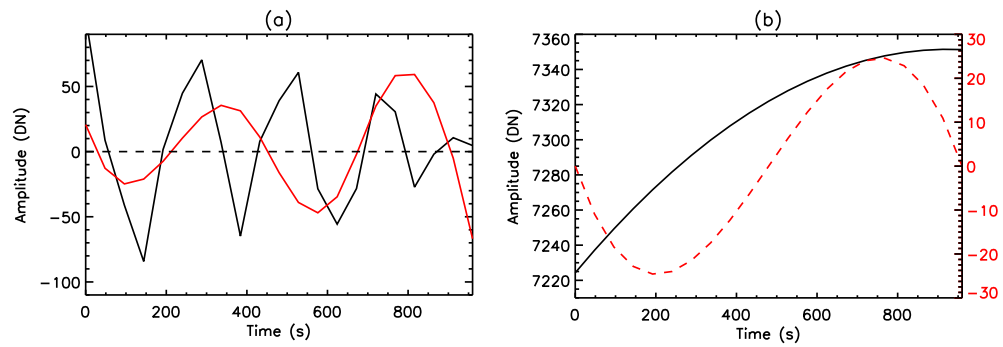


Figure 7: EMD IMF's. (a) IMF_1 (black) and IMF_2 (red) with (b) IMF_3 (red) and IMF_4 (black).

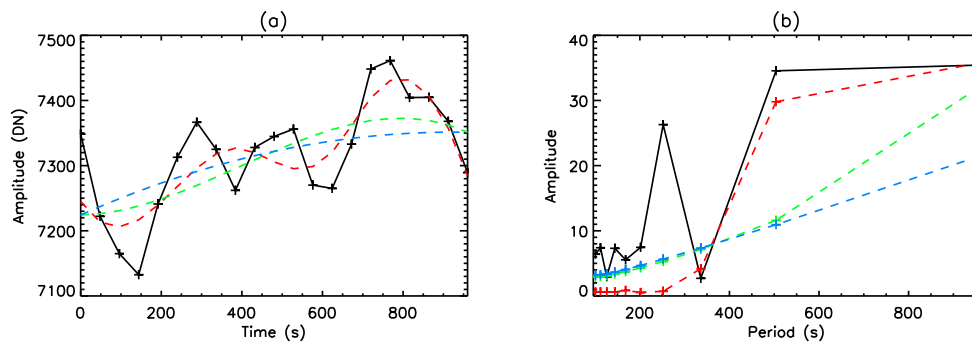


Figure 8: EMD background trends. (a) background trends and (b) FFT's of the trends in (a). Signal (black), $\sum_{i=2}^4 IMF_i$ (red), $IMF_3 + IMF_4$ (green) and IMF_4 (blue).

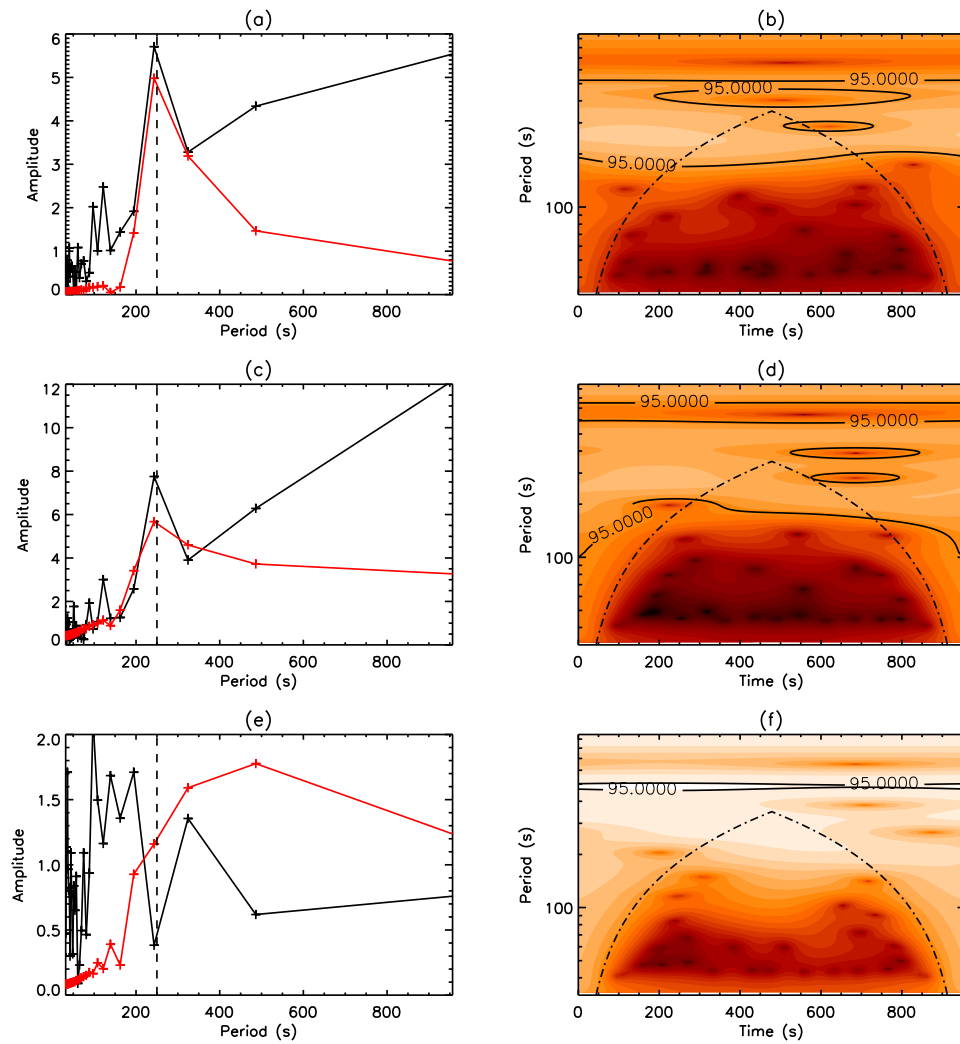


Figure 9: (left) FFT and (right) wavelet analysis of IMF_3 . (a) and (b) O IV (554 Å), (c) and (d) O V (629 Å) and (e) and (f) Mg IX (367 Å).

29th April 2003 - 23:02 UT

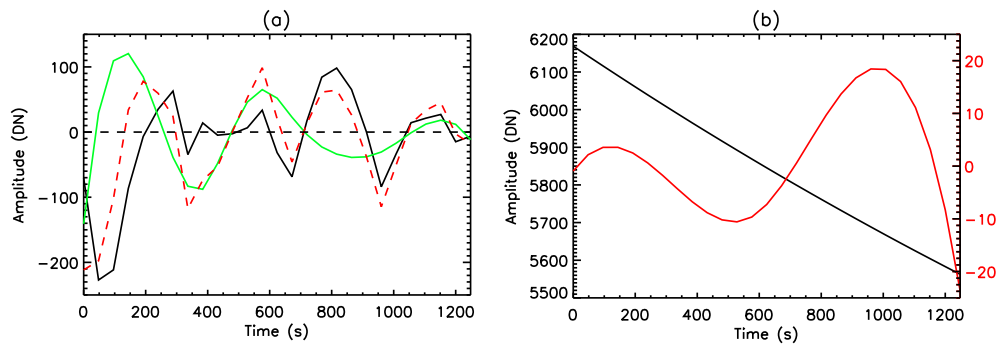


Figure 10: EMD IMF's. (a) IMF_1 (black), IMF_2 (green) and $IMF_1 + IMF_2$ (red) with (b) IMF_3 (red) and IMF_4 (black).

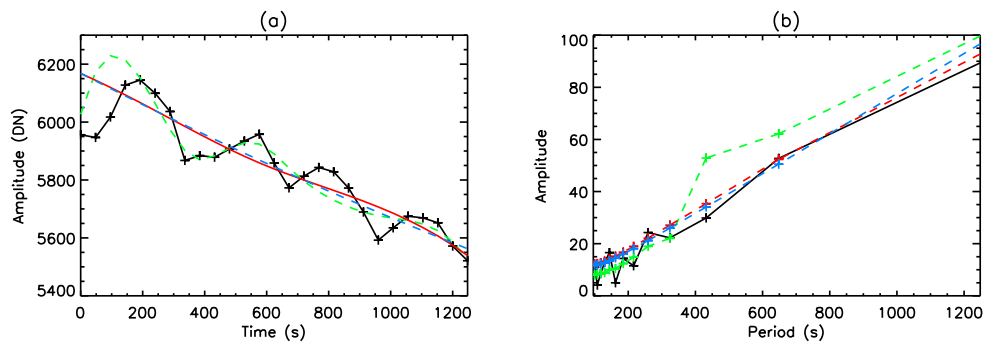


Figure 11: EMD background trends. (a) background trends and (b) FFT's of the trends in (a). Signal (black), $\sum_{i=2}^4 IMF_i$ (green), $IMF_3 + IMF_4$ (red) and IMF_4 (blue).

Bibliography

- Arber, T. D., Longbottom, A. W., Gerrard, C. L., and Milne, A. M. (2001). A Staggered Grid, Lagrangian-Eulerian Remap Code for 3-D MHD Simulations. *Journal of Computational Physics*, 171:151–181.
- Aschwanden, M. J. (2004). The Role of Observed MHD Oscillations and Waves for Coronal Heating. In Walsh, R. W., Ireland, J., Danesy, D., and Fleck, B., editors, *SOHO 15 Coronal Heating*, volume 575 of *ESA Special Publication*, pages 97–+. *****.
- Banerjee, D., Erdélyi, R., Oliver, R., and O’Shea, E. (2007). Present and Future Observing Trends in Atmospheric Magnetoseismology. *Sol. Phys.*, 246:3–29.
- Banerjee, D., Teriaca, L., Gupta, G. R., Imada, S., Stenborg, G., and Solanki, S. K. (2009). Propagating waves in polar coronal holes as seen by SUMER and EIS. *A&A*, 499:L29–L32.
- Berghmans, D. and Clette, F. (1999). Active region EUV transient brightenings - First Results by EIT of SOHO JOP80. *Sol. Phys.*, 186:207–229. *****.
- Bradshaw, S. J. and Mason, H. E. (2003). The radiative response of solar loop plasma subject to transient heating. *A&A*, 407:1127–1138.
- Brynildsen, N., Maltby, P., Kjeldseth-Moe, O., and Wilhelm, K. (2003). Oscillations in the wings of sunspot transition region lines. *A&A*, 398:L15–L18. *****.
- Chorley, N., Hnat, B., Nakariakov, V. M., Inglis, A. R., and Bakunina, I. A. (2010). Long period oscillations in sunspots. *A&A*, 513:A27+.
- Culhane, J. L., Harra, L. K., James, A. M., Al-Janabi, K., Bradley, L. J., Chaudry, R. A., Rees, K., Tandy, J. A., Thomas, P., Whillock, M. C. R., Winter, B., Doschek, G. A., Korendyke, C. M., Brown, C. M., Myers, S., Mariska, J., Seely, J., Lang, J., Kent, B. J., Shaughnessy, B. M., Young, P. R., Simnett, G. M., Castelli, C. M., Mahmoud, S., Mapson-Menard, H., Probyn, B. J., Thomas, R. J., Davila, J., Dere, K., Windt, D., Shea, J., Hagood, R., Moye, R., Hara, H., Watanabe, T., Matsuzaki, K., Kosugi, T., Hansteen, V., and Wikstol, Ø. (2007). The EUV Imaging Spectrometer for Hinode. *Sol. Phys.*, 243:19–61.
- De Moortel, I. (2005). An overview of coronal seismology. *Royal Society of London Philosophical Transactions Series A*, 363:2743–2760. ***.
- De Moortel, I. (2006). Propagating magnetohydrodynamics waves in coronal loops. *Royal Society of London Philosophical Transactions Series A*, 364:461–472.
- De Moortel, I. (2009). Longitudinal Waves in Coronal Loops. *Space Science Reviews*, 149:65–81.
- De Moortel, I. and Bradshaw, S. J. (2008). Forward Modelling of Coronal Intensity Perturbations. *Sol. Phys.*, pages 139–+.
- De Moortel, I. and Hood, A. W. (2000). Wavelet analysis and the determination of coronal plasma proper-

- ties. *A&A*, 363:269–278. *****.
- De Moortel, I. and Hood, A. W. (2003). The damping of slow MHD waves in solar coronal magnetic fields. *A&A*, 408:755–765. ***.
- De Moortel, I. and Hood, A. W. (2004). The damping of slow MHD waves in solar coronal magnetic fields. II. The effect of gravitational stratification and field line divergence. *A&A*, 415:705–715. ***.
- De Moortel, I., Hood, A. W., Gerrard, C. L., and Brooks, S. J. (2004a). The damping of slow MHD waves in solar coronal magnetic fields. III. The effect of mode coupling. *A&A*, 425:741–752. ***.
- De Moortel, I., Hood, A. W., Ireland, J., and Walsh, R. W. (2002a). Longitudinal intensity oscillations in coronal loops observed with TRACE I. Overview of Measured Parameters. *Sol. Phys.*, 209:61–88. *****.
- De Moortel, I., Hood, A. W., Ireland, J., and Walsh, R. W. (2002b). Longitudinal intensity oscillations in coronal loops observed with TRACE II. Discussion of Measured Parameters. *Sol. Phys.*, 209:89–108. *****.
- De Moortel, I., Ireland, J., Hood, A. W., and Walsh, R. W. (2002c). The detection of 3 & 5 min period oscillations in coronal loops. *A&A*, 387:L13–L16. *****.
- De Moortel, I., Ireland, J., and Walsh, R. W. (2000). Observation of oscillations in coronal loops. *A&A*, 355:L23–L26. *****.
- De Moortel, I. and McAteer, R. T. J. (2004). Waves and wavelets: An automated detection technique for solar oscillations. *Sol. Phys.*, 223:1–2. *****.
- De Moortel, I., Munday, S. A., and Hood, A. W. (2004b). Wavelet Analysis: the effect of varying basic wavelet parameters. *Sol. Phys.*, 222:203–228. *****.
- De Moortel, I. and Nakariakov, V. M. (2012). An overview of coronal seismology. *Phil. Trans. A*, accepted/in press.
- De Pontieu, B., Erdélyi, R., and De Moortel, I. (2005). How to Channel Photospheric Oscillations into the Corona. *ApJL*, 624:L61–L64. *****.
- De Pontieu, B. and McIntosh, S. W. (2010). Quasi-periodic Propagating Signals in the Solar Corona: The Signature of Magnetoacoustic Waves or High-velocity Upflows? *ApJ*, 722:1013–1029.
- DeForest, C. E. and Gurman, J. B. (1998). Observation of Quasi-periodic Compressive Waves in Solar Polar Plumes. *ApJL*, 501:L217+. *****.
- Delaboudinière, J.-P., Artzner, G. E., Brunaud, J., Gabriel, A. H., Hochedez, J. F., Millier, F., Song, X. Y., Au, B., Dere, K. P., Howard, R. A., Kreplin, R., Michels, D. J., Moses, J. D., Defise, J. M., Jamar, C., Rochus, P., Chauvineau, J. P., Marioge, J. P., Catura, R. C., Lemen, J. R., Shing, L., Stern, R. A., Gurman, J. B., Neupert, W. M., Maucherat, A., Clette, F., Cugnon, P., and van Dessel, E. L. (1995). EIT: Extreme-Ultraviolet Imaging Telescope for the SOHO Mission. *Sol. Phys.*, 162:291–312.
- Dere, K. P., Landi, E., Mason, H. E., Monsignor Fossi, B. C., and Young, P. R. (1997). CHIANTI - an atomic database for emission lines. *A&AS*, 125:149–173.
- Domingo, V., Fleck, B., and Poland, A. I. (1995). The SOHO Mission: an Overview. *Sol. Phys.*, 162:1–2.
- Erdélyi, R., Petrovay, K., Roberts, B., and Aschwanden, M. (2003). *Turbulence, Waves and Instabilities in the Solar Plasma*. Turbulence, Waves and Instabilities in the Solar Plasma, Eds. R. Erdélyi, K. Petrovay, B. Roberts; and M. Aschwanden, Kluwer Academic Publishers, 2003.

- Erdélyi, R. and Taroyan, Y. (2008). Hinode EUV spectroscopic observations of coronal oscillations. *A & A*, 489:L49–L52. *****.
- Farge, M. (1992). Wavelet transforms and their applications to turbulence. *Annual Review of Fluid Mechanics*, 24:395–457.
- Fedun, V., Erdélyi, R., and Shelyag, S. (2009). Oscillatory Response of the 3D Solar Atmosphere to the Leakage of Photospheric Motion. *Sol. Phys.*, pages 105–+.
- Feldman, U., Mandelbaum, P., Seely, J. F., Doschek, G. A., and Gursky, H. (1992). The potential for plasma diagnostics from stellar extreme-ultraviolet observations. *ApJS*, 81:387–408.
- Fludra, A. (2001). Transition region oscillations above sunspots. *A & A*, 368:639–651.
- Freeland, S. L. and Handy, B. N. (1998). Data Analysis with the SolarSoft System. *Sol. Phys.*, 182:497–500.
- Fröhlich, C., Romero, J., Roth, H., Wehrli, C., Andersen, B. N., Appourchaux, T., Domingo, V., Telljohann, U., Berthomieu, G., Delache, P., Provost, J., Toutain, T., Crommelynck, D. A., Chevalier, A., Fichot, A., Däppen, W., Gough, D., Hoeksema, T., Jiménez, A., Gómez, M. F., Herreros, J. M., Cortés, T. R., Jones, A. R., Pap, J. M., and Willson, R. C. (1995). VIRGO: Experiment for Helioseismology and Solar Irradiance Monitoring. *Sol. Phys.*, 162:101–128.
- Gabriel, A. H., Grec, G., Charra, J., Robillot, J.-M., Roca Cortés, T., Turck-Chièze, S., Bocchia, R., Boumier, P., Cantin, M., Cespédes, E., Cougrand, B., Crétole, J., Damé, L., Decaudin, M., Delache, P., Denis, N., Duc, R., Dzitko, H., Fossat, E., Fourmond, J.-J., García, R. A., Gough, D., Grivel, C., Herreros, J. M., Lagardère, H., Moalic, J.-P., Pallé, P. L., Pétrou, N., Sanchez, M., Ulrich, R., and van der Raay, H. B. (1995). Global Oscillations at Low Frequency from the SOHO Mission (GOLF). *Sol. Phys.*, 162:61–99.
- Gupta, G. R., O’Shea, E., Banerjee, D., Popescu, M., and Doyle, J. G. (2009). On the statistical detection of propagating waves in polar coronal holes. *A & A*, 493:251–257. *****.
- Handy, B. N., Acton, L. W., Kankelborg, C. C., Wolfson, C. J., Akin, D. J., Bruner, M. E., Carvalho, R., Catura, R. C., Chevalier, R., Duncan, D. W., Edwards, C. G., Feinstein, C. N., Freeland, S. L., Friedlaender, F. M., Hoffmann, C. H., Hurlburt, N. E., Jurcevich, B. K., Katz, N. L., Kelly, G. A., Lemen, J. R., Levay, M., Lindgren, R. W., Mathur, D. P., Meyer, S. B., Morrison, S. J., Morrison, M. D., Nightingale, R. W., Pope, T. P., Rehse, R. A., Schrijver, C. J., Shine, R. A., Shing, L., Strong, K. T., Tarbell, T. D., Title, A. M., Torgerson, D. D., Golub, L., Bookbinder, J. A., Caldwell, D., Cheimets, P. N., Davis, W. N., Deluca, E. E., McMullen, R. A., Warren, H. P., Amato, D., Fisher, R., Maldonado, H., and Parkinson, C. (1999). The transition region and coronal explorer. *Sol. Phys.*, 187:229–260.
- Harrison, R. A., Sawyer, E. C., Carter, M. K., Cruise, A. M., Cutler, R. M., Fludra, A., Hayes, R. W., Kent, B. J., Lang, J., Parker, D. J., Payne, J., Pike, C. D., Peskett, S. C., Richards, A. G., Gulhane, J. L., Norman, K., Breeveld, A. A., Breeveld, E. R., Al Janabi, K. F., McCalden, A. J., Parkinson, J. H., Self, D. G., Thomas, P. D., Poland, A. I., Thomas, R. J., Thompson, W. T., Kjeldseth-Moe, O., Brekke, P., Karud, J., Maltby, P., Aschenbach, B., Bräuning, H., Kühne, M., Hollandt, J., Siegmund, O. H. W., Huber, M. C. E., Gabriel, A. H., Mason, H. E., and Bromage, B. J. I. (1995). The Coronal Diagnostic Spectrometer for the Solar and Heliospheric Observatory. *Sol. Phys.*, 162:233–290.
- Huang, N. E., Shen, Z., and Long, S. R. (1999). A NEW VIEW OF NONLINEAR WATER WAVES: The Hilbert Spectrum1. *Annual Review of Fluid Mechanics*, 31:417–457.

- Huang, N. E., Shen, Z., Long, S. R., Wu, M. C., Shih, H. H., Zheng, Q., Yen, N., Tung, C. C., and Liu, H. H. (1998). The empirical mode decomposition and the Hilbert spectrum for nonlinear and non-stationary time series analysis. *Royal Society of London Proceedings Series A*, 454:903–+.
- Huang, N. E., Wu, M., Long, S. R., Shen, S. S. P., Qu, W., Gloersen, P., and Fan, K. L. (2003). A confidence limit for the empirical mode decomposition and Hilbert spectral analysis. *Royal Society of London Proceedings Series A*, 459:2317–2345.
- Huang, N. E. and Wu, Z. (2008). A review on Hilbert-Huang transform: Method and its applications to geophysical studies. *Reviews of Geophysics*, 46:2006–+.
- Ireland, J. and De Moortel, I. (2002). Application of wavelet analysis to transversal coronal loop oscillations. *A & A*, 391:339–351. *****.
- King, D. B., Nakariakov, V. M., Deluca, E. E., Golub, L., and McClements, K. G. (2003). Propagating EUV disturbances in the Solar corona: Two-wavelength observations. *A & A*, 404:L1–L4. *****.
- Kjeldsen, H., Bedding, T. R., Arentoft, T., Butler, R. P., Dall, T. H., Karoff, C., Kiss, L. L., Tinney, C. G., and Chaplin, W. J. (2008). The Amplitude of Solar Oscillations Using Stellar Techniques. *ApJ*, 682:1370–1375. *****.
- Klimchuk, J. A., Tanner, S. E. M., and De Moortel, I. (2004). Coronal Seismology and the Propagation of Acoustic Waves along Coronal Loops. *ApJ*, 616:1232–1241.
- Kneer, F. and Bello González, N. (2011). On acoustic and gravity waves in the solar photosphere and their energy transport. *A & A*, 532:A111+.
- Kohl, J. L., Esser, R., Gardner, L. D., Habbal, S., Daigneau, P. S., Dennis, E. F., Nystrom, G. U., Panasyuk, A., Raymond, J. C., Smith, P. L., Strachan, L., van Ballegooijen, A. A., Noci, G., Fineschi, S., Romoli, M., Ciaravella, A., Modigliani, A., Huber, M. C. E., Antonucci, E., Benna, C., Giordano, S., Tondello, G., Nicolosi, P., Naletto, G., Pernechele, C., Spadaro, D., Poletto, G., Livi, S., von der Lühe, O., Geiss, J., Timothy, J. G., Gloeckler, G., Allegra, A., Basile, G., Brusa, R., Wood, B., Siegmund, O. H. W., Fowler, W., Fisher, R., and Jhabvala, M. (1995). The Ultraviolet Coronagraph Spectrometer for the Solar and Heliospheric Observatory. *Sol. Phys.*, 162:313–356.
- Komm, R. W., Hill, F., and Howe, R. (2001). Empirical Mode Decomposition and Hilbert Analysis Applied to Rotation Residuals of the Solar Convection Zone. *ApJ*, 558:428–441.
- Kosugi, T., Matsuzaki, K., Sakao, T., Shimizu, T., Sone, Y., Tachikawa, S., Hashimoto, T., Minesugi, K., Ohnishi, A., Yamada, T., Tsuneta, S., Hara, H., Ichimoto, K., Suematsu, Y., Shimojo, M., Watanabe, T., Shimada, S., Davis, J. M., Hill, L. D., Owens, J. K., Title, A. M., Culhane, J. L., Harra, L. K., Doschek, G. A., and Golub, L. (2007). The Hinode (Solar-B) Mission: An Overview. *Sol. Phys.*, 243:3–17.
- Lin, S.-L., Tung, P.-C., and Huang, N. E. (2009). Data analysis using a combination of independent component analysis and empirical mode decomposition. *Phys. Rev. E*, 79(6):066705–+.
- Luciani, J. F., Mora, P., and Virmont, J. (1983). Nonlocal heat transport due to steep temperature gradients. *Physical Review Letters*, 51:1664–1667. *****.
- Mariska, J. (2010). EIS Pointing. *Solarsoft IDL EIS Software Notes*, 9.
- Marsh, M. S., Ireland, J., and Kucera, T. (2008). Bayesian Analysis of Solar Oscillations. *ApJ*, 681:672–679. *****.
- Marsh, M. S. and Walsh, R. W. (2006). p-Mode Propagation through the Transition Region into the Solar Corona. I. Observations. *ApJ*, 643:540–548. *****.

- Marsh, M. S., Walsh, R. W., De Moortel, I., and Ireland, J. (2003). Joint observations of propagating oscillations with SOHO/CDS and TRACE. *A&A*, 404:L37–L41. *****.
- Marsh, M. S., Walsh, R. W., de Moortel, I., and Ireland, J. (2004). Longitudinal Oscillations in Coronal Loops - Joint Observations with SOHO/CDS and TRACE. In Lacoste, H., editor, *ESA SP-547: SOHO 13 Waves, Oscillations and Small-Scale Transients Events in the Solar Atmosphere: Joint View from SOHO and TRACE*, pages 519–+. *****.
- Marsh, M. S., Walsh, R. W., and Plunkett, S. (2009). Three-dimensional Coronal Slow Modes: Toward Three-dimensional Seismology. *ApJ*, 697:1674–1680.
- Mazzotta, P., Mazzitelli, G., Colafrancesco, S., and Vittorio, N. (1998). Ionization balance for optically thin plasmas: Rate coefficients for all atoms and ions of the elements H to NI. *A&AS*, 133:403–409.
- McEwan, M. P. and De Moortel, I. (2006). Longitudinal intensity oscillations observed with TRACE: evidence of fine-scale structure. *A&A*, 448:763–770. *****.
- McIntosh, S. W. and Jefferies, S. M. (2006). Observing the Modification of the Acoustic Cutoff Frequency by Field Inclination Angle. *ApJL*, 647:L77–L81.
- Miralles, M. P. (2011). *The Sun, the Solar Wind, and the Heliosphere*, volume 4. IAGA Special Sopron Book Series.
- Morton, R. J., Erdélyi, R., Jess, D. B., and Mathioudakis, M. (2011). Observations of Sausage Modes in Magnetic Pores. *ApJL*, 729:L18+.
- Nakariakov, V. M., Inglis, A. R., Zimovets, I. V., Foullon, C., Verwichte, E., Sych, R., and Myagkova, I. N. (2010). Oscillatory processes in solar flares. *Plasma Physics and Controlled Fusion*, 52(12):124009–+.
- Nakariakov, V. M. and Verwichte, E. (2005). Coronal Waves and Oscillations. *Living Reviews in Solar Physics*, 2:3–+.
- Nakariakov, V. M., Verwichte, E., Berghmans, D., and Robbrecht, E. (2000). Slow magnetoacoustic waves in coronal loops. *A&A*, 362:1151–1157. *****.
- Nightingale, R. W., Aschwanden, M. J., and Hurlburt, N. E. (1999). Time Variability of EUV Brightenings in Coronal Loops Observed with TRACE. *Sol. Phys.*, 190:249–265. *****.
- Ofman, L., Nakariakov, V. M., and Deforest, C. E. (1999). Slow Magnetosonic Waves in Coronal Plumes. *ApJ*, 514:441–447. *****.
- Ofman, L., Nakariakov, V. M., and Sehgal, N. (2000a). Dissipation of Slow Magnetosonic Waves in Coronal Plumes. *ApJ*, 533:1071–1083.
- Ofman, L., Romoli, M., Poletto, G., Noci, G., and Kohl, J. L. (1997). Ultraviolet Coronagraph Spectrometer Observations of Density Fluctuations in the Solar Wind. *ApJL*, 491:L111+. *****.
- Ofman, L., Romoli, M., Poletto, G., Noci, G., and Kohl, J. L. (2000b). UVCS WLC Observations of Compressional Waves in the South Polar Coronal Hole. *ApJ*, 529:592–598. *****.
- Ofman, L. and Wang, T. (2002). Hot Coronal Loop Oscillations Observed by SUMER: Slow Magnetosonic Wave Damping by Thermal Conduction. *ApJL*, 580:L85–L88. *****.
- O’Shea, E. and Doyle, J. G. (2009). On oscillations found in an active region with EIS on Hinode. *A&A*, 494:355–360. *****.
- O’Shea, E., Muglach, K., and Fleck, B. (2002). Oscillations above sunspots: Evidence for propagating waves? *A&A*, 387:642–664. *****.

- Owen, N. R., de Moortel, I., and Hood, A. W. (2009). Forward modelling to determine the observational signatures of propagating slow waves for TRACE, SoHO/CDS, and Hinode/EIS. *A&A*, 494:339–353.
- Peter, H., Gudiksen, B. V., and Nordlund, Å. (2006). Forward Modeling of the Corona of the Sun and Solar-like Stars: From a Three-dimensional Magnetohydrodynamic Model to Synthetic Extreme-Ultraviolet Spectra. *ApJ*, 638:1086–1100.
- Priest, E. R. (1982). *Solar magneto-hydrodynamics*. Dordrecht, Holland ; Boston : D. Reidel Pub. Co. ; Hingham,.
- Robbrecht, E., Verwichte, E., Berghmans, D., Hochedez, J. F., Poedts, S., and Nakariakov, V. M. (2001). Slow magnetoacoustic waves in coronal loops: EIT and TRACE. *A&A*, 370:591–601. *****.
- Roberts, B. (2004). MHD Waves in the Solar Atmosphere. In Lacoste, H., editor, *ESA SP-547: SOHO 13 Waves, Oscillations and Small-Scale Transients Events in the Solar Atmosphere: Joint View from SOHO and TRACE*, pages 1–+.
- Roberts, B., Edwin, P. M., and Benz, A. O. (1984). On coronal oscillations. *ApJ*, 279:857–865. *****.
- Scherrer, P. H., Bogart, R. S., Bush, R. I., Hoeksema, J. T., Kosovichev, A. G., Schou, J., Rosenberg, W., Springer, L., Tarbell, T. D., Title, A., Wolfson, C. J., Zayer, I., and MDI Engineering Team (1995). The Solar Oscillations Investigation - Michelson Doppler Imager. *Sol. Phys.*, 162:129–188.
- Schrijver, C. J., Title, A. M., Berger, T. E., Fletcher, L., Hurlburt, N. E., Nightingale, R. W., Shine, R. A., Tarbell, T. D., Wolfson, J., Golub, L., Bookbinder, J. A., Deluca, E. E., McMullen, R. A., Warren, H. P., Kankelborg, C. C., Handy, B. N., and de Pontieu, B. (1999). A new view of the solar outer atmosphere by the Transition Region and Coronal Explorer. *Sol. Phys.*, 187:261–302.
- Shelyag, S., Erdélyi, R., and Thompson, M. J. (2006). Forward Modeling of Acoustic Wave Propagation in the Quiet Solar Subphotosphere. *ApJ*, 651:576–583.
- Shelyag, S., Zharkov, S., Fedun, V., Erdélyi, R., and Thompson, M. J. (2009). Acoustic wave propagation in the solar sub-photosphere with localised magnetic field concentration: effect of magnetic tension. *A&A*, 501:735–743.
- Singh, J., Hasan, S. S., Gupta, G. R., Banerjee, D., Muneer, S., Raju, K. P., Bagare, S. P., and Srinivasan, R. (2009). Intensity Oscillation in the Corona as Observed during the Total Solar Eclipse of 29 March 2006. *Sol. Phys.*, 260:125–134.
- Taroyan, Y. and Bradshaw, S. (2008). Coronal loop oscillations and diagnostics with Hinode/EIS. *A&A*, 481:247–252. *****.
- Taroyan, Y., Erdélyi, R., Wang, T. J., and Bradshaw, S. J. (2007). Forward Modeling of Hot Loop Oscillations Observed by SUMER and SXT. *ApJL*, 659:L173–L176. *****.
- Terradas, J., Oliver, R., and Ballester, J. L. (2004). Application of Statistical Techniques to the Analysis of Solar Coronal Oscillations. *ApJ*, 614:435–447.
- Tian, H., Xia, L.-D., and Li, S. (2008). Long-period oscillations in solar coronal bright points. *A&A*, 489:741–745. *****.
- Tomczyk, S., McIntosh, S. W., Keil, S. L., Judge, P. G., Schad, T., Seeley, D. H., and Edmondson, J. (2007). Alfvén Waves in the Solar Corona. *Science*, 317:1192–.
- Torrence, C. and Compo, G. P. (1998). A Practical Guide to Wavelet Analysis. *Bulletin of the American Meteorological Society*, vol. 79, Issue 1, pp.61-78, 79:61–78. *****.
- Tsiklauri, D. and Nakariakov, V. M. (2001). Wide-spectrum slow magnetoacoustic waves in coronal loops.

- A & A, 379:1106–1112. *****.
- Uchida, Y. (1970). Diagnosis of Coronal Magnetic Structure by Flare-Associated Hydromagnetic Disturbances. *PASJ*, 22:341–+.
- Verwichte, E., Nakariakov, V. M., Ofman, L., and Deluca, E. E. (2004). Characteristics of transverse oscillations in a coronal loop arcade. *Sol. Phys.*, 223:77–94. *****.
- Wang, T. (2011). Standing Slow-Mode Waves in Hot Coronal Loops: Observations, Modeling, and Coronal Seismology. *Space Science Reviews*, pages 90–+.
- Wang, T. J. (2004). Coronal Loop Oscillations: Overview of Recent Results In Observations. In Lacoste, H., editor, *SOHO 13 Waves, Oscillations and Small-Scale Transients Events in the Solar Atmosphere: Joint View from SOHO and TRACE*, volume 547 of *ESA Special Publication*, pages 417–+. *****.
- Wang, T. J., Ofman, L., Davila, J. M., and Mariska, J. T. (2009). Hinode/EIS observations of propagating low-frequency slow magnetoacoustic waves in fan-like coronal loops. *ArXiv e-prints*.
- Wilhelm, K., Curdt, W., Marsch, E., Schühle, U., Lemaire, P., Gabriel, A., Vial, J.-C., Grewing, M., Huber, M. C. E., Jordan, S. D., Poland, A. I., Thomas, R. J., Kühne, M., Timothy, J. G., Hassler, D. M., and Siegmund, O. H. W. (1995). SUMER - Solar Ultraviolet Measurements of Emitted Radiation. *Sol. Phys.*, 162:189–231.
- Williams, D. R., Phillips, K. J. H., Rudawy, P., Mathioudakis, M., Gallagher, P. T., O’Shea, E., Keenan, F. P., Read, P., and Rompolt, B. (2001). High-frequency oscillations in a solar active region coronal loop. *MNRAS*, 326:428–436. *****.
- Wright, A. N. and Garman, A. R. (1998). MHD wave coupling in the geomagnetic tail with field-aligned density variations. *J. Geophys. Res.*, 103:2377–2384.
- Wu, Z. and Huang, N. E. (2009). Ensemble Empirical Mode Decomposition: A Noise-assisted Data Analysis Method. *Advances in Adaptive Data Analysis*, 1:1–41.
- Wu, Z., Huang, N. E., Long, S. R., and Peng, C.-K. (2007). On the trend, detrending, and variability of nonlinear and nonstationary time series. *Proceedings of the National Academy of Science*, 104:14889–14894.
- Young, P. R., Landi, E., Bromage, G. E., del Zanna, G., Dere, K. P., Landini, M., and Mason, H. E. (2003). CHIANTI – An Atomic Database for UV and X-ray Cool star spectroscopy. In Brown, A., Harper, G. M., and Ayres, T. R., editors, *The Future of Cool-Star Astrophysics: 12th Cambridge Workshop on Cool Stars, Stellar Systems, and the Sun (2001 July 30 - August 3)*, eds. A. Brown, G.M. Harper, and T.R. Ayres, (University of Colorado), 2003, p. 1119-1122., volume 12, pages 1119–1122.
- Yuan, D., Nakariakov, V. M., Chorley, N., and Foullon, C. (2011). Leakage of long-period oscillations from the chromosphere to the corona. *A & A*, 533:A116+.
- Zhang, J., Yan, R., Gao, R. X., and Feng, Z. (2010). Performance enhancement of ensemble empirical mode decomposition. *Mechanical Systems and Signal Processing*, 24:2104–2123.